THE UNIVERSITY OF CHICAGO

ENGINEERING LONG-LIVED RARE EARTH DOPANTS FOR SCALABLE HYBRID QUANTUM INTERCONNECTS

A DISSERTATION SUBMITTED TO
THE FACULTY OF THE DIVISION OF THE PHYSICAL SCIENCES
IN CANDIDACY FOR THE DEGREE OF
DOCTOR OF PHILOSOPHY

DEPARTMENT OF PHYSICS

BY
SHOBHIT GUPTA

CHICAGO, ILLINOIS
AUGUST 2023

Copyright © 2023 by Shobhit Gupta

All Rights Reserved

Dedication Text

In the loving memory of Purrcella.

TABLE OF CONTENTS

LIST OF FIGURES vi

LIST OF TABLES xxi

ACKNOWLEDGMENTS xxii

ABSTRACT xxiv

1 INTRODUCTION 1
1.1 Quantum internet 3
1.2 Quantum interconnects 8
1.3 Optically active solid-state spin defects 9

2 SPIN HAMILTONIAN AND DYNAMICS OF RARE-EARTH IONS 16
2.1 Rare-earth ions in solid state hosts 16
2.2 Spin Hamiltonian of Kramers rare-earth ions 23
2.3 Spin relaxation and decoherence mechanisms 31
2.4 Approaches to mitigate spin decoherence 41

3 ELECTRON SPIN RESONANCE TECHNIQUES 47
3.1 ESR spectrometers 49
3.2 Cavity Quantum Electrodynamics 56
3.3 Continuous Wave ESR 61
3.4 Pulsed ESR 74
3.5 Optically saturated ESR spectroscopy 93

4 SPIN DYNAMICS AND HYPERFINE STRUCTURE OF ERBIUM-DOPED YTTRIUM OXIDE 95
4.1 Introduction 95
4.2 X-Band continuous wave ESR 97
4.3 Spin Hamiltonian fitting 99
4.4 C-band continuous wave ESR 100
4.5 Spin dynamics at cryogenic temperatures (4 Kelvin) 103
4.6 Discussion 107

5 MILLISECONDS COHERENCE TIME OF ERBIUM SPINS IN YTTRIUM OXIDE CERAMICS. 109
5.1 Introduction 109
5.2 Spin dynamics of $^{167}Er^{3+}$:Y_2O_3 at sub-Kelvin temperatures 110
5.3 Spin dynamics in $^{166}Er^{3+}$:Y_2O_3 at sub-Kelvin temperatures 130
5.4 Discussion 132

6 ERBIUM SPINS IN EPITAXIAL YTTRIUM OXIDE THIN FILMS INTERFACED WITH SUPERCONDUCTING RESONATORS 134
6.1 Introduction 134
6.2 Epitaxial Er^{3+}:Y_2O_3 thin film grown on silicon 135
6.3 Low impedance superconducting microwave resonators 135
6.4 Er^{3+} spins in Y_2O_3 thin films with milliseconds coherence time 149
6.5 Towards high cooperatively Er^{3+}spins-resonator coupling 176
6.6 Discussion 184

7 OPTICALLY ADDRESSED SINGLE ERBIUM IN YTTRIUM OXIDE THIN-FILMS 186
7.1 Introduction 186
7.2 Erbium optical transition in yttrium oxide 186
7.3 Cryogenic fiber Fabry-Perot cavity 188
7.4 Er^{3+} ions in C_2 site addressed with fiber cavity 191
7.5 Er^{3+} ions in C_{3i} site addressed with fiber cavity 200
7.6 Comparison of C_2 and C_{3i} site optical homogeneous linewidth 204

8 CONCLUSION AND OUTLOOK 206
8.1 Rare-earth ion-based scalable quantum interconnects 206
8.2 Future directions 208

A APPENDIX 223
A.1 Estimation of magnetic noise sensitivity of transitions using Easyspin 223
A.2 Customized dynamical decoupling 223

REFERENCES 227

LIST OF FIGURES

1.1 An arbitrary quantum state can be represented on a Bloch sphere, defined by two projection angles, θ and ϕ. 2

1.2 A global-scale quantum internet will be composed of nodes connected by photons propagating through a quantum channel. Quantum nodes will contain quantum memories to store and process information while the quantum channel will be implemented by an optical fiber and communication satellites. Image extracted from ref. [138]. 3

1.3 Entanglement creation across a long-distance quantum network using a quantum repeater. A long channel of length L between nodes A and Z is divided into n segments with nodes B-Y across the ends of each individual segment. Entanglement is first generated across the nearest quantum nodes, followed by an iterative entanglement swapping until A-Z are entangled. Image extracted from ref. [157]. 4

1.4 Entanglement generation between atomic ensemble quantum memories in the DLCZ protocol. Image extracted from ref. [157]. 4

1.5 Quantum interconnects implemented using solid-state optically active spin qubits can act as an interface between optical and microwave domain qubits [71] as well as enable long-distance quantum networks using quantum repeaters. 9

2.1 Erbium qubits in bulk crystals implemented with evanescent coupling scheme [140] [128]. (a) The shallow ions(qubits) closer to the surface preferentially driven by the evanescent field are noisier than the ions deep (bulk) within the crystal (b) Comparison of the spin and optical coherence times of Er^{3+} qubits and bulk ensembles in YSO [140] [87] [32] and $CaWO_4$ [128] [48]. 17

2.2 Photonic mode can be confined strongly inside thin films with dimensions smaller than or comparable to the wavelength of light. A mode maxima inside the thin film will preferentially address the ion farther from the surface, potentially leading to long coherence times. 21

2.3 Thin films allow for large-scale heterogeneous integration with superconducting and photonic devices. 22

2.4 The 4f subshell for rare earth ions is highly localized around the nucleus and shielded from the host lattice by the outer shells. 24

2.5 Electron probability density for gadolinium (Gd^{3+}). The unpaired electrons in the 4f subshell exhibit a high degree of localization around the nucleus and are protected from the lattice by 5s, 5p, and 6s subshells. Image extracted from ref. [34]. 25

2.6 Energy level diagram of $^{167}Er^{3+}$ ion. The spin-orbit coupling leads to splitting of ≈ 200 THz between the $^4I_{15/2}$ and $^4I_{13/2}$ levels. Crystal fields of the host further split the spin-orbit levels in Kramers doublets with a typical splitting of THz. . 27

2.7 Electron Zeeman and nuclear hyperfine interaction for a system with S= $\frac{1}{2}$ and I= $\frac{1}{2}$. 28

2.8 Magnetic DC and driving field for a spin system with an anisotropic g tensor. . 32

2.9 Spectral diffusion induced by a spin bath with known composition, density, and flip rates. 39

2.10 Spin polarization (red), spin flip-flop rate(blue), and direct-process(green) spin relaxation rate for a spin at the splitting of 5 GHz as a function of temperature. 42
2.11 Comparison of CPMG sequence performance for a longitudinal initial state with a transverse initial state. The transverse initial state shows an increase in coherence time with pulse separation τ indicating pulse imperfection as the dominant source of decoherence for all τ. On the other hand, for the longitudinal state, the environment-induced decoherence is dominant over pulse errors for most τ. Figure extracted from ref. [177]. 44
2.12 A combination of cryogenic cooling and customized dynamical decoupling can be used to enhance spin coherence times. 45

3.1 Equivalent circuit model of LCR resonators used for electron spin resonance studies in this work. Application of magnetic field (B) results in Zeeman splitting of the electron spins. When the resonance frequency of spin is tuned on resonance with the LCR resonator, the spin can inductively couple to the resonator with a single spin coupling strength g_0. 50
3.2 Comparison of the minimum number of spin N_{spin} sensitivities of three-dimensional metallic cavities used for studying polycrystalline bulk samples and superconducting planar microresonators used for studying thin-films. While three-dimensional cavities offer a sensitivity of $N_{spin} = 10^{13}$, two-dimensional superconducting microresonators offer orders of magnitude higher sensitivity $N_{spin} \lessapprox 10^4$ spins due to their small mode volume and high-quality factor. The estimated $N_{spin} \approx 10^6$ in thin-films makes it necessary to use superconducting microresonators. 51
3.3 Simulated AC magnetic field magnitude of the LGR mode for the two modes of the loop gap resonator (a) Low-frequency mode (b) High-frequency mode 54
3.4 Simulated AC magnetic field magnitude of the LGR mode for an input energy of 1 Joule (a) Side view (b) Top view showing the confinement of AC magnetic field in a uniform region around the central loop. 54
3.5 The measured external quality factor, internal quality factor, and the cavity dip (reflection at resonance frequency) for an aluminum loop gap resonator. The external quality factor (blue) of the loop gap resonator can be tuned by varying the length of the antenna. A longer antenna than L=18 mm corresponded to an overcoupled cavity. The critical coupling point is reached when the internal (orange) and external quality factors (blue) are the same, which corresponds to the narrowest cavity dip (red). 55
3.6 Simulated surface current magnitude (J_{surf}) of the for the two modes of the low impedance superconducting resonator (a) Low-frequency mode with larger current density in the inductor loop (b) High-frequency mode with reduced current density in the inductor. Inset shows the zoomed-in plot around the inductor loop. 56

3.7 MilliKelvin ESR setup used for CW and pulsed studies on bulk samples (a) Schematics of the setup showing the cryogenic components (b) Picture of the cavity mounted on the mixing chamber stage (7-10 mK) (c) Aluminum loop gap cavity with sample mounted (d) Orientation of the DC B field relative to the crystal axes of YSO crystal. 57
3.8 (a) The direction of the applied magnetic field with respect to the MgO crystal axis (b) Reflection spectrum ($S_{11}(\omega)$) of the loop-gap cavity measured as a function of the magnetic field applied along the 100 axes of magnesium oxide shows a strong resonance from Ni^{2+} ions (g=2.24) at 160 mT and a smaller peak from Cr^{3+} ions (g=1.98) at 180 mT. White dashes trace the center frequency of the cavity as the magnetic field is swept across Ni^{2+} resonance (c) Cavity frequency shows dispersive shifts and (d) The cavity linewidth shows absorptive broadening due to resonance with Ni^{2+} and Cr^{3+} spin ensemble. 61
3.9 Continuous wave ESR spectroscopy measures the derivative of the spin ensemble absorption signal on resonance with a microwave cavity. Application of magnetic field brings spin ensemble on resonance with the resonator, resulting in absorption of microwaves. A derivative of the absorption signal obtained by frequency or field modulation is commonly referred to as the ESR signal. 62
3.10 Reflection spectrum of the loop-gap cavity (S_{11}(dB)) measured at 4 Kelvin as a function of the magnetic field applied along the D_1 axis of YSO shows resonance from Nd^{3+} ions in site 1 (g=1.43) and site 2 (g=4.06) of YSO. 63
3.11 Continuous wave ESR on Nd^{3+}:YSO sample showing the cavity dispersive frequency shifts measured as a function of the magnetic field at 30 mK and 4K. The cavity shows larger frequency shift Δf = 150 kHz at 30 mK as compared to Δf = 46 kHz at 4 Kelvin. 65
3.12 Cavity reflection spectrum $|S_{11}(\omega)|$ (a) and the error signal $\epsilon(\omega)$ (b) plotted as a function of the frequency offset from the cavity center. 69
3.13 (a) Experimental setup used for the demonstration of frequency modulation technique for CW-ESR (b) Measured error signal for the microwave cavity (c) Dependence of error signal slope on the frequency modulation (FM) deviation. . . 71
3.14 Continuous wave (CW) ESR obtained by measuring the dispersive frequency shifts of the cavity using the frequency modulation setup. The magnetic field was applied along the D_1 axis of YSO at 4 Kelvin show ESR signal from both $^{142,146,148}Nd^{3+}$ isotopes with I=0 and satellite lines from $^{145}Nd^{3+}$ with 21.1% I=7/2. 73
3.15 Continuous wave (CW) ESR on satellite lines from $^{145}Nd^{3+}$ with 21.1% I=7/2 allows to estimate the minimum number of detectable spins. 74
3.16 Simplified model of a chain of amplifiers with gain G_i and noise temperature T_i with an input noise temperature T_{in}. 77
3.17 The attenuator selection used inside the Bluefors LD 250 dilution refrigerator for experiments in this thesis. The attenuator combination is selected in order to allow a low thermal noise temperature at the 10 milliKelvin stage. 78

3.18 Schematic and operation of a (a) double-sideband mixer and (b) a single-sideband (IQ) mixer. 80
3.19 Schematics of the pulsed ESR setup used for measurements on bulk samples with a 3D microwave cavity. 84
3.20 Simplified schematic of the ESR setup showing the SPDT switch configuration and signal path (a) during spin driving pulses and (b) during spin echo acquisition time. 85
3.21 Spin driving, switch control, and readout pulses generated by the AWG. 86
3.22 Spin dynamics on the Bloch sphere during the spin echo sequence. The spin magnetization is transferred to the XY plane by the first $\pi/2$ pulse, and subsequently, the magnetization undergoes fast decay due to inhomogeneous broadening in the spin ensemble, also referred to as free-induction decay. The inversion pulse is applied at time τ after the first pulse and the dephasing due to inhomogeneity is reversed leading to a spin echo at time 2τ. Image extracted from ref. [139]. . . . 87
3.23 Spin coherence time of Nd^{3+}:YSO at 7 milliKelvin (a) Spin T_2 of 266 mT transition from $^{142,146,148}Nd^{3+}$ isotopes with I=0 (b) Spin T_2 of transition at 257 mT(satellite line) from $^{145}Nd^{3+}$ with 21.1% I=7/2. 89
3.24 Echo detected field sweeps on Nd^{3+}:YSO sample showing two pulse-echo spin signals measured as a function of the magnetic field at 7 mK. The two large peaks between 250 - 300 mK are from two magnetically inequivalent subsites of $^{142,146,148}Nd^{3+}$ isotopes with I=0 and satellite lines are from $^{145}Nd^{3+}$ with 21.1% I=7/2. 90
3.25 Spin relaxation time of Nd^{3+}:YSO at 7 milliKelvin (a) Measurement using inversion recovery approach (b) Measurement using spin echo saturation method. . . 92
3.26 Optically saturated ESR spectrosopy. 94

4.1 (a) CW-ESR spectroscopy provides spin Hamiltonian parameters for an electron spin in the lowest doublet of $^4I_{15/2}$ under magnetic field. Inset Left: Er^{3+} substitutes Y^{3+} in the lower symmetry C_2 site (bottom) and the higher symmetry C_{3i} site (top), Inset Right: Energy levels of g=12.20, 12.28, 3.32, 4.89, and 1.64 for Er^{3+} I=0 isotopes as a function of field (right) as a function of the B field, where X-band transitions are shown with black lines. CW-ESR on natural isotopic purity Er^{3+}:Y_2O_3 shows transitions from C_2 (red) and C_{3i} (blue) closely modelled by simulations. (b) The g = 12.20 levels under close inspection reveal strong lines around 55 mT from I = 0 isotopes of Er^{3+} along with two sets of 8 satellite 5 lines corresponding to $^{167}Er^{3+}$ from C_2 g = 12.28 and C_{3i} g = 12.20. Inset: the g = 12.20 lines from C_2 and C_{3i} show different saturation with power. 98

4.2 (a) $^{167}Er^{3+}$ X-band CW-ESR (black) compared with simulation for C_2 g = 12.28, g = 4.78, g = 1.64 and C_{3i} g = 12.20, 3.28 lines. Simulated spectra using Easyspin [175] show close agreement with the experimental spectrum. The predicted resonance fields for transitions are shown in dashed vertical dashes, grouped together for each g-factor. (b) and (c) $^{167}Er^{3+}$:Y_2O_3 simulated energy levels for (b) C_2 and (c) C_{3i} (blue) sites as a function of the field generated with Easyspin. Red lines show the high-intensity X-band (9.3 GHz) transitions while the grey lines show lower-intensity forbidden transitions. 101

4.3 $^{167}Er^{3+}$ 5 GHz CW-ESR spectrum (black) compared with spectra simulated from C_2 g=12.20, g=4.78 and C_{3i} g=12.2, g=3.28 lines. Simulated spectra. Simulated spectra using Easyspin [175] show close agreement with the experimental spectrum. The predicted transition fields are shown in dashes, grouped together for each g factor. 102

4.4 X-band pulsed ESR on $^{167}Er^{3+}$:Y_2O_3 at 4 K. (a) Echo detected field sweep shows ESR transition from hyperfine levels of C_2 g = 12.28, 4.78 and C_{3i} g = 12.20, 3.28 along with a short-lived broad unresolved signal due to $^{167}Er^{3+}$ interaction. At pulse separation of 1.5 μs only signal from C_{3i} $m_s = +7/2$ remains. (b) C_2 g = 1.64 component shows slow decay and persists up to 3 μs at 4 K while decays completely at 20 K. (c) The echo decay of g = 1.64 signal shows stretched exponential decay corresponding to the coherence time of 24.4 μs superimposed to electron spin echo envelope modulation (ESEEM). (d) The fast Fourier transform of three pulse ESEEM (frequency domain) for g =1.64 component reveals Larmor frequencies for $1^{167}Er^{3+}$ and $^{89}Y^{3+}$ nuclei at 413.9 mT. (e) The integrated area echo decay for C_2 g = 4.89 transition shows a coherence time of 0.5 μs with further improvement to 6.5 μs after applying XY-16-π-XY-16 DD sequence. (f) Instantaneous diffusion measurement on C_2 g = 4.78 and C_{3i} g = 3.28 with slope 0.84 and 0.71 MHz respectively. (g) T_1 measurement on C_2 g = 4.78 and C_{3i} g = 3.28 transition with inversion recovery sequence. 108

5.1 (a) Cryogenic mounting of three dimension loop gap cavity with optical double pass setup on the mixing chamber (10 mK) stage. (b) Schematics of the microwave-optical spectroscopy setup. The Er^{3+} doped Y_2O_3 sample is placed at the center of the microwave cavity, along the optical double pass setup, where it can be addressed with both microwave and optics. The laser was focused on a mirror placed on a nanopositioner below the cavity with a beam spot size on sample $\approx$ 2 mm and reflected light was coupled back to the fiber in a double-pass configuration. 111

5.2 (a), (c) Er^{3+}:Y_2O_3 crystal structure showing the unit cell and Er^{3+} substituting in C_2 and C_{3i} sites, respectively. (b), (d) Zeeman and hyperfine energy levels for $^{167}Er^{3+}$ in C_2 and C_{3i} sites, respectively generated with Easyspin [175]. The red lines show the allowed ESR transitions at 5.67 GHz resonance frequency. (e) MilliKelvin pulsed ESR setup. (f) Echo detected field sweep of $^{167}Er^{3+}$: Y_2O_3 showing predicted transitions as dashes grouped by their g factors. (g) Rabi nutation of echo signal obtained by varying refocusing pulse length. 112

5.3 Electron spin coherence and relaxation times of $^{167}Er^{3+}$: Y_2O_3 at milliKelvin temperatures. (a) Spin lifetime (T_1) (black triangles) was measured using saturation recovery. Spin coherence time measured with two pulse echo (T_2, red dots) and with XY8 dynamical decoupling (T_2^{XY8}, blue triangles) showed coherence times exceeding 1 millisecond spin coherence time (green dashed line) for lower g transitions. Red and blue boxes highlight the longest XY8 and Hahn echo coherence times, respectively. (b) Echo decays for the two transitions with the longest Hahn echo and XY8 coherence times, as highlighted in (a). 114
5.4 Spin coherence time (red, left) and stretch factor(blue, right) of $^{167}Er^{3+}$: Y_2O_3 at milliKelvin temperatures. An increase in stretch factor with the B field is indicative of the predominance of spectral diffusion as a source of decoherence for higher field transitions. 115
5.5 Decoherence mechanisms at sub-Kelvin temperatures for the $^{167}Er^{3+}$ g=1.64 (259 mT) transition. (a) Temperature dependence of relaxation and decoherence processes: spin lifetime (T_1, black dots) fitted with Eq. 5.2 (black line); coherence time (T_2, red dots) fitted with the T_2 model described in the text (red line); XY8 dynamical decoupling coherence time (T_2^{XY8}) measured by sending 30 XY8 pulses. Inset shows time domain Hahn echo decays for the range of temperatures measured. (b) Spectral diffusion was measured with three pulse echoes at a base temperature of 26 mK. 117
5.6 Calibration of sample temperature:(a) Spin echo area and the spin polarization model as a function of temperature (b) Recorded temperature is corrected using spin polarization model (red points). The lowest temperature data points are calculated by linear extrapolation of the corrected temperature model (blue points).119
5.7 (a)Electron spin echo modulation (ESEEM) obtained two pulse-echo measurements for C_2 transition at a field 98.75 mT shows strong modulation of spin echo amplitude due to interaction with $^{89}Y^{3+}$ nuclei. (b) The Fourier transform of echo amplitude reveals a sharp peak around 0.34 MHz due to dipolar interaction between Er^{3+} electron spin and $^{89}Y^{3+}$ nuclei. 123
5.8 Instantaneous diffusion measured at 26 mK by repeating Hahn echo measurement as a function of π pulse power shows no dependence of the spin coherence time on pulse power within uncertainties. 124
5.9 Presence of impurities, defects, and verification of Er for transition around 259 mT in $^{167}Er^{3+} : Y_2O_3$. (a) High-field echo-detected field-swept (EDFS) spectra for $^{167}Er^{3+} : Y_2O_3$ st 4.96 GHz shows the presence of ESR transitions up to 900 mT, with broad peaks around 450 mT (g=0.8) and 500 mT(g=0.7). (b) EDFS spectra taken with continuous wave laser heating show a sharp peak at g = 1.97 corresponding to F^+ center vacancy defect. (c) Er 259 mT transition shows saturation of spin echo in response to pulsed laser resonant with $^{167}Er^{3+} : Y_2O_3$ which is coincident with measured C_2 site optical absorption at the same field. (d) A comparison of the spin echo signal with the sequence of microwave and optical pulses reversed shows a stronger echo, thereby ruling out steady-state heating as a mechanism of spin echo saturation after the optical pulse. 127

5.10 Measurements on undoped Y_2O_3 sample. (a) EDFS spectra of $^{167}Er^{3+} : Y_2O_3$ (black) and undoped Y_2O_3 sample (red). Features from $^{167}Er^{3+}$ including hyperfine lines from g=4.8, 3.3 and g=1.6 plateau (270 mT) are not present in undoped Y_2O_3 sample. Broad impurity transitions are seen in 165-250 mT for both samples. (b) Transition around 259 mT for undoped Y_2O_3, shows 126 ms spin T_1 compared to 730 ms for same field transition in $^{167}Er^{3+} : Y_2O_3$ at similar temperature. 128
5.11 Transition at 259 mT for undoped Y_2O_3, shows 0.86 ms coherence time at 9.3 mK compared to 1.46 ms for same field transition in $^{167}Er^{3+} : Y_2O_3$ at 7.5 mK. 128
5.12 (a) Noise sensitivity (∂E/ ∂B) in units of μ_B for ESR transitions in $^{167}Er^{3+} : Y_2O_3$ at 5.67 GHz for crystallites with magnetic field aligned with the principal axis of the g tensor was simulated using Easyspin. Points with the same color belong to the same site and orientation of crystallite and correspond to different hyperfine transitions. (b) Average noise sensitivity (∂E/ ∂B) in units of μ_B was calculated by averaging over all possible orientations of crystallites that are on-resonant at a given B field. Average (∂E/ ∂B) was found to be $\approx g_{eff}$ indicating electron-nuclear mixing does reduce the magnetic noise sensitivity of the transitions measured at 5.67 GHz. 129
5.13 Dynamical decoupling noise spectroscopy performed on g=1.6 transition of $^{167}Er^{3+} : Y_2O_3$ using a modified setup with high power pulses. Measuring the coherence time under dynamical decoupling sequence $T_{2,DD}$ as a function of pi pulse separation 2τ allows obtaining the noise spectrum of the spectral diffusion noise. 131
5.14 Continuous wave (CW) and Pulsed ESR measurements on purified $^{166}Er^{3+} : Y_2O_3$. Red lines denote the CW-ESR signal and blue lines denote the two pulse echo detected field sweep (EDFS) signal. While all transitions from g=12.2, 3.2, 4.8, and 1.6 are resolved in the CW-ESR spectrum, the EDFS scan showed a stronger signal from the high field(low g transitions). The two pulse echo spin coherence time measurements for different transitions (green dots) show an increase in spin T_2 for the high field transitions. 132

6.1 On-chip superconducting resonators can serve as a sensitive instrument to study small magnetic volume paramagnetic samples such as thin films as discussed in this chapter. Integrating lithographically defined paramagnetic thin cylinders will enable the development of microwave-to-optical transducers, as well as the study of novel physics of spatial spin-spin relaxation. 136
6.2 High-resolution images of the low impedance niobium superconducting resonator on silicon taken with scanning electron microscope (SEM) with increasing levels of magnification from (a)-(d) show the interdigitated finger capacitors in a triangular pattern surrounding the center omega loop inductor. The resonator is capacitively coupled to a superconducting transmission line. 137

6.3 Cryogenic mounting of the superconducting resonator with Er^{3+} doped Y_2O_3 film sample flip-chip mounted (a) A copper PCB (top right) was used to mount the niobium superconducting resonator device (bottom right) consisting of a Er^{3+} doped Y_2O_3 film mounted on a niobium superconducting resonator. The PCB was mounted on a cold finger on the mixing chamber stage (left) (b) A copper holder was used to mount the superconducting device consisting of three niobium superconducting resonators (bottom), each mounted with Er^{3+} doped Y_2O_3 film samples taken from different positions along a slice of Y_2O_3 wafer. The copper holder was also mounted on the mixing chamber stage (top). 138
6.4 (a) Er^{3+} doped Y_2O_3 film sample flip-chip mounted on superconducting resonator using vacuum grease applied to the side of the resonator chip. Wire bond bridges are applied across the transmission line to obtain a common ground throughout the chip (b) Wire bonding of the resonator chip to the copper PCB. 3-4 wire bonds are made between the transmission line pads and the coaxial line on the copper PCB. Additional wire bonds are added between the ground plane of the resonator chip and the chassis ground of the copper PCB. 139
6.5 Simulated single spin coupling above the resonator for spins with $g_{AC} = 7$ a) Device schematic with the sample mounted on the resonator in a flip-chip configuration b) Coupling in the plane z=0.83 μm above the resonator c) Coupling along a cross-section taken in the plane x=20 μm d) Three line cuts from (c) show a decrease in amplitude and an increase in spatial homogeneity of g over the inductor loop with distance z. 141
6.6 Resonator geometry and magnetic field scan angle compared to orientations of the C_2 (cuboid) and C_{3i} (cylinder) sub-sites of Er^{3+} in Y_2O_3. 142
6.7 Pulsed ESR setup used for studying two-dimensional resonators coupled with Er^{3+} doped thin-films. Electronics depicted here include room-temperature electronics and instruments as well as cryogenic amplifiers and isolators. 146
6.8 Processing of the spin echo signal (a) Time domain spin echo signal (I' quadrature) (b) Fast Fourier transform (FFT) of the signal over 1500 ns window. The signal is integrated over a 20 MHz window and the noise background (blue) is estimated by integrating the FFT in two 10 MHz windows to the left and right of the signal integration area (green). The total noise background(blue dash) can be estimated as a sum of the area in green dashes (background 1 and background 2) and is subtracted from the signal to get the background-subtracted signal for each I' and Q' quadrature. 147
6.9 Continuous-wave optimization of the pump power and frequency of the traveling wave parametric amplified (TWPA) (a) Scan of pump power at a fixed frequency of 6.026 GHz (b) Scan of the pump frequency at a fixed power of -7.5 dBm (c) Gain of the TWPA as a function of input signal power (d) Gain of 22 dB in signal and 12 dB in noise floor is observed when TPWA is turned on, leading to a total SNR gain of 10 dB. 148

6.10 Pulsed optimization of the pump power of the traveling wave parametric amplified (TWPA) using CPMG spin echo sequence (a) CPMG signal from C_2 g=3.6 transition with pump off(red) and pump on (blue) (b) Increase in the noise background of the spin echoes with pump power (c) Gain of spin echo area as a function of pump power (d) Total in gain in signal to noise ratio of spin echo. Data in (b)-(d) is normalized with respect to the signal and noise with TWPA off. 150
6.11 (a) Resonator frequency (ω) with magnetic field for different ratios of B_z and B_{xy}. The optimum ratio (orange) corresponds to the weakest dependence of resonator frequency on the magnetic field (b) Resonator intrinsic quality factor (Q_i) with magnetic field for different ratios of Bz and Bxy. The optimum ratio (orange) corresponds to the minimum degradation of the internal quality factor with the magnetic field. 152
6.12 Dispersive coupling of Er^{3+} spin in Y_2O_3 to superconducting resonators. Cavity frequency shows dispersive shifts ($\Delta\omega$) when on-resonant with spins resulting in a characteristic increase of cavity frequency followed by a decrease as the magnetic field is swept. A strong dispersive signal can be clearly resolved for high field transitions with lighter shades of blue(red) representing lower(higher) cavity frequency around zero. White dotted line show predicted transitions based on simulations and yellow dots show the center of the measured transition. . . . 153
6.13 Dispersive coupling signal for $\theta = 40^\circ$ showing transitions from C_2 site at 46 mT, 113 mT, 116 mT and a transition from C_{3i} site at 135 mT. Dashed red lines show the fit to the expression $\Delta\omega = \omega_0 - \Omega^2\Delta/(\gamma_s^2 + \Delta^2)$ used to extract the ensemble coupling strength and inhomogeneous linewidth. The narrowest inhomogeneous linewidth for C_2 site was measured to be 60.1 MHz for the transition at 113 mT. 154
6.14 Absorptive coupling of Er^{3+} spin in Y_2O_3 to superconducting resonators. Absorptive coupling results in a broadening of resonator intrinsic linewidth (Δk_i) when on resonant with spins. Low-field transitions show up with greater contrast in the absorptive scan. White dotted line show predicted transitions based on simulations and yellow dots show the center of the measured transition. 156
6.15 Absorptive coupling signal showing narrowest spin inhomogeneous linewidth measured for Er^{3+} in C_2 site. A Lorentzian fit was performed on the absorptive coupling signal to extract the spin inhomogeneous linewidth (γ), ensemble coupling strength to the resonator (Ω). 157
6.16 Angle dependence of spin inhomogeneous linewidth δg (red dot) and effective g factor squared g^2 (blue triangle) for Er^{3+} ions in two C_2 sub-sites ((a) and (b)) show close agreement with the model (blue, red line) with a similar functional dependence on the angle of the magnetic field θ suggesting strain induced variation of the local environment as a mechanism of inhomogeneous broadening. 157
6.17 Angle dependence of spin inhomogeneous linewidth Γ (red triangle) and ensemble coupling strength to the resonator Ω (blue triangle) for Er^{3+} ions in (a) A C_2 sub-sites and (b) C_{3i} sub-site. 158

6.18 Echo vs field sweep spectrum obtained by performing two-pulse echo measurement at pulse separation τ =4 μs and sweeping field in 100-140 mT range. The large peak at 130 mT corresponds to C_{3i} site while the smaller peaks around 115 mT correspond to C_2 site. 159
6.19 Rabi nutation experiments carried out varying the flip angle of the second pulse for the C_2 transition at 113 mT, 40-degree angle. Increasing the power leads to saturation of the spin echo amplitude due to the spatial inhomogeneity of the resonator driving field [165]. 160
6.20 (a) Spin T_2 for C_2 transition at a field of 113 mT was measured to be 0.17 ms with two-pulse echo and 1.11 ms with CPMG dynamical decoupling (b) Spin T_2 for C_{3i} transition at a field of 130 mT was measured to be 0.38 ms with two-pulse echo and 1.14 ms with CPMG dynamical decoupling. 161
6.21 Spin coherence properties on a wafer scale (a) Samples were taken from three different radial positions (r) with respect to the center of a slice of Er^{3+} doped Y_2O_3 wafer and mounted separately on three spectrally separated microwave resonators coupled to the same transmission line (b) Transmission spectrum of the device at 12.5 mK shows three distinct features from the three resonators (c) Estimated effective Er^{3+} spin density (n_{eff}) and fluctuating magnetic noise amplitude (δB) plotted as a function of distance from the center were obtained from (d) Hahn echo (T_2^{Hahn}, red dots) and CPMG (T_2^{CPMG}, blue dots) spin coherence time and spin lifetime (T_1, black triangles) measurements. Low magnetic noise amplitude δB=11-13 nT is obtained on a wafer-scale with increasing T_2^{CPMG},T_1 indicating a reduction in spin-spin interaction for larger r (edges of the wafer) due to decreased spin spectral density. 165
6.22 Time domain data for the spin coherence properties for C_{3i} transition with g=3.2 for samples taken from different points on the wafer (r) (a) Hahn echo spin T_2 was fitted with a stretched exponential decay $e^{-(2\tau/(T_2))^n}$ with n=2.1,10,2.0 for r=14, 20 and 30 mm respectively (b) CPMG spin coherence time T_2 and (c) Spin lifetime T_1, measurements. 166
6.23 (a) Effective linewidth $\Gamma_{Eff} = 1/\pi T_2$ as a function of waiting time (T_W) obtained by sweeping τ for C_{3i} g=3.2 transition at 130 mT and fitting the linewidth (b) Spin echo area (A) as a function of τ obtained by sweeping waiting time(T_W) for C_{3i} g=3.2 transition at 130 mT. 167
6.24 Spin T_2 temperature dependence measured for the C_{3i} transition at 130 mT with g=3.2 (a) Spin echo area corrected for T_2 fitted to the polarization model (b) $\gamma = 1/T_2$ (blue dots) as a function of corrected temperature (T_{Corr}) and the fitted paramagnetic spin bath induced decoherence model (red line). 168
6.25 (a)Electron spin echo modulation (ESEEM) obtained two pulse-echo measurements for C_{3i} transition at a field 135 mT shows modulation of spin echo amplitude due to interaction with $^{89}Y^{3+}$ nuclei. (b) The Fourier transform of echo amplitude reveals a broad peak centered around 0.55 MHz due to contribution from different $^{89}Y^{3+}$ nuclei. 170

6.26 Identical spin coherence time (T_2^{Hahn}) was measured for C_{3i} g=3.2 transition for different in-plane angle θ corresponding to different g factor of C_2 subsites, thereby confirming the near unity polarization of Er^{3+} C_2 site spin-bath at the base temperature of 12.5 mK. 171
6.27 Spin coherence time with CPMG dynamical decoupling pulses (T_2^{CPMG}) as a function of the number of pulses (N) for samples taken from different positions (r) on the wafer. 173
6.28 Comparison of the spin inhomogeneous linewidth as a function of distance from the center of the wafer (r) for low and high field transitions (a) The inhomogeneous linewidth of a low field transition for the sample closer to the center of the wafer (r=14 mm, blue) compared to the sample farther from the center (r= 20 mm, red). The Er^{3+} spin ensemble far from the center (red) shows at least 3.43 times larger inhomogeneous linewidth than the broadest linewidth measured for a similar transition for the sample closest to the center (blue) (b) The inhomogeneous linewidth for a high field transition for another sample even farther from the center (r= 33 mm, red) compared with the same sample closest to the center (r=14 mm, blue). The sample even farther from the center shows a 5 times broader inhomogeneous linewidth than the same transition for the sample closer to the center (blue). 173
6.29 Magnetic and electrical TLS in rare-earth/superconducting hybrid device (a) A broad g=2 feature was observed along with a smaller satellite peak CW-ESR scans suggesting the presence of magnetic TLS for the device used in Fig 2. The magnetic TLS could be attributed to paramagnetic defects or impurities in the bulk of material or surface spins (b) Electrical TLS: Power-dependent quality factor measurements on three different devices from Fig. 6.21. indicate the presence of electrical TLS (c) Noise sources in rare-earth/superconducting hybrid devices: Magnetic TLS such as paramagnetic impurities, surface spins, defects, Er in different sub-sites, and electrical TLS such as dangling bonds and vacancy defects can be a significant source of loss and decoherence in hybrid devices. 176
6.30 (a) Continuous wave-ESR on high doping sample shows the cavity linewidth as a function of the in-plane angle of the field. The cavity linewidth shows a strong broadening signal, which is consistent with predicted transitions from C_2 site (b) Spin inhomogeneous linewidth of 339.8 MHz was measured for low field transition at -15 degree angle. A relatively large linewidth for the higher Er^{3+} density samples indicates the accumulation of strain and increased spin-spin interaction. 179
6.31 (a) Echo vs field sweep spectrum obtained by performing two-pulse echo measurement as a function of the magnetic field. The peak at 125 mT corresponds to Er^{3+} in C_{3i} site while the peak around 135 mT could be likely from C_2 site (b) Spin coherence time for 125 mT transition was measured to be 4.3 μs with two pulse echo, 37.6 μs with CPMG and 57.3 μs with XY4 dynamical decoupling. 179

6.32 (a) Long spin relaxation time of 3.4 s was measured for the 125 mT transition C_{3i} at 7 milliKelvin (b) Spin relaxation time vs temperature for 125 mT transition. A weak dependence of spin lifetime on temperature up to 90 mK indicates a direct process-dominated spin relaxation. 181
6.33 Threepulse echo measurement on the C_2 125 mT transition. A spin-bath flip rate R of 2.3 kHz measured here is 10 times larger than the measurement on the low-density sample in Section. 6.4.2, indicating a strongly interacting dense Er^{3+} spin-bath. 182
6.34 Noise from rare-earth superconducting interfaces in ESR device (a) Signature of magnetic TLS was observed in CW-ESR scans as g=2 signal along with a smaller satellite peak. The g=2 signal could be attributed to surface spins or paramagnetic specie in the bulk of material while the smaller satellite peak can be attributed to surface hydrogen (b) Measuring spin echo while scanning microwave frequency across the superconducting resonators shows a fast decaying broadband background signal off-resonant to the resonator. This suggests coupling of electrical TLS to superconducting coplanar waveguide (c) Observed electrical TLS signal shows fast relaxation with timescale 5.6 μs (d) Resonator intrinsic quality factor (Q_i) shows weak dependence on intracavity photons $\langle n \rangle$ suggesting interacting TLS. 184

7.1 (a) Schematics of the experimental Er^{3+} qubit device concept. It consists of a tunable cryogenic fiber Fabry-Perot cavity coupled to ${}^4I_{15/2}\, Z_1 \rightarrow {}^4 I_{13/2}\, Y_1$ optical transition of Er^{3+} in Y_2O_3 and a low impedance superconducting microwave resonator coupled to Er^{3+} spin transition at 5.8 GHz. The illustration shows a coplanar superconducting resonator based on niobium. (b) The reflection spectrum of the fiber Fabry-Perot cavity shows a Q of $50,000 - 300,000$ and mode volume of $5(\frac{\lambda}{n})^3$. The superconducting microwave resonator shows low power intrinsic Q of $\approx 12,000 - 370,000$ and an estimated maximum single spin coupling strength $\approx 4\,\mathrm{kHz}$. SNSPD: superconducting nanowire single photon detector; TWPA: traveling wave parametric amplifier; HEMT: high electron mobility transistor. 187
7.2 (a) The cryogenic mount for the fiber Fabry-Perot cavity consists of a bottom mirror and sample sitting on a nanopositioner (b) Fiber with top mirror is mounted on a fiber chuck and nanopositioner is moved to bring the sample in contact with top mirror (c) The cavity operated in $3\lambda/2$ length. The optical mode shows maximum overlap with the Y_2O_3 thin film (d) The cavity can be fine-tuned with piezo voltage with a rate of 1.3 GHz/V. 190
7.3 Photoluminescence after an excitation pulse shows a range of decay rates between a fast and a slow PL decay rate due to a distribution of Purcell enhancement rates among different ions. 191
7.4 Fast and slow PL decay rate, as a function of detuning between the laser and the cavity center show close agreement with the Purcell enhanced T_1 model. 191

7.5 Inhomogeneous linewidth of Er^{3+} in C_2 site. Inset: Total PL counts (N) as a function of cavity detuning from the center of the inhomogeneous line for Er^{3+} in C_2 site. . . . 193
7.6 (a) Sharp lines from single ions from Er^{3+} in C_2 site (b) Fitted linewidth of single ion. . . . 194
7.7 $g^{(2)}(\tau)$ autocorrelation measurement shows anti-bunching close to zero time bin with $g^2(0) = 0.06$ confirming emission from single Er^{3+}. . . . 195
7.8 (a) Purcell enhanced decay time of single ion (T_1=0.14 ms) compared with bulk Er^{3+} (T_1=8.5 ms) in C_2 site corresponds to an enhancement factor of 50.1 (b) Taking into account the branching ratio (β=0.22) of the Er^{3+} optical transition in C_2 site, the effective Purcell factor is F_P = 271.4. . . . 196
7.9 Transient spectral hole burning method measures the spectral diffusion broadened homogeneous linewidth. . . . 196
7.10 Spectral diffusion linewidth measured as a function of laser power shows close agreement with instantaneous spectral diffusion. Red dashed lines indicate fit to the model. . . . 197
7.11 Changing laser detuning from cavity frequency allows tuning of Er^{3+} T_1 . Optical spectral diffusion measurement using transient spectral hole burning at zero fields (black) and 350 mT fields (violet) lines show freezing of magnetic spectral diffusion with an applied magnetic field. . . . 198
7.12 PL counts as a function of laser frequency measurement provides an inhomogeneous linewidth of 48.2 GHz for Er^{3+} in C_{3i} site. . . . 200
7.13 (a) Single ion linewidth of 0.76 MHz was measured for Er^{3+} in C_{3i} site at zero magnetic fields (b) Purcell enhanced decay of single ion compared with bulk Er^{3+} in C_2 site. . . . 201
7.14 Spectral hole half-width shows a strong dependence on (a) magnetic field and (b) laser power (Rabi frequency) for Er^{3+} in C_{3i} site. . . . 203
7.15 Single ion linewidth of Er^{3+} in C_2 compared with the potential single Er^{3+} in C_{3i} site. . . . 205

8.1 Er^{3+} doped Y_2O_3 thin-films provide coherence times rivaling those of their bulk polycrystalline counterparts. Thus Er^{3+} doped Y_2O_3 thin-films offer a material platform that can allow for integration with photonics without degradation of coherence properties as observed in bulk crystals([140] [87] [32] [128] [48]). This is due to a combination of a high-purity film with low impurity and defect concentration, and the controllable doping of erbium away from the interfaces. . 206

8.2 Zero field ZEFOZ transition for Er^{3+} in C_2 site for B field applied along the g_x (g=1.6) direction of the principal axis of the g tensor (a)(b) shows energy levels with zero gradients with the magnetic field (b) Shows the noise sensitivity S_1 (μ_B) as a function of B field for transitions among the energy levels (a) with intensity ≥ 5 % compared to the ESR transition intensity for high field transitions. (d) The transition intensity for high-field ESR transitions approaches 0.6. (e) (f) Zoomed in view of the transition in (c) (d) show the presence of zero fields ZEFOZ transitions with vanishing S1 and non-zero transition intensity, which offer reduced sensitivity to noise approaching zero at 0 fields. 211
8.3 Low field ZEFOZ transition for Er^{3+} in C_2 site for B field applied along the g_z (g=12.2) direction of the principal axis of the g tensor (a)(b) shows energy levels with zero gradients with the magnetic field (b) Shows the noise sensitivity S_1 (μ_B) as a function of B field for transitions among the energy levels (a) with intensity ≥ 5 % compared to the ESR transition intensity for high field transitions. (d) The transition intensity for high field ESR transitions approaches 1. (c) (d) show the presence of zero fields ZEFOZ transitions with vanishing S1 and non-zero transition intensity, which offer reduced sensitivity to noise approaching zero at low fields. 212
8.4 Spectral diffusion limited spin coherence time predicted for Er^{3+} in C_2 site for B field applied along the (a) g_x (1.64) and (b) g_z (g=12.2) direction of the principal axis of the g tensor. The magnetic noise fluctuation (δB) is assumed to be 10 nT, and both first-order (S_1) and second-order coefficients(S_2) are taken into account ($1/T_2 = \pi(S_1\delta B + S_2\delta B^2)$) (c) Shows the predicted coherence time(ms) in heatmap field for zero fields ZEFOZ transitions corresponding to B field applied along g_x (d) Shows the predicted coherence time (ms) for low field ZEFOZ transition for field applied along g_z. While zero field ZEFOZ transitions (c) show the lowest sensitivity to noise allowing for predicted coherence time up to 80 ms, the magnetic noise might be significantly larger than 10 nT due to the presence of an unpolarized spin bath at 0 field. The low field ZEFOZ transition (d) might be advantageous in this regard as the fluctuating magnetic field noise due to paramagnetic spin bath noise might be partially suppressed at low fields. 214
8.5 Pick-and-place method for coupling Y_2O_3 film to the superconducting resonator can lead to gaps between the film and resonator leading to reduced spin-resonator coupling strength g by a factor of 10. 216
8.6 Power dependent quality factor measurements for niobium superconducting resonator with lithographically defined Y_2O_3 cylinder at 20 mK. 217
8.7 TLS model fitting for niobium superconducting resonator with lithographically defined Y_2O_3 cylinder. 217
8.8 Microwave to optical transducer device employing niobium superconducting resonator with lithographically defined Er_2O_3 cylinder and optical fiber Fabry-Perot cavity. 218

A.1 Coherence enhancement with customized dynamical decoupling. (a) Comparison of coherence times under different dynamical decoupling sequences with a common 25 kHz filter center frequency. T_2 for Seq.B shown is an estimated upper bound. (b) Noise spectrum computed from CPMG T_2 measurement and comparison of the filter functions of all sequences. Filters are normalized in the whole spectrum, but, only the 0-50kHz range is shown given the measured noise spectrum range. (c) Customized dynamical decoupling pulse sequences in increasing order of the target ratio of disorder to interaction, along with Seq.B. 224
A.2 Noise spectrum measurement using CPMG sequences. 226

LIST OF TABLES

3.1 Comparison of ensemble coupling strength Ω, and spin inhomogeneous linewidth Γ_{inh}. 65

4.1 Spin Hamiltonian parameters for Er^{3+} I=0 in Y_2O_3. 100
4.2 Spin Hamiltonian parameters for $^{167}Er^{3+}$ I=7/2 in Y_2O_3. 100
4.3 Spin coherence and relaxation time for Er^{3+} I=0 in Y_2O_3 at 4 Kelvin. 106
4.4 Spin coherence and relaxation time for $^{167}Er^{3+}$ I=7/2 in Y_2O_3 at 4 Kelvin. . . 106

6.1 Summary of measured Niobium devices on Silicon at $\approx$ -60 dBm power at 10 milliKelvin. All fit uncertainties are <5 %. 140
6.2 Simulated and measured frequency and quality factor of microwave resonators using in Section. 6.4. 144
6.3 Power dependence fit parameters for superconducting devices used in Fig. 6.21 . 174
6.4 Power dependence fit parameters for superconducting devices used in Fig. 6.30a. 183

8.1 Power dependence fit parameters for superconducting devices patterned around Y_2O_3 cylinder. 215

ACKNOWLEDGMENTS

Starting as a beginner in the field, nearly five years ago, it has been an arduous and fulfilling journey. I would like to thank Prof. Tian Zhong for his exceptional leadership and mentorship, and for providing me with the opportunity to learn spectroscopy and build exciting new tools in the process. I learned a great deal about the value of being efficient and productive with time and resources, asking deeper questions as well as how to give an effective presentation. The opportunity to work on every aspect of a project, be it simulations, cleanroom fabrication, or measurements helped me develop a diverse skillset.

I am grateful to Prof. David Schuster and his lab, including, but, not limited to Dr. Tanay, and Ankur who had been very helpful during the process. I was able to learn a lot about microwave electronics and circuits as well as use the cleanroom recipes developed by the Schuster group, thanks to their openness in sharing the knowledge. I am also thankful to Prof. Tijana Rajh who performed the X-band ESR measurements and greatly helped us with discussions. I would also like to acknowledge collaborators at Corning Inc, Dr. Haitao Zhang, and Dr. Jun Yang, collaborators at Argonne National Lab in Guha Lab, who grew some of the material used in this work, and Prof Richard Warburton and Dr. Natasha Tomm at the University of Basel who helped with preparing the fiber cavity. I would also like to thank my committee members Prof. Jeff McMahon, Prof. Micahel Levin, and Prof. Cheng Chin for their support throughout the process.

My experience in grad school was significantly better due to the community of people around me. I am greatly indebted to Dr. Yizhong Huang, who developed the optical spectroscopy setup, performed the erbium spectroscopy measurements mentioned in this thesis, and provided a great deal of support as a teammate. I will greatly cherish the long work hours spent troubleshooting experiments in the lab, the "one pullup every time your experiment fails" motto, the weeks spent in the machine shop as well as the late afternoon coffee conversations. I would also like to acknowledge Dr. Eilon Poem, Shihan Liu, Yuxi-

ang Pei, and Xuntao Wu all of whom I had the pleasure to work with during the past few years. My fellow grad students roommates Bipul, Suhail, and Ankur were also great support throughout the time.

I am thankful to my family who supported me during the entire period and prioritized my education over their needs. I also would like to dedicate this work in memory of my late cat Purrcella, who was with me during the most challenging yet productive part of my work.

ABSTRACT

This thesis studies rare-earth ions doped in solid-state hosts for scalable quantum interconnects. Rare-earth ions are an ideal candidate for long-distance entanglement between physically distant and disparate quantum systems due to their long spin coherence times and narrow optical linewidths. Among the family of rare-earth elements, trivalent erbium (Er^{3+}) is particularly interesting due to its optical emission in the low-loss telecom C-band used in existing fiber-optic networks. However, prior demonstrations of erbium qubits are limited to dopants in bulk host crystals with either degraded optical coherence or short spin coherence times, which prevent further advancement of this emerging quantum technology.

We develop a new rare-earth qubit platform based on epitaxially grown, single crystal thin films to address these challenges. Specifically, using cavity-enhanced, spin and optical spectroscopy, we demonstrate milliseconds spin coherence times of Er^{3+} qubits in yttrium oxide (Y_2O_3) thin-films and gain an understanding of the environment induced decoherence mechanisms with suitable techniques to mitigate them. We also study the role played by symmetry in protecting erbium from environmental noise and report kHz optical dephasing rate of erbium telecom qubits. These results combined demonstrate a significant prospect of rare-earth qubits in epitaxial single-crystal films as a spin-photon interface for quantum network applications.

CHAPTER 1

INTRODUCTION

Superposition and entanglement are central features of a quantum mechanical description of objects which separate it from a much-familiar classical description of the world. A two-level quantum system with basis states given as $|0\rangle$ and $|1\rangle$, also referred to as qubit can exist in an arbitrary superposition state $|\psi\rangle$ which can be expressed on a two-dimensional Bloch sphere as,

$$|\psi\rangle = (\sin(\theta/2))|0\rangle + \mathrm{e}^{\mathrm{i}\phi}(\cos(\theta/2))|1\rangle \tag{1.1}$$

where ϕ is the angle made from the X-axis and θ is the angle made from the Y-axis of the Bloch sphere (Fig. 1.1). The above state can also be represented in a density matrix formalism as a 2x2 matrix,

$$\rho = \begin{pmatrix} \sin^2(\theta/2) & -(e^{-i\phi}\cos(\theta))/2 \\ (e^{i\phi}\sin(\theta))/2 & \cos^2(\theta/2) \end{pmatrix} \tag{1.2}$$

Interaction with the surrounding environment, however, causes the loss of coherent information contained in the phase(ϕ) of a quantum state, also referred to as decoherence or dephasing [204]. Thus, the timescale associated with the loss of coherence is referred to as phase memory time or coherence time (T_2). The central challenge of quantum information processing is therefore to be able to control individual quantum qubits of a large quantum system while simultaneously suppressing the decoherence due to interaction with the environment.

Entanglement refers to the correlation between quantum states between two such systems A and B such that the state of the joint system A-B $|\psi\rangle_{\mathrm{AB}}$ cannot be decomposed into a tensor product of individual states in the Hilbert state of A and B, $|\psi\rangle_{\mathrm{A}} \otimes |\psi\rangle_{\mathrm{B}}$,

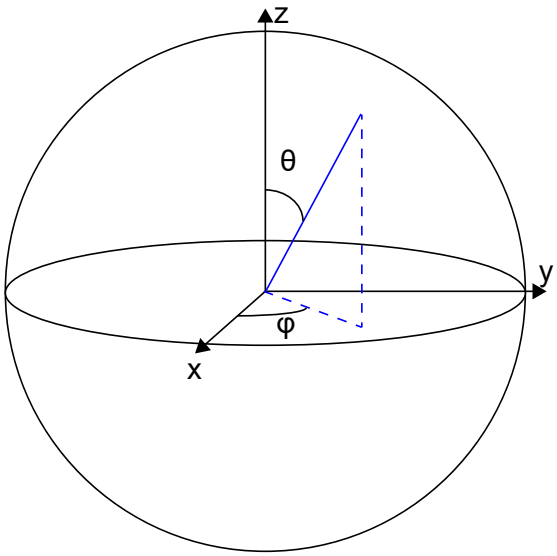


Figure 1.1: An arbitrary quantum state can be represented on a Bloch sphere, defined by two projection angles, θ and ϕ.

$$|\psi\rangle_{\mathrm{AB}} = (\sin(\theta))|0\rangle_{\mathrm{A}} \otimes |1\rangle_{\mathrm{B}} + (\cos(\theta))|1\rangle_{\mathrm{A}} \otimes |0\rangle_{\mathrm{B}} \tag{1.3}$$

The systems A and B here are entangled such that measurements on either of the qubits A or B will project the system into the state $|0\rangle_{\mathrm{A}} \otimes |1\rangle_{\mathrm{B}}$ with probability $\sin^2(\theta)$ and state $|1\rangle_{\mathrm{A}} \otimes |0\rangle_{\mathrm{B}}$ with a probability $\cos^2(\theta)$. Thus, the measurement process will cause the system to project in one of the eigenstates of the measurement basis and cause the loss of entanglement between A and B.

Entanglement between systems thus results in non-local correlations which can be used to transfer quantum states between physically distant quantum systems, performing remote quantum information processing and high-sensitivity quantum sensing and metrology using distant entangled systems. The potential of utilizing superposition and entanglement principles has spurred the growth of quantum technologies such as quantum computing [107], quantum communication [184], quantum sensing [51], and metrology [182]. Entanglement

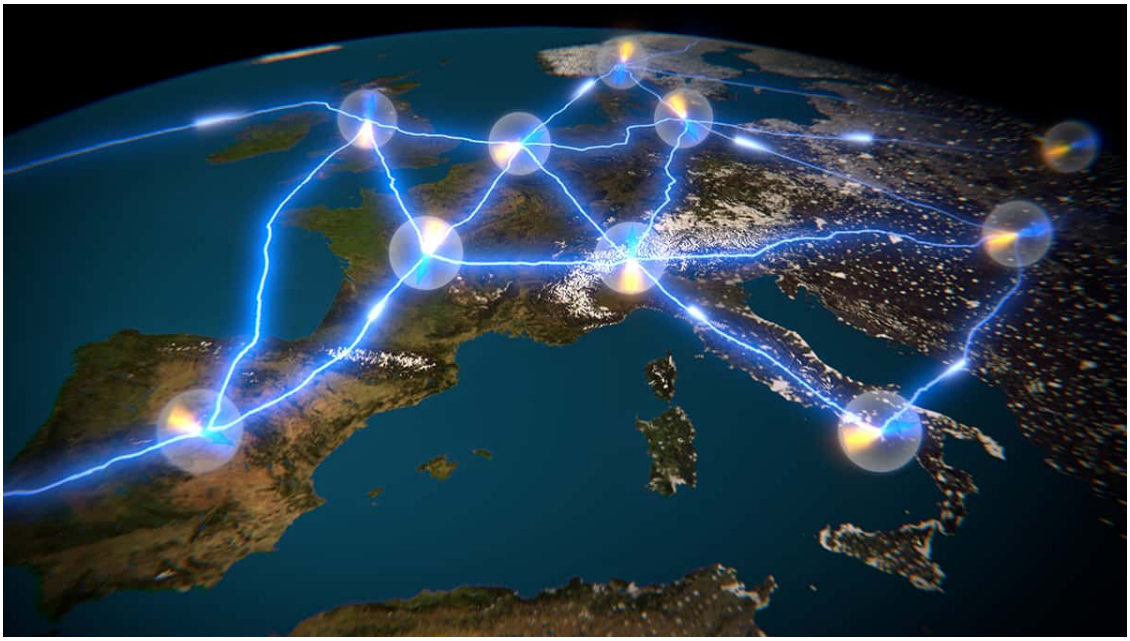


Figure 1.2: A global-scale quantum internet will be composed of nodes connected by photons propagating through a quantum channel. Quantum nodes will contain quantum memories to store and process information while the quantum channel will be implemented by an optical fiber and communication satellites. Image extracted from ref. [138].

of physically distant and disparate qubits is arguably a key to demonstrating large-scale quantum systems which can perform quantum computational, communication, and sensing operations beyond what can be achieved with their classical analogue [17].

1.1 Quantum internet

The quantum internet [44] has been proposed as a network of physically distant nodes connected by a communication channel (Fig. 1.2). The nodes consist of light-matter interfaces such as trapped ions, atoms, defects in solids that can store, and process quantum information, as well as map it onto optical photons. Photons due to their fast transmission speed are ideal flying qubits and information can be encoded in the polarization or the arrival time of photons. The photonic transmission channel could be either free space (satellites) or the optical communication fiber network. Thus entanglement can be established across

physically distant quantum systems across the transmission channel which can be used for quantum teleportation, quantum key distribution, distributed quantum computation as well as quantum sensing [96].

1.1.1 Quantum repeater

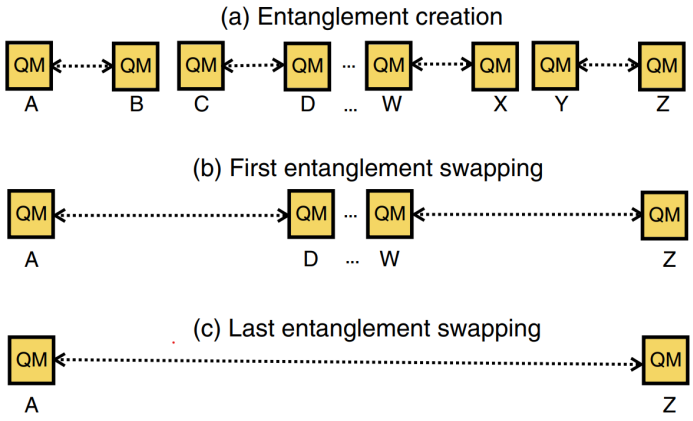


Figure 1.3: Entanglement creation across a long-distance quantum network using a quantum repeater. A long channel of length L between nodes A and Z is divided into n segments with nodes B-Y across the ends of each individual segment. Entanglement is first generated across the nearest quantum nodes, followed by an iterative entanglement swapping until A-Z are entangled. Image extracted from ref. [157].

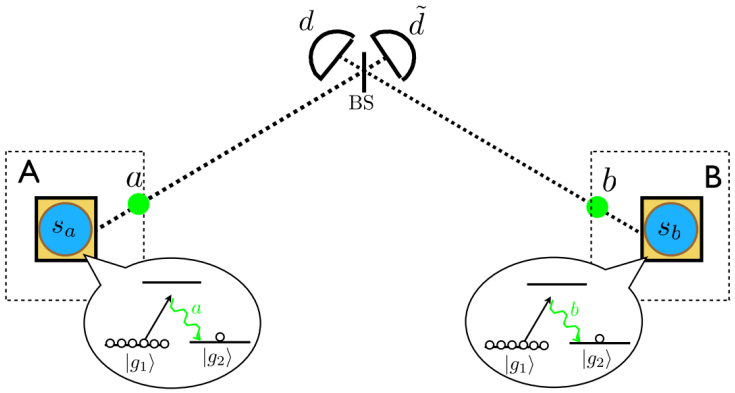


Figure 1.4: Entanglement generation between atomic ensemble quantum memories in the DLCZ protocol. Image extracted from ref. [157].

Optical fiber based quantum network

Fiber-optic communication systems have revolutionized classical information transfer and form the basis of modern communication networks. The pre-existing massive infrastructure of optical cables laid across the globe can be leveraged to implement a large-scale quantum network. However, optical fibers even in the lowest loss telecom C-band have a photon absorption of 0.2 dB/km. This information loss in the channel has been addressed in classical communication through the amplification of photons. However, due to the no-cloning theorem, quantum information cannot be replicated. Therefore photons over a fiber link of 100 km would suffer 20 dB loss or in other words, 1 in 100 photons would be transferred across the channel. The photon loss grows exponentially with distance making it practically challenging to send photon across larger distances. Further, noise in the communication channel such as polarization noise would reduce the fidelity of information carried by a photon.

A quantum repeater corrects for the loss and operations errors induced in the fiber-optic channel [124]. The quantum repeater architecture consists of a communication channel of length L, divided into n segments consisting of n+1 quantum nodes separated by a distance of $L/n \approx$ 100-200 km (Fig. 1.3). The choice of distance is a trade-off between the photon loss induced due to a longer fiber length and the physical infrastructure required to set closely separated nodes. The quantum nodes consist of a quantum memory with an optical interface such that the memory can generate optical photons entangled to the state of the quantum memory. Fig. 1.4 taken from ref. [157] illustrates one such scheme of entanglement generation across the nearest nodes using ensemble quantum memory with a Raman scattering scheme. The photons from two adjacent nodes entangled with their respective quantum memories can be transferred through the optical fiber and interfered with on a 50-50(balanced) beamsplitter followed by detection on one of the two photodetectors. The balanced beamsplitter and two photodetectors together erase the "which-path" information such that the detection of one click on either of the photodetectors would herald the entanglement of the two quantum memories on the adjacent nodes. This process, also referred to as heralded entan-

glement generation (HEG) accounts for the photon loss errors by post-selecting successful entanglement attempts [124]. A successful entanglement creation is followed by classical communication between to the two adjacent nodes. Therefore, the quantum memory needs to be coherent for at least as long as the time taken for two-way classical signaling [124]. Further, in order to erase the which-way information between the photons emitted from the two quantum memories, the photons emitted from the nodes need to be indistinguishable. Thus high-efficiency entanglement generation requires a minimum quantum memory storage time of 1 ms (200 km) and the coherent emission of indistinguishable photons entangled to the memories. Once the quantum memories in adjacent nodes are entangled, the process is repeated iteratively by re-emitting photons stored in the quantum memories until the entanglement is established across the two end nodes (Fig. 1.3).

The entanglement generation protocol described here corresponds to the first generation of quantum repeaters, as described in ref. [124]. The first generation of quantum repeater uses HEG to establish entanglement across adjacent nodes followed by heralded entanglement purification [166] [24] where multiple pairs of low-fidelity entangled qubits are used to generate higher-fidelity entangled pairs. This operation corrects the fidelity loss induced in the communication channel and quantum memory nodes. The second generation of quantum repeater used HEG along with quantum error correction to improve the fidelity of entangled qubit pairs. The third generation of repeaters on the other hand utilizes quantum error correction to correct for both loss and fidelity errors which only required on-way classical signaling, thereby increasing the communication rate. However, this also comes with a requirement of performing high-fidelity CNOT gates as well as high coupling efficiency of photons from their emission from the quantum memory to their detection. Therefore, later generations of quantum repeaters require single qubits coupled with cavities to perform high-fidelity gates. The first generation of quantum repeater on the other hand can also be implemented with an ensemble of atoms where the collective coupling of many atoms can

enhance the light-matter interaction.

1.1.2 Quantum memory

Quantum memory can be implemented with long-lived atomic transitions such that photonic states can be mapped into single or collective excitation of atomic spin or optical states. Quantum memories, most commonly realized as a spin-photon interface are a key component of quantum repeaters required to store and distribute entanglement. Quantum memories can be broadly categorized into 3 types following the discussion in ref. [110].

Linear absorptive memory (LAM)

Linear absorptive memories can be realized through an ensemble of atoms that can map information in photons onto collective atomic excitations by control fields. LAM quantum memory protocols such as electromagnetically induced transparency (EIT) [69], controlled reversible inhomogeneous broadening (CRIB) [5], atomic frequency comb (AFC) [2], and the revival of silenced echo (ROSE) [47] have been widely used to demonstrate high fidelity and bandwidth quantum memory.

Emissive absorptive memory (EAM)

EAM memory protocols involve the emission of a photon to herald the storage of photon excitation in atomic modes. The Duan-Lukin-Cirac-Zoller (DLCZ) scheme [60] has been widely adopted for long-distance quantum communication. The scheme uses a spontaneous Raman scattering process where a write pulse can result in the storage of excitation in shelving states of collective atomic modes followed by the emission of a Stokes photon. The probabilistic emission of the Stokes photon is entangled with the collective excitation of the ensemble. Photons from distant quantum memories in adjacent quantum nodes can be directed to a beamsplitter and a pair of photodetectors to entangle distant quantum

memories. The stored excitations can later be recovered through a second laser using anti-Stokes emission to perform entanglement swapping.

Non-linear atomic memory(NLAM)

Non-linear atomic memories can be implemented in systems with strong photon-atom, and atom-atom interaction [110]. A strong atom-cavity interaction can alter the cavity transmission such that a photon can be reflected off the cavity, leading to a deterministic atom-cavity entanglement. NLAM-based memories have been demonstrated in Rb atoms trapped in a cavity [172], SiV in diamond coupled to nanophotonic resonators [26].

1.2 Quantum interconnects

Quantum interconnects (QuIc) [17] refers to systems and processes that can allow for the transfer of quantum states between physically distant systems as well as between different degrees of freedom and qubit modalities. Quantum interconnects can enable scaling quantum technologies such as quantum computing by connecting physically distant modules, quantum sensing, and metrology by creating a sensor network as well as long-distance quantum communication. Quantum systems such as atomic or vacancy defects in solids that possess an optical transition along with electron and nuclear spin degree of freedom will provide a "one-stop" solution for implementing quantum interconnects. This is for several reasons. Firstly, the electron spins owing to their stronger magnetic moments can act as communication qubits which can allow for establishing entanglement across the nearest nodes of a quantum network. Electron spins precess at 5 GHz at $\approx$ 180 mT magnetic fields, and can strongly couple to microwave frequency photons and phonons which allows them to interface with microwave frequency qubits such as superconducting qubits, silicon/germanium quantum dots. Secondly, nuclear spins owing to their smaller magnetic moment possess significantly longer spin coherence times than electron spins and can be used as a memory qubit

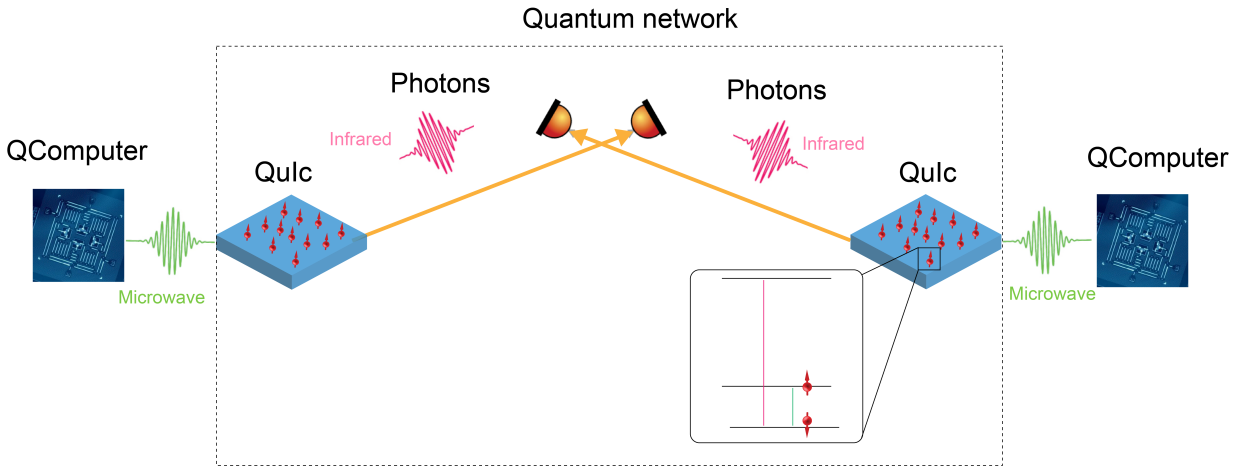


Figure 1.5: Quantum interconnects implemented using solid-state optically active spin qubits can act as an interface between optical and microwave domain qubits [71] as well as enable long-distance quantum networks using quantum repeaters.

for the storage of entanglement for times as long as hours [207] which enables a global-scale long-distance quantum network. Thirdly, an optical transition allows for a fast readout of the electron/nuclear spin states and the generation of photons entangled with the spin states which can be used in quantum communication.

1.3 Optically active solid-state spin defects

Optically active solid-state spin defects possess certain features which make them attractive for implementing quantum interconnects. Firstly, the solid-state hosts provide a stable environment for the spin qubit and do not require additional trapping lasers. Solid-state qubit technologies can be readily integrated with on-chip photonics such as light sources, modulators, and single photon counters which can significantly miniaturize the setup, allowing for scalability, as well as increase the efficiency of information processing. On the other hand, solid-state qubits also have certain challenges. Firstly, the presence of a host environment also comes with additional sources of noise such as paramagnetic defects and impurities, host nuclear spins, and charge traps which can lead to shorter coherence times. Secondly, the deterministic creation of spin defects is still an open challenge. Thirdly, solid-state qubits

integrated with devices can suffer from additional sources of decoherence due to proximity to interfaces that possess a higher density of two-level systems.

1.3.1 Key metrics for solid-state spin defects

Key metrics for evaluating the suitability of optically active spin defects for application in quantum interconnects include a long spin coherence time, emission of indistinguishable coherent photons entangled with spins, scalability, and the ability to interface with different physical degrees of freedom.

Long spin coherence time

A long spin coherence time is necessary in order to implement a quantum memory to account for the latency in the generation of entanglement across nodes and classical signaling. Taking into account the finite time taken to convey classical information between adjacent nodes spaced by 100-200 km, a minimum coherence time of 1 ms is essential for quantum memory. This would enable the establishment of entanglement across the nearest nodes in a quantum network The above requirement however is the bare minimum as several other factors such as the entanglement creation rate would add additional overheads on the coherence time requirements. Further, the establishment of entanglement across multiple nodes would require freeing up the communication qubit and nuclear spin memories would be essential in this regard to store the information. Therefore, electron spins (communication qubits) with a coherence time of a millisecond and nuclear spins (memory qubits) with a coherence time of several hundred milliseconds-seconds would be essential for the development of a large-scale quantum network.

Emission of indistinguishable photons

The emission of indistinguishable photons is required for generating a high-efficiency spin-photon entanglement by erasing the "which-path" information. This requirement can also be expressed as near-transform limited or radiatively limited optical linewidths. In other words, if the optical transition has coherence time $T_2 = 2T_1$, the homogeneous linewidth of the ion is transform-limited. In order to obtain coherent photons, the optical transition decay should be sufficiently fast such that the rate of emission is faster than the timescale of decoherence. While the optical lifetime of an emitter is determined by the atomic defect specie, its charge state, and its local site symmetry in a host, optical cavities can be used to enhance the relaxation of the optical transition through the Purcell effect [12]. Thus, a cavity enhancement of T_1 can be advantageous in obtaining indistinguishable photons.

The two key parameters for the evaluation of the optical transition coherence properties are the Debye-Waller factor (DWF) and quantum efficiency [197]. The Debye-Waller factor describes the ratio of photon emission into a zero-phonon-line (ZPL) to the total emission efficiency. The interaction of an atom in optically excited states with phonons in the host lattice can lead to an incoherent emission of photons also referred to as the phonon-sideband emission while the coherence optical emission free of phonon interactions is referred to as the ZPL. Quantum efficiency on the other hand describes the ratio of events that result in the emission of a photon with all excitation events. An ion in an optically excited state can also decay through non-radiative channels which can result in a reduced efficiency of spin-photon entanglement generation. Thus a high quantum efficiency and high Debye-Waller factor (DWF) are desirable to efficiently generate spin-photon entanglement.

Coupling to physically disparate quantum systems

Coupling to different degrees of freedom such as microwave photons or phonons will allow interfacing quantum systems such as superconducting qubits to an optical quantum net-

work. This will enable scaling quantum computers in a modular scheme and allow for blind distributed quantum computing. However, this requires a high efficiency and high fidelity interface between the optically active spin qubits and superconducting qubits with sufficient bandwidths to allow for the operation of remote quantum gates at speeds comparable to the local qubit gate speeds. Nevertheless, hybrid quantum systems can benefit from leveraging the individual advantages of each qubit modality. For example, superconducting qubits with fast gates can be interfaced with long coherence time spin qubits as a quantum memory.

Scalability

Scalability is a widely used and often an ill-defined metric when describing quantum systems. Scaling quantum systems generally refers to adding more physical qubits which can be used to improve the performance of a quantum computer or quantum repeater by encoding multiple physical qubits with finite error rates into a single logical qubit. Scalability is also key to quantum communication in order to perform operations such as frequency multiplexing, entanglement purification, or quantum error correction to mitigate the photon loss and infidelity induced by the quantum channel and quantum memory decoherence. In this work, scalability primarily refers to the ability to create multiple quantum devices consisting of a superconducting/photonic cavities coupled to optically active spin qubits with long coherence times. This requires a wafer-scale host matrix with a low-noise environment that can allow for large-scale device integration as well as long coherence times.

Additional metrics

In addition to the aforementioned metrics, the list of useful metrics for solid-state spin defects includes:

- Optical transition in the low loss telecom C (1550 nm) or O-band (1300 nm)

- A bright optical emission for fast readout
- Spin selective optical emission
- High cyclicity for the optical readout of the spin state
- A large splitting of the ground state manifold to suppress phonon-induced spin decoherence. Often this requirement can be satisfied in systems with a large spin-orbit coupling.
- Compatibility with liquid helium temperature ($\gtrapprox$ 4 Kelvin) operation

1.3.2 State of the art

A plethora of spin defects have been studied for application in quantum information processing in general and quantum interconnects in particular. While several candidates, in general, satisfy some of the few metrics, no defect system, in particular, satisfied all the aforementioned requirements. This section discusses only a few defect systems for application in quantum interconnects.

1.3.3 Defects in diamond

The most prominent and well-studied system is NV^- center in diamond, which possesses long spin coherence time (seconds [20]), the presence of nuclear spins, the ability to operate at room temperature [75], and a spin-selective fast optical emission ($T_1 \approx$ ns). However, the NV^- center due to its large electric dipole moment is extremely sensitive to charge noise and suffers from strong spectral diffusion of the optical transtion when placed in proximity to interfaces [119] [38]. Further, the optical transition has a large phonon-sideband emission with 3.2 % DWF [7]. The incoherent optical emission makes it challenging to use NV ensembles for applications such as microwave to optical transducers, and ensemble quantum memory.

Further, diamond due to its high refractive index (2.42) presents a challenge for efficient light collection [187] [186]. As of the writing of this work, NV center in diamond remains at the forefront with demonstrations on loophole-free Bell inequality violation [83], heralded entanglement generation [25], and quantum teleportation three-node quantum network [84].

Group (IV) defects in diamonds such as SiV^- [176] [130] [131], and SnV^- [92] [92], have been studied in recent years due to their inversion symmetry leading to first-order insensitivity to electric fields and therefore a highly coherent optical emission (10 %- 80 % Quantum efficiency, 60 %- 80 % DWF) [92]. SiV^-, in particular, possesses an electron-nuclear spin integrated with a nuclear spin quantum memory [173], a highly coherent fast optical emission ($T_1 \approx 1.7$ ns) [65]. However, SiV^-, suffers from extremely fast spin-phonon relaxation due to its small ground state manifold splitting, resulting in requirements of milliKelvin operational temperatures to suppress phonon-induced spin decoherence [130] [176]. Alternative approaches such as straining SiV^-, centers have increased the operating temperature to a few Kelvin by increasing the ground state manifold splittings [170].

1.3.4 Defects in silicon carbide

Defects in silicon carbide (3H/4H/6H) such as the neutral divacancy, silicon vacancy, Cr^{4+} [55], and V^{4+} [196] have been investigated in recent years due to the compatibility of the hosts with commercial semiconductor electronics and good prospects for scalability. The neutral divacancy, in particular, has demonstrated an extremely long electron spin coherence time of 6 s [10], the ability to control nuclear spin as quantum registers [33], and fast optical emission ($T_1 \approx 90$ ns [43]).

Another interesting candidate, V^{4+} in SiC possesses a fast telecom O-band optical emission ($T_1 \approx$ 11-167 ns) [196]. However, the V^{4+} suffers from small ground state splittings leading to fast phonon relaxation in the ground state manifold, requiring milliKelvin temperatures for suppressing phonon-induced spin relaxation [16].

These defects in SiC also suffer from incoherent interaction with phonons resulting in a phonon-sideband emission with a small DWF (3 % -40 %) [43] [196].

1.3.5 Trivalent rare-earth ions

Trivalent rare-earth ions (RE^{3+}) offer extremely coherent optical transitions transition in the 4f subshell with near-unity quantum efficiency and the lack of phonon-sideband. They possess long electron and nuclear spin coherence times, optical transition in the telecom C-band (Er^{3+}), and a large spin-orbit coupling making them compatible with operation at a few Kelvin temperatures. Rare-earth ions have been widely used in optical quantum memory, quantum transduction, and sensing. Rare-earth ions however, lack a spin-selective optical emission and exhibit an extremely weak optical emission ($T_1 \approx$ ms), making it extremely challenging to address single ions without the aid of an optical cavity. Further, state-of-the-art demonstrations have been performed on RE^{3+} doped in bulk crystals, which offer limited prospects for scalability and degraded performance of ions integrated into devices. This work, therefore, focuses on developing a scalable RE^{3+} doped platform which can be used to implement hybrid quantum interconnects.

CHAPTER 2

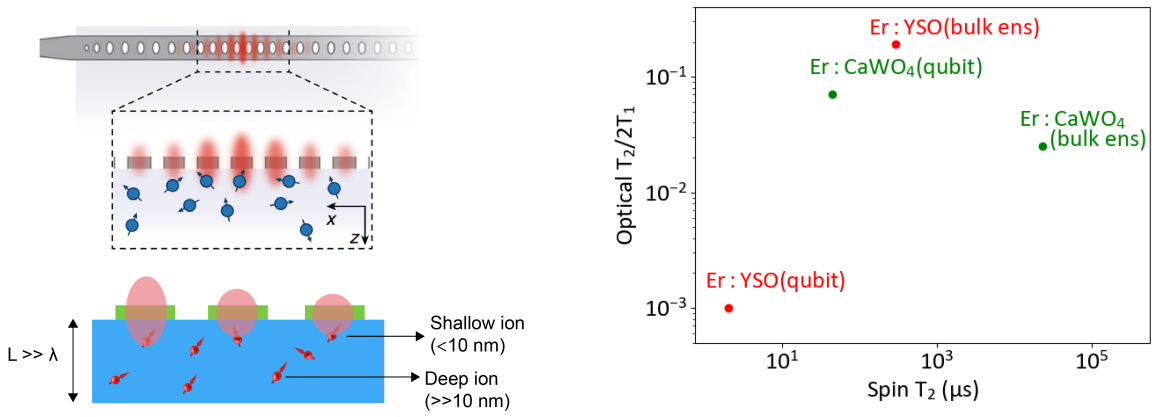
SPIN HAMILTONIAN AND DYNAMICS OF RARE-EARTH IONS

2.1 Rare-earth ions in solid state hosts

Trivalent Rare-Earth (RE^{3+}) ions possess weakly allowed transition in the unpaired 4f subshell which are shielded by the closed 5s, 5p subshells. This leads to remarkably consistent spectroscopic properties of the intra-4f transition across a range of hosts and host crystal fields can be treated as perturbations to the free ion Hamiltonian [114]. The intra-4f subshell transitions also exhibit extremely narrow optical linewidth with near-unity high quantum efficiency at cryogenic temperatures. Rare-earth ion doped in crystals such as YVO_4, Y_2SiO_5, Y_2O_3, YAG, $LiNbO_3$ has been extensively used as laser gain medium, fiber amplifiers and components for optical signal processing and storage such as circulator, electro-optical modulators. Rare-earth crystals lightly doped with ions such as Er^{3+}, Eu^{3+}, Nd^{3+}, Yb^{3+} have been used in recent years for optical quantum memory [209], quantum sensing [102], quantum transduction [194] as well as for demonstrated optically addressed single spin qubits [140]. Moreover, isotopes such as $^{167}Er^{3+}$, $^{153}Eu^{3+}$, $^{171}Yb^{3+}$, $^{143}Nd^{3+}$ possess a non-integer nuclear spin which provides long-lived nuclear spin and hybridized electron-nuclear mixed states with long coherence times approaching 6 hours [207].

2.1.1 Bulk single crystals

Bulk crystals have been the workhorse of the rare-earth community with the longest spin [207] [127] and optical coherence times [32] reported being measured for ensembles of rare-earth ions in bulk crystals. This is due to their high degree of crystallinity which provides the ions embedded deep inside the crystal ($\gtrapprox$ 1μm depth) with a low noise environment relatively free of defects. In order to address a single rare-earth optically, Purcell enhancement of the



(a) (b)

Figure 2.1: Erbium qubits in bulk crystals implemented with evanescent coupling scheme [140] [128]. (a) The shallow ions(qubits) closer to the surface preferentially driven by the evanescent field are noisier than the ions deep (bulk) within the crystal (b) Comparison of the spin and optical coherence times of Er^{3+} qubits and bulk ensembles in YSO [140] [87] [32] and $CaWO_4$ [128] [48].

slow optical emission rate of the intra-4f subshell transition is required. A large size of bulk crystals ($\approx mm^3$), provides a challenge for photonic integration required for addressing single qubits. The two approaches to demonstrate RE qubits involve transferring nanophotonics to the RE surface [40] [140] [54] [128] (Fig. 2.1(a)) or patterning nanophotonic structures on the surface of bulk crystals [210] [209] [98] [153]. While the former approach arguably has greater prospects for scalability, the near-surface ions suffer from excess decoherence due to surface spins, charge traps, and other two-level systems.

Fig. 2.1(b) compares the spin coherence time and the degree of transform-limited optical transition ($T_2/2T_1$) for Er^{3+} qubits in YSO (red) [140] [87] [32] and $CaWO_4$ (green) [128] [48] bulk crystals. While Er^{3+} bulk ensembles (deep ions) in YSO exhibit long spin coherence times and near-transform limited optical linewidths, the measurements on near-surface evanescently coupled Er^{3+} qubits show degradation of both optical and spin coherence properties. This can be explained by a low site symmetry (C_1) of Er^{3+} in YSO which leads to sensitivity of the optical transition to electric fields. Thus, near-surface ions suffer from excess magnetic noise and electric noise from surface spins and charge traps leading to

degraded coherence properties. The degradation of optical coherence properties can be addressed by choosing a host with inversion symmetry such as $CaWO_4$. Er^{3+} qubits in $CaWO_4$ (Fig. 2.1(b)) exhibit optical coherence times rivalling those of ensembles. However, spin the coherence times of Er^{3+} qubits in $CaWO_4$ are 500 times lower than the measurements in the deep ensembles. Out of the 500x discrepancy between the spin coherence times, about 20x can be accounted for by a difference in the measurement temperatures [48] [143], while the remaining 25x indicates the presence of excess paramagnetic impurities in the $CaWO_4$ qubit sample.

Therefore, bulk crystals have limited prospects for scalable integration with nanophotonic/superconducting structures and suffer from degraded coherence properties of RE ions due to surface noise as well as background impurities in the host crystal.

2.1.2 Nanostructured rare-earth doped hosts

While the majority of work has been centered around bulk crystals due to their pristine crystalline properties, nanostructured forms such as nanoparticles, ceramics, and thin films provide a miniaturized host for rare-earth ions which can be readily integrated into nanophotonic/superconducting structures. The close proximity of the RE ion in nanostructure hosts can offer insight into the fast decoherence experienced by near-surface RE qubits in bulk crystals. Nanostructured hosts can suffer from additional decoherence sources other than surface noise, such as higher defect density due to distortion of the lattice, higher impurity concentration, and bulk charge defects [114]. A broader inhomogeneous linewidth reported in low dimensional forms of RE hosts can be advantageous for spectral multiplexing of single qubits and high bandwidth optical memory protocols. Low dimensional hosts can also modify the phononic density of states and thus the RE spin-phonon interaction [115]. Therefore, the study of RE ions in low dimensional hosts can offer insights into decoherence sources of RE ions and allow for the study of novel physics of spin-phonon interactions.

Nanoparticles

Nanoparticles are created either with a bottom-up approach using chemical synthesis or with a top-down approach by grinding bulk crystals. Nuclear spin coherence times exceeding ms have been measured in $^{151}Eu^{3+} : Y_2O_3$ nanoparticles [163] which makes them an interesting candidate for application in quantum memory. Nanoparticles can also allow for the engineering of phonon modes [116] to suppress phonon-induced decoherence. However, nanoparticles can suffer from additional sources of decoherence compared to bulk single crystals such as magnetic two-level systems (TLS), surface charge traps, and elastic two-level systems which can result in broadened optical linewidths [208].

Transparent ceramics

Transparent ceramics can be prepared by sintering nanoparticles at high temperatures and pressures (HIP). Ceramics have demonstrated optical and spin coherence properties rivaling bulk-single crystals [70] [208] which makes them an interesting low-cost alternative to bulk single crystals for application in quantum information processing. Ceramics benefit from the ability to mass produce them using chemical synthesis as compared to Czochralski growth commonly used for single crystals. While long optical coherence times have been measured at sufficiently low temperatures and moderate magnetic fields, ceramics exhibit significant broadening of linewidth due to magnetic and electric TLS. The TLS could partly result from oxygen vacancies in oxide ceramics, as annealing in different oxygen conditions post-HIP process has been shown to mitigate the optical dephasing [208]. Polycrystalline forms such as nanoparticles and ceramics suffer from broad spin inhomogeneous linewidth, as well as broad optical linewidth due to polycrystallinity. This results in limited optical depths, as well as resonance offset errors in spin control due to the overlap of different transitions from different sub-orientations of the crystal grains. These challenges make their application in ensemble-based quantum memory protocol challenging. However, both ceramics and nanoparticles are

promising alternatives for single-emitter-based quantum information processing.

Thin-films

Top-down approaches

Top-down approaches reduce the dimensionality of crystals to obtain monolithic thin films compatible with nanophotonic integration. This approach can help maintain the crystallinity and low noise observed in bulk crystals in thin films. Ion sliced (SmartCut) thin films of lithium niobate (LN) on an insulator have been demonstrated with a long optical coherence time of waveguide coupled Er^{3+} ions on par with bulk crystals [188] and small surface roughness allowing for creating of nanophotonic cavities with quality factors approaching 10^5 [203]. Electro-optical and piezoelectric properties of LN further allow for fast control of optical cavities and the RE emitter. Measurements of single Er^{3+} ions in Smart Cut lithium niobate [203] have however, observed broad homogeneous linewidths, partly attributed to measurement conditions. Lithium niobate thin films implanted with Yb^{3+} ions exhibit broad homogeneous linewidths of the order of 247 MHz [202]. This might indicate the creation of defects due to the implantation of RE ions or the creation of surface noise for ions embedded in nanophotonic structures leading to broad single-emitter linewidths. Further, the creation of strain and additional lattice defects due to the grinding process is conceivable. While long optical coherence time has been measured for an ensemble of RE ions in LN thin films, narrow single emitter linewidths and long spin coherence times are yet to be demonstrated.

Bottom-up approaches: Epitaxial MBE grown thin-films

Er^{3+} doped Y_2O_3 thin films can be grown epitaxially on silicon (111) direction using molecular beam epitaxy [167] technique owing to a small lattice mismatch between Y_2O_3 and Si (111) direction. Yttrium oxide is a low magnetic noise host with the ionic radii of yttrium closely matched to the erbium dopant, making yttrium oxide an ideal choice for host of erbium. Further, yttrium oxide has a rich symmetry of sites, with a low symmetry C_2

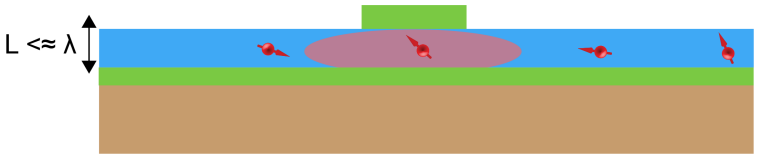


Figure 2.2: Photonic mode can be confined strongly inside thin films with dimensions smaller than or comparable to the wavelength of light. A mode maxima inside the thin film will preferentially address the ion farther from the surface, potentially leading to long coherence times.

site providing a fast emitter control due to a large optical dipole moment as well as a high symmetry site (C_{3i}) providing protection from electric noise due to the lack of permanent electric dipole moment.

The molecular beam epitaxy grown Er^{3+} doped Y_2O_3 films [167] can address several challenges with the state-of-the-art bulk crystals:

Noise environment

Molecular beam epitaxy-grown single-crystal films can provide a noise environment on par with or exceeding bulk crystals. This is due to a control of the noise environment through a high-purity single-crystal growth relatively free of paramagnetic defects and impurities and the ability to control the positioning of the RE ion away from noisy crystal interfaces. The former leads to a low noise environment in the bulk of the crystal while the latter reduces the effect of noise from the surface/interface. Further, thin films with dimensions equal to or smaller than the light wavelength can allow strong confinement of photonic mode inside the material which preferably addresses ions inside the bulk of the film as compared to noisier near-surface noise (Fig. 2.2).

Heterostructure integration

Thin films allow for easier heterogeneous integration with nanophotonics, superconducting circuits, and surface acoustic wave resonators. This is enabled by a small thickness (thickness

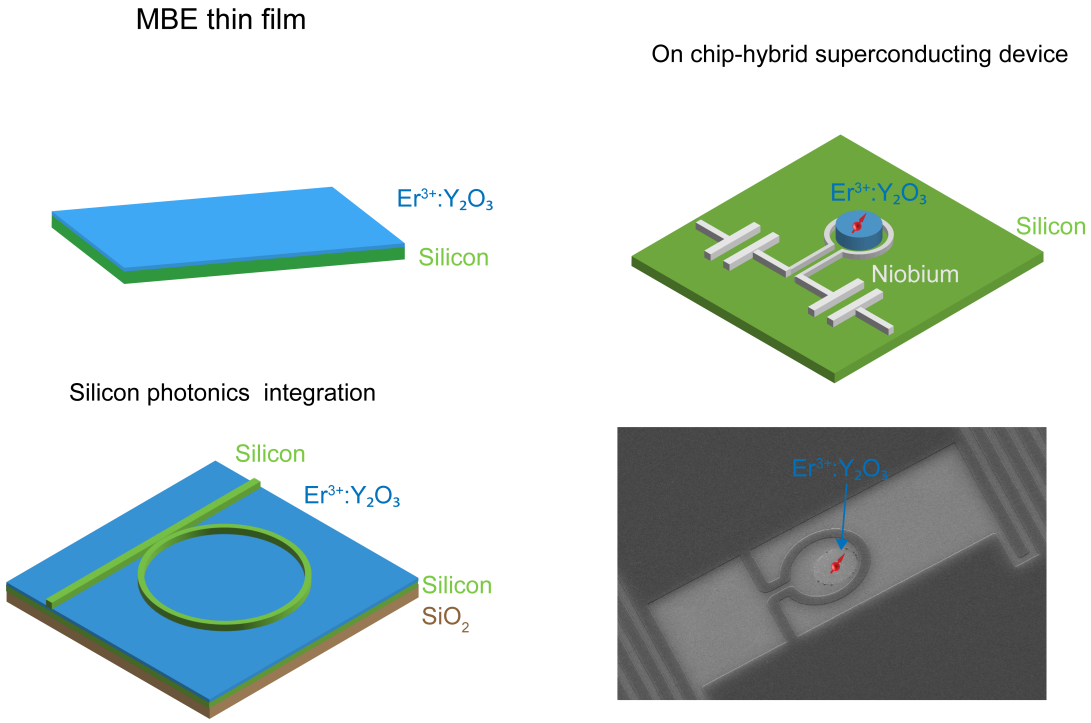


Figure 2.3: Thin films allow for large-scale heterogeneous integration with superconducting and photonic devices.

$\lessapprox$ 1500 nm) of the film, which can confine optical modes of fiber Fabry-Perot cavities or nanophotonics cavities where typical mode dimensions are $\lessapprox \lambda = 1.5$ μm. Thin films also have advantages for coupling to surface acoustic waves, where scattering due to the presence of bulk acoustic wave modes can be avoided and a good overlap of the surface acoustic wave mode with nanophotonic cavity and thin film can be simultaneously obtained. While certain oxide hosts can have a high microwave loss tangent, which could be detrimental for coupling to superconducting resonators, thin films can be patterned into lithographically defined structures to avoid overlap with capacitive elements of the resonator.

2.2 Spin Hamiltonian of Kramers rare-earth ions

The spin Hamiltonian of an ion with atomic number Z and N number of electrons in the absence of external fields can be described as [114],

$$\mathcal{H} = \mathcal{H}_{\mathcal{O}} + \mathcal{H}_{\mathcal{C}} + \mathcal{H}_{\mathcal{SO}} \tag{2.1}$$

where,

$$\mathcal{H}_{\mathcal{O}} = \sum_{i=0}^{N} \frac{\hbar^2}{2m}\Delta_i^2 - \sum_{i=0}^{N} \frac{Ze^2}{r_i} \tag{2.2}$$

$$\mathcal{H}_{\mathcal{C}} = \sum_{i<j} \frac{e^2}{r_{ij}} \tag{2.3}$$

$$\mathcal{H}_{\mathcal{SO}} = \sum_{i}^{N} \xi(r_i) l_i \cdot S_i \tag{2.4}$$

The first term $\mathcal{H}_{\mathcal{O}}$ describes the kinetic energy and potential energy of N electrons interacting with a nucleus with charge Ze. The second term $\mathcal{H}_{\mathcal{C}}$ represents the Coulomb repulsion between electrons and the third term $\mathcal{H}_{\mathcal{SO}}$ describes the spin-orbit coupling interaction with the spin-orbit coupling term $\xi(r_i)$ for each electron. Due to the highly localized nature of the 4f subshell, the intra-4f transitions can be treated by a combination of the theory of atomic spectroscopy to determine the energy level structure of a free ion and point group theory to determine the symmetry and energy of crystal field splitting in a host matrix [114]. Under the central field approximation, the potential of a nucleus and the average potential of N-1 electrons can be represented by an average central potential $\mathrm{U(r_i)}$ such that $\mathrm{U(r_i)} = -\sum_{\mathrm{i=0}}^{\mathrm{N}} \frac{\mathrm{Ze^2}}{\mathrm{r_i}} + \langle \sum_{\mathrm{i<j}} \frac{\mathrm{e^2}}{\mathrm{r_{ij}}} \rangle_{\mathrm{j}}$. The solutions to the free-atom Hamiltonian $\mathcal{H}_{\mathcal{F}} = \sum_{i=0}^{N} \frac{\hbar^2}{2m}\Delta_i^2 + U(r_i)$ can be found in terms of the free-electron wavefunction by Hatree-

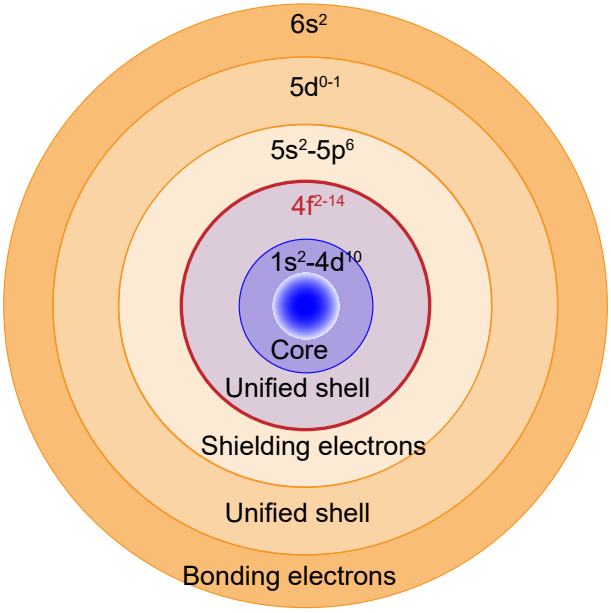


Figure 2.4: The 4f subshell for rare earth ions is highly localized around the nucleus and shielded from the host lattice by the outer shells.

Fock method [156].

2.2.1 Spin-orbit coupling

Spin-orbit interaction is a result of coupling between the spin and orbital angular momentum and the spin-orbit interaction Hamiltonian can be represented as,

$$\mathcal{H}_{\mathcal{SO}} = \lambda \mathbf{S} \cdot \mathbf{L} \tag{2.5}$$

where λ is the spin-orbit coupling strength, $\mathbf{L} = \sum_{\mathbf{i}} \mathbf{l_i}$ and $\mathbf{S} = \sum_{\mathbf{i}} \mathbf{S_i}$ are the product of individual electron orbital and spin angular momentum and the total angular momentum is defined as $\mathbf{J} = \mathbf{L} + \mathbf{S}$. The spin-orbit interaction scales as Z^4 and therefore lighter elements follow the L-S coupling scheme, and heavier elements with stronger interaction follow the j-j coupling scheme. Rare earth elements with atomic numbers between 57 -71 belong to the intermediate coupling scheme [114]. The $4f^n$ subshell (Fig. 2.4, Fig. 2.5) in rare-earth ion is

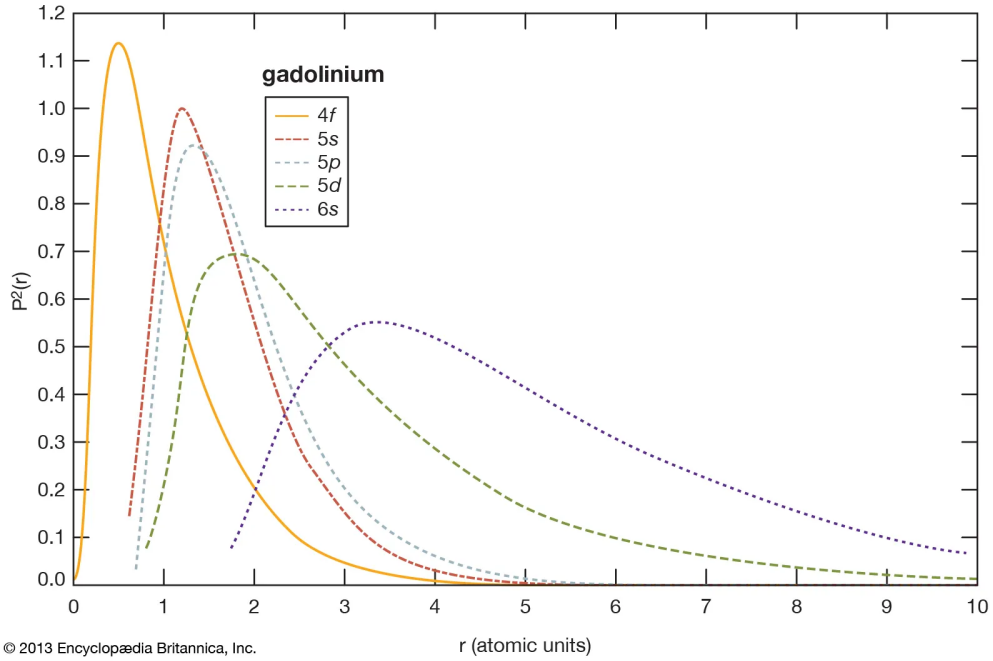


Figure 2.5: Electron probability density for gadolinium (Gd^{3+}). The unpaired electrons in the 4f subshell exhibit a high degree of localization around the nucleus and are protected from the lattice by 5s, 5p, and 6s subshells. Image extracted from ref. [34].

localized around the nucleus and shielded from the lattice by the closed $5s - 5p$ subshells, which results in phenomenal optical properties of the intra-4f subshell transition.

2.2.2 Crystal field splitting

Electric fields from the host lattice break the symmetry of the atom in free space, resulting in the splitting of the spin-orbit levels $^{2S+1}L_J$ further up to $J + 1/2$ crystal field doublets, with the splitting depending on the strength and symmetry of the crystal field. The crystal field Hamiltonian is written as [88],

$$\mathcal{H}_{\mathcal{CF}} = \sum_{k,q} B_q^k C_q^{(k)} \tag{2.6}$$

where B_q^k are coefficients corresponding to the spherical tensor operator $C_q^{(k)}$. Solving for $\mathcal{H}_{\mathcal{CF}}$ for a given spin-orbit manifold $^{2S+1}L_J$ would provide the crystal field levels.

Fig. 2.6 shows the relevant energy levels for $^{167}Er^{3+}$ ion. The ground state spin-orbit level $^4I_{15/2}$ splits into $J + 1/2 = 8$ Kramers doublets, labelled as Z_1 to Z_8. Similarly the first excited spin-orbit level $^4I_{13/2}$ splits into 7 Kramers doublets, labeled as Y_1 to Y_7 and the 1.5 μm optical transition studied in the thesis corresponds to the transition between the lowest crystal fields levels of $^4I_{15/2}$ (Z_1) and $^4I_{13/2}$ (Y_1). The degeneracy of the lowest $^4I_{15/2}$ doublet Z_1 is further lifted under an external magnetic field into spin-up and spin-down levels with a typical splitting of 5 GHz at 60 mT assuming at typical g factor of 6. The presence of nuclear spin I=7/2 for $^{167}Er^{3+}$ leads to hyperfine sublevels with a splitting of ≈ 0.6 GHz. The hyperfine sublevels of $^4I_{13/2}$ Y_1 states are not displayed in Fig 2.6 for clarity.

The typical crystal field splitting between the Z_1 and Z_2 is $\approx$ THz [149] for hosts with sufficiently low symmetry crystal fields [86]. This splitting corresponds to an equivalent temperature ($T = \Delta E/k_B$) of 48 K. Therefore at cryogenic temperatures (T <10 K), only the lowest lying $^4I_{15/2}$ doublet Z_1 is occupied and the system can be approximated as an effective electron spin 1/2.

2.2.3 Electron Zeeman interaction

The electron Zeeman interaction resulting from the interaction of the electron spin with an external magnetic field is defined as,

$$\mathcal{H}_{Ze} = \mu_e \mathbf{B} \cdot \mathbf{g} \cdot \mathbf{S} \tag{2.7}$$

where $\mathbf{B}$ is the magnetic field vector, $\mathbf{S}$ is the spin operator, $\mathbf{g}$ is a rank-2 tensor with components g_{ij} where i and j could be x, y or z. The g tensor is diagonal with respect to its principle axis, with only three non-zero components g_{xx}, g_{yy} and g_{zz}. The full determination of the g tensor and its principle axis for a rare-earth ion involves magnetic field sweeps performed at different angles of the B field with respect to the crystal axis. Polycrystalline

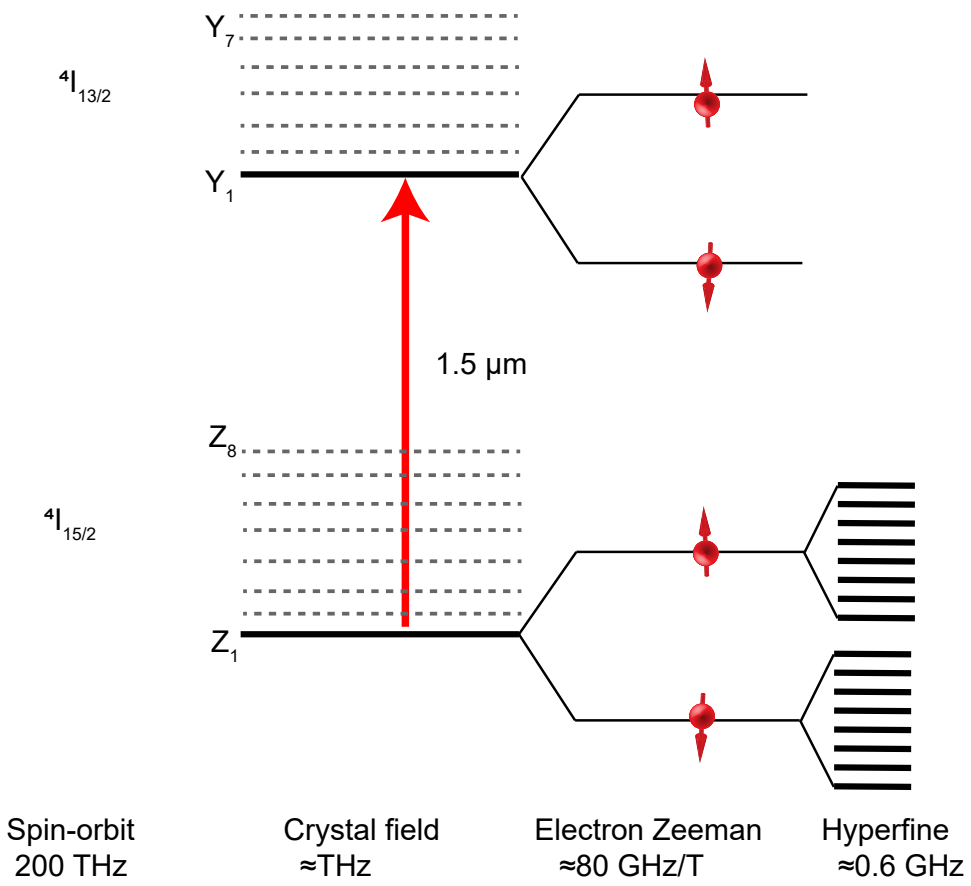


Figure 2.6: Energy level diagram of $^{167}Er^{3+}$ ion. The spin-orbit coupling leads to splitting of $\approx$ 200 THz between the $^4I_{15/2}$ and $^4I_{13/2}$ levels. Crystal fields of the host further split the spin-orbit levels in Kramers doublets with a typical splitting of THz.

samples could be alternatively used to obtain the g tensor as the features in the ESR spectra of a polycrystalline sample correspond to the principal values of the g tensor [190]. However, the information on the orientation of the principle axis of the g tensor cannot be obtained from the ESR spectra of polycrystalline samples.

A strong spin-orbit interaction results in the mixing of the spin and orbital angular momentum and thus the modification of the g from the free electron g value of $g_e = 2.0023$. The correction to the free electron g due to spin-orbit interaction can be calculated using second-order perturbation theory as [190],

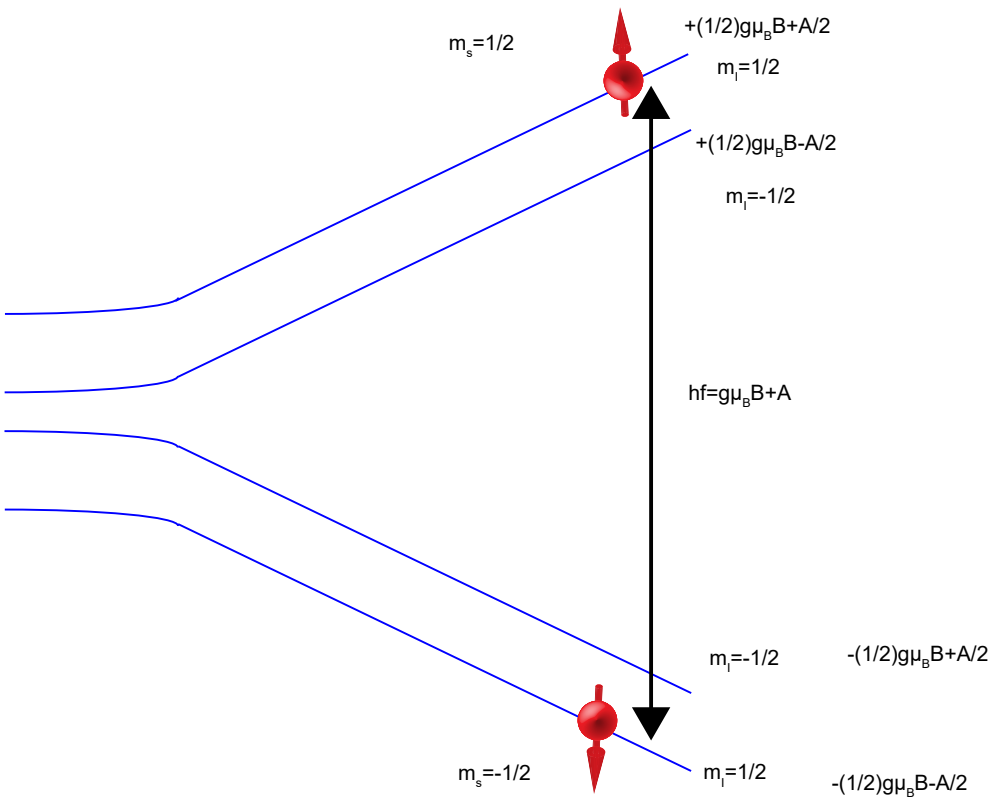


Figure 2.7: Electron Zeeman and nuclear hyperfine interaction for a system with S= $\frac{1}{2}$ and I= $\frac{1}{2}$.

$$\mathbf{g} = g_e\mathbf{I} + 2\lambda\mathbf{\Lambda} \tag{2.8}$$

where λ is the spin-orbit coupling, $\mathbf{\Lambda}$ is a matrix introducing mixing due to orbital levels, given as ,

$$\Lambda_{ij} = -\sum_{n\neq G} \frac{\langle G|L_i|n\rangle\langle n|L_j|\rangle}{E_n^0 - E_G^0} \tag{2.9}$$

where G is the spin-orbit ground state, n is summed over the spin-orbit levels split under the crystal field of the host, E_n^0 are their corresponding energy eigenvalues, and L_i and L_j are orbital angular momentum operators. The g tensor of Kramers rare-earth ions is therefore highly anisotropic in low symmetry sites.

2.2.4 Hyperfine interaction

Hyperfine interaction between electron and nuclear spins results from two components, an isotropic contact term, and an anisotropic dipolar term [190],

$$\mathcal{H}_{HF} = \mathcal{H}_{Iso} + \mathcal{H}_{dip} \tag{2.10}$$

The isotropic term can be further written as,

$$\mathcal{H}_{Iso} = A_0 \mathbf{S} \cdot \mathbf{I} \tag{2.11}$$

The dipolar term can be written as,

$$\mathcal{H}_{dip} = -\frac{\mu_0}{4\pi} g_e g_n \beta_e \beta_n \Big(\frac{\mathbf{S} \cdot \mathbf{I}}{r^3} - 3 \frac{(\mathbf{S} \cdot \mathbf{r})(\mathbf{I} \cdot \mathbf{r})}{r^5} \Big) \tag{2.12}$$

After expanding the operators $\mathbf{S}$ and $\mathbf{I}$, and calculating the expected values of terms containing r over the electron wavefunction [190], we can simplify the above equation to the form $\mathcal{H}_{dip} = \mathbf{S} \cdot \mathbf{T} \cdot \mathbf{I}$, which allows us to combine the isotropic and anisotropic hyperfine as,

$$\mathcal{H}_{HF} = \mathbf{S} \cdot \mathbf{A} \cdot \mathbf{I} \tag{2.13}$$

with $\mathbf{A} = A_0 \mathbf{I} + \mathbf{T}$ and $\mathrm{A_0} = \frac{2\mu_0}{3} \mathrm{g} \beta_\mathrm{e} \beta_\mathrm{n} |\psi(0)|^2$.

Rare earth ions display a strong anisotropic hyperfine interaction, which results in zero-field clock transitions as well as zero-field splitting as high as 5 GHz for $^{167}\mathrm{Er}^{3+}$. The study of the electron Zeeman and hyperfine interaction and its symmetry is a critical prerequisite for their application in zero-field quantum transducers and microwave quantum memory.

2.2.5 Nuclear quadrupole interaction and Zeeman

Nuclei with greater than half-integer spin ($I > 1/2$) have a non-spherical charge distribution inside the nucleus. This asymmetric charge distribution causes a non-zero electric quadrupole moment (Q) and this electric quadrupole moment can couple with an electric field gradient caused by nearby electrons and nucleus leading to the nuclear quadrupole interaction [161]. The nuclear quadrupole interaction is generally treated as a perturbation to the electron Zeeman and hyperfine interaction due to its small interaction strength and generally causes a shift of the ESR transition and the presence of forbidden transitions. However, for Kramers rare-earth ions such as $^{167}Er^{3+}$, a strong quadrupole interaction leads to the mixing of the electron-nuclear spin transitions and results in forbidden ESR transitions ($\Delta m_I \neq 0$) with intensity comparable to the intensity of allowed transitions $\Delta m_I = 0$ [73] [41]. The nuclear quadrupole interaction is described by a traceless tensor Q,

$$\mathcal{H}_Q = \mathbf{I} \cdot \mathbf{Q} \cdot \mathbf{I} \tag{2.14}$$

The nuclear Zeeman interaction results from the interaction of the nucleus with an external magnetic field and is described as,

$$\mathcal{H}_{Ze,n} = \mu_n g_n \mathbf{B} \cdot \mathbf{I} \tag{2.15}$$

where μ_n is nuclear magnetic ratio, equal to 7.6 MHz/T and g_n is the g factor of the nucleus. At the typical magnetic fields (<0.5 T) used in the measurements in this thesis, the nuclear Zeeman splitting of the Yttrium nucleus ($g_n \approx 0.25$) is <1 MHz. Therefore, the contribution of the nuclear Zeeman interaction to the $^{167}Er^{3+}$ hyperfine energy levels can be ignored in comparison to the quadrupole interaction Q.

2.2.6 AC g factor

An anisotropic g-factor for rare-earth ions leads to a difference in the effective g-factor along the direction of the DC magnetic field and the direction of driving AC B field [1] [136]. This case is illustrated in Fig. 2.8 where the DC magnetic field is applied along the axis(x) with g=1.6 while the driving field is applied along the axis(z) with the highest g factor(12.2). In this scenario, the Zeeman splitting will be determined by the g factor along the DC field (g=1.6) while the Rabi frequency will be determined by the g factor along the AC field ($g_{AC} = 12.2$. The DC g-factor, hereby referred to as simply the g factor determines the energy splitting in response to an applied DC magnetic field (B). $\Delta E = g\mu_B B$

The AC g-factor, (called g_1) in this document determines the coupling rate for a transition between energy levels with spin M, $M-1$ split by a DC magnetic field B. $\Gamma = g_1\langle M|S^-|M+1\rangle$. For any given DC magnetic field $\vec{B}$ and AC magnetic field $\vec{B}_1$ the AC,DC g factor are given as ,

$$g^2 = l^2 g_x^2 + m^2 g_y^2 + n^2 g_z^2 \tag{2.16}$$

$$g_1^2 = \frac{1}{g^2}(g_x^2 g_y^2 (l_1 m - l m_1)^2 + g_z^2 g_y^2 (m_1 n - m n_1)^2 + g_x^2 g_z^2 (n_1 l - n l_1)^2) \tag{2.17}$$

where (l, m, n) and (l_1, m_1, n_1) are the direction cosines of DC (B) and AC (B_1) magnetic field respectively with respect to the principle axis of the g tensor.

2.3 Spin relaxation and decoherence mechanisms

Electrons possess an intrinsic spin angular momentum $\mathbf{S}$, which results in a magnetic moment $\mu = -g\mu_B\mathbf{S}$ where $\mu_B = e\hbar/2m_e$. Electron spin resonance experiments measure the net magnetization of the sample M, which is formed from the addition of individual magnetic moments of all electrons in ion $M = \sum_i \mu_i$ [161]. The behavior of the spin ensembles in a

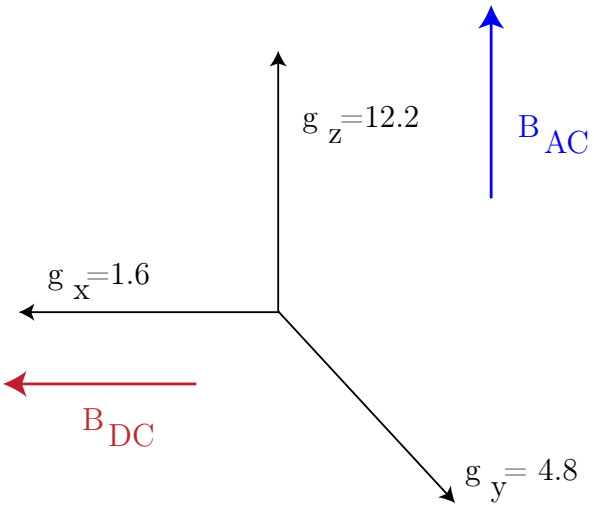


Figure 2.8: Magnetic DC and driving field for a spin system with an anisotropic g tensor.

paramagnetic sample can be described in a semi-classical manner by a net magnetization M. Electron spin magnetization M in a sample in the presence of an effective magnetic field B undergoes precession about the field with a frequency $\omega_\mu = \frac{g\mu_B B}{\hbar}$ [190],

$$\frac{d\mathbf{M}}{dt} = \frac{g\mu_B}{\hbar}\mathbf{M} \times \mathbf{B} \tag{2.18}$$

Assuming a B field applied along the z direction (0,0, B) the equation can be simplified as,

$$\frac{dM_x}{dt} = \omega_\mu M_y \tag{2.19}$$

$$\frac{dM_y}{dt} = -\omega_\mu M_x \tag{2.20}$$

$$\frac{dM_z}{dt} = 0 \tag{2.21}$$

These equations describe the total magnetization oscillating about the Z axis with a frequency ω_μ. While in the steady state, the net initial magnetization M_0 will be aligned parallel or anti-parallel to the effective B field, the application of a driving pulse on-resonant

with the spin precession frequency ω_μ will result in non-zero XY magnetization M_{xy}. Spin ensembles in solids undergo a longitudinal relaxation of the Z magnetization M_z on a timescale defined as T_1 and a (generally) faster relaxation of the XY magnetization M_{xy} at timescale T_2,

$$\frac{dM_x}{dt} = \omega_\mu M_y - \frac{M_y}{T_2} \tag{2.22}$$

$$\frac{dM_y}{dt} = -\omega_\mu M_x - \frac{M_x}{T_2} \tag{2.23}$$

$$\frac{dM_z}{dt} = \frac{M_0 - M_x}{T_1} \tag{2.24}$$

Under the application of an external oscillating magnetic field with circular polarization $B_1 = (B_1 \cos\omega_m t, B_1 \sin\omega_m t, 0)$ the system undergoes oscillation about a net magnetic field. It is convenient to describe the spin dynamics in a rotating frame that is oscillating with the frequency of the applied oscillating microwave field ω_m [161],

$$\frac{dM_x}{dt} = (\omega_\mu - \omega_m) M_y - \frac{M_y}{T_2} \tag{2.25}$$

$$\frac{dM_y}{dt} = -(\omega_\mu - \omega_m) M_x - \frac{M_x}{T_2} - \omega_1 M_z \tag{2.26}$$

$$\frac{dM_z}{dt} = \frac{M_0 - M_x}{T_1} + \omega_1 M_y \tag{2.27}$$

where $\omega_1 = \frac{g_{AC}\mu_B B_1}{\hbar}$ is the precession frequency due to the oscillating microwave field, also referred to as Rabi frequency in ESR experiments. Equations 2.26 and 2.27 describe the rotating of the magnetization in the Y-Z plane due to the application of the microwave driving field about the X-axis of the Bloch sphere in the rotating frame. This forms the

basis of pulsed manipulation of spins in ESR where an oscillating magnetic field is used to coherently manipulate the spin population. The duration of the application of microwave field t_p can be tuned to rotate the magnetization by a fixed flip-angle θ_p, such that $\omega_1 t_p = \theta_p$. Application of microwave pulses also results in a broadening of the excitation bandwidth in the frequency domain, such that $\Delta\omega_1 \approx 1/t_p$. When the spin precession frequency is set equal to microwave frequency $\omega_\mu = \omega_m$, the first term in equations 2.25 and 2.27 vanish, therefore, on-resonantly driven spins do not precess about the Z axis in the rotating frame. On the other hand, when $\omega_\mu \neq \omega_m$, the net precession is about an axis, which is along the vector sum of $(\omega_\mu - \omega_m)\hat{z}$ and $\omega_1 \hat{x}$, which can result in pulse errors in the scenario when an ensemble of spin with a range of oscillation frequencies $\Delta\omega_\mu$ is driven by small bandwidth microwave pulses $\Delta\omega_1 < \Delta\omega_\mu$.

2.3.1 Longitudinal spin relaxation (T_1)

The longitudinal spin-relaxation time represents the decay time of the spin population excited in the spin-up state. A long spin lifetime is required in order to allow for spectral holeburning, and optical spin initialization as well as for achieving a long spin coherence time. Spin relaxation time for dilute rare-earth ion ensembles is determined primarily by spin-phonon interaction at liquid helium temperatures. For samples with higher concentrations, the dipolar interaction between spins can lead to a significant rate of spin-spin interaction(flop-flop) mediated spin relaxation. While the spontaneous decay for spins at 8 GHz splitting is 10^{-12} Hz, high-quality factor, low mode volume superconducting resonators have recently demonstrated several orders of magnitude higher Purcell enhanced spontaneous relaxation of electron spins at 2.7 Hz [28] [27].

Spin-lattice relaxation

Spin-lattice or spin-phonon is the primary mechanism of spin relaxation in solid state systems due to their extremely low spontaneous emission rates [161]. Spin-phonon interaction results from the interaction of spins with the thermal motion of the lattice described as phonons. Phonons induce a modulation of the spin-orbit interaction, which generates fluctuating magnetic fields and results in energy exchange between spins and the phonon bath [161].

Direct process

The direct process involves the absorption or emission of a phonon by spin and the relaxation rate scales as $R_D \propto B^{-5}\coth(g\mu_B B/2k_B T)$ [112]. The direct process is the dominant relaxation mechanism in Kramers rare-earth ions at temperatures below $\approx$ 4 Kelvin [112] [35]. Measurements in $Er^{3+} : Y_2SiO_5$ at low magnetic fields (<10 mT) have demonstrated phonon-bottlenecked spin-lattice relaxation with a timescale of 10 hours at 20 mK [35].

Two-phonon processes

Two phonon processes include nonresonant (Raman) and resonant (Orbach) processes scaling as $R_R \propto T^{-9}$ and $R_O \propto e^{-\Delta/k_B T}$, which are dominant at temperatures above $\approx$ 4 K [112]. Two-phonon processes show a stronger dependence on temperature than the direct process.

Spin-spin relaxation

Spin-spin interaction can result in resonant flip-flops where two spins with small energy separation ΔE can exchange energy through dipole-dipole interaction [46]. Spin flip-flops can be observed in the decay of spectral holes in optical holeburning experiments, as well as through spatial spin diffusion [27] in certain micro-ESR experiments. Spin-spin relaxation rate scales as [46],

$$R_{ff} = (\beta(\theta, \phi, \eta) n^2/\Gamma)\mathrm{sech}^2(g\mu_B B/2k_B T) \tag{2.28}$$

where the term $\beta(\theta, \phi, \eta)$ captures the anisotropic dependence of the flip-flop rate on the angle of B field with respect to the principle axis of the g tensor. Spin flip-flops are suppressed when the inhomogeneous linewidth γ is larger than the strength of dipole-dipole interaction [112] [111] as well as at low temperatures with $T < (g\mu_B B)/k_B$, which typically corresponds to T <200 mK at $g\mu_B B \approx 5$ GHz.

Purcell enhanced spontaneous emission

The spontaneous emission rate of electron spins scaling can be as low as $8x10^{-9}$ Hz for splittings as high as 1 THz [161]. However, recent works have demonstrated Purcell enhanced decay of electron spin ensembles in several systems such as Bismuth in Silicon [28] [145] [4], P donors in Silicon [64] and erbium in $CaWO_4$ [48] with relaxation rates in excess of several Hz. This was enabled by low mode volume superconducting microwave resonators with single spin coupling strength g ≈ 50 Hz -1 kHz and quality factors in excess of several thousand as well as low intrinsic spin relaxation rate(spin-phonon, spin-spin relaxation) in the systems. The Purcell enhanced decay rate is given as [64],

$$R_P = 4\kappa g^2/(\kappa^2 + 4\delta^2) \tag{2.29}$$

where g is the single spin coupling strength, κ is the resonator linewidth and δ is frequency detuning from the center of the resonator.

2.3.2 Transverse spin relaxation (T_2)

The transverse relaxation time also referred to as coherence time (T_2) is the relaxation time of the transverse (XY) component of the average spin magnetization. The spin coherence time is a key metric for several applications such as quantum memory, and quantum sensing where it represents the average timescale during, which quantum information can be processed or

stored by the system. Spin coherence time is ultimately bounded by $2T_1$, however, in most solid-state systems the coherence times are significantly reduced due to a range of factors such as noise generated by a spin-bath composed of paramagnetic impurities/defects, nuclear spins, dipolar-interaction with like spins as well as control errors. Understanding the relevant decoherence mechanisms and engineering methods to mitigate decoherence is essential to evaluate a system for application in quantum information processing. The spin coherence time in the frequency domain corresponds to a homogeneous linewidth $\Gamma_h = 1/\pi T_2$.

Spin inhomogeneous linewidth

Spins in solid state experience an inhomogeneous environment due to differences in local structure due to strain, paramagnetic defect density, and nuclear spin environment, which leads to a distribution of the g factors, hyperfine splittings, and therefore the precession frequency ($\Delta\omega$) in an external magnetic field. These effects result in an inhomogenous broadening of spin ensemble represented as inhomogeneous linewidth (Γ_{inh}). While inhomogeneous broadening can lead to fast dephasing of an ensemble on a timescale $T_2^* \approx 1/\Gamma_{inh}$, this effect can be reversed by a refocusing pulse. Moreover, certain quantum memory applications such as atomic frequency comb (AFC), and spectral multiplexing can benefit from the maximization of the ratio of inhomogeneous to homogeneous linewidth (Γ_{inh}/Γ_h).

Spectral diffusion

Spectral diffusion is the drift of the spin precession frequency ω_s due to dynamic changes in the local magnetic field δB, which results in an effective broadening of the spin homogeneous linewidth over time. Spectral diffusion in Kramers rare-earth ions is caused due to magnetic field fluctuations caused by a spin-bath composed of other Kramers ions, which is coupled to the spins under investigation under magnetic dipole-dipole (ZZ) interaction, as well as paramagnetic impurities/defects and host nuclear spin. The estimated root mean square

(RMS) magnetic noise amplitude can be estimated from the spectral diffusion limited spin coherence time and the known sensitivity of the transition to the magnetic field as [207],

$$1/\pi T_{2,SD} = S_1 \delta B + S_2 \delta B^2 \tag{2.30}$$

where S_1 is the first-order sensitivity to magnetic noise, which is generally proportional to $g\mu_B/h$ ($\approx 14 \times g\,MHz/mT$) with g being the Lande g factor and S_2 is the second order sensitivity to magnetic noise. For isotopes with zero nuclear spin (I=0) $S_1 = g\mu_B/h$ and $S_2 = 0$ while for isotopes with ($I \neq 0$), S_1 can approach zero due to electron-nuclear spin mixing leading to "clock" or "ZEFOZ" (zero first-order Zeeman) transitions with long coherence times [127] [142]. In the latter cases, the relative contribution of S_2 to the coherence times can be significant [142].

Magnetic noise (δB) from spin flips as well as flip-flops in a paramagnetic spin bath can induce spectral diffusion. At sub-Kelvin temperatures where spin-lattice relaxation is suppressed, measurements show close agreement with spin flip-flop-induced spectral diffusion [143]. Spectral diffusion due to spin flip-flops in a paramagnetic spin bath can be described by a simple model [135] [178] [59],

$$\frac{1}{T_{2,SD}(T)} = \frac{\xi}{(1 + e^{T_{Ze}/T})(1 + e^{-T_{Ze}/T})} \tag{2.31}$$

where, ξ is a temperature-independent parameter with strength proportional to the dipolar coupling to paramagnetic spin bath inducting spectral diffusion, and $T_{Ze} = g_s\mu_B B/2k_B$ is the Zeeman temperature of the spin bath. The denominator can also be expressed as $\mathrm{sech}^2(T_{Ze}/T)$, which represents the product of spin-up and spin-down populations. As the temperature is T is reduced below T_{Ze}, near unity spin polarization leads to suppression of the sech term to zero. This model is agnostic to the spin bath flip/flip-flop rate and temperature dependence of the spin coherence time at sub-Kelvin temperatures was closely

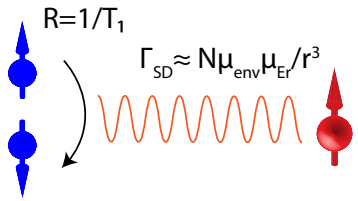


Figure 2.9: Spectral diffusion induced by a spin bath with known composition, density, and flip rates.

modeled by eq. 2.31 in Chapter 6.

A more general approach for modeling spectral diffusion-induced decoherence requires the knowledge of two spectral diffusion parameters, the average spin-bath flip rate R and the dipolar coupling to the spin-bath described by the spectral diffusion linewidth Γ_{SD}. This approach was used in modeling the spectral diffusion at sub-Kelvin temperatures in Chapter 5. The spectral diffusion limited coherence time, $T_{2,SD}$ can be modeled using a Lorentz diffusion model with a stretch factor 2 [100] [112],

$$T_{2,SD}^{-1} = \frac{\sqrt{\pi \Gamma_{SD} R}}{2} \tag{2.32}$$

where Γ_{SD} depends on the density of the spin bath (n), the measurement temperature, and the magnetic field.

Both spin-flips and flip-flops can result in spectral diffusion and contribute to the average spin-flip rate R and the predominance of one mechanism over the other depends on the density of the spin bath, the spin-lifetimes. The total spin-flip rate can be expressed as,

$$R(T) = R_d \coth(g_s \mu_B B/2k_B T) + R_{ff} \mathrm{sech}^2(g_s \mu_B B/2k_B T) \tag{2.33}$$

where g_s is the g factor of the spin-bath and R_d and R_{ff} are the rates of direct process and flip-flop processes respectively.

The spectral diffusion linewidth Γ_{SD} at a given temperature can be modelled as,

$$\Gamma_{SD} = \Gamma_{SD,max}\mathrm{sech}^2(g_s\mu_B B/2k_B T) \tag{2.34}$$

where $\Gamma_{SD,max}$ is the maximum spectral diffusion linewidth and sech term describes the suppression of Γ_{SD} due to spin-bath polarization. For a central spin with g-factor g_a interacting with a spin-bath with density n_s, g-factor g_s, the maximum spectral diffusion linewidth can be estimated as [32],

$$\Gamma_{SD,max} = \frac{\pi\mu_0 g_a g_s \mu_B^2 n_s}{9\sqrt{3}h} \tag{2.35}$$

The values of R(T) and Γ_{SD}(T) can be measured from two pulse and three pulse-echo measurements at different temperatures [143] and the temperature dependence could be fitted to obtain the parameters R_d, R_{ff}, g_s and $\Gamma_{SD,max}$. The knowledge of these parameters allows us to elucidate the dynamics and composition of the paramagnetic spin bath.

Instantaneous diffusion

Instantaneous diffusion arises from dipolar interaction (ZZ) between spins during refocusing pulses. Spin inversion during refocusing pulses produces a change in the local fields at the neighbor dipole-coupled spins leading to decoherence. Instantaneous diffusion limited T_2 is given as [112],

$$\frac{1}{T_{2,ID}} = \frac{2\pi^2\mu_0 h n_{eff}\gamma^2}{9\sqrt{3}}\langle\sin^2\frac{\theta}{2}\rangle \tag{2.36}$$

where n_{eff} is the effective density of spins being addressed, $\gamma = \frac{g\mu_B}{\hbar}$ is the gyromagnetic ratio of the electron, $\langle\sin^2\frac{\theta}{2}\rangle$ is the average spin-flip probability over the spin inhomogeneous linewidth. Instantaneous diffusion scales linearly with the effective density of the spins n_{eff} and therefore reducing n_{eff} can lead to suppression of instantaneous diffusion. Approaches such as reducing the average spin-flip angle of the pulse by reducing the pulse power or

decreasing the effective density of spins by broadening the spin inhomogeneous linewidth can lead to longer coherence times [181].

2.4 Approaches to mitigate spin decoherence

This section discusses the general guidelines to prolong spin coherence times for Kramers rare-earth ions, which are also applicable for other substitutional dopants and defects in solid-state hosts.

2.4.1 Cryogenic cooling to sub-Kelvin temperatures

Spectral diffusion induced by paramagnetic spin bath is the dominant source of decoherence for rare-earth ions in crystals [143] [77] as discussed in section 2.3.2. Cryogenic cooling to milliKelvin temperatures at moderate magnetic fields (O(100 mT)) can be achieved by a combination of superconducting magnets and dilution refrigerators. This regime allows for near unity spin polarization ($k_BT < g\mu_BB$) while maintaining long spin coherence time electron splitting in a range of 3-6 GHz where it can be readily addressed with microwaves. Fig. 2.9 illustrates the degree of spin polarization ($\coth(hf/2k_BT)$, red), rate of spin flip-flop processes ($\mathrm{sech}^2(hf/2k_BT)$, blue) and direct process ($\tanh(hf/2k_BT)$, green) with temperature for a spin system with splitting hf equal to 5 GHz. A combination of low temperature and moderate field results in near unity polarization of the paramagnetic spin bath leading to the suppresses of spin-flip flop rate (blue) as well as suppression of the direct-process limited spin-phonon relaxation rate (green) and thus long spin coherence times.

2.4.2 Clock/ZEFOZ transition

Spectral diffusion induced by spin-bath is a dominant source of spin decoherence, with the first and second-order sensitivity to magnetic noise (ΔB) given as S_1 and S_2 respectively

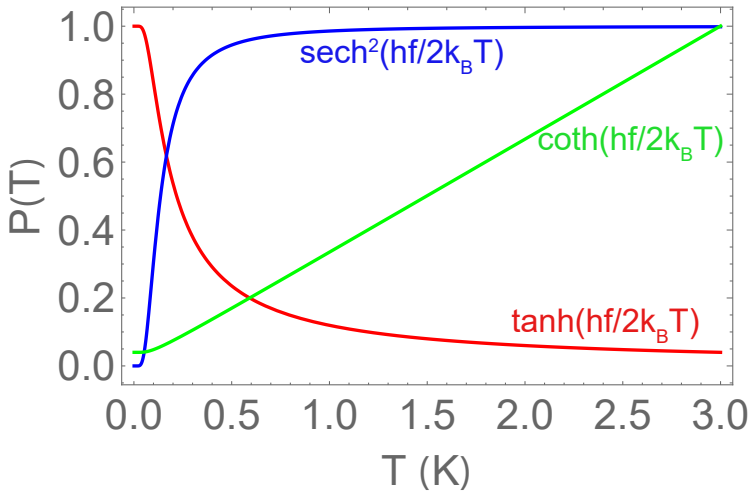


Figure 2.10: Spin polarization (red), spin flip-flop rate(blue), and direct-process(green) spin relaxation rate for a spin at the splitting of 5 GHz as a function of temperature.

(eq. 2.30). Specific transitions where the first-order sensitivity to magnetic noise S_1 vanishes in all three spatial dimensions are referred to as clock transitions. Clock transitions also referred to as ZEro First Order Zeeman(ZEFOZ) transitions have been widely applied for solid-state spin defects in hosts such as silicon [199], silicon-carbide [126] as well for rare-earth ions in solid-state hosts [142] [127] [207]. The spin coherence time at such ZEFOZ points is expected to be dominated by second-order sensitivity to noise (S_2) and therefore transitions with both vanishing S_1 and small S_2 can be expected to exhibit the longest coherence times. Clock-transitions in Kramers rare-earth ions are a result of mixing between the electron Zeeman and nuclear hyperfine states at extremely low or zero fields, where the strength of electron Zeeman splitting is comparable to the hyperfine interaction [127] [142]. However, the magnetic noise amplitude due to unpolarized paramagnetic spin bath as well as the decoherence due to superhyperfine interaction peaks at such low fields limits the effectiveness of the ZEFOZ technique in hosts with paramagnetic and nuclear spin bath [6].

2.4.3 Dynamical decoupling and Hamiltonian engineering

Dynamical decoupling(DD) techniques use periodic driving of spin with pulses with varying amplitude/phase to preserve an arbitrary quantum state from environment-induced dephasing [171]. Dynamical decoupling techniques control the spin-bath interaction by periodic driving in order to obtain a zero-time average Hamiltonian $\langle H_{SB} \rangle = 0$ [177]. Dynamical decoupling pulses can also be interpreted in the frequency domain as filter functions $F(\omega)$ acting on the noise power spectral density $S(\omega)$. Under this interpretation, DD sequences with pulses separated by a time τ make the spin selectively sensitive to signal/noise oscillating at a particular frequency ($f = 1/2\tau$). For preserving quantum states against decoherence, f is chosen such that the environment noise power spectral density $S(\omega)$ has a minimum, usually at high frequencies due to the 1/f nature of the noise power spectral density. Therefore, the application of DD pulses with short separation τ generally results in an increase in coherence times. Conversely, for applications in quantum sensing, f is chosen at the expected frequency of the target signal to achieve maximum sensitivity. Application of a large number of dynamical decoupling pulses N, at a fixed pulse separation $f = 1/2\tau$ results in narrowing of the DD sequence filter function $F(\omega)$, thereby resulting in efficient filtering of the noise [39].

While DD sequences such as Car-Purcell-Meiboom-Gill (CPMG) [37], XYN [171], and KDD [154] are used to suppress spin-bath induced spectral diffusion, another class of DD sequences such as WAHUHA [189], MREV [118] symmetrize the dipole-dipole interaction Hamiltonian to time average the decoherence due to dipolar interaction to zero. A new series of DD sequences such as DROID-60 have been developed in recent years to address both spectral diffusion and dipolar interaction simultaneously [213].

Robust dynamical decoupling sequences such as XYN, have built-in tolerance to control errors due to frequency offsets, and flip-angle offsets. While the CPMG sequence preserves only a specific spin state [177] and can result in an artificial elongation of the coherence times

in the presence of pulse errors [129], XYN pulse sequences offer a robust performance against pulse errors leading to efficient suppression of spectral diffusion close to the instantaneous diffusion limit for an arbitrary spin state.

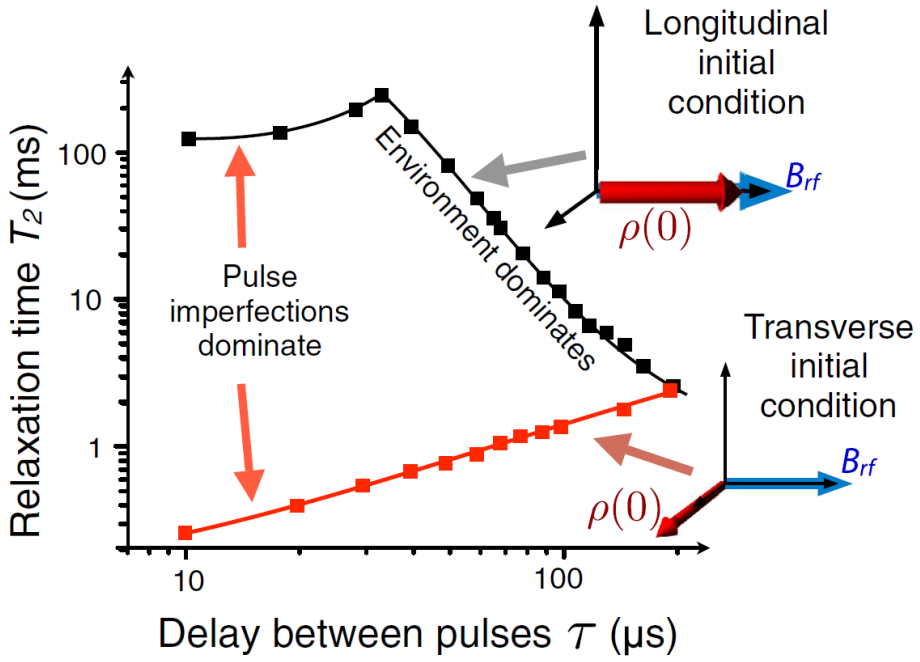


Figure 2.11: Comparison of CPMG sequence performance for a longitudinal initial state with a transverse initial state. The transverse initial state shows an increase in coherence time with pulse separation τ indicating pulse imperfection as the dominant source of decoherence for all τ. On the other hand, for the longitudinal state, the environment-induced decoherence is dominant over pulse errors for most τ. Figure extracted from ref. [177].

Accumulation of pulse errors can be an additional source of decoherence due to dynamical decoupling [177]. This issue is exemplified when comparing the performance of the CPMG sequence for the transverse and longitudinal initial conditions (Fig. 2.11). While the longitudinal initial state results in spin-locking effects, which minimize pulse errors, a transverse initial state can lead to fast decoherence due to the accumulation of pulse errors. As a result, the spin coherence time instead decreases with decreasing delay between the pulses τ (alternatively increasing DD filter frequency f) [8]. The measurement of coherence time as a function of pulse separation τ is therefore essential to obtain the noise power spectral density as well as for elucidating the decoherence mechanisms under dynamical decoupling.

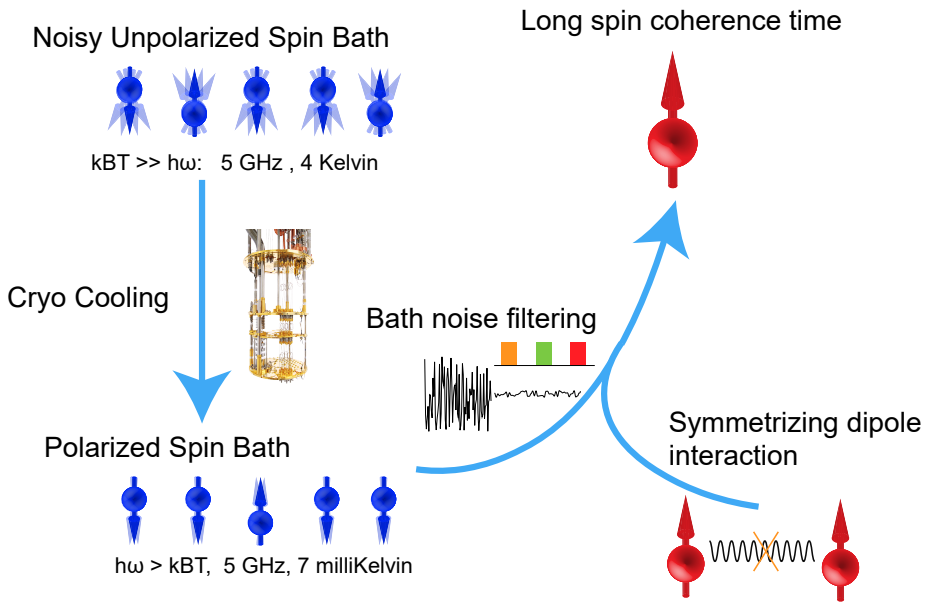


Figure 2.12: A combination of cryogenic cooling and customized dynamical decoupling can be used to enhance spin coherence times.

2.4.4 Low flip angle pulses

Low flip angle pulses address a subset of the spin ensemble, which effectively lowers the concentration of spins being addressed and therefore the resulting instantaneous diffusion. While this approach can project the coherence time under the limit of a very low density of spins [181], its application for ensemble-based quantum information processing is limited due to reduced collective coupling to spins.

2.4.5 Host matrix engineering

Host matrix engineering includes approaches to engineering the host environment to reduce the density of nuclear spins, paramagnetic impurities, and defects in the vicinity of the spin qubit. Paramagnetic defects can be reduced by the growth of high-purity single crystals while a choice of high-purity precursors to the crystal and low contamination in the growth chamber is also critical to minimize background impurity spins. Approaches such as molecular beam epitaxy can be used to grow high purity single crystal films with low impurity concentration

(<< ppm [208]), exceeding the purity of commercially available bulk crystals ($\approx$ 10 ppm [143]).

Near-surface/near-interface spins suffer from additional decoherence arising from surface noise [95], which can be mitigated by a combination of surface passivation [155] and positioning of the spin qubit away from the interface.

While the above approaches can reduce the density of paramagnetic spins, spin decoherence will be limited by the host nuclear spins and isotopic purification of the host crystal can be used to further suppress the magnetic noise environment [93] [18] [181].

CHAPTER 3

ELECTRON SPIN RESONANCE TECHNIQUES

Electron spin resonance spectroscopy (ESR) also known as electron paramagnetic resonance (EPR) spectroscopy aims to study the paramagnetic response of electron magnetic moments processing under an external applied static magnetic field [161]. At an external magnetic field of 178 mT, an electron spin with Lande g-factor = 2 will undergo Larmor precession at an angular frequency $\omega/2\pi \approx 5$ GHz in the microwave frequency range. ESR spectroscopy, therefore, employs microwave frequency resonators, which enhance the interaction of spins to microwave frequency photons. An external magnetic field (B) is ramped up to split the electron spin energy levels due to the Zeeman effect. When the electron spin splitting is on-resonant to a microwave resonator, the oscillating magnetic field of the resonator (B_1) can coherently manipulate the spin population. Resonant absorption of the microwave by paramagnetic sample results in a change in the resonator quality factor, which is used to obtain structural information on the paramagnetic sample. These continuous-wave experiments, also known as CW-ESR have been widely used across the scientific community to obtain information on the local site structure, symmetry, the electron g-factor, hyperfine splitting A, etc.

Pulsed ESR experiments on the other hand use the transient response of the paramagnetic sample to microwave pulses to obtain information on spin longitudinal relaxation (T_1) and transverse relaxation(T_2) mechanisms in addition, to the structure and local site symmetry of a paramagnetic specie. The pulsed ESR experiments are of particular interest for the application of solid-state spin qubits for quantum information processing as dephasing (T_2) times represent the limit on the duration of the coherent operation. Pulsed ESR can therefore serve as an indispensable tool to study the spin dephasing mechanisms and this knowledge could be used to optimize the material growth, processing as well as measurement conditions to obtain long spin coherence times necessary for quantum information processing.

ESR was first experimentally reported by E.K. Zaviosky at Kazan State University where absorption from $CuCl_2.2H_2O$ was measured [62] [161]. Pulsed ESR was subsequently reported by the same author in 1946 [63] using a 3 GHz resonator, similar in design to a loop-gap resonator, a common resonator type, which is also used in certain experiments in this thesis. After the initial reports, pioneering work in the field of pulsed ESR was led by the group of W.B. Mims at Bell Labs [161]. The field of pulsed ESR underwent widespread adoption across different scientific disciplines in the 1980s [161]. This was partly enabled by the development of fast electronics required for the control and readout of transient spin response, which is typically 3 orders of magnitude faster than the nuclear spin response given the 1000 times higher magnetic moment of electron spins. Following the rapid commercialization of the pulsed ESR technique, commercial setups were available operating in the frequency range of 3-9 GHz and operating down to 2 Kelvin in liquid helium cryostats.

While commercial X-band (9 GHz) ESR spectrometers have a sensitivity of $\approx 10^{13}$ spins [28], work has been done in recent years in improving the sensitivity of ESR spectrometers, to be able to detect a single spin inductively. This effort was led by the groups of John Morton and Patrice Bertet in recent years, who developed high-sensitivity ESR spectrometers employing near-quantum-limited cryogenic amplifiers, along with lithographically defined superconducting microresonators with spin sensitivity $O(10^4)$ spins [64] [27]. These spectrometers operate at milliKelvin temperatures in a dilution refrigerator, which further, improves their sensitivity due to near unity spin polarization as well as results in extremely long spin coherence and relaxation times due to polarization of the paramagnetic spin bath. This chapter discusses the instrumentation developed in our lab, which started with a modest setup employing 3D bulk cavities and low noise amplifiers with few Kelvins of noise temperature, and in the subsequent chapters, the setup was upgraded with superconducting microresonators and near-quantum-noise limited Josephson amplifiers to achieve spin sensitivity comparable to the state of the art demonstrations.

To illustrate the experimental spin resonance techniques used in the thesis, we perform proof-of-concept experiments on a 40 parts-per-million(ppm) neodymium Nd^{3+} doped yttrium orthosilicate Y_2SiO_5(YSO) sample with a three-dimensional aluminum loop gap resonator in Fig. 3.7(a). The crystal was grown by Scientific materials and cut along D_1, D_2 axis, as shown in the Fig. 3.7(d), with an estimated number of $\approx 10^{14}$ spins in the resonator mode volume. Neodymium occupies two sites in YSO, site 1, and site 2, where site 1 is preferentially occupied [57]. Each site splits into 2 magnetic inequivalent subsites related by inversion symmetry. The setup was mounted on the 10 milliKelvin stage of a dilution refrigerator and DC magnetic field was applied using a 3-axis vector magnet. For a magnetic field applied in D_1 - D_2 plane or along the b axis, the two subsites are equivalent [57]. While Nd^{3+}:YSO is an interesting system in its own right for application in quantum information processing [57] [111] [198], for this work, it is used for calibration and characterization of the ESR setup.

The techniques demonstrated here are agnostic to the specific cavity/spin system and have been applied to the measurements in Chapters 4 and 5 on samples with a much lower spin concentration and more complex level structures like $^{167}Er^{3+}$. Moreover, effects of milliKelvin temperature on spin properties, such as extremely long spin relaxation time, and a high degree of spin polarization observed on the Nd^{3+}:YSO single-crystal sample are also observed on Er^{3+} doped polycrystals and thin-films.

3.1 ESR spectrometers

ESR spectrometers employing three-dimensional microwave cavities have been widely used for the time domain as well as continuous-wave ESR spectroscopy on paramagnetic solids. Microwave resonators used in this work can be understood as LCR oscillators with an effective inductance L, capacitance C, and loss R (Fig. 3.1). The energy in the LCR resonator oscillates at a frequency $\omega_0 = 2\pi/\sqrt{LC}$, which for our experiments is chosen to be around

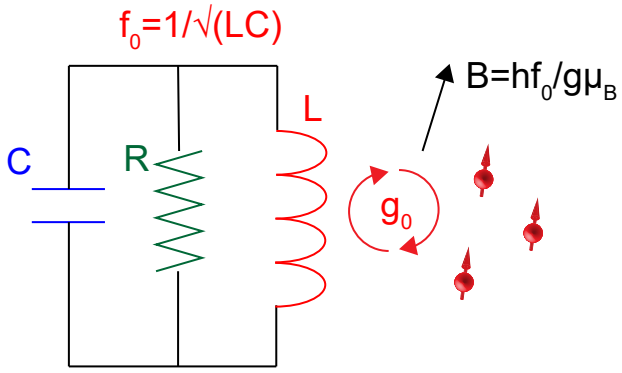


Figure 3.1: Equivalent circuit model of LCR resonators used for electron spin resonance studies in this work. Application of magnetic field (B) results in Zeeman splitting of the electron spins. When the resonance frequency of spin is tuned on resonance with the LCR resonator, the spin can inductively couple to the resonator with a single spin coupling strength g_0.

5-6 GHz. Microwave photon associated with oscillating current in the inductor L couple to a single spin with a coupling strength $g_0 = cg\mu_B\omega_0/\sqrt{8\hbar Z}$ where $c = B_1/I$ is a constant describing the oscillating magnetic field strength B_1 per unit current I [64] and $Z = \sqrt{\frac{L}{C}}$ is the impedance. Thus, in order to produce the largest single-spin coupling strength g_0, we need a low impedance Z. This can be intuitively explained using the LCR circuit model where the energy stored in the inductor is $E = \frac{LI^2}{2}$. For a fixed amount of energy $E = \frac{\hbar\omega}{2}$, a small L would result in the larger current I, and hence a stronger single spin coupling g_0. However, the requirement of $\omega_0 = 1/\sqrt{LC}$ = 5-6 GHz, a large capacitor is required to maintain the resonance frequency in the microwave frequency band of interest. The LCR circuit has losses that are characterized by the resistive element R. This results in a decay of energy from the resonator at a rate κ where $\kappa = \kappa_i + \kappa_e$ with κ_i being the intrinsic loss rate and κ_e being the external loss rate. The quality factor of the resonator defined as $Q = \omega/\kappa$ characterizes the number of bounces of the microwave photon inside the resonator before being dissipated or lost to the external transmission line. Thus higher-quality factor resonators temporally enhance the interaction of microwave photons with spin ensembles.

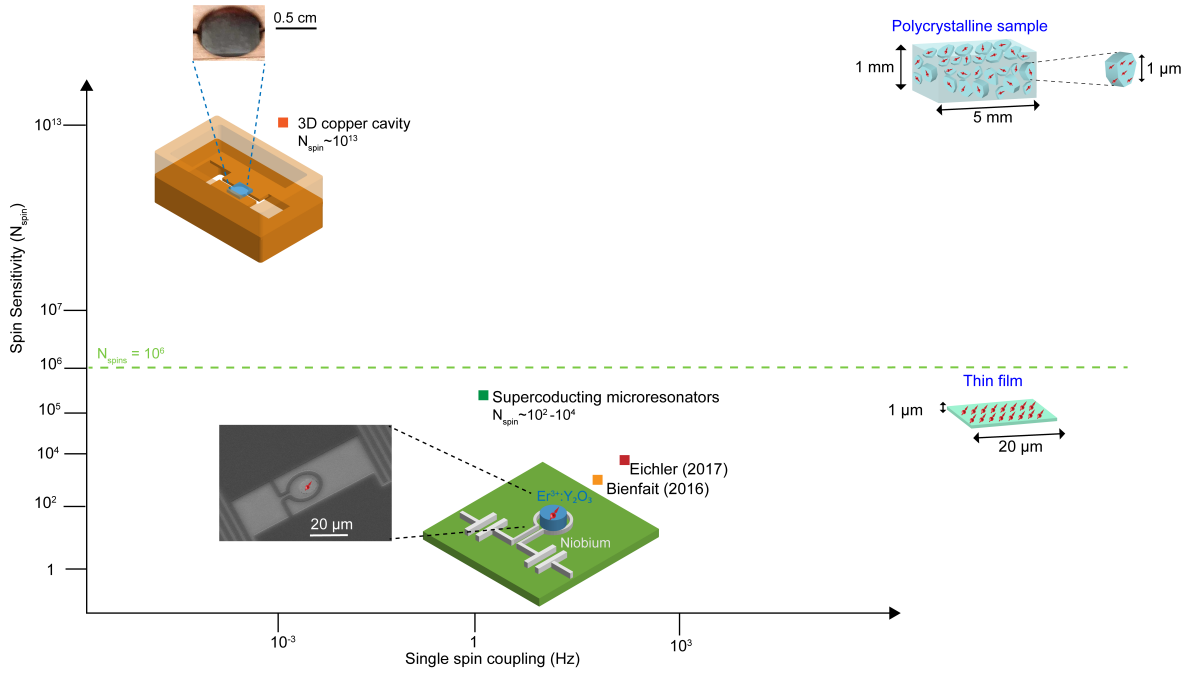


Figure 3.2: Comparison of the minimum number of spin N_{spin} sensitivities of three-dimensional metallic cavities used for studying polycrystalline bulk samples and superconducting planar microresonators used for studying thin-films. While three-dimensional cavities offer a sensitivity of $N_{spin} = 10^{13}$, two-dimensional superconducting microresonators offer orders of magnitude higher sensitivity $N_{spin} \lessapprox 10^4$ spins due to their small mode volume and high-quality factor. The estimated $N_{spin} \approx 10^6$ in thin-films makes it necessary to use superconducting microresonators.

3.1.1 Three dimensional resonators

Three-dimensional cavity-based ESR spectrometers operating down to 4 K have been commercialized for continuous-wave as well as pulsed ESR on a diverse range of samples such as bulk crystals, nanoparticles, and solutions. 3D cavities are easy to fabricate, and compatible with a diverse range of sample geometry such as solutions, nanoparticles, and crystals and allow for easy integration with optics. 3D cavities are ideal for applications that involve addressing a large volume of spins (mm^3) with typical absolute spin number sensitivity $\approx 10^{11}$ spins. Commonly used ESR cavities are based on TE_{102} mode of a rectangular cavity [150]. However, the large mode volume of these cavities leads to low single spin coupling $g \approx 0.01 - 0.1\,Hz$. These cavities are typically made out of metals, which leads to quality

factors of approximately 10,000 limited by ohmic losses. Alternative geometries such as dielectric resonators and lumped-element resonators are alternatively used for applications such as pulsed ESR at X-band as well as for both CW and pulsed ESR below X-band frequency due to smaller physical dimensions of these resonators compared to TE_{102} based cavities [150].

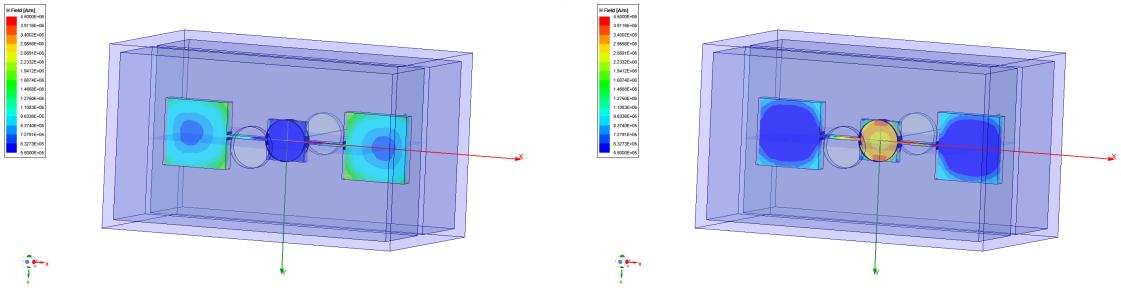
Loop gap resonator

The loop gap resonator (LGR) is a lumped-element resonator consisting of spatially separated inductive elements (loop) and capacitive elements (gap) [200] [89] [150]. The loop-gap resonator shares similarity with the split-ring resonator proposed by Hardy and Whitehead [81], however, for this work, we will focus on the loop-gap resonator. The loop gap resonator consists of capacitive gaps and inductive loops, which determine the mode of the resonator and the operating frequency. The simplest design consists of two loops connected by a gap however, designs with multiple loops and gaps have been used in ESR for their unique advantages [200]. Loop gap resonators offer advantages such as large driving field uniformity, high filling factor, and small physical size for frequencies below X-band compared to cavity resonators [150].

Three-loop two-gap resonators in particular offer advantages such as easier integration with optics, which makes them suitable for applications such as microwave to optical quantum transduction and hybrid quantum systems (Fig. 3.2) [19] [195]. Three-loop two-gap (3L-2G) resonators have two modes corresponding to zero magnetic flux flowing through the inner loop in the low-frequency mode and large magnetic flux through the center loop for the high-frequency model as shown in simulated field profile in Fig. 3.3 [200] for the resonator used in the measurements in this work. This makes the high-frequency model suitable for ESR measurements with the sample mounted on the center loop and through holes in the walls of the resonator to allow for laser access.

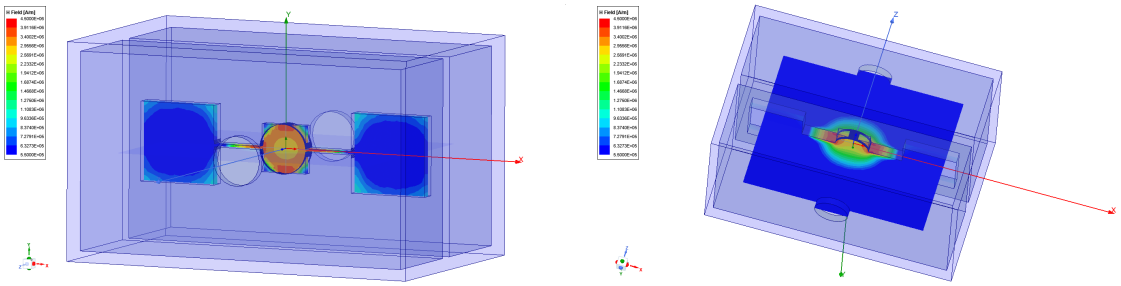
Fig. 3.4(a) and Fig. 3.4(b) show the simulated mode profile for the high-frequency mode of a loop gap resonator used in measurements. The design frequency was f=3.0 GHz for the low-frequency mode and f =5.6 GHz for the high-frequency mode. The measured room temperature quality factor of 1500 for an aluminum loop gap resonator and 2000 for a copper loop gap was in close agreement with HFSS eigenmode simulations. A reduction in Ohmic losses at cryogenic temperatures (4 K) leads to a higher internal quality factor (Q_i) of 6000 for both the oxygen-free copper and aluminum resonator. Microwaves were coupled to the resonator using SMA (Sub-Miniature Version A) flange mount connectors connected with a non-insulating copper wire to form an antenna. The antenna length was tuned by cutting the copper wire, which allowed for tuning the external quality factor of the resonator [19]. Fig. 3.5 shows the measured external quality factor, internal quality factor, and the cavity dip (reflection at resonance frequency) for an aluminum loop gap resonator shown in Fig. 3.7. The external quality factor Q_e (blue in Fig. 3.5) shows an exponential dependence on the antenna length in the overcoupled-critically coupled region and linear dependence on antenna length in the critically coupled-undercoupled region. Taking into account the improvement in internal quality factor Q_i by a factor (F) of 3-4 at cryogenic temperatures, in order to critically couple the resonator at cryogenic temperatures, the resonator should be undercoupled at room temperature such that $Q_e = F \times Q_i$ or alternatively $\kappa_e = \kappa_i/F$. A critically coupled cavity is ideal for continuous-wave ESR measurements due to high sensitivity of the cavity dip to a change in Q_i with spin resonance. On the other hand, an overcoupled cavity is preferable for transient measurements where the ringdown effects of a high-quality factor cavity need to be suppressed in order to measure fast spin dynamics. The degree overcoupling is decided by a trade-off between the reduced sensitivity and the increasing spin manipulation speed. As a rule of thumb, for an expected spin coherence time of x μs, the resonator should be overcoupled such that the resonator linewidth $\kappa = \kappa_i + \kappa_e$ satisfies the relation $\kappa \geq 5/x$ MHz. In other words, the power from the resonator should

decay to 1/e in $1/5^{\text{th}}$ of the spin coherence time.



(a) (b)

Figure 3.3: Simulated AC magnetic field magnitude of the LGR mode for the two modes of the loop gap resonator (a) Low-frequency mode (b) High-frequency mode



(a) (b)

Figure 3.4: Simulated AC magnetic field magnitude of the LGR mode for an input energy of 1 Joule (a) Side view (b) Top view showing the confinement of AC magnetic field in a uniform region around the central loop.

3.1.2 Superconducting planar resonators

Superconducting planar resonators have been widely utilized for coupling to electron spins for storing quantum information as well as for high-sensitivity ESR on samples with small paramagnetic volumes [123]. These resonators increase the cooperativity of the spin-resonator interaction by shrinking the mode volume and increasing the quality factor and therefore allow for fast low power manipulation of spins at cryogenic temperatures. Superconducting resonators suffer from losses induced by magnetic fields, which can be detrimental to the quality factor of the resonator. While aluminum thin-film-based resonators have a critical

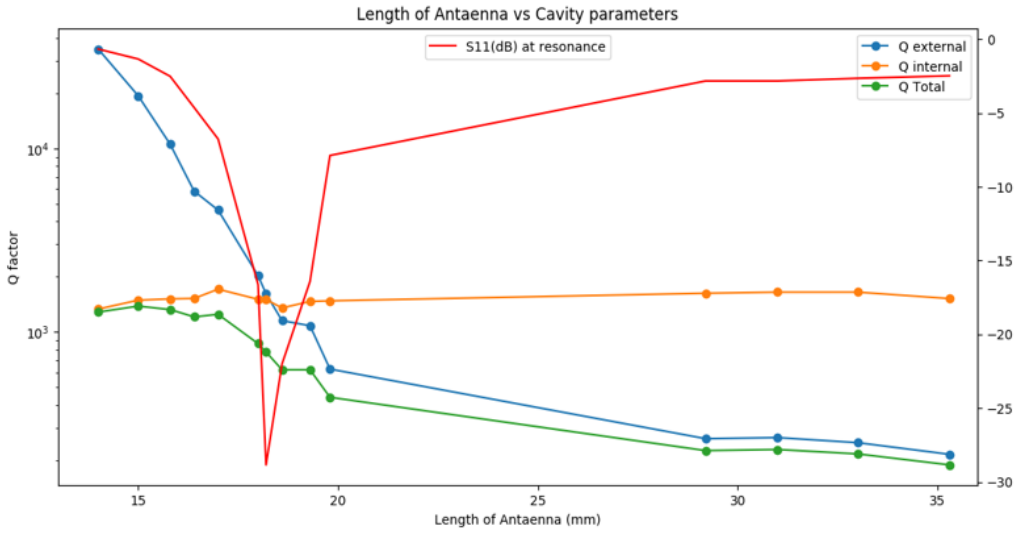


Figure 3.5: The measured external quality factor, internal quality factor, and the cavity dip (reflection at resonance frequency) for an aluminum loop gap resonator. The external quality factor (blue) of the loop gap resonator can be tuned by varying the length of the antenna. A longer antenna than L=18 mm corresponded to an overcoupled cavity. The critical coupling point is reached when the internal (orange) and external quality factors (blue) are the same, which corresponds to the narrowest cavity dip (red).

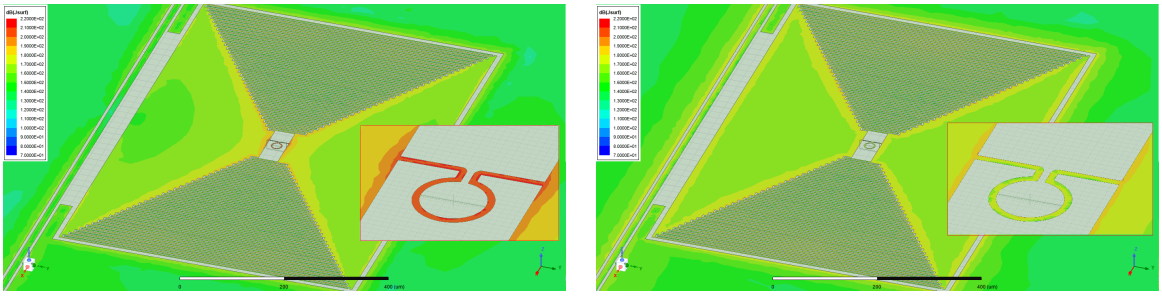
magnetic field of 10 mT, niobium thin-film (Nb, NbTiN, NbN) based resonators allow for in-plane magnetic fields as high as several Tesla [120]. Quality factors as high as 10^5 have been reported for superconducting resonators at an applied magnetic field [28].

Low impedance resonators

Low impedance resonators and lumped element resonators designed with a large capacitance (C) and small inductance (L) leading to a large surface current and therefore large single spin coupling (g) to the magnetic field fluctuations to the vacuum mode in the range of 50-1000 Hz [28] [64] [120]. Low-impedance resonators have been designed with a pair of large interdigitated (IDF) capacitors on the two sides of the central inductor allowing for keeping the design frequency around 5-6 GHz while maintaining a low design inductance. A large single spin coupling makes low impedance resonators suitable for studies on magnetic

samples with small volumes such as thin films (Fig. 3.2).

The design consists of two sets of capacitor arrays on the two sides of an omega inductor loop. The choice of inductor loop was to introduce a uniform z-direction spin driving and to allow for integration with optical access from the top. This would allow for novel applications such as correlated microwave-optical spectroscopy on the same setup as well as on-chip microwave-to-optical transduction. Fig. 3.6 (a) and (b) show the simulated surface current profile (J_{surf}) for the baseline design. The resonator consists of two modes [120], the low-frequency mode with a higher current density on the inductor wire and a high-frequency mode with reduced current density. The resonator design, simulation, and fabrication are covered in detail in Section. 6.3.



(a) (b)

Figure 3.6: Simulated surface current magnitude (J_{surf}) of the for the two modes of the low impedance superconducting resonator (a) Low-frequency mode with larger current density in the inductor loop (b) High-frequency mode with reduced current density in the inductor. Inset shows the zoomed-in plot around the inductor loop.

3.2 Cavity Quantum Electrodynamics

Cavity quantum electrodynamics (c-QED) describes the coherent dynamics of two-level system(s) coupled to cavities. Cavities enhance the interaction of electromagnetic radiation with two-level systems by spatial and temporal confinement of energy in the mode of the cavity. Optical and microwave cavities have been used to enhance the decay rate of solid-state spins through the Purcell effect as well as perform cavity-enabled atom/spin cooling.

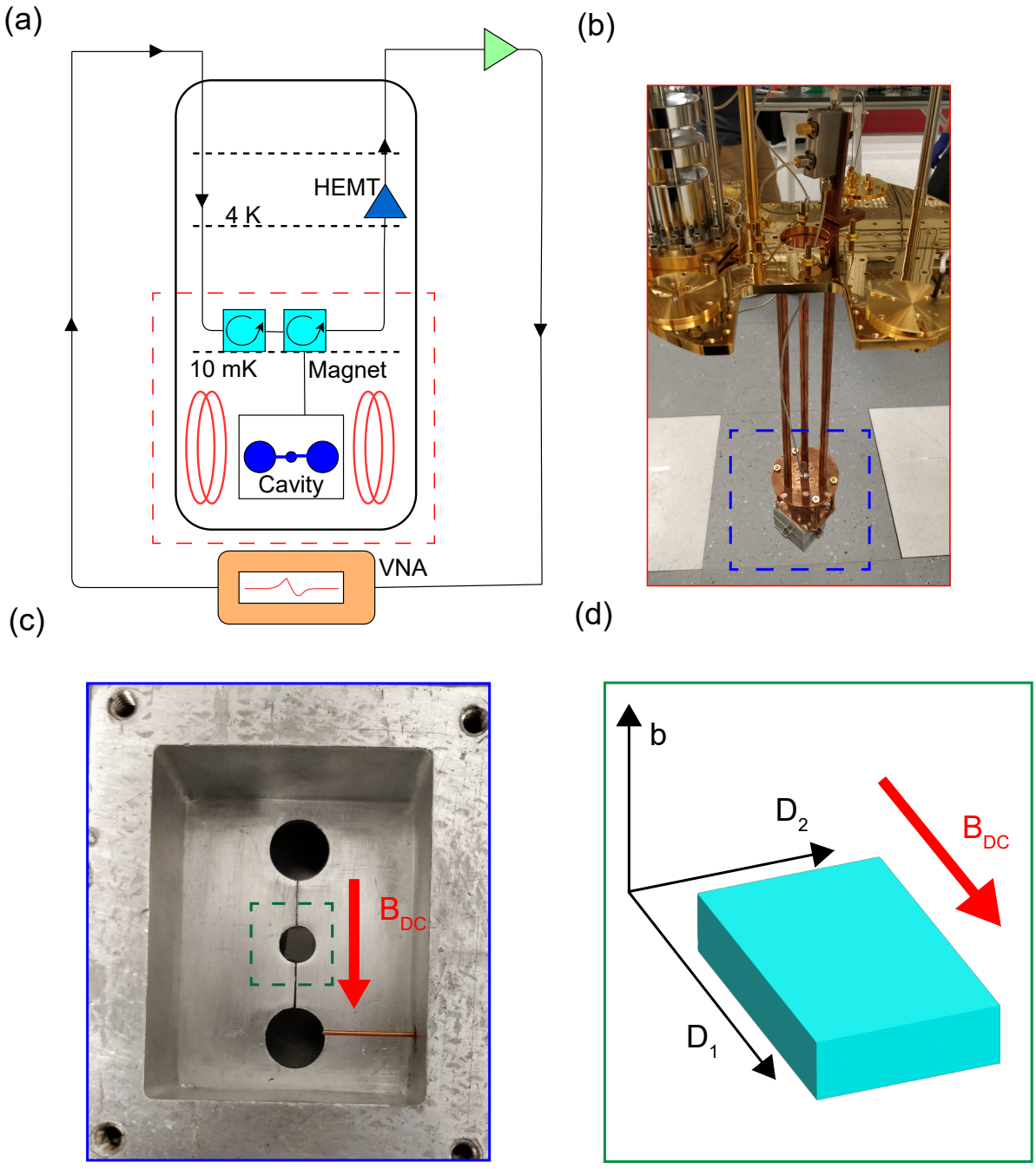


Figure 3.7: MilliKelvin ESR setup used for CW and pulsed studies on bulk samples (a) Schematics of the setup showing the cryogenic components (b) Picture of the cavity mounted on the mixing chamber stage (7-10 mK) (c) Aluminum loop gap cavity with sample mounted (d) Orientation of the DC B field relative to the crystal axes of YSO crystal.

Due to high loss in coaxial cables at microwave frequency and low energy of a microwave photon as compared to optical frequency (THz) photons microwave cavities are essential for the manipulation and readout of microwave frequency qubits such as electron spins qubits and superconducting qubits.

The dynamics of emitters coupled to a cavity can be described through input-output formalism [45] [56]. For a cavity mode represented by the Bosonic operator a frequency ω_0 and an ensemble of N emitters described by Bosonic mode b_k and frequency ω_k, the Hamiltonian can be written as [56],

$\mathrm{H_a} = \hbar\omega_0 \mathrm{a}^\dagger \mathrm{a}$

$\mathrm{H_b} = \hbar \sum \omega_\mathrm{k} \mathrm{b}_\mathrm{k}^\dagger \mathrm{b_k}$

The interaction of the cavity mode with emitter modes with a coupling strength $\mathrm{g_k}$ can be represented as,

$\mathrm{H_{int}} = \mathrm{i}\hbar \sum \mathrm{g_k}(\mathrm{a}^\dagger \mathrm{b_k} - \mathrm{b}_\mathrm{k}^\dagger \mathrm{a})$

For a one-port cavity with an external energy loss rate through the port $\mathrm{k_e}$, internal cavity energy loss rate $\mathrm{k_i}$ and the atomic dissipation rate γ, the input-output relations can be written as,

$$\dot{\mathrm{a}} = -[(\kappa_\mathrm{i} + \kappa_\mathrm{e})/2 - \mathrm{i}(\omega_0 - \omega)]\mathrm{a} + \sum_\mathrm{k} \mathrm{g_k b_k} - \sqrt{\kappa_\mathrm{e}}\mathrm{c_{in}} + \mathrm{f_{n,a}(t)} \tag{3.1}$$

$$\dot{\mathrm{b}}_\mathrm{k} = -[(\gamma)/2 - \mathrm{i}(\omega_\mathrm{k} - \omega)]\mathrm{b_k} - \mathrm{g_k a} + \mathrm{f_{n,b}(t)} \tag{3.2}$$

$$\mathrm{c_r} = \mathrm{c_{in}} + \sqrt{\mathrm{k_e a}} \tag{3.3}$$

where $\mathrm{f_{n,b}(t)}$ and $\mathrm{f_{n,a}(t)}$ are noise operators. Taking the steady state solution where $\dot{\mathrm{a}}$ and $\dot{\mathrm{b}}_\mathrm{k}$ vanish, the reflection amplitude ($\mathrm{S_{11}}$) is given as,

$$S_{11}(\omega) = 1 + \sqrt{k_e}\langle a\rangle/\langle c_{in}\rangle \tag{3.4}$$

Solving eliminating $\langle b_k\rangle$ from the equations 3.1 and 3.2, we substitute for $(\langle a\rangle)/(\langle c_{in}\rangle)$ in eq. 3.3 to get,

$$S_{11}(\omega) = 1 + \frac{k_e}{[i(\omega-\omega_0) - (k_i+k_e)/2 + \sum g_k^2/(i(\omega-\omega_k) - \gamma/2)]} \tag{3.5}$$

For the case of an ensemble of N spin coupled to a microwave resonator, we can substitute $\Omega^2 = \sum_k g_k^2$, $\gamma/2 = \Gamma_{inh}$ and $\omega_k = \omega_r$ in equation. 3.5, where Ω is the collective coupling of the spin ensemble, Γ_{inh} is the spin inhomogeneous half-width and ω_r is the center of the inhomogeneously broadened spin line. We perform further simplification on eqn. 3.5 to obtain,

$$S_{11}(\omega) = 1 + \frac{k_e}{\Big(- (k_i+k_e)/2 - \frac{\Omega^2\Gamma_{inh}}{(\Gamma_{inh}^2+(\omega-\omega_r^2))} + i(\omega-\omega_0) - i\frac{\Omega^2(\omega-\omega_r)}{(\Gamma_{inh}^2+(\omega-\omega_r^2))}\Big)} \tag{3.6}$$

Identifying the following expressions,

$$k_i' = k_i + \frac{\Omega^2\Gamma_{inh}}{\Gamma_{inh}^2 + (\omega-\omega_r)^2} \tag{3.7}$$

and,

$$\omega_0' = \omega_0 - \frac{\Omega^2(\omega-\omega_r)}{\Gamma_{inh}^2 + (\omega-\omega_r)^2} \tag{3.8}$$

we can rewrite eqn. 3.6 in the absence of emitters ($g_i = 0$) in the following form,

$$S_{11}(\omega) = 1 + \frac{k_e}{i(\omega-\omega_0') - (k_i'+k_e)/2} \tag{3.9}$$

Therefore the coupling of a spin ensemble to a cavity would results in dispersive frequency shifts, as well as absorptive linewidth broadening when the term $(\omega-\omega_r)$ is small, or

equivalently when spins are on-resonance with the cavity. The dispersive frequency shift is maximized when $\omega - \omega_r = \pm\Gamma_{inh}$ and absorptive linewidth broadening is maximized when $\omega - \omega_r = 0$. To compare the relative strength of coupling between the spin ensemble and the cavity Ω and the energy dissipation rate of the cavity $\kappa = \kappa_i + \kappa_e$ and the spin ensemble Γ_{inh}, we use the cooperativity C, defined as [57],

$$C = \frac{\Omega^2}{\kappa\Gamma_{inh}} \tag{3.10}$$

To illustrate these concepts, a continuous wave spin resonance experiment was performed on a 400 ppm Ni^{2+} doped magnesium oxide (MgO) sample at 8 mK, mounted on the same setup described in Fig. 3.7 [132]. The sample was chosen due to its high spin density, which would result in a high cooperativity coupling of spin ensembles to the microwave cavity. A two-dimensional sweep of microwave around the cavity frequency and magnetic field around Ni^{2+} resonance is shown in Fig. 3.8(b). The cavity frequency shows dispersive shifts as shown by dotted white lines and Fig. 3.8(c), reaching maximum and minimum frequency at 153 mT and 167 mT respectively, which corresponds to the ends of the Ni^{2+} spin inhomogeneous line. The cavity linewidth also shows broadening, as shown in Fig. 3.8(d), reaching nearly background levels of the signal at 160 mT (Fig. 3.8(b)), corresponding to the center of the Ni^{2+} absorption line. Thus we observe both dispersive and absorptive ESR signals due to the coupling of the Ni^{2+} spin ensemble to the microwave resonator. The coupling signal also allows us to estimate the spin inhomogeneous linewidth $\Gamma_{inh} = \frac{\Delta B}{B} \times \omega_0 = 400$ MHz and $\frac{\Omega^2}{\Gamma_{inh}}$ = 7 MHz. We, therefore, extract an ensemble coupling strength $\Omega = 53$ MHz and combining with separately measured cavity linewidth $\kappa = 1.3$ MHz, we can obtain the cooperativity $C = \frac{\Omega^2}{\kappa\Gamma_{inh}} = 5.4$, which represents a high cooperativity coupling of the spin ensemble to the cavity.

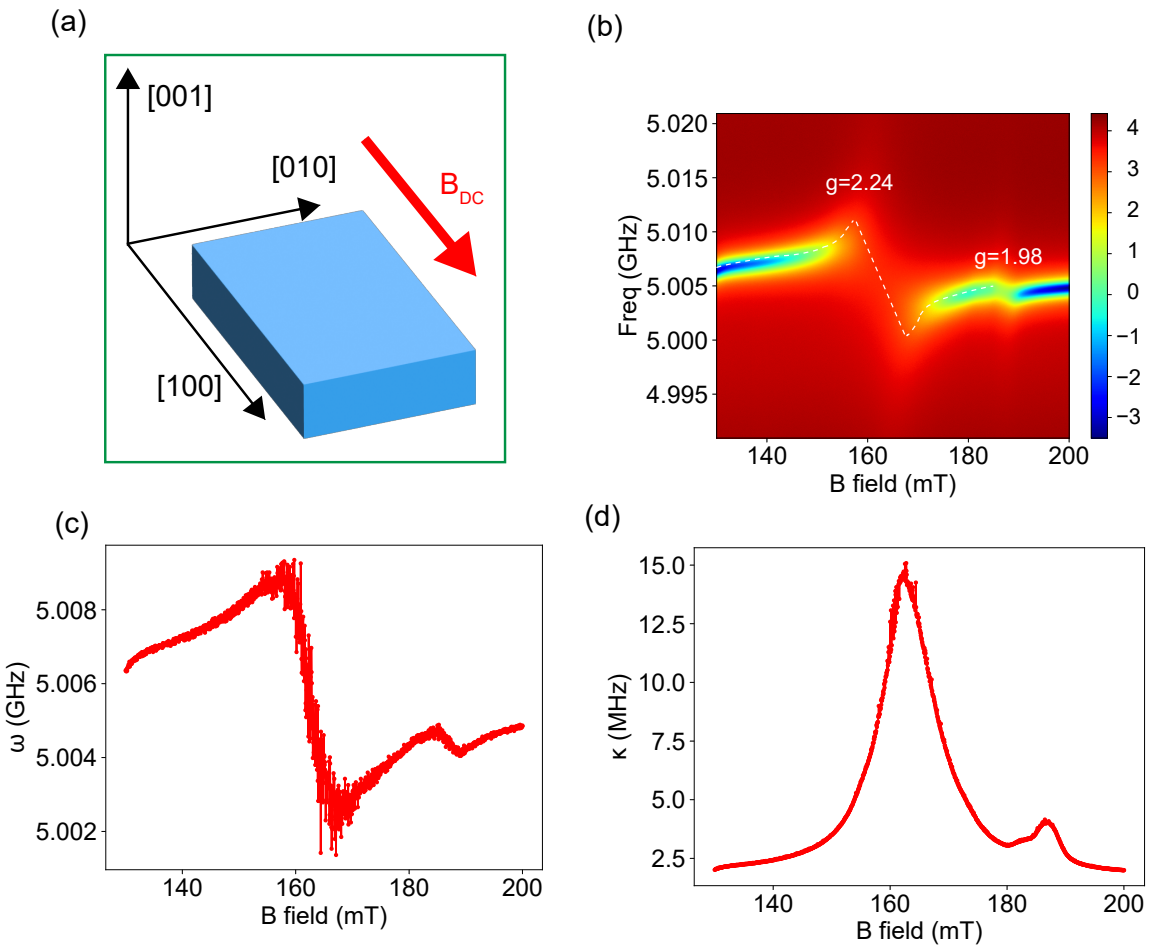


Figure 3.8: (a) The direction of the applied magnetic field with respect to the MgO crystal axis (b) Reflection spectrum ($S_{11}(\omega)$) of the loop-gap cavity measured as a function of the magnetic field applied along the 100 axes of magnesium oxide shows a strong resonance from Ni^{2+} ions (g=2.24) at 160 mT and a smaller peak from Cr^{3+} ions (g=1.98) at 180 mT. White dashes trace the center frequency of the cavity as the magnetic field is swept across Ni^{2+} resonance (c) Cavity frequency shows dispersive shifts and (d) The cavity linewidth shows absorptive broadening due to resonance with Ni^{2+} and Cr^{3+} spin ensemble.

3.3 Continuous Wave ESR

Continuous-wave ESR or (CW ESR) uses the change in the steady response of a microwave cavity to detect spin resonance. Spin resonance due to the application of magnetic field results in absorptive and dispersive coupling of the spins (Section 3.2) to the microwave cavity. The cavity linewidth shows an absorptive linewidth broadening while the resonance

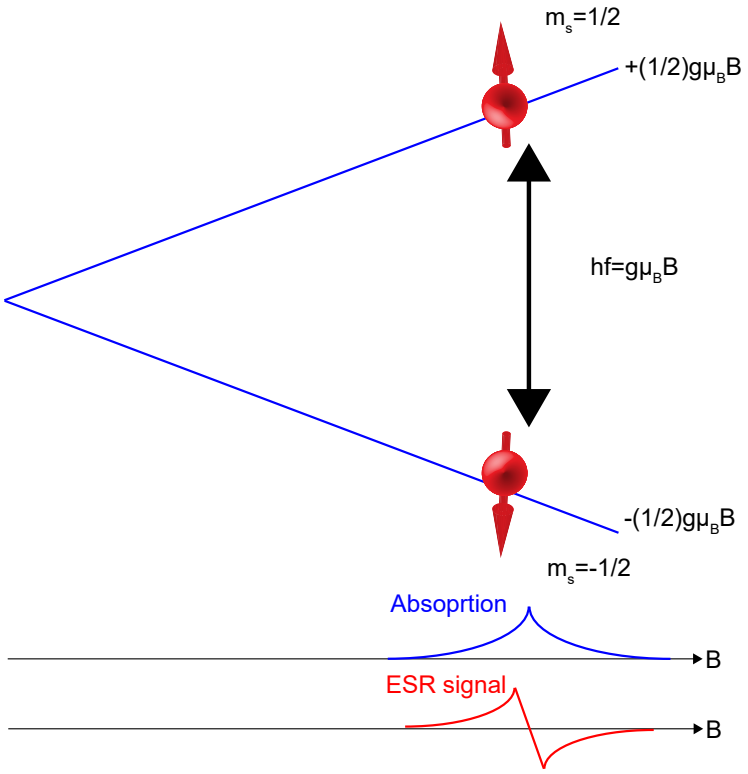


Figure 3.9: Continuous wave ESR spectroscopy measures the derivative of the spin ensemble absorption signal on resonance with a microwave cavity. Application of magnetic field brings spin ensemble on resonance with the resonator, resulting in absorption of microwaves. A derivative of the absorption signal obtained by frequency or field modulation is commonly referred to as the ESR signal.

frequency shows dispersive shifts as spins are brought in and out of resonance with the microwave cavity. Critically coupled microwave cavities ($\kappa_e = \kappa_i$) are very sensitive to changes in intrinsic linewidth (κ_i) and show a large change in the microwave absorption at the cavity frequency $S_{11}(\omega_0)$ when k_i increases due to spin absorption. The signal-to-noise ratio of the ESR signal depends on the cooperatively of the cavity coupling to the spin ensemble, and while high-quality factor cavities are essential to study extremely dilute samples or small magnetic volumes, instrumentation techniques such as phase-sensitive detection can be used to detect extremely small changes in cavity response in the weak cooperativity regime ($C << 1$).

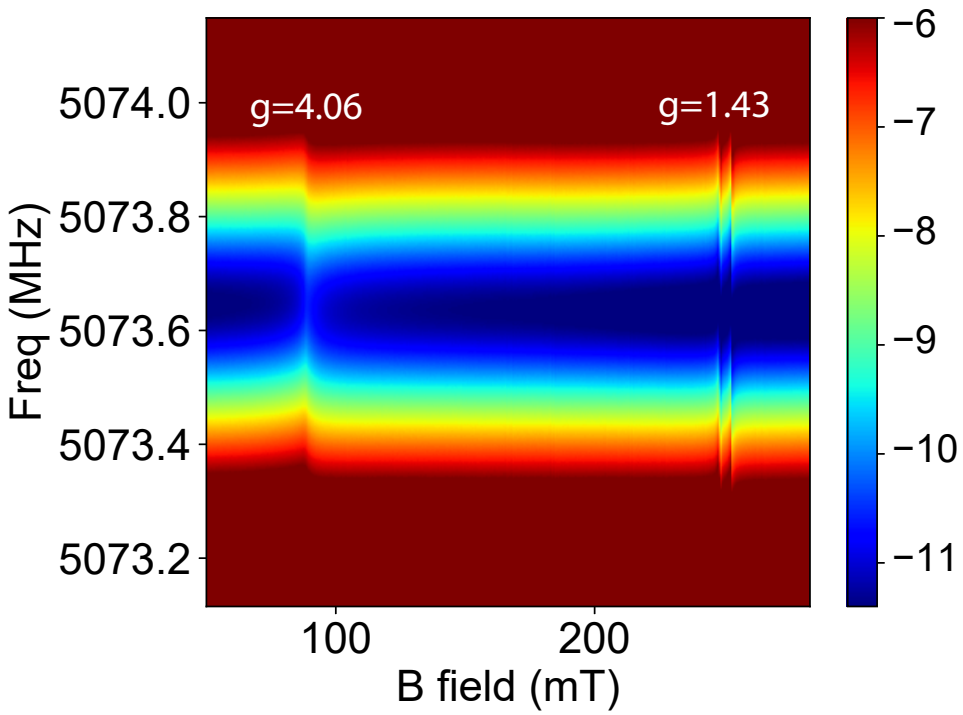


Figure 3.10: Reflection spectrum of the loop-gap cavity (S_{11}(dB)) measured at 4 Kelvin as a function of the magnetic field applied along the D_1 axis of YSO shows resonance from Nd^{3+} ions in site 1 (g=1.43) and site 2 (g=4.06) of YSO.

3.3.1 Characterization of spin-resonator system at sub-Kelvin temperatures

In order to characterize the CW-ESR setup and to study the spin-resonator hybrid system at sub-Kelvin temperatures, CW ESR measurement performed a 4 Kelvin (Fig. 3.10) on the Nd^{3+}:YSO was also repeated at 30 mK. Fig. 3.11 compares the dispersive frequency shift of the resonator at 4 Kelvin and 30 milliKelvin.

The dispersive frequency shift of the resonator (eqn. 3.7) is proportional to $\Omega = g^2N$, where g is the single spin coupling strength and N is proportional to the total number of spins N_{spin}. The temperature dependence of N is given as,

$$N(T) = N_{spin}P(T) \tag{3.11}$$

where P(T) is the spin polarization given as,

$$P(T) = P\downarrow - P\uparrow = \frac{e^{(\hbar\omega/2k_BT)}}{e^{(\hbar\omega/2k_BT)} + e^{(-\hbar\omega/2k_BT)}} - \frac{e^{(-\hbar\omega/2k_BT)}}{e^{(\hbar\omega/2k_BT)} + e^{(-\hbar\omega/2k_BT)}} = \tanh(\hbar\omega/2k_BT) \tag{3.12}$$

Therefore a high degree of spin polarization at low temperatures can increase the ensemble spin coupling strength to the microwave cavity and hence the CW ESR signal. While commercial ESR spectrometers can only operate down to a few Kelvin, at 5 GHz frequency the spin is relatively unpolarized with a polarization P= 3 % at 4 Kelvin, an ESR spectrometer operating at 30 mK in a dilution refrigerator can achieve near unity spin polarization at temperatures below 100 mK (e.g. P = 99.93 % at 30 mK). Therefore, CW ESR spectrometers operating at milliKelvin temperatures can demonstrate significantly higher sensitivity due to a high degree of spin polarization.

To compare the ensemble coupling strength Ω at 30 mK and 4 K in Fig. 3.11, the resonator frequency was fitted with eqn. 3.7. Table. 3.1 shows the fitted Ω and Γ_{inh} for the two transitions in Fig. 3.11. The ensemble coupling strength Ω increases from 0.56 MHz at 4 K to 1.45 MHz at 30 mK, an increase by a factor of 2.58. While the expected increase in Ω of 5.77 ($\sqrt{\tanh((\hbar \times 5.07\text{GHz})/(k_B \times 4))/\tanh((\hbar \times 5.07\text{GHz})/(k_B \times 0.03))}$) is higher than the measuring increase of 2.58, the discrepancy can be accounted for by saturation of the spin ensemble during the measurement at 30 mK due to extremely long spin T_1 at sub-Kelvin temperatures. The observed asymmetric lineshape at 30 mK is also in close agreement with similar observations on Er^{3+}:YSO in the presence of extremely long spin relaxation at milliKelvin temperatures [35].

Assuming a near unity spin polarization at 30 mK, we can estimate N_{spin} based on the known doping of the sample and the sample volume:

$N_{spin} = 1.95 \times 10^{22}\,\text{atoms/cm}^3 \times 0.006\,\text{cm}^3 \times 0.8(\text{isotope}) \times 40 \times 10^{-6}(\text{doping})$

$\times 0.25(\text{sites}) = 9 \times 10^{14}\,\text{spins}$

The measured ensemble coupling strength $\Omega = 1.46$ MHz, along with estimated N_{spin} allows

T	Γ_1	Γ_2	Ω_{inh1}	Ω_{inh2}	Br_1	Br_2
4 K	6.02 MHz	7.30 MHz	0.53 MHz	0.56 MHz	0.251 T	0.255 T
30 mK	14.57 MHz	16.01 MHz	1.36 MHz	1.45 MHz	0.251 T	0.255 T

Table 3.1: Comparison of ensemble coupling strength Ω, and spin inhomogeneous linewidth Γ_{inh}.

us to estimate the single spin coupling strength of the resonator $g = \Omega/\sqrt{N_{spin}} = 0.05$ Hz.

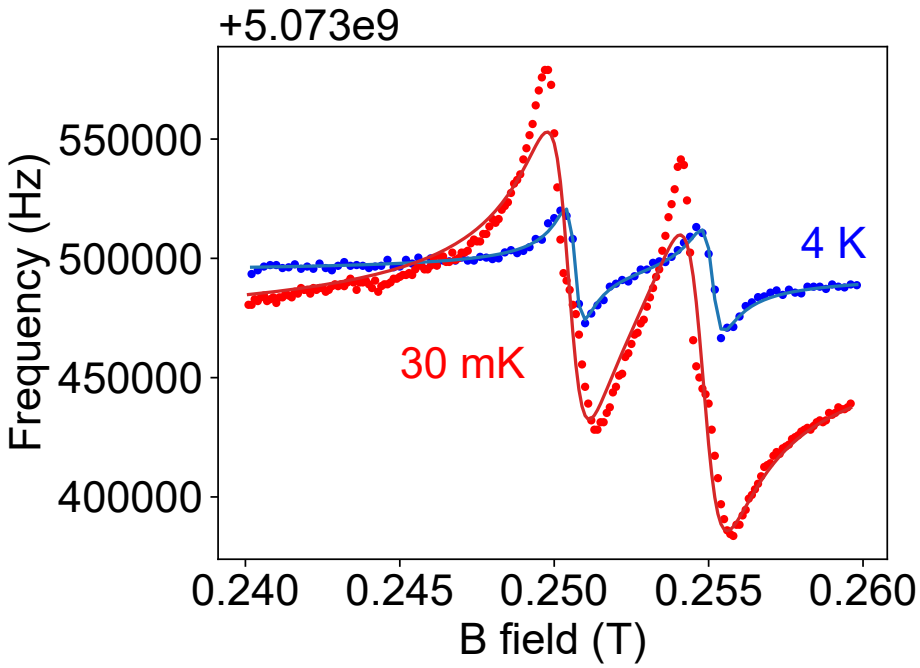


Figure 3.11: Continuous wave ESR on Nd^{3+}:YSO sample showing the cavity dispersive frequency shifts measured as a function of the magnetic field at 30 mK and 4K. The cavity shows larger frequency shift $\Delta f = 150$ kHz at 30 mK as compared to $\Delta f = 46$ kHz at 4 Kelvin.

3.3.2 Modulation techniques to enhance CW-ESR sensitivity

Modulation techniques are employed in ESR spectrometers to enhance the detection sensitivity of the electronics using phase-sensitive detection to allow for the measurement of

spin ensembles with extremely low cooperativity coupling to microwave resonators. Two alternative, but, related approaches of magnetic field modulation and microwave frequency modulation allow for measurement of the first derivative of the ESR absorption [61]. While the two modulation techniques can provide a similar ESR spectrum [90] [61], the techniques are not generally equivalent [212].

Magnetic field modulation

The magnetic field modulation approach is based on the absorptive coupling signal of the spin ensemble to the microwave cavity. Absorptive coupling of a spin ensemble to a critically coupled cavity results in a change in microwave absorption at the cavity resonance frequency. When external field modulation coils are placed around the microwave cavity to produce a modulation of the magnetic field δB at a frequency δf, this modulation of the net magnetic field $B = B_0 + \delta B$ around the spin resonance field B_0 results in modulation of the microwave absorption by the cavity. Thus, there is a transfer of modulation from field modulation to the modulation of the microwave carrier signal from the cavity during spin resonance [85]. The reflected microwave signal from the cavity is mixed with a reference signal at the modulation frequency (δf) using lock-in detection. The advantages of the field modulation approach include the ability to tune the modulation amplitude δB, which can be used to filter out broad background ESR features. This approach uses relatively simple electronics and versatility along with a higher signal-to-noise ratio, which makes it the more commonly used approach in commercial X-band ESR spectrometers.

Magnetic field modulation however, requires the installation of external field modulation coils, which could be challenging for integration with three-dimensional vector magnets due to two constraints, firstly, the requirement of applying magnetic field modulation in the same direction as the external field, and, secondly, the limited physical space within a vector magnet. The interaction between the modulation coils ($F \propto B \times I$) carrying a current I and

external magnetic field B can be a significant source of mechanical vibrations. The modulation coils produce a spatially inhomogeneous modulation field, which leads to a deviation of the ESR signal from the derivative of spin absorption [85]. Further, this approach is not compatible with ESR experiments using two-dimensional superconducting microresonators where the application of magnetic field results in a decrease in the resonator quality factor and therefore a change in net microwave absorption with an applied magnetic field. This changing absorption due to the resonator response to the field can produce a significant background signal, which can interfere with the absorption signal from electron spins.

Microwave frequency modulation

The frequency modulation approach is based on detecting the dispersive frequency shifts of the cavity upon resonance with electron spins. Extremely small frequency shifts of the resonator of the order of several Hz can be detected using principles from the Pound-Drever-Hall (PDH) technique commonly used for stabilizing the frequency of lasers.

Pound-Drever-hall method based frequency reference

The pound-Drever-hall technique is key to several applications including the frequency stabilization of lasers. [29], microwave sources [133], and the detection of gravitational waves using interferometer techniques [31] The technique relies on creating an error signal based on the difference in the frequency of a stable frequency reference cavity and an 'unstable' source frequency. For laser stabilization, the error signal is fed back to the laser in order to stabilize the laser to a higher stability reference cavity.

The discussion on error signal in this section has been adapted based on the discussion on Pound-Drever-Hall (PDH) laser frequency stabilization in ref. [29]. A microwave resonator probed in reflection is described by equation 3.5,

$$S_{11}(\omega) = 1 + \frac{k_e}{i(\omega - \omega_0) - (k_i + k_e)/2} \tag{3.13}$$

A microwave source producing a signal at frequency ω is provided with an external phase modulation signal at a modulation frequency ω_m such that the resulting voltage is described by,

$$V(t) = V_0 e^{i(\omega t + \beta \sin \omega_m t)} = V_0(J_0(\beta) + 2iJ_1(\beta)\sin\omega_m t)e^{i\omega t}$$
$$= V_0(J_0(\beta)e^{i\omega t} + J_1(\beta)e^{i(\omega+\omega_m)t} - J_1(\beta)e^{i(\omega-\omega_m)t})$$

where β is the modulation depth and $J_n(\beta)$ is Bessel's function of n^{th} order. The external phase modulation signal can be provided by the internal reference of a lock-in amplifier. The resultant signal V(t) can be visualized as a sum of three components, a carrier signal at frequency ω and two sidebands at frequency $\omega - \omega_m$ and $\omega + \omega_m$. The signal V(t) is sent to the microwave cavity and the reflected signal gets modulated by the cavity response S_{11},

$$V_{ref}(t) = V_0(S_{11}(\omega)J_0(\beta)e^{i\omega t} + S_{11}(\omega+\omega_m)J_1(\beta)e^{i(\omega+\omega_m)t} - S_{11}(\omega-\omega_m)J_1(\beta)e^{i(\omega-\omega_m)t}) \tag{3.14}$$

The reflected signal $V_{ref}(t)$ is demodulated on a PIN diode (microwave power detector), which produces an output voltage $V_{out}(t)$ proportional to the input power $V_{out}(t) = cP_{ref} = c|V_{ref}(t)|^2$. The signal $V_{out}(t)$ has three components, a DC component V_1, a component oscillating at frequency $V_2(\omega_m)$ ω_m and a component V_3 at frequency $2\omega_m$,

$$V_{out}(t) = V_1 + V_2(\omega_m) + V_3(2\omega_m) \tag{3.15}$$

$$V_1 = cV_0^2(|J_0(\beta)|^2|S_{11}(\omega)|^2 + |J_1(\beta)|^2|S_{11}(\omega+\omega_m)|^2 + |J_1(\beta)|^2|S_{11}(\omega-\omega_m)|^2) \tag{3.16}$$

$$V_2(\omega_m) = 2cV_0^2J_0(\beta)J_1(\beta)[\mathrm{Re}(S_{11}^*(\omega+\omega_m)S_{11}(\omega) - S_{11}(\omega-\omega_m)S_{11}^*(\omega))]\cos\omega_m t$$
$$+2cV_0^2J_0(\beta)J_1(\beta)[\mathrm{Im}(S_{11}^*(\omega+\omega_m)S_{11}(\omega) - S_{11}(\omega-\omega_m)S_{11}^*(\omega))]\sin\omega_m t \tag{3.17}$$

The output of the microwave diode (V_{out}) is fed to the lock-in amplifier, which demodulates the signal component $V_2(\omega_m)$ at frequency ω_m while the DC component V_1 and the high-frequency component $V_3(2\omega_m)$ are filtered out.

In the slow modulation regime where ω_m is small compared to the cavity frequency, the term $\sin\omega_m t$ vanishes while the $\cos\omega_m t$ term survives. Therefore, the mixer inside the lock-in amplifier demodulates the $\cos\omega_m t$ with its internal frequency reference and produces a signal at DC frequency, which is referred to as the error signal $\epsilon(\omega)$,

$$\epsilon(\omega) = 2cV_0^2 J_0(\beta)J_1(\beta)\mathrm{Re}[S_{11}^*(\omega+\omega_m)S_{11}(\omega) - S_{11}(\omega-\omega_m)S_{11}^*(\omega)] \tag{3.18}$$

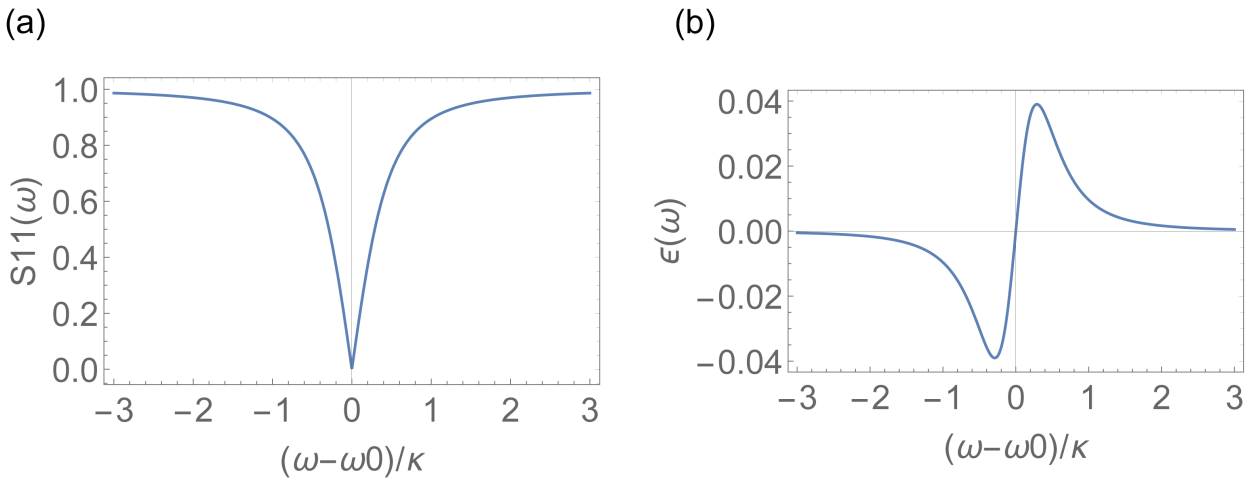


Figure 3.12: Cavity reflection spectrum $|S_{11}(\omega)|$ (a) and the error signal $\epsilon(\omega)$ (b) plotted as a function of the frequency offset from the cavity center.

Substituting the expression for the cavity reflection spectrum (S_{11}) from eq. 3.13 into the error signal as derived in eq. 3.18, we obtain a characteristic dispersive shape of the error signal. This is illustrated numerically in Fig. 3.12 (a) and (b) plotted for the cavity parameters $\kappa_i = 0.5$ MHz, $\kappa_e = 0.499$ MHz, $\kappa = \kappa_i + \kappa_e = 0.999$ MHz and modulation amplitude $\omega_m = 30$ kHz. In the regime of slow modulation (dithering), the error signal shows a dispersive shape with a linear region around the cavity center. The slope of the error signal in V/Hz can be used to read out the frequency offset between the microwave

source frequency and cavity frequency in terms of the error signal amplitude.

In order to read the ESR signal from the error signal, a stable microwave source is used to generate a frequency-modulated signal at a carrier frequency equal to the cavity resonance frequency. The modulation signal is supplied by an external lock-in amplifier and the signal reflected from the cavity is demodulated on a microwave diode. The output of the diode is fed to the lock-in amplifier to obtain the error signal, which serves as a linear reference to the cavity frequency with respect to the microwave source. To acquire the CW ESR signal, the microwave source is kept fixed at the initial cavity frequency, and the magnetic field is swept. As electron spins come in and out of resonance with the microwave, the cavity frequency shifts up and then down as illustrated in Fig. 3.8. As long as the microwave source frequency is within the linear region of the error signal, the frequency shifts of the cavity will result in a proportional change in the error signal amplitude. The error signal depends on the cavity linewidth, frequency modulation amplitude, frequency modulation deviation, and response of the microwave diode. The PDH-based technique has also been previously used in some studies for the fast characterization of superconducting resonators [113] as well as for ESR experiments [49].

The microwave frequency modulation setup used in this thesis was built with the contributions of Yuxiang Pei. Fig. 3.13(a) shows the schematics of the frequency modulation setup used to detect CW-ESR. The microwave signal generator (Agilent N5181A) is provided with an external FM reference from a lock-in amplifier (SRS865A). The frequency-modulated signal at 5.08 GHz carrier frequency is sent to a microwave cavity (κ = 1.5 MHz) mounted inside the 10 mK stage of the dilution refrigerator. The reflected signal is amplified by room-temperature amplifiers (ZX60-83LN+) and demodulated at a microwave power detector (ZX47-60-S+). The output from the power detector is fed into the same lock-in amplifier and the error signal is measured at the in-phase (X) output of the lock-in amplifier after adjusting the phase of the internal mixer. Fig. 3.13(b) shows the measured error signal ϵ

obtained after sweeping the frequency of the source across the cavity frequency. The error signal shows a characteristic dispersive shape along with a linear region around the cavity frequency. The sensitivity of the setup is proportional to the slope of the linear region of the error signal (red dashes, Fig. 3.13(b)). The FM modulation frequency ω_m in the measurement was kept at 60 kHz, while the FM deviation was swept in order to maximize the slope of the error signal. Fig. 3.13(c) shows an increase in the error signal slope with an initial increase in FM deviation until a maximum slope (S) of 175 mV/MHz is reached for deviations larger than 500 kHz. The measured slope, along with separately measured RMS noise level at the lock-in amplifier output $V_{noise} = 0.1$ mV would result in the smallest detectable frequency shift of the cavity $\Delta f_{min} = V_{noise}/S = 570$ Hz.

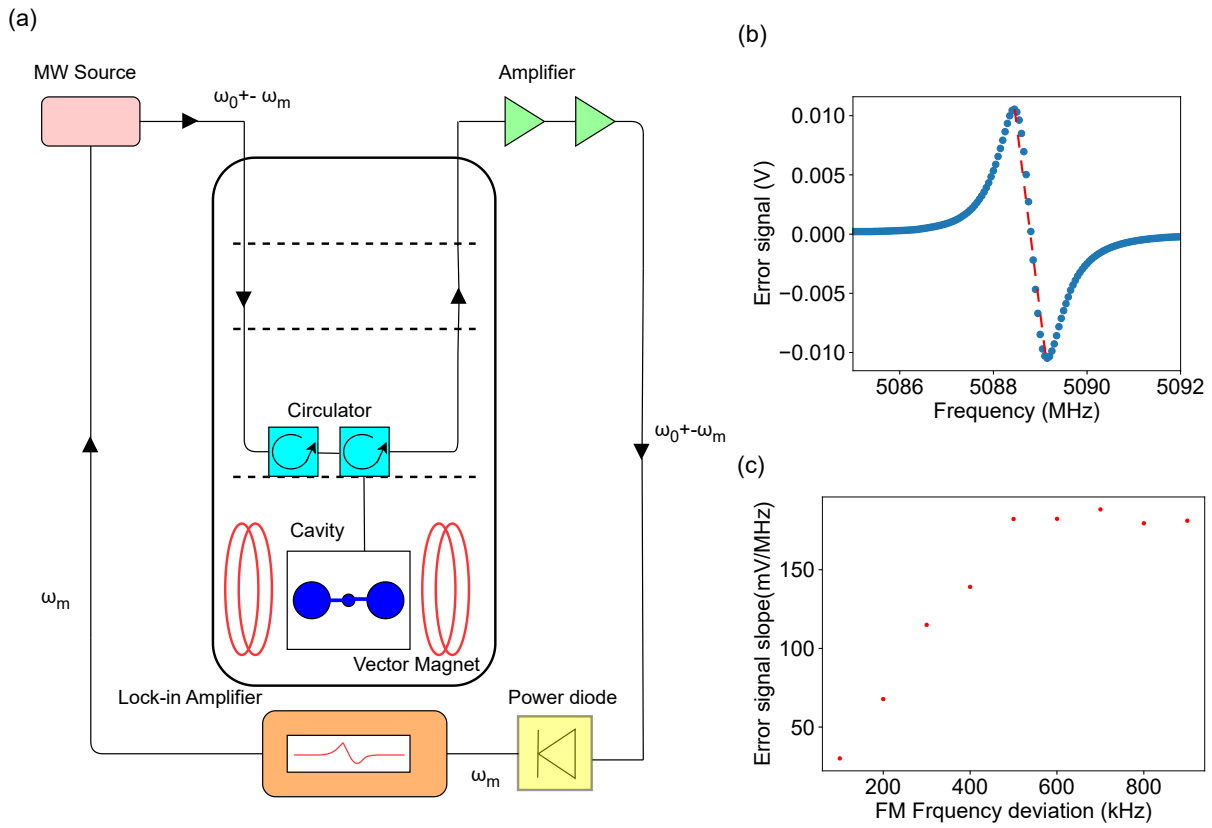


Figure 3.13: (a) Experimental setup used for the demonstration of frequency modulation technique for CW-ESR (b) Measured error signal for the microwave cavity (c) Dependence of error signal slope on the frequency modulation (FM) deviation.

Fig. 3.10 and Fig. 3.14 illustrate CW ESR measurements performed on Nd^{3+} : YSO with cavity reflection spectrum measurements using a vector network analyzer and with frequency modulation technique respectively. While reflection spectrum measurements in Fig. 3.10 provide information on the absorptive coupling signal as well along with the dispersive signal, the approach has limited sensitivity, and only the strongest ESR signal from the $^{142,146,148}Nd^{3+}$ isotopes with I=0 with 78.9% abundance could be observed. On the other hand for the same scan performed using the frequency modulation technique, in Fig. 3.14 we also observe small satellite lines corresponding to ESR transitions from $^{143}Nd^{3+}$, $^{145}Nd^{3+}$ with I=7/2 and 21.1% abundance. This demonstrates the sensitivity enhancement due to the frequency modulation approach. CW ESR scans performed using the frequency modulation approach are also significantly faster than the reflection spectrum measurement method, as while the former measures the frequency shifts in real-time, the latter involves averaging the spectrum several times over a large frequency range in order to complete a scan.

The minimum number of detectable spins can be estimated by fitting the satellite transitions from the I=7/2 isotopes. Fig. 3.15 shows the transition at 170 mT, with a peak-to-peak frequency shift Δf of 2 kHz, inhomogeneous linewidth Γ_{inh} of 51 MHz and collective coupling Ω of 0.2 MHz. With the observed noise level of $\lessapprox$ 0.5 kHz, the signal-to-noise ratio (SNR) of the transition is ≈ 4. The maximum number of spins in for one transition from I=7/2 isotope is $N = 4.5 \times 10^{13}$. With the expected spin polarization of 6.1 % at 4 Kelvin, 5.89 GHz, this corresponds to an effective number of spins $N = 2.7 \times 10^{12}$. Therefore, the minimum number of detectable spins with SNR=1 would be $N_{min} = 6.75 \times 10^{11}$, which is comparable to the state-of-the-art commercial CW-ESR spectrometers.

The frequency modulation approach is therefore ideal for CW ESR on low-density samples with three-dimensional resonators for application in setups where the primary source of frequency measurement error is instrument noise. This approach, however, suffers from certain challenges, including the lack of ability to filter out broad ESR signals by adjusting the

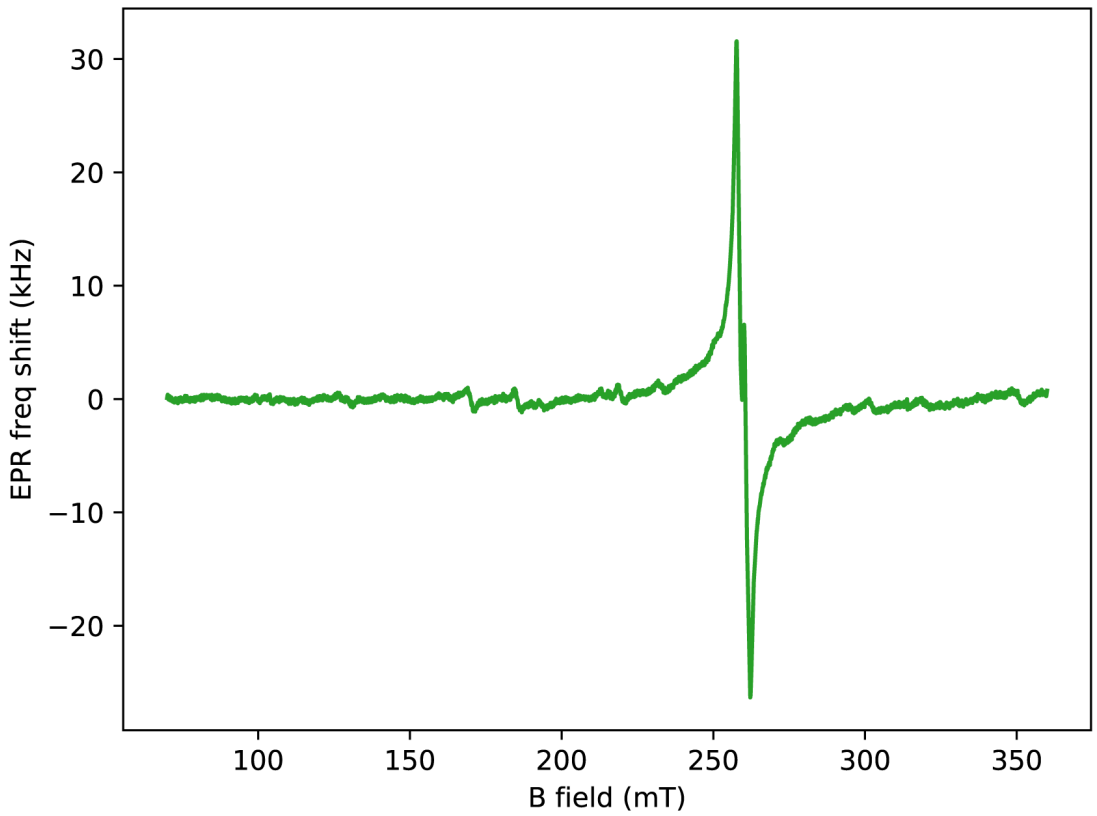


Figure 3.14: Continuous wave (CW) ESR obtained by measuring the dispersive frequency shifts of the cavity using the frequency modulation setup. The magnetic field was applied along the D_1 axis of YSO at 4 Kelvin show ESR signal from both $^{142,146,148}Nd^{3+}$ isotopes with I=0 and satellite lines from $^{145}Nd^{3+}$ with 21.1% I=7/2.

modulation amplitude, the complexity of the electronics involved, as well as the calibration required to maximize the error signal amplitude in order to obtain the maximum sensitivity to cavity frequency shifts. Moreover, the technique also assumes the error signal is linear to the difference in the frequency of the carrier and the cavity. This is only applicable in the cases of weak cooperatively when the dispersive cavity frequency shifts are much smaller than the cavity linewidth. For example, for high-quality factor superconducting cavities and resonators, the error signal itself would show a change in shape due to a significant broadening of the cavity linewidth, and therefore the error signal amplitude would depend non-linearly

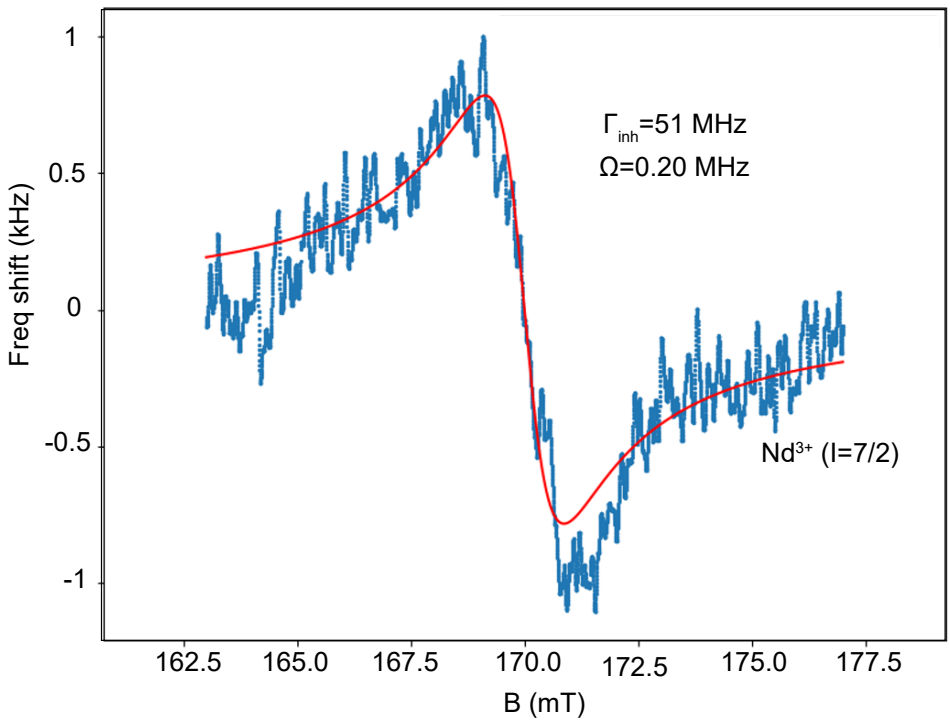


Figure 3.15: Continuous wave (CW) ESR on satellite lines from $^{145}Nd^{3+}$ with 21.1% I=7/2 allows to estimate the minimum number of detectable spins.

on the frequency shift of the cavity. Further, two-dimensional superconducting resonators deal with an inherent instability of the resonator frequency due to noise induced by the tuning of magnetic flux as the main source of source, therefore, sensitivity enhancement due to the modulation approach would not significantly improve the signal-to-noise ratio of the measurement.

3.4 Pulsed ESR

Pulsed ESR broadly refers to time-domain electron spin resonance techniques used to study the relaxation and decoherence mechanisms. The most commonly used pulsed ESR techniques involve the detection of a two-pulse (Hahn [78]) echo signal, which is proportional to the average magnetization of the paramagnetic sample. Pulsed ESR offers higher sensitivity over CW detection but involves a complex electronics setup including microwave

sources, arbitrary waveform generators (AWGs), IQ mixers, microwave switches, fast oscilloscopes/digitizers as well as room temperature and cryogenic electronics, all coordinated to detect extremely small spin echo signals. The unique aspects of pulsed ESR developed in the thesis include a high-sensitivity cryogenic setup to allow for the detection of extremely weak spin echo signals by cryogenic preamplification, the generation of phase-controlled spin echo pulses by using fast AWG along with an IQ mixer for upconversion, and heterodyne detection of spin echo. This section covers all the aspects of the pulsed ESR electronics and instrumentation in detail.

3.4.1 High sensitivity pulsed ESR with cryogenic electronics

The central challenge with pulsed ESR is the detection of a relatively weak spin echo signal in the presence of significant thermal noise background. The spin echo efficiency (η_{echo}) defined as the fraction in input photons emitted in the echo depends on the cooperativity C and the cavity loss rates κ_{e} and κ as $\eta_{\text{echo}} = (4\text{C}(\kappa_{\text{e}}/\kappa))^2$ [144]. Spin echo efficiencies in the range of 10^{-3} and 10^{-10} have been reported in experiments [201] [144] [165][134]. While commercial pulsed ESR spectrometers use high-power pulses (Watts to kiloWatts [165]) to generate spin echo signals with nanoWatts power, the use of high-power pulses is not feasible for milliKelvin ESR spectrometers. Firstly, the typical cooling power at 10 mK temperature is about 20 μW. This limits the peak on-chip power of spin echo pulses to a few mW (0 dBm). Further, for ESR measurements using superconducting resonators, the peak power is typically limited to several microWatts or nanoWatts (≈ -30 to -60 dBm) to avoid exceeding the critical current density of the superconductor. Assuming a peak power of -60 dBm and echo efficiency of 10^{-6}, the expected average spin echo power is -120 dBm, which is lower than the room temperature noise power of -114 dBm in a bandwidth of 1 MHz. Therefore, in order to detect weak spin echo signals with peak powers lower than the room temperature noise power, the use of high gain, low noise cryogenic preamplifiers is critical. To illustrate

these concepts, we use a model of a cascade of amplifiers, each with a gain $G_i = S_{out}/S_{in}$ and noise temperature $T_i = P^i_{noise}/Bk_B$ where B is the measurement bandwidth (Fig. 3.16). The cascade of amplifiers acts as an effective unit with a gain $G_{eff} = G_1G_2G_3$ and noise temperature T^{eff}_{noise} given as [174],

$$G_1G_2G_3T^{eff}_{noise} = G_1G_2G_3(T_{in} + T_1) + G_2G_3(T_2) + G_3T_3 \tag{3.19}$$

or,

$$T^{eff}_{noise} = (T_{in} + T_1) + T_2/G_1 + T_3/(G_1G_2) \tag{3.20}$$

Detection of low power signals requires simultaneously a high gain G_{eff} as well as low noise temperature T^{eff}_{noise}. Equation. 3.20 indicates that the noise temperature of the chain of amplifiers is primarily determined by the noise temperature of the first amplifier of the chain ($T_{in} + T_1$). Therefore, with a choice of near-quantum noise-limited Josephson traveling-wave parametric (TWPA) [117] amplifiers as the first stage (G_1=18 dB, $T_1 \approx 0.3$ K), HEMT (high electron mobility transistor) as the second stage (G_2=42 dB, $T_2 \approx 4$ K) and room-temperature amplifiers (G_3=25 dB, $T_3 = 325$ K) we get an effective noise temperature $T^{eff}_{noise} = T_{in} + 0.37\,\mathrm{K}$, which is near-limited by the noise floor of TWPA and input noise T_{in}. The input noise temperature T_{in} can be lowered by attenuating the thermal noise photons from the room temperature as well as higher temperature stages inside a dilution refrigerator from entering the 10 milliKelvin stage. Fig. 3.17 shows the attenuator selection used for different experiments in this thesis. The readout lines have zero dB attenuators for thermalization however, all the signal input lines have a total attenuation between 16 - 52 dB depending on the specific experiments. The superconducting device lines have an attenuation of 42 dB with a noise temperature of 237 mK, which is comparable to the noise temperature of a TWPA [117]. The 3D cavity ESR line has total 16 dB attenuation with a resulting

thermal noise temperature of 12 Kelvin at the 10 mK stage, which is comparable to the noise temperature of the HEMT amplifier. Ideally, higher attenuation at the low-temperature stages (T <4 K) would maximally attenuate the noise, however, heating generated due to attenuation of the signal would also significantly increase the temperature of the low-temperature stages. Therefore, attenuation at each stage is optimized to balance the heating generated by the attenuation of a stronger signal with the necessary attenuation of the high-temperature thermal noise.

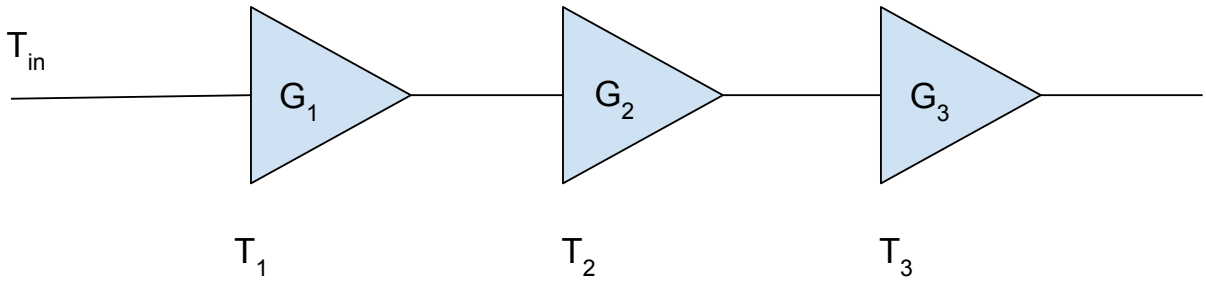


Figure 3.16: Simplified model of a chain of amplifiers with gain G_i and noise temperature T_i with an input noise temperature T_{in}.

3.4.2 Generating phase-controlled ESR pulses

Robust spin control requires the ability to generate phase-controlled, shaped microwave pulses for applications like spin initialization and dynamical decoupling. While microwave switches operating with TTL (transistor-transistor logic) DC pulses on a continuous wave microwave source can be used to generation of shaped microwave pulses, the phase of the carrier cannot be controlled for each pulse within the pulse sequence. This challenge can be addressed by utilizing fast arbitrary waveform generators (AWG), which allow for the generation of pulses with arbitrary amplitude and phase. An arbitrary waveform file is synthesized point-by-point and written in a text file to be uploaded to the AWG sequencer memory, which combines several such arbitrary waveforms and plays them in a pre-determined sequence at

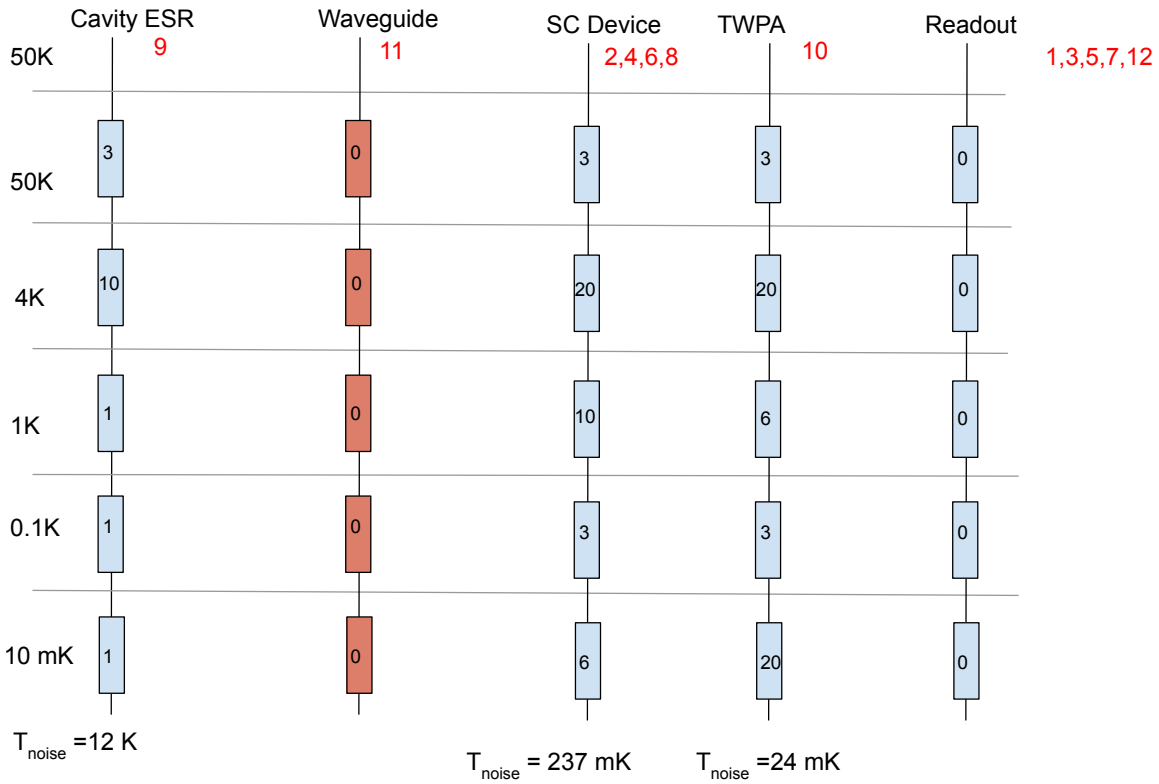


Figure 3.17: The attenuator selection used inside the Bluefors LD 250 dilution refrigerator for experiments in this thesis. The attenuator combination is selected in order to allow a low thermal noise temperature at the 10 milliKelvin stage.

a fixed sampling rate. This method of uploading a point-by-point generated waveform text file into the AWG sequencer was used in the experiments described in Chapters 2 and 5. This 'conventional' approach is, however, limited by the internal memory of the AWG, which limits the total length of the arbitrary sequence. For instance, the total number of dynamical decoupling sequence pulses was limited to N $<$248 in the measurements in Chapter 5.

Several advanced FPGA (Field Programmable Gate Array) based AWGs allow for uploading waveform generation scripts to the AWG sequencer directly. This approach of uploading scripts is limited only by the size of the code as compared to the size of the waveform itself for the conventional approach, therefore, FPGA-based AWGs allow for the generation of an

arbitrarily large number of pulses.

However, even the fastest AWGs operate only up to 750 MHz, which is significantly lower than the typical ESR frequencies of 5-6 GHz. This necessitates the use of IQ (In-phase and quadrature) mixer-based upconversion technique to upconvert the phase-controlled pulses generated at 100s of MHz by the AWG to 5-6 GHz.

Spin control pulse generation with IQ upconversion

A double-sideband microwave mixer multiplies two input signals (Fig. 3.18(a)), a carrier with frequency f_{LO} incident on the L port and an intermediate frequency signal at frequency f_{IF} incident on the I port to produce two sidebands, a red sideband at frequency $f_{LO} - f_{IF}$ and a blue sideband at frequency $f_{LO} + f_{IF}$ along with the carrier f_{LO} on the R port. The process can be described by the multiplication of two sine waves,

$$\sin(f_{LO}t)\sin(f_{IF}t) = 1/2(\cos(f_{LO} - f_{IF})t - \cos(f_{LO} - f_{IF})t)$$

The mixing process, therefore, produces two sidebands along with the carrier as shown in the inset Fig. 3.18(a). For application in control of electron spins with microwave cavities, one of the sidebands could be on-resonant with the cavity. However, the other sideband along with the carrier could result in either driving the spin ensemble when $f_{IF} < \kappa$ or producing background signals, which could interfere with the spin echo signal. These effects can be avoided with a single sideband mixer, also referred to as an image rejection mixer or IQ mixer. Fig. 3.18(b) illustrates the schematics of an IQ mixer, which consists of two double sideband mixers, connected together such that the LO for the bottom mixer is kept out of phase by 90°. The input at the first mixer is called I (in-phase) while the input for the other mixer is called Q (quadrature). Supplying a sine wave at the I port and a cos wave at the Q port would result in the sum $(-\cos(f_{LO} - f_{IF})t - \cos(f_{LO} - f_{IF})t))$ and difference $((\cos(f_{LO} - f_{IF})t - \cos(f_{LO} - f_{IF})t))$ of the two sideband signals produced at the two R ports. The output from two R ports is added together resulting in only one sideband at

the R output of the mixer. The choice of phase between the I and Q signal would determine the suppression of either the red or the blue sideband [91]. For the measurements in this thesis, a phase of -90° was added to the Q port with respect to the I port, which would result in suppression of the red sideband, as shown in the inset of Fig. 3.18(b). The output at the R port an IQ mixer in this configuration can be written as,

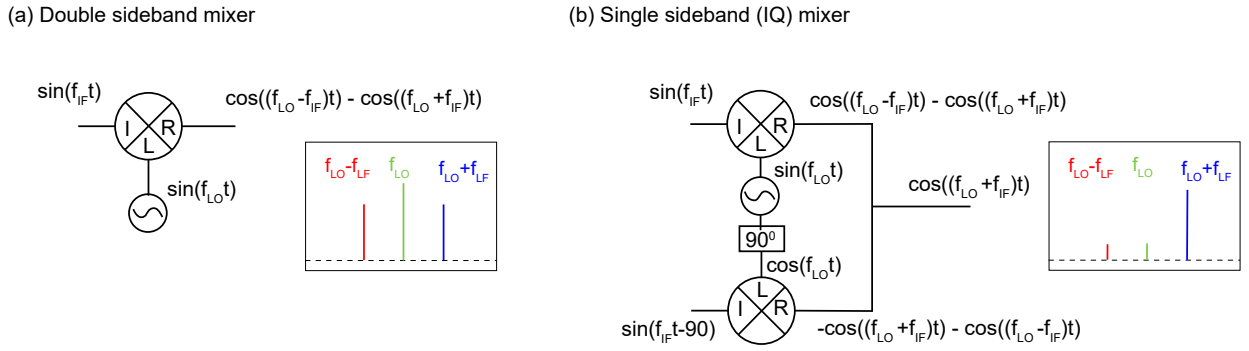


Figure 3.18: Schematic and operation of a (a) double-sideband mixer and (b) a single-sideband (IQ) mixer.

$$\mathrm{R} = [\mathrm{A_I}\sin(\mathrm{f_{IF}t})]\sin(\mathrm{f_{LO}t}) + [\mathrm{A_Q}\sin(\mathrm{f_{IF}t}+\phi)]\cos(\mathrm{f_{LO}t}) \tag{3.21}$$

For an ideal IQ mixer, the two individual DSB mixers are identical and the phase shift of LO is exactly 90°. Therefore, with the choice of $\mathrm{A_I} = \mathrm{A_Q}$ and $\phi = -90^\circ$, we obtain,

$$\mathrm{R} = \mathrm{A}[\sin(\mathrm{f_{IF}t})\sin(\mathrm{f_{LO}t}) + \sin(\mathrm{f_{IF}t}-90^\circ)\cos(\mathrm{f_{LO}t})] \tag{3.22}$$

or,

$$\mathrm{R} = -\mathrm{A}[\cos(\mathrm{f_{LO}}+\mathrm{f_{IF}})\mathrm{t}] \tag{3.23}$$

which produces the upper sideband as illustrated in the schematic in the inset of Fig. 3.18(b). In practice, however, due to a small difference in the two DSB mixers (amplitude imbalance) and a difference in phase shift from 90° (phase imbalance), the choice of $\mathrm{A_I} = \mathrm{A_Q}$ and $\phi = -90^\circ$ will not fully suppress the red sideband. Therefore, precise calibration of the

IQ mixer is necessary in order to suppress the red sideband and LO leakage by $\gtrapprox$ 50 dB.

Calibration of an IQ mixer for suppression of LO and sideband leakage

Effective suppression of one of the sidebands and the LO leakage from an IQ mixer requires calibration at every frequency. The red sideband and LO can be suppressed following the process below

- Connect the LO port of the IQ mixer to an MW source at f_{LO} = 5-6 GHz and I, Q port to two channels of an AWG (ch1, ch2) producing continuous wave output at f_{IF} = 200 MHz.
- Set the amplitude of the MW source in the optimum LO drive power specified by the mixer, as well as the voltages of the two AWG channels, ch1, ch2 to V1 and V2. For the mixer used in this setup, the MW output at the LO port is $\approx$ 17 dBm while the voltage of the AWG channels is V1 = V2 $\approx$ 1 V.
- Set phase of the AWG channel ch1 connected to the I port to 0, phase of the channel ch2 connected to port 2 Q port to $\phi = -90°$.
- Connect the R output of the IQ mixer to a spectrum analyzer and scan around f_{LO} in a range slightly larger than $2f_{IF}$.
- Turn on the MW output of the source and the AWG to observe the LO, as well as two sidebands on the spectrum analyzer.
- Reduce the voltages V1 or V2 to slightly below 1 V, in order to suppress the red sideband ($f_{LO} - f_{IF}$). Based on the amplitude imbalance of the mixer ports, reduction either of V1 or V2 will result in suppression of the red sideband.
- Adjust the phase of the AWG channel 2, around $\phi = -90°$ to further suppress the red sideband.

- Repeat the last two steps iteratively until the red sideband ($f_{LO} - f_{IF}$) is $\approx$ 50 dB smaller than the blue sideband ($f_{LO} + f_{IF}$).

- To suppress the LO leakage, add a small voltage offset (a few mV) to both ch1 or ch2 of the AWG. The voltage offset to the individual channels could be a different value, either positive or negative. Repeat the process in small voltage steps until the LO amplitude is minimized.

3.4.3 Pulsed ESR setup

Figure 3.19 shows the pulsed ESR setup used for experiments using a 3D cavity coupled to a bulk paramagnetic sample and a cryogenic HEMT for preamplification of the spin echo. Microwave local oscillator (LO) signal in the range of 5-6 GHz is generated using Agilent N5181A source at -3 dBm power, and split (Amplifier1: Mini-Circuits ZX10-2-71-S+) after amplification (Amplifier1: Mini-Circuits ZVA-183-S+, +26 dB). One branch of the signal after LO is sent to an IQ mixer (Marki MMIQ 0218LXPC), where phase-controlled I and Q pulses at 100-200 MHz generated by an AWG (Keysight 33622a/Zurich Instruments HDAWG) are upconverted to 5-6 GHz and the output of the mixer with is sent to an SPDT (single pole double throw) microwave switch (ZASWA-2-50DR+). The microwave switch (input gate) is controlled using TTL pulses generated by the market channel of the AWG is used to isolate (60 dB isolation) the noise amplified by the mixers from entering the cryostat when the spin echo pulses are off. The signal from IQ mixers has a power of $\approx$ -8 dBm, which can be amplified by 15 dB by a room-temperature low-noise amplifier to have a maximum power of $\approx$ 7 dBm entering the fridge. However, for experiments utilizing a cryogenic HEMT, there are two additional considerations that limit the gain of amplifiers amplifying the spin-driving pulses before entering the fridge. Firstly, the input noise temperature at HEMT should be a few Kelvin, which requires 16-20 dB attenuation between the room temperature stage and the 10 mK stages of the input line to suppress the thermal noise. Secondly,

cryogenic HEMTs have a low peak power <0 dBm which limits the maximum on-chip power that can be used at the sample. While some experiments have used fast cryogenic switches [215] to overcome the problem of low peak power of HEMT, this approach will only allow for $\approx$ 10 dB higher peak power along with the requirement of setting up significantly involved cryogenic electronics. Therefore, in this work, an optimum combination of amplifiers and attenuators is chosen to allow for maximum power on the sample allowed by the HEMT (<0 dBm) while at the same time maintaining a low input noise temperature. The spin-driving pulses are reflected back from the microwave cavity and dissipated at room temperature by the output gate SPDT switch (ZASWA-2-50DR+), which is turned off during the spin-driving pulses by TTL pulses from the marker channel of the AWG (Fig. 3.20). A diode limiter (Pasternack PE8023) is further added before the output gate in order to limit the maximum power below the damage threshold of the output gate switch.

The spin echo signal, which is emitted at a time τ after the spin inversion pulse is collected from the cavity by a cryogenic circulator (Low noise factory LNF − CICIC4_8A) and amplified by a HEMT (Low noise factory LNF − LNC4_8F +44 dB/LNF − LNC0.3_14a +36 dB) at the 4K stage. Bandpass filters with 4.9-6 GHz passband (Mini-Circuits VBFZ-5500-S+) are placed in the pulse generation and readout chain to avoid amplifier saturation. The spin echo is further amplified with room temperature amplifier (Amplifier2: ZX60-83-LNS+,+21 dB) followed by demodulation (Marki MMIQ0218LXPC mixer) to obtain I′, Q′ signals at 200 MHz. The local oscillator (LO) signal to the demodulation mixer was supplied by the same source used for pulse generation. The demodulated spin echo is amplified by a low noise amplifier (Amplifier3: Mini-Circuits ZX-60-P103LN+, +23 dB) to obtain I′, Q′ traces on a fast oscilloscope (Tektronix TDS5104), which are added in quadrature on a computer after collecting the signal trace from the oscilloscope.

This setup was further upgraded with additional electronics for high-sensitivity ESR using planar microresonators, as described in detail in Fig. 6.7.

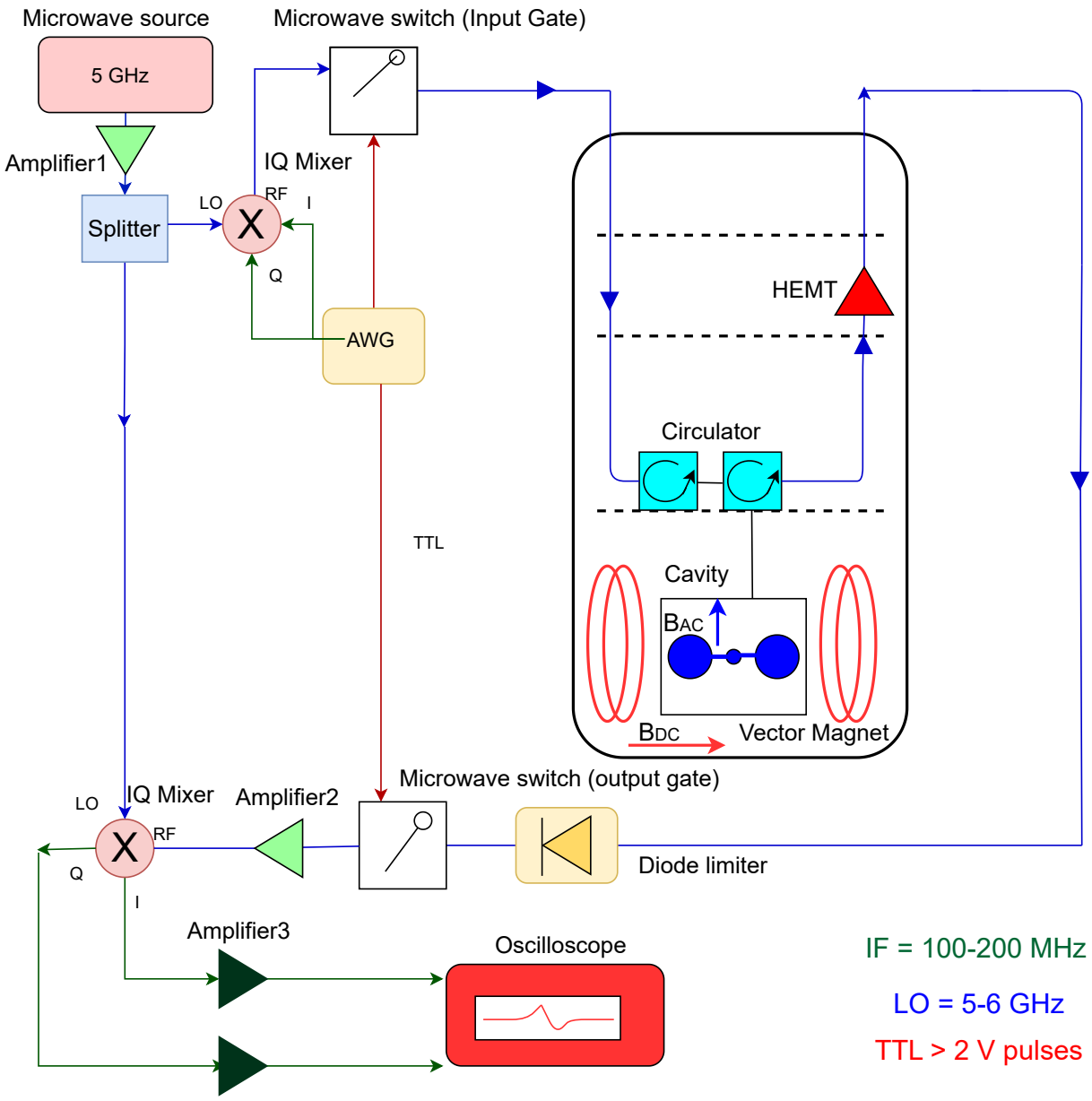


Figure 3.19: Schematics of the pulsed ESR setup used for measurements on bulk samples with a 3D microwave cavity.

Synchronization of spin driving, and data acquisition pulses

Detection of spin echo requires dynamic control on the amplifier chain, in order to protect the room temperature amplifiers from saturation due to high power spin driving pulse as well

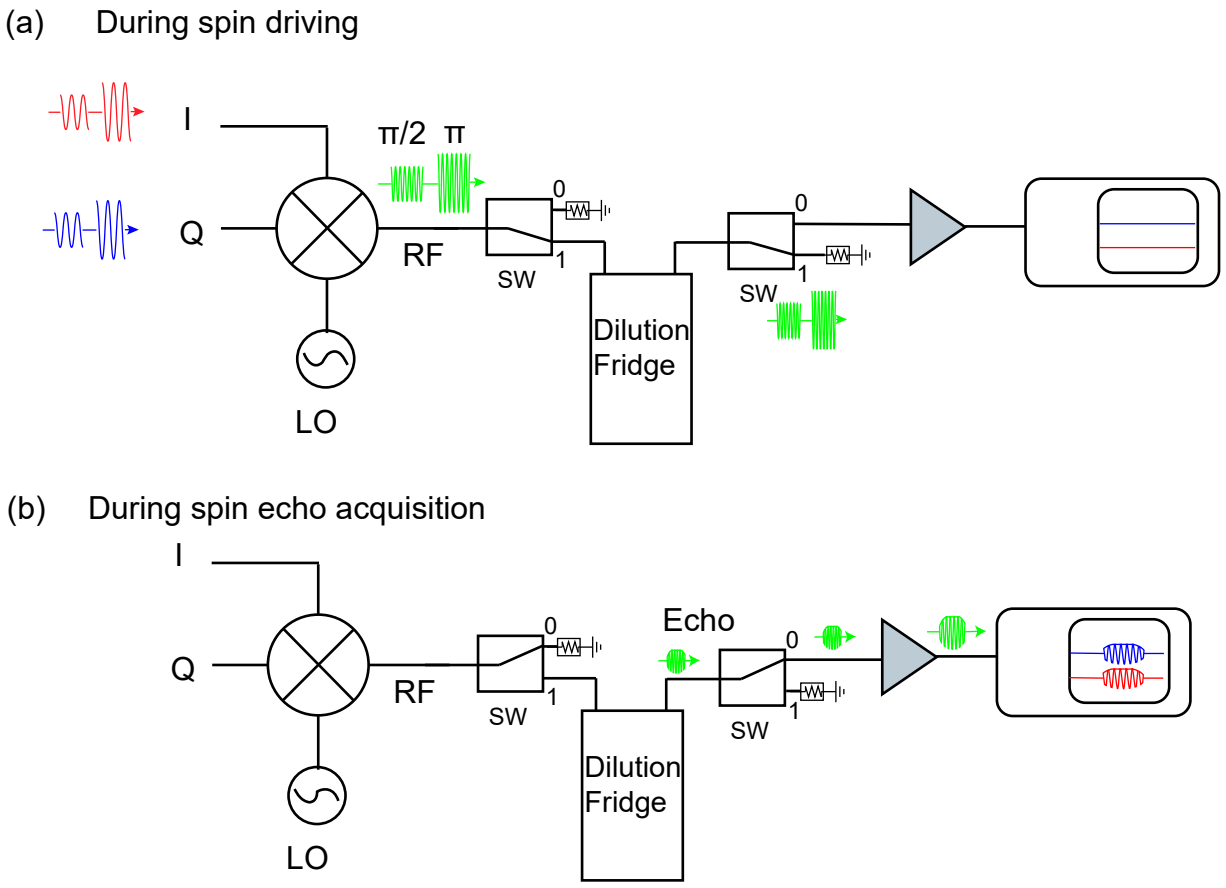


Figure 3.20: Simplified schematic of the ESR setup showing the SPDT switch configuration and signal path (a) during spin driving pulses and (b) during spin echo acquisition time.

as to turn on the amplification during the spin echo acquisition time. This is achieved by a combination of input and output SPDT switches, which switch between two output ports based on the voltage of the TTL input. Fig. 3.20 (a) illustrates the switch configuration during the spin-driving pulses. During the spin driving pulses both switches are on, which diverts the signal to port 1. The input switch is configured to pass spin-driving pulses to the cryogenic setup and the reflected pulses are diverted by the output switch to a terminated port. This configuration protects the room-temperature amplifiers from damage due to high input power. During the spin echo acquisition time, both the input and output switches are instead off and the signal is directed to port 0. This configuration blocks the noise generated

by input amplifiers from reaching the cryogenic setup while at the same time passing the spin echo signal through the output amplifier to the room-temperature amplifier chain. The amplified echo is finally demodulated and read from a triggered oscilloscope.

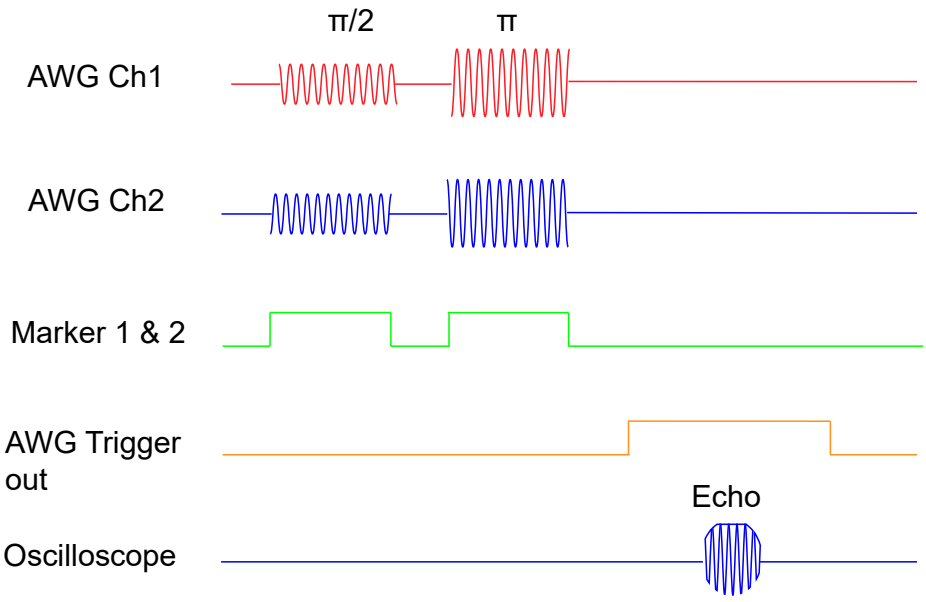


Figure 3.21: Spin driving, switch control, and readout pulses generated by the AWG.

The synchronization of the spin driving, switch control, and oscilloscope trigger is performed through the AWG. Fig. 3.21 illustrated the spin-driving pulses from channel 1 (red) and channel 2 (blue) of the AWG, which are sent to the IQ mixer for upconversion. The AWG has a marker output (Fig. 3.21 green) for each channel, which produces a constant voltage pulse synchronous with the spin-driving pulses. The output from marker 1 and marker 2 is sent to the two SPDT switches, such that the switches are directing the signal to port 1 during the spin-driving pulses. If the spin-driving pulses are sent at a pulse separation τ, the spin echo is expected at a time τ after the second pulse. The trigger output from the AWG is turned on (Fig. 3.21 yellow) before the expected spin echo emission time and the echo is measured on the oscilloscope (Fig. 3.21 blue). Thus, an AWG with at least 2 channels, 2 markers, and a trigger output can be used to synchronize the spin-driving pulses with the readout electronics and instrument.

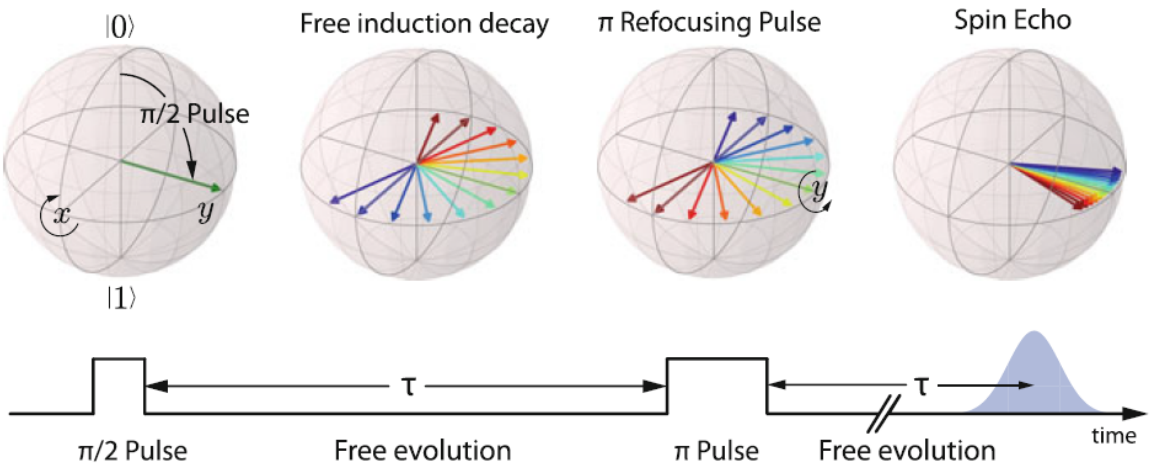


Figure 3.22: Spin dynamics on the Bloch sphere during the spin echo sequence. The spin magnetization is transferred to the XY plane by the first $\pi/2$ pulse, and subsequently, the magnetization undergoes fast decay due to inhomogeneous broadening in the spin ensemble, also referred to as free-induction decay. The inversion pulse is applied at time τ after the first pulse and the dephasing due to inhomogeneity is reversed leading to a spin echo at time 2τ. Image extracted from ref. [139].

3.4.4 Hahn echo

Two pulse echo, also referred to as Hahn echo [78] is the basis for all the time domain spin resonance experiments demonstrated in this thesis. The techniques involve two microwave pulses with an average flip angle of $\pi/2$ and π respectively. The first pulse flips the magnetization in the XY plane of the Bloch sphere where the average magnetization dephases due to the difference in the precession frequency of individual spins. This dephasing can be reversed by the application of a π pulses at a time τ and the magnetization rephases at a time τ after the first pulse. Sweeping the separation between the $\pi/2$ and π pulses is used to measure the coherence time T_2.

The spin echo amplitude $A(\tau)$ is directly proportional to the spin polarization P and shows an exponential dependence on the ratio of pulse separation 2τ and spin coherence (dephasing) time T_2,

$$A(\tau) = A(0)e^{-(2\tau/T_2)} \tag{3.24}$$

$$A = A_{max}\tanh(\hbar\omega/k_B T) \tag{3.25}$$

where,

$$\tanh(\hbar\omega/2k_B T) = P\uparrow - P\downarrow = \frac{e^{(\hbar\omega/2k_B T)}}{e^{(\hbar\omega/2k_B T)} + e^{(-\hbar\omega/2k_B T)}} - \frac{e^{(-\hbar\omega/2k_B T)}}{e^{(\hbar\omega/2k_B T)} + e^{(-\hbar\omega/2k_B T)}} \tag{3.26}$$

is the degree spin polarization for a spin with splitting $\hbar\omega$ and temperature T. The Hahn echo spin amplitude can be used to calibrate the sample temperature.

Spin coherence time measurement

Figure 3.23 shows the Hahn echo spin coherence time measured at 7 mK from (a) 266 mT transition from $^{142,146,148}Nd^{3+}$ isotopes with I=0 and (b) transition at 257 mT(satellite line) from $^{145}Nd^{3+}$ with 21.1% I=7/2. Sweeping the separation between the pulses τ shows an exponential decay of echo amplitude on a timescale defined as the spin coherence time T_2. Nd^{3+} spins with I=0 show a T_2 of 69.4 μs while spins with I=7/2 show a longer T_2 of 102.4 μs owing to a lower density and hence reduced $Nd^{3+} - Nd^{3+}$ dipolar interaction.

Electron spin echo envelope modulation (ESEEM)

Electron spin echo decay during spin echo measurements can show modulations in the echo amplitude as a function of the separation between the pulses τ [152]. This modulation is a result of the hyperfine interaction between the electron and host nuclear spins. Local nuclei in the vicinity of an electron spin experience strong magnetic fields scaling approximately as $\frac{1}{r^3}$ along with an externally applied field B, which preferentially orients the nuclei parallel or anti-parallel to the effective local field from the electron spin. Application of microwave driving pulses to the electron spins results in a change in the spin orientation and therefore a fast change in the local field at the nuclei. This change in the local field results in the precession of the nuclei about the new effective field direction. The precession frequency of

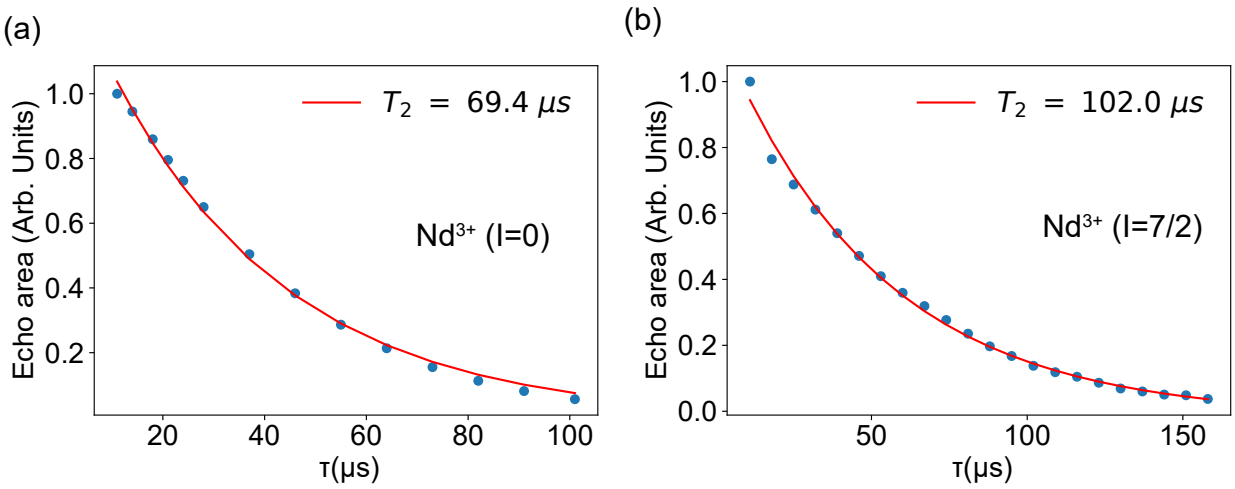


Figure 3.23: Spin coherence time of Nd^{3+}:YSO at 7 milliKelvin (a) Spin T_2 of 266 mT transition from $^{142,146,148}Nd^{3+}$ isotopes with I=0 (b) Spin T_2 of transition at 257 mT(satellite line) from $^{145}Nd^{3+}$ with 21.1% I=7/2.

the nuclei is determined by the nuclear magnetic moments, the strength of external field B as well as the strength of the dipolar interaction with electron spins. The typical nuclear precession frequency is $\mathcal{O}$(100 kHz - 1 MHz) for magnetic fields below 0.5 T. The nuclear spin precession is three orders of magnitude slower than the electron spin precession frequency, and the precessing nuclei effectively create a slow-modulating magnetic field at the position of electron spin. This slow modulation adds phase offsets to the electron spin precession and therefore produces a modulation of the echo amplitude after a refocusing pulse. The echo modulation depth is proportional to the dipole-dipole interaction between nuclear and electron spins. High-resolution ESEEM scans offer insights into the local site structure as well as the dynamics of the surrounding environment around an electron spin defect in a host crystal.

Echo detected field sweep

Echo detected field sweep (EDFS) also called two pulse field swept echo (2P-FSE) technique performs two pulse Hahn echo measurements as a function of the magnetic field. The EDFS technique measures the spin absorption signal, as opposed to the derivative of the absorption signal measured by the CW-ESR technique. While both techniques can be used to obtain

information on the spin Hamiltonian, the pulsed technique offers a higher signal-to-noise ratio. This is evident when comparing the CW ESR (Fig. 3.10) and EDFS (Fig. 3.24) of Nd^{3+} : YSO. While the satellite lines in the CW ESR scan have a signal-to-noise ratio of $\approx$ 5-10, EDFS measurement has an SNR of $\approx$ 100. The pulsed technique has a higher SNR since it measures the transient response of spins in a small detection window and the background is dominated by the small noise floor of the cryogenic amplifiers. The CW-ESR technique on the other hand looks for a small steady-state change in the resonator linewidth or the center frequency, both of which, are of the order of several MHz, to GHz. Therefore, it is inherently challenging to detect small changes of the order of several Hz for a feature of several MHz scale.

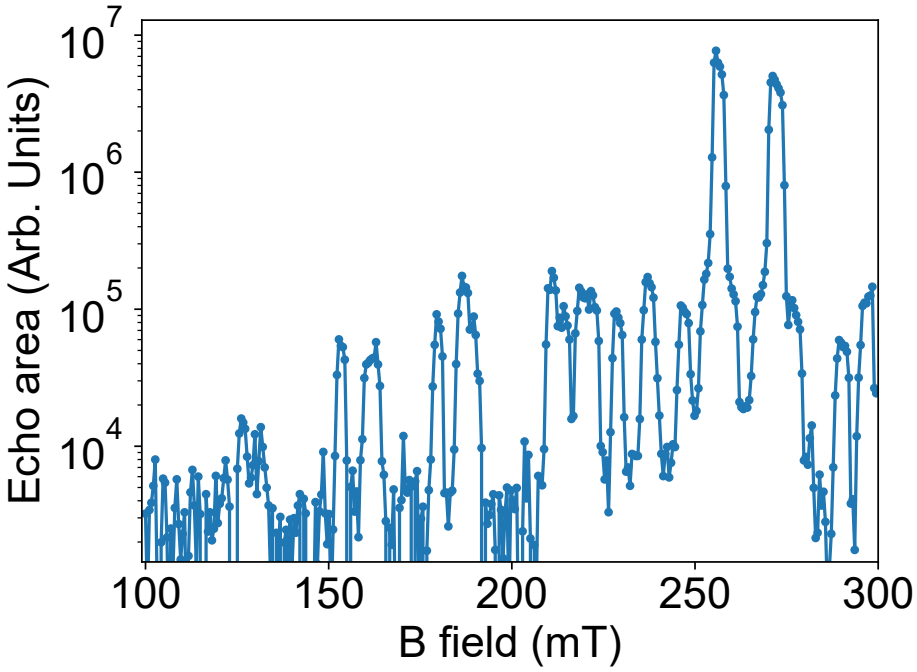


Figure 3.24: Echo detected field sweeps on Nd^{3+}:YSO sample showing two pulse-echo spin signals measured as a function of the magnetic field at 7 mK. The two large peaks between 250 - 300 mK are from two magnetically inequivalent subsites of $^{142,146,148}Nd^{3+}$ isotopes with I=0 and satellite lines are from $^{145}Nd^{3+}$ with 21.1% I=7/2.

Spin lifetime measurement

Inversion recovery

The inversion recovery technique measures the decay of the spin population inverted by a π pulse before the spin echo pulse. The spin echo amplitude is proportional to the net magnetization of the spin ensemble and a spin echo signal with a negative amplitude will show a positive amplitude right after the inversion pulse. This is illustrated in the inset of Fig. 3.25(a) where a negative spin echo signal (orange) shows a net positive amplitude right after an inversion pulse. It is noted that the inverted echo shows reduced amplitude, which is due to partial inversion of the spin ensemble given the small Rabi frequency (125 kHz) compared to the spin inhomogeneous linewidth (26 MHz) and spectral diffusion. Inversion recovery also suffers from echo recovery due to the spectral diffusion process occurring on timescales faster than T_1^{-1} [94].

The inversion recovery measurement on the 266 mT transition (Fig. 3.25(a)) shows a fast decay of timescale 1.7 ms and a long time scale day of 45 ms. The fast decay with a timescale of 1.7 ms is indicative of spectral diffusion on a 1 ms timescale. Measuring spin lifetime for a timescale > 1 s is often prohibitive due to the significantly long duty cycle of the pulse and the large number of averages required to obtain a large signal-to-noise ratio.

Saturation methods

Saturation methods such as echo-detected saturation allow for the use of long pulses and do not suffer from spectral diffusion-induced recovery [94]. Saturation-based methods are also preferable when significant inversion of the spin ensemble is not possible due to a limited Rabi frequency compared to the spin inhomogeneous linewidth or in the presence of significant pulse errors.

This thesis also explores alternative saturation techniques to measure the spin lifetime. The technique referred to as the spin echo saturation method involves performing two pulse spin echo measurements with a repetition time T_{rep}. When the repetition time T_{rep} is shorter

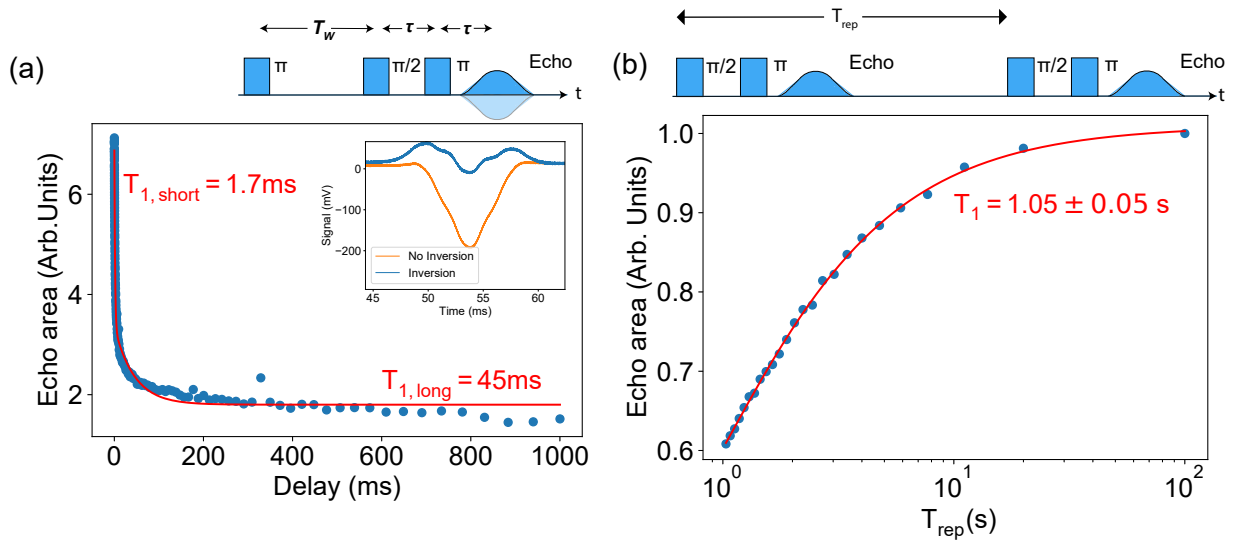


Figure 3.25: Spin relaxation time of Nd^{3+}:YSO at 7 milliKelvin (a) Measurement using inversion recovery approach (b) Measurement using spin echo saturation method.

than the spin relaxation time T_1, the spin echo amplitude is suppressed in the steady state due to population pumping in the spin-up state. Therefore, the spin echo amplitude is expected to increase as T_{rep} is increased, following a phenomenological expression,

$$A(T_{rep}) = A_0 e^{-T_1/T_{rep}} \tag{3.27}$$

The spin echo saturation method was used to measure the spin T_1 of the 266 mT transition of Nd^{3+} : YSO on a timescale greater than 1 second. The spin echo amplitude (Fig. 3.25(b)) measured as a function of T_{rep} shows a close agreement with the fit based on equation 3.27 and suggests a spin T_1 of 1 s in which is a close agreement with other measurements on Nd^{3+} : YSO at similar temperatures [59].

3.4.5 Spin sensitivity (N_{min}) of the pulsed ESR setup

In order to estimate the minimum number of spin detectable by the pulsed setup (N_{min}), we look at the EDFS sweep (Fig. 3.24). The pair of lines between 250 - 270 mT correspond to 9×10^{14} spins. The number of spins with a linewidth of 15 MHz being addressed in the

resonator bandwidth of 1.5 MHz is $1.5/15 \times 9 \times 10^{14} = 9 \times 10^{13}$. With an observed signal-to-noise ratio of 10^4 (Fig. 3.24), we get $N_{min} = 9 \times 10^{13}/10^4 = 9 \times 10^9$ spins. The number can be further reduced by at least 1 order of magnitude by measuring spin echo using the heterodyne mixing technique instead of the homodyne technique, as the noise floor will reduce at high frequencies scaling as 1/f. With these modifications the N_{min} with the 3D cavity setup can be easily reduced to at least 10^9 spins, which is only 2 orders of magnitude higher than N_{min} of 10^7 demonstrated using 2D coplanar waveguide superconducting resonators and exceeding the sensitivity of commercial pulsed ESR spectrometers [165] [28].

3.5 Optically saturated ESR spectroscopy

Optical saturation of the ESR technique is used for correlating the optical response of an optically active paramagnetic defect to its ESR response. The technique is applicable for both CW and Pulsed ESR. Fig. 3.26 illustrates the optical saturation of the spin echo signal, which has been used in Chapter 4 for confirmation of the assignment of an ESR signal to Er^{3+}. The technique involves an optical pulse, on-resonant with the Er^{3+} $^4I_{13/2}$ to $^4I_{15/2}$ optical transition, which is used to pump the spin population away from the spin ground state of the $^4I_{15/2}$ level. The optical pulse is followed up with a microwave spin echo sequence after a delay time of T_D. In the presence of long-lived electron spin or hyperfine shelving states in the $^4I_{15/2}$ level, the spin echo signal will show a decreased amplitude due to optical pumping effects and this can serve as a confirmation of the optical response of an ESR transition. While steady-state heating effects due to optical illumination can serve as a source of systematic errors, it can be ruled out if changing the order of microwave and optical pulses results in different spin echo amplitudes.

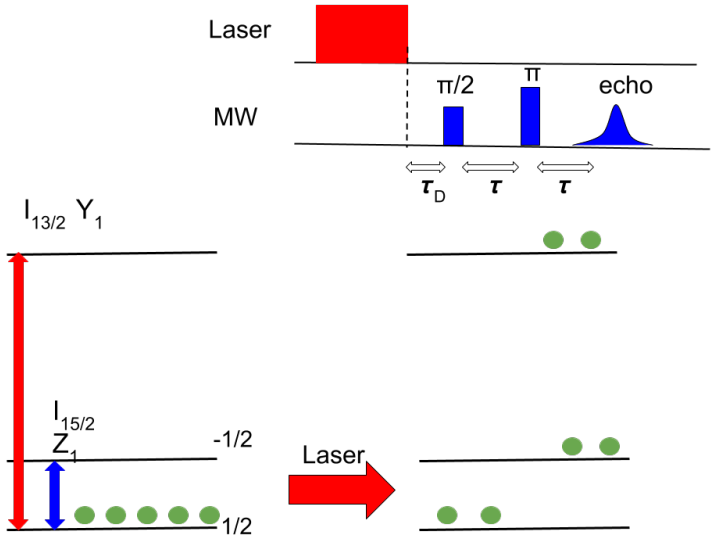


Figure 3.26: Optically saturated ESR spectrosopy.

CHAPTER 4

SPIN DYNAMICS AND HYPERFINE STRUCTURE OF ERBIUM-DOPED YTTRIUM OXIDE

4.1 Introduction

Rare-earth (RE) ions in solids possess shielded 4f intra-shell optical and spin transitions with narrow linewidths and long coherence times [179] [207] [147], making them ideal candidates for applications such as quantum memory [179] [109] in a quantum network [96], microwave-to-optical quantum transduction [105] and quantum sensing [51]. Among RE ions, Erbium (Er^{3+}) in particular, constitutes a unique system that simultaneously possesses optical fiber-compatible telecom C-band optical transition (1535 nm), high electron g-factor (14.6 $Er^{3+} : Y_2SiO_5$) [41] with long nuclear spin coherence time of 1.3 seconds at 1 K ($Er^{3+} : Y_2SiO_5$) [147]. $^{167}Er^{3+}$ with a nuclear spin I = 7/2 exhibits strong anisotropic hyperfine interactions, resulting in electron-nuclear hybridized states in low symmetry sites with reduced sensitivity to magnetic field noise at zero field – known as the Zero First-Order Zeeman (ZEFOZ) transitions [193] as well as large zero-field transition frequencies in the microwave range. Narrow optical homogeneous and inhomogeneous linewidth [70] [205] have been demonstrated in $Er^{3+} : Y_2SiO_5$ [147]. Comparable to YSO, yttrium oxide (Y_2O_3) is another low magnetic noise host with a similar ionic radius of Y^{3+} to Er^{3+} (1.04 vs. 1.03 Å) and can be synthesized in a diverse range of material platforms compatible with nanoscale integration [208] including thin films [158] [167], nanoparticles [22] [162], and transparent polycrystalline ceramics [205]. This combination makes the characterization of spin Hamiltonian of $^{167}Er^{3+} : Y_2O_3$ crucial to further develop this quantum platform by exploiting its long-coherence time hyperfine transitions as well as performing coherent control of $^{167}Er^{3+}$ spins as a resource for quantum technology applications.

In this chapter, we report X-band (9.5 GHz) electron spin resonance (ESR) (continuous

wave and pulsed) spectroscopic studies of the atomic environment and dynamics of the Er^{3+} spins in Y_2O_3 polycrystalline matrix. We investigate the electronic structure of Er^{3+} using CW ESR and characterize Er^{3+} local structure variations in different crystalline environments (C_2 and C_{3i}) in cubic Y_2O_3 by determining the Zeeman, hyperfine and quadrupole interactions. We compare X-band ESR with low-field C-band (5 GHz) ESR to verify the spin Hamiltonian in a regime where the Zeeman energy is comparable to hyperfine energy. The hyperfine transitions in $^{167}Er^{3+}$ introduce mixed states that show a relatively slow spin relaxation, which can be detected at temperatures of 4.0 – 6.0 K. We measure a long spin coherence time of 24.4 μs at 4 K for the lowest g-factor transition. The limits for coherence relaxation times given by spin-lattice relaxation (characterized as T_1) is 5 ms at 4.0 K. Our study provides a comprehensive spin spectroscopy of $^{167}Er^{3+}$ in Y_2O_3, which shows significant prospects of this platform for future applicable quantum technologies.

The Er^{3+} ion contains $4f^{11}$ electrons, which result in a total spin quantum number of S = 3/2, an orbital quantum number of 6 and total angular momentum of J = 15/2. The ground level $^4I_{15/2}$ is 16-fold degenerate and in the presence of a crystal field of low symmetry, it can split into 8 (J+ $\frac{1}{2}$) Kramer doublets. The energy of microwave radiation generated in conventional X-band ESR experiments (9.5 GHz) is generally sufficient to probe only the lowest-lying doublet of the $^4I_{15/2}$ manifold of trivalent erbium. As a result, common studies of Er^{3+} in metal oxides consider only the lowest-lying Kramer doublet with an effective spin S = 1/2 system to account for the features of Er^{3+} ESR spectra

$$\mathcal{H} = \mu_e \mathbf{B} \cdot \mathbf{g} \cdot \mathbf{S} + \mathbf{I} \cdot \mathbf{A} \cdot \mathbf{S} + \mathbf{I} \cdot \mathbf{Q} \cdot \mathbf{I} \tag{4.1}$$

where the first Zeeman term represents the energy of the electronic spin in a magnetic field B0 and the second term accounts for the hyperfine interaction with nuclear spins and the third term is nuclear quadrupole interaction, μ_B is the Bohr magneton and g, A, and Q are interaction tensors, which reflect local structure particularities of the paramagnetic complex.

4.2 X-Band continuous wave ESR

ESR spectrum of Y_2O_3 doped with a natural abundance of Er^{3+} is shown in Fig. 4.1(a). The sample has a nominal Er^{3+} doping of 20 parts per million (ppm) and was prepared by sintering 20 nm-sized nanocrystals into polycrystalline ceramics according to the method reported in ref. [205]. For X-band ESR measurement, the sample was ground to microparticles to increase the filling factor of the microwave cavity. Fig. 4.1(a) inset shows the crystal structure of cubic Y_2O_3 with annotated different local sites available for the substitution of Y^{3+} with Er^{3+}. Two possible sites are a lower symmetry C_2 site whose substitution should result in a rhombic ESR signal and a higher symmetry trigonal C_{3i} site whose substitution should result in an axial ESR signal. Indeed, we clearly observe four main transitions, three for a rhombic signal (g_z = 12.20, g_y =4.89, and g_x =1.64) and the main signal for a trigonal symmetry site ($g_\perp$ = 3.32). Upon close inspection of the lowest rhombic component using small modulation amplitude, we find that the lowest signal at g = 12.20 is composed of two signals, one with g = 12.20, which is approximately 5 times more intense than the one with g = 12.08 (Fig. 4.1(b)). The two signals have different saturation properties suggesting their association with different sites (Inset, Fig. 4.1(b)). Simulation of the experimental spectra with even isotope $^{166}Er^{3+}$ (33.5 % natural abundance) using the above-listed parameters for the parallel component of the axially symmetric signal (C_{3i}) perfectly matched observed transitions and signal intensity. The average g factors (g_{avg}) for both C_2 and C_{3i} systems were found to be 6.243, suggesting Γ_7 ground state (g_{avg} = 6.0) rather than Γ_6 (g_{avg} = 6.8) usually found in Er^{3+} doped samples [1] [169] [14]. The g_z component simulations using a natural distribution of Er^{3+} isotopes fit well with the observed hyperfine structure (HFS) in Er^{3+} spectra. $^{167}Er^{3+}$ isotope with a nuclear spin I= 7/2 and 23 % abundance resulted in an approximately symmetrical HFS pattern of 8 satellite lines with 3.7% amplitude of the central line and with hyperfine splitting A_z= 1288 MHz, A_y = 518 MHz and A_x = 120 MHz for C_2 symmetry and $A_\parallel$ = 1260 MHz and $A_\perp$ = 350 MHz for C_{3i}. However, g_z component

of a rhombic C_2 signal and the $g_{||}$ component of a C_{3i} signal in the odd nuclear isotope $^{167}Er^{3+}$ were slightly shifted from that associated with even isotopes and found to be 12.28 and 12.20, respectively (Fig. 4.1(b). This indicates that odd isotope $^{167}Er^{3+}$ experiences slightly different environmental effects caused by a different effective crystal field.

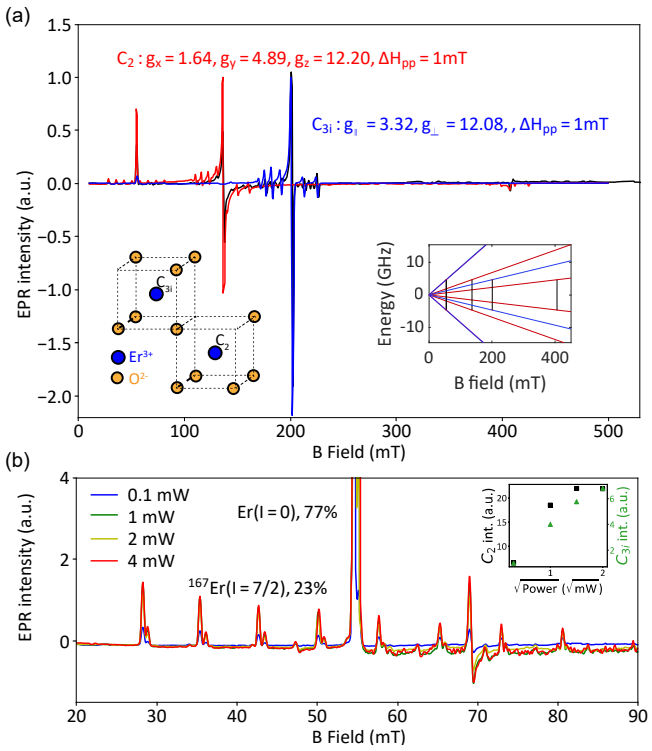


Figure 4.1: (a) CW-ESR spectroscopy provides spin Hamiltonian parameters for an electron spin in the lowest doublet of $^4I_{15/2}$ under magnetic field. Inset Left: Er^{3+} substitutes Y^{3+} in the lower symmetry C_2 site (bottom) and the higher symmetry C_{3i} site (top), Inset Right: Energy levels of g=12.20, 12.28, 3.32, 4.89, and 1.64 for Er^{3+} I=0 isotopes as a function of field (right) as a function of the B field, where X-band transitions are shown with black lines. CW-ESR on natural isotopic purity Er^{3+}:Y_2O_3 shows transitions from C_2 (red) and C_{3i} (blue) closely modelled by simulations. (b) The g = 12.20 levels under close inspection reveal strong lines around 55 mT from I = 0 isotopes of Er^{3+} along with two sets of 8 satellite 5 lines corresponding to $^{167}Er^{3+}$ from C_2 g = 12.28 and C_{3i} g = 12.20. Inset: the g = 12.20 lines from C_2 and C_{3i} show different saturation with power.

4.3 Spin Hamiltonian fitting

To elucidate how hyperfine states affect the spin electronic structure and relaxation dynamics, we synthesized an isotopically purified $^{167}Er^{3+}$ doped Y_2O_3 sample with 20 ppm doping and observed a spectrum with a high density of hyperfine transitions. indicative of nuclear spin for $^{167}Er^{3+}$. The lowest field components g_z and $g_{||}$ components are composed of eight lines, each as expected from I = 7/2 (Fig. 4.2(a)). Importantly, the central line associated with transitions of even isotopes at g = 12.20 was significantly reduced, testifying to the isotopic purity of the sample. The g_y component for C_2 state of $^{167}Er^{3+}$, however, does not show an expected 8-line pattern, instead, 16 major lines of different intensities were observed. This spectrum could not be deconvoluted to the set of octets if one would assume the existence of two nonidentical sites leading to two different hyperfine structures previously found in ref. [185]. Our spectrum has very irregular line positions and intensities with separations that can be closely simulated with simple I = 7/2 nuclear hyperfine interactions A along with strong nuclear quadrupole interaction Q. Nuclear quadrupole interactions impose additional torque acting on $^{167}Er^{3+}$ nuclei and affect quantization directions, thereby shifting energy levels and magnetic resonance transitions while also leading to forbidden transitions. Similarly, the $g_\perp$ component for C_{3i} state is now composed of more than 8 lines each, suggesting the presence of forbidden transitions. A similar observation was made for $^{167}Er^{3+}$ in YSO [41] where forbidden transitions with intensity comparable to allowed transitions were described with a traceless nuclear quadrupole interaction (Q).

The spin Hamiltonian was fitted to the resonance fields for hyperfine transitions obtained from the experimental spectrum. We also assumed that g, A, and Q tensors have coincident principal axes and can be simultaneously diagonalized as limited information about the orientation of the tensor can be derived from a powder spectrum alone for an anisotropic spin Hamiltonian. The low field transitions could be successfully fitted with g_z, A_z components of C_2 (g_z= 12.28, A_z = 1280 MHz) and $g_{||}$ of C_{3i} sites ($g_{||}$ = 12.20, $A_{||}$ = 1268 MHz), in both

	C_2	C_{3i}
Electron Zeeman(g)	$g_x = 1.64$, $g_y = 4.78$, $g_z = 12.28$	$g_\perp = 3.28$, $g_\parallel = 12.20$

Table 4.1: Spin Hamiltonian parameters for Er^{3+} I=0 in Y_2O_3.

	C_2	C_{3i}
Electron Zeeman(g)	$g_x = 1.64$, $g_y = 4.89$, $g_z = 12.20$	$g_\perp = 3.32$, $g_\parallel = 12.08$
Hyperfine(A) (MHz)	$A_x = 212$, $A_y = 480$, $A_z = 1280$	$A_\perp = 310$, $A_\parallel = 1268$
Quadrupole (Q) (MHz)	$Q_x = 10$, $Q_y = 40$, $Q_z = -(Q_x + Q_y)$	$Q_\perp = 12.5$, $Q_\parallel = -2Q_\perp$

Table 4.2: Spin Hamiltonian parameters for $^{167}Er^{3+}$ I=7/2 in Y_2O_3.

peak positions and their intensity. Intermediate field transitions were fitted to obtain g_y, A_y, Q [Q_x, Q_y, Q_z] terms of the C_2 site ($g_y = 4.78$, $A_y = 480$ MHz, Q = [10, 40, -50] MHz) and $g_\perp$, $A_\perp$, Q [$Q_\parallel$, $Q_\perp$] terms of the C_{3i} site ($g_\perp = 3.28$, $A_\perp = 310$ MHz, Q = [12.5, -25] MHz). The C_2 g_x component at g_x= 1.64 had broad transitions with a small intensity, which limited the number of hyperfine transitions to be resolved. Therefore, A_x was estimated from the difference in splitting of the lowest and highest field hyperfine transitions observed in the experimental spectrum ($g_x = 1.64$, $A_x = 212$ MHz). The simulated spectrum for C_2 site (red) and C_{3i} site (blue) generated using the fitted spin Hamiltonian shows a close agreement to the experimental spectrum in terms of peak position, shape as well as relative intensity (Fig. 4.2(a) and Fig. 4.2(b)). Tables 4.1 and 4.2 summarize the principal values of g tensor for Er^{3+} (I = 0) and g, A, Q for $^{167}Er^{3+}$ (I = 7/2), respectively.

4.4 C-band continuous wave ESR

The predictions from an anisotropic $^{167}Er^{3+}$ spin Hamiltonian fitted with the X-band ESR have been shown to exhibit disagreement with the low-field ESR measurements in low-

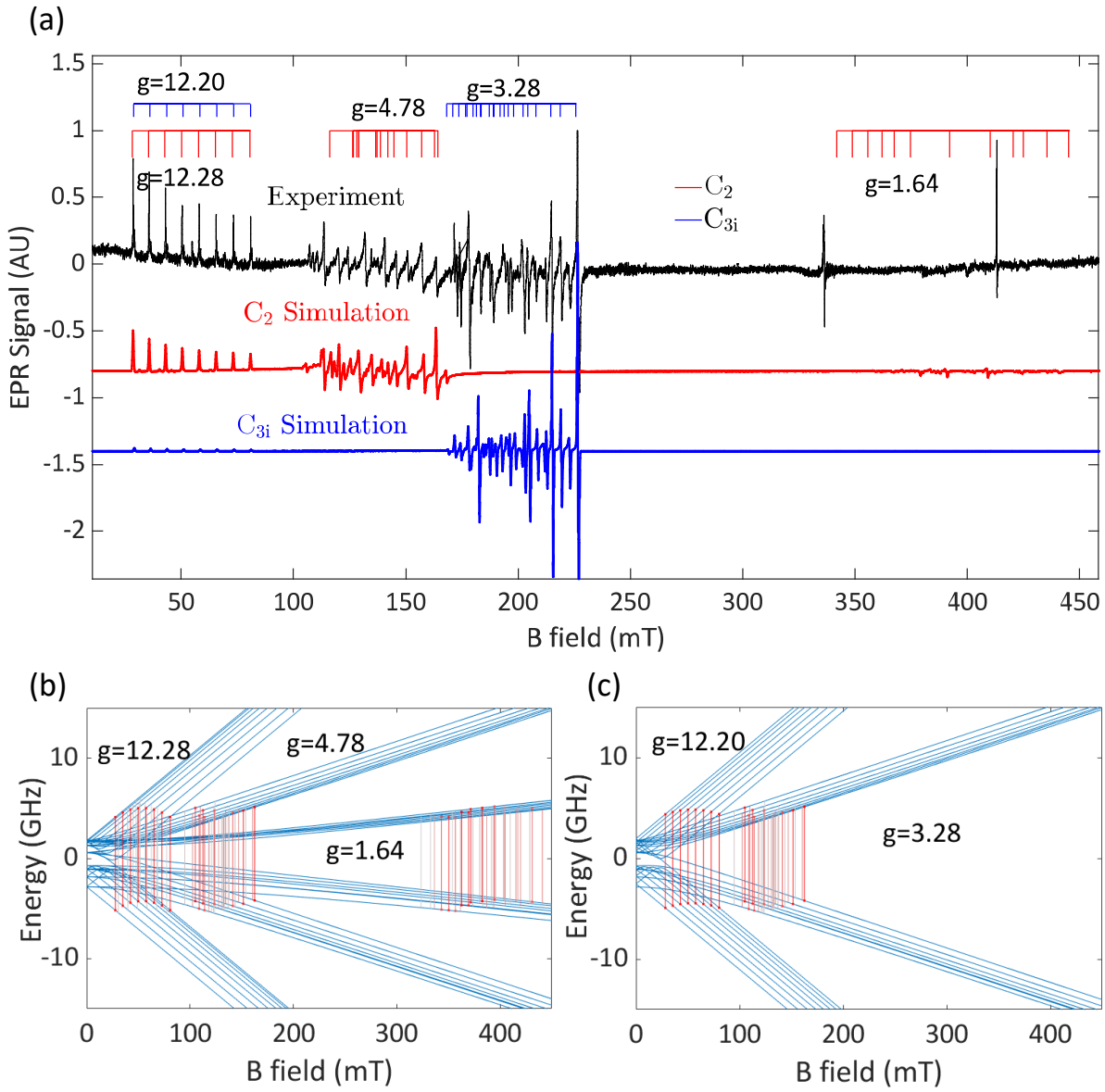


Figure 4.2: (a) $^{167}Er^{3+}$ X-band CW-ESR (black) compared with simulation for C_2 g = 12.28, g = 4.78, g = 1.64 and C_{3i} g = 12.20, 3.28 lines. Simulated spectra using Easyspin [175] show close agreement with the experimental spectrum. The predicted resonance fields for transitions are shown in dashed vertical dashes, grouped together for each g-factor. (b) and (c) $^{167}Er^{3+}$:Y_2O_3 simulated energy levels for (b) C_2 and (c) C_{3i} (blue) sites as a function of the field generated with Easyspin. Red lines show the high-intensity X-band (9.3 GHz) transitions while the grey lines show lower-intensity forbidden transitions.

symmetry hosts such as Y_2SiO_5 [21]. Therefore, to validate the fitted spin Hamiltonian at a lower field, we performed C-band CW-ESR on the $^{167}Er^{3+}$:Y_2O_3 sample with a C-band microwave (resonance frequency of 4.96 GHz) loop-gap cavity. The experimental spectra (Fig. 4.3) show close agreement with the simulated spectrum from C_2 and C_{3i} sites and suggest a good estimate of ESR parameters. The fitted g values are also in close agreement with previous optical and ESR measurements [82] [160] [159].

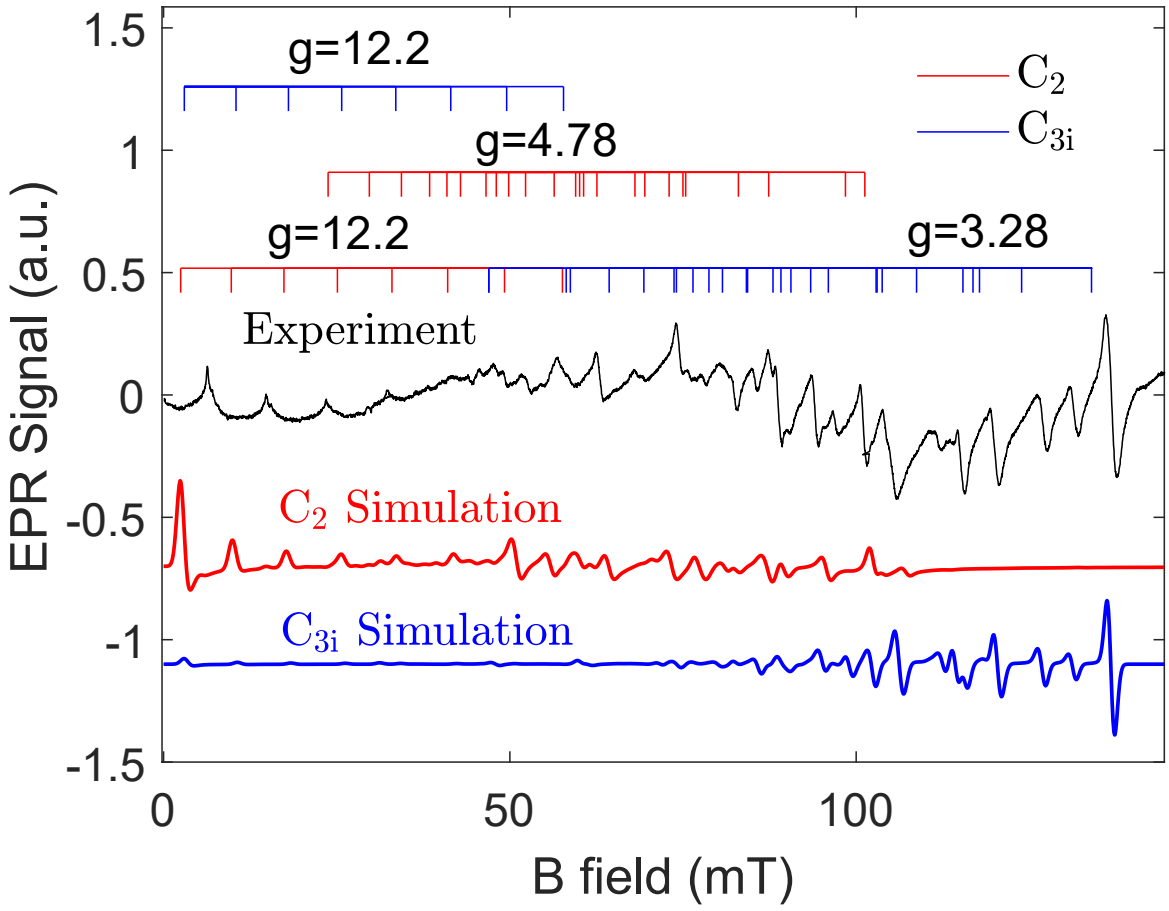


Figure 4.3: $^{167}Er^{3+}$ 5 GHz CW-ESR spectrum (black) compared with spectra simulated from C_2 g=12.20, g=4.78 and C_{3i} g=12.2, g=3.28 lines. Simulated spectra. Simulated spectra using Easyspin [175] show close agreement with the experimental spectrum. The predicted transition fields are shown in dashes, grouped together for each g factor.

4.5 Spin dynamics at cryogenic temperatures (4 Kelvin)

We sent $\pi/2$ and π pulses and swept the magnetic field to obtain two pulse-field swept echo, (2P-FSE), ($\pi/2$-τ- π- τ – echo, $\tau = 250$ ns) spectrum of $^{167}Er^{3+}$ in X-band. Fig. 4.4 shows the ESR transition from hyperfine split levels, which show similarities to the CW ESR spectrum of the same sample. The signal is temperature-dependent, disappearing at 15 K, which is indicative of ESR signals of $^{167}Er^{3+}$ ions. Four different regions of discrete multiline transitions are observed in addition, to a broad underlined absorption that suggests the existence of unresolved hyperfine structures of strongly interacting $^{167}Er^{3+}$ ions. The signal intensity ratio for C_{3i}:C_2 states in the 2P-FSE spectrum is higher compared to their intensity ratio in CW ESR, suggesting different spin dynamics of C_{3i} and C_2 states. Moreover, the 2P-FSE spectrum features are strongly dependent on the delay time τ between $\pi/2$ and π pulses, revealing individual dynamic features of C_2, C_{3i}, and strongly interacting $^{167}Er^{3+}$ sites. The strongly interacting sites show the fastest decay. Fig. 4.4(a) shows the change of the 2P-FSE spectra with the change of the delay time τ between two pulses. As τ increases from 250 to 400 ns, the first signal to lose the intensity is the broad feature under the discrete transitions that we associate with strongly interacting $^{167}Er^{3+}$ sites. In the same time frame, discrete transitions become even more intense, possibly because of their diminished relaxation due to the decay of the strongly interacting species. At later times both C_2 and C_{3i} sites lose their intensity, and at $\tau = 1.5$ µs only one pronounced transition remains, corresponding to the energetically highest $m_s = +7/2$ hyperfine state of C_{3i}.

While all low field spectral features for $^{167}Er^{3+}$ in rhombic crystalline environment C_2 vanish for the pulse delay of 1.5 μs, Fig. 4.4(b) shows the decay of the spectral features for high field g = 1.64 C_2 component with increasing delay time τ. These features, although weak, persist for up to τ delay time of 3 μs, suggesting their long coherence time. Temperature dependence of this signal is consistent with the temperature behavior of Er^{3+} signals at g = 4.8 and 12.2, which also disappear at 15 K. The g = 1.64 transitions exhibited very

slow stretched exponential echo decay with T_2 = 24.4 μs measured at 4.3 K, which was superimposed with slow nuclear modulation (Fig. 4.4(c)). The Fourier transform of electron spin envelope echo modulations ESEEM (obtained using 3P-ESEEM, $\pi/2$-τ- $\pi/2$-τ- $\pi/2$ - τ – echo, with 16 step phase cycling) shown in Fig. 4.4(d) reveals two modulation frequencies, one stronger component of 0.45 MHz consistent with modulation of $^{167}Er^{3+}$ and one 0.80 MHz consistent with modulation of $^{89}Y^{3+}$ suggesting that the interaction with $^{167}Er^{3+}$ ions from C_{3i} sites and to a lesser extent weakly coupled ^{89}Y matrix nuclei contribute as a source of decoherence. However, due to the weak signal intensity, we were not able to measure spin-lattice relaxation T_1 of the transition with g = 1.64.

Transitions with higher g factors (g = 12.2, 4.78, 3.28) exhibit stronger sensitivity to magnetic noise leading to the fast echo decay with a shorter T_2 time of approximately (0.5 – 0.9 μs) (Fig. 4.4(e) for g = 4.78 and Table 4.4). The g = 4.78 transition could be effectively dynamically decoupled from the sources of decoherence by applying a single XY16 [76] sequence, prolonging its T_2 for an order of magnitude to 3.9 μs. Extending of coherence time obtained by applying dynamic decoupling sequences with multiple rotation axes such as XY16 demonstrates the presence of spectral diffusion as a source of fast spin decoherence. However, applying multiple sequences of XY16 only shortens spin coherence time T_2 due to pulse error. Only after the sign of the signal was inverted by applying a pi pulse between two XY16 sequences, we obtained further enhancement of the spin coherence to 6.5 µs. The signal obtained after dynamic decoupling reveals slow modulations reminiscent of those obtained in 3P-ESEEM measurements of g = 1.64 transition, suggesting that the same ions participate in the relaxation of spins with g = 4.78. Instantaneous diffusion [3] arising from the dipole interaction of resonant $^{167}Er^{3+}$ spins during inversion pulses is another mechanism of spin decoherence. We investigated instantaneous diffusion by applying the Hahn echo ($\pi/2$ -τ - θ - τ – echo) sequence with various spin-flip angles. Fig. 4.4(f) shows the dependence of $1/T_2$ of C_2 g = 4.89 measured as a function of different spin-flip probability ($\sin^2\theta/2$,

where θ is spin-flip angle). We obtain a linear dependence of the $1/T_2$ on the average spin-flip probability with the slope of 0.8 MHz, suggesting an effective concentration of resonant spins with density 1.38 x 10^{17} spin/cm^3 (equivalent dopant density of 5 ppm) with g = 4.78 contributing to instantaneous diffusion. The instantaneous diffusion determined for the spins in C_{3i} symmetry (Fig. 4.4(f)) shows a very similar dependence of $1/T_2$ on the spin-flip probability $\sin^2\theta/2$ (slope of 0.7 MHz) corresponding to an estimated density of 2.53 x 10^{17} spins/cm^3 with g = 3.28. The electron spins in highly symmetric C_{3i} sites also experience spectral diffusion from spin flips of neighboring spins that could be mitigated through XY16 dynamic decoupling pulse sequences. Applying the multiple XY16 sequences separated by a sign inversion π pulse extends coherence time T_2 of C_{3i} states up to 6 μs measured at 4.2 K. However, decoupling schemes do not extend the coherence time up to the T_1 limits given by spin-lattice relaxation. Spin lattice relaxation times were determined through three pulse inversion recovery sequences ($\pi - \tau - \pi$ /2 $- \tau - \pi - \tau -$ echo with 4 step phase cycling) and were found to be biexponential with a larger fraction of the slow component (Table 4.4). The determined slow component of T_1 is long for $^{167}Er^{3+}$ in C_{3i} states, reaching 0.6 ms at 4.2 K. As T_1 spin-lattice relaxation bounds coherence time, long T_1 times suggest orders of magnitude improvement of electron spin coherence times by eliminating spectral and instantaneous diffusion. The spin-lattice relaxation times of C_2 states are even longer ranging from 0.7 ms for g = 4.78, to 5 ms for g = 12.20 at 4.2 K. The T_1 times for $^{167}Er^{3+}$ are significantly longer than that of natural isotopic abundance Er^{3+} sample with three orders of magnitude longer T_1 for C_2 g = 12.2, an order of magnitude for C_2 g = 4.8 and for C_{3i} g = 3.3 (Table 4.4). These results suggest that isotope inhomogeneity in natural isotope promotes spin-lattice decay.

g	B field (mT)	Site	$T_1(\mu s)$	$T_2(\mu s)$
12.2	53.4	C_2/C_{3i}	1.7	<0.2
4.9	138.9	C_2	16	1.5
3.2	204.5	C_{3i}	7.6	1.1
1.6	412.11	C_2	16	0.6

Table 4.3: Spin coherence and relaxation time for Er^{3+} I=0 in Y_2O_3 at 4 Kelvin.

g	B field (mT)	Site	T_1(long)	T_1(short)	Ratio(long:short)	$T_2(\mu s)$
12.2	31.4	C_2/C_{3i}	4.8 ms	0.1 ms	5:3	0.9
12.2	38.6	C_2/C_{3i}	3.2 ms	0.8 ms	4:3	0.8
12.2	58.6	C_2/C_{3i}	2.8 ms	0.9 ms	1.4:3	0.5
4.8	112.5	C_2	700 μs	13 μs	4:1	0.4
4.8	118.9	C_2	640 μs	12 μs	4:1	0.4
4.8	137.2	C_2	620 μs	47 μs	5:1	0.4
3.2	185.8	C_{3i}	580 μs	4 μs	4:1	0.4
3.2	195.8	C_{3i}	580 μs	4 μs	4:1	0.4
3.2	234.2	C_{3i}	580 μs	4 μs	4:1	0.4
1.6	413.9	C_2				24.4

Table 4.4: Spin coherence and relaxation time for $^{167}Er^{3+}$ I=7/2 in Y_2O_3 at 4 Kelvin.

4.6 Discussion

We have comprehensively characterized the spin Hamiltonian of ground state $^{167}Er^{3+}$ in both C_2 and C_{3i} sites of Y_2O_3 using X-band ESR. The spin Hamiltonian exhibited an anisotropic g, A matrix with a strong nuclear quadrupole interaction Q leading to forbidden ESR transitions and showed good agreement with the 5 GHz CW-ESR spectra. The measured strong anisotropic hyperfine interaction of $^{167}Er^{3+}$ in both C_2 and C_{3i} sites of Y_2O_3 suggests the presence of zero first-order Zeeman (ZEFOZ) transitions at low fields with possibly long spin coherence times [142] [127]. The spin dynamics of $^{167}Er^{3+}$ studied using X-band pulsed ESR shows a long coherence time reaching 24.4 μs for g = 1.64 transitions at 4 K. The spin coherence time was found to be limited by spectral diffusion and instantaneous diffusion for both C_2 and C_{3i} sites. With lower doping concentration the spin coherence time could be further improved at 4 K. Addressing low-field ZEFOZ transitions and utilizing pulsed sequences aimed at decoupling dipolar interaction and spectral diffusion [213] could be future steps in maximizing the coherence of this system for enabling quantum technologies.

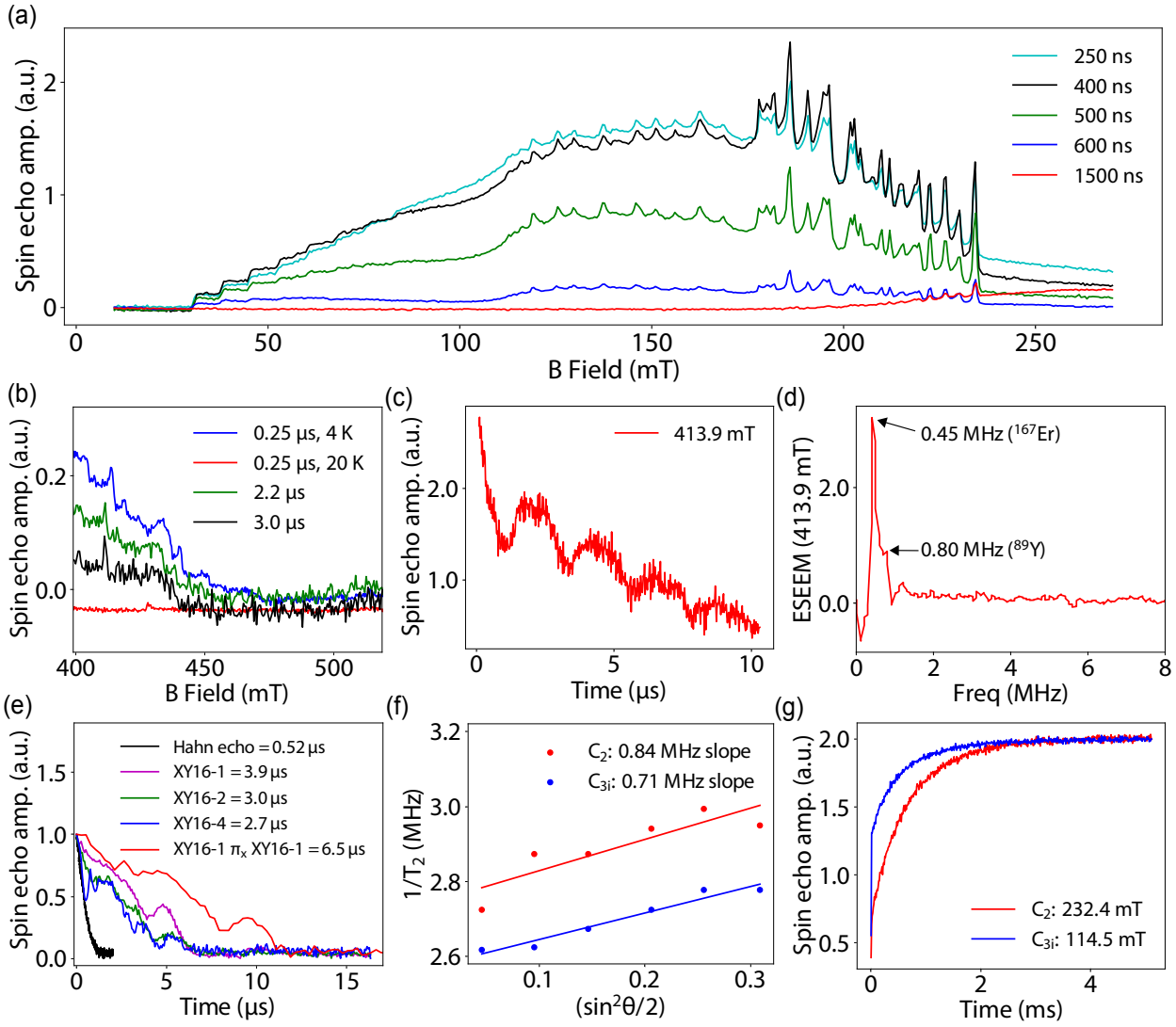


Figure 4.4: X-band pulsed ESR on $^{167}Er^{3+}$:Y_2O_3 at 4 K. (a) Echo detected field sweep shows ESR transition from hyperfine levels of C_2 g = 12.28, 4.78 and C_{3i} g = 12.20, 3.28 along with a short-lived broad unresolved signal due to $^{167}Er^{3+}$ interaction. At pulse separation of 1.5 μs only signal from C_{3i} $m_s = +7/2$ remains. (b) C_2 g = 1.64 component shows slow decay and persists up to 3 μs at 4 K while decays completely at 20 K. (c) The echo decay of g = 1.64 signal shows stretched exponential decay corresponding to the coherence time of 24.4 μs superimposed to electron spin echo envelope modulation (ESEEM). (d) The fast Fourier transform of three pulse ESEEM (frequency domain) for g =1.64 component reveals Larmor frequencies for $1^{167}Er^{3+}$ and $^{89}Y^{3+}$ nuclei at 413.9 mT. (e) The integrated area echo decay for C_2 g = 4.89 transition shows a coherence time of 0.5 μs with further improvement to 6.5 μs after applying XY-16-π-XY-16 DD sequence. (f) Instantaneous diffusion measurement on C_2 g = 4.78 and C_{3i} g = 3.28 with slope 0.84 and 0.71 MHz respectively. (g) T_1 measurement on C_2 g = 4.78 and C_{3i} g = 3.28 transition with inversion recovery sequence.

CHAPTER 5

MILLISECONDS COHERENCE TIME OF ERBIUM SPINS IN YTTRIUM OXIDE CERAMICS.

5.1 Introduction

Rare-earth-ion dopants in solids exhibit exceptionally long spin coherence times and narrow optical linewidths [179] [147] [207], making them a prime candidate for quantum memories and quantum transduction [106] in an optical quantum network [96], and with a good prospect for quantum sensing [51]. Kramers rare-earth-ions with unpaired 4f electrons possess effective electron spin S=1/2, and Er^{3+}, in particular, demonstrate telecom-wavelength optically addressable spins that are ideal for realizing quantum spin-photon interfaces in a fiber-based quantum communication network [140, 15]. For such a network, the Er spin coherence time needs to be at least a millisecond in order to efficiently generate and store entanglement over the photon transit time between adjacent network nodes, assuming a typical repeater node interval of 200 km [148]. Once generated, the entanglement between remote Er^{3+} spins can be transferred to $^{167}Er^{3+}$ nuclear spin registers for long-term storage while the electron spins are freed up for subsequent entanglement generation.

Due to large magnetic dipole moment, however, Er^{3+} electron spins experience strong decoherence from magnetic noise created by either Er^{3+} or other paramagnetic spin flip-flops, limiting their coherence to microseconds range in most prior reports [135] [193] [121] [87]. Milliseconds Er^{3+} spin coherence time has only been demonstrated recently in bulk single crystals with low nuclear spin density at milliKelvin temperatures: $T_2 = 1.3$ ms in 20 parts per million (ppm) doped Er^{3+}: $CaWO_4$ [146]; $T_2 = 23$ ms in undoped $CaWO_4$ [48]). Another approach to prolonging the Er^{3+} spin coherence considers $^{167}Er^{3+}$ isotope, which possesses 7/2 nuclear spin with long-lived hyperfine transitions [147]. This gives rise to hybridized electron-nuclear spins [127] [142] with Zero First-Order Zeeman (ZEFOZ)

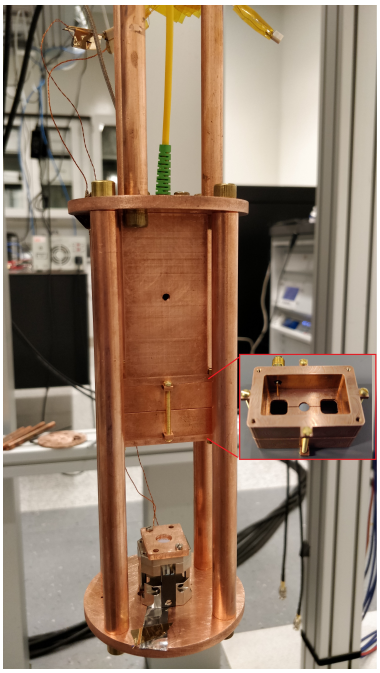
transitions showing reduced sensitivity to noise. Nevertheless, ZEFOZ transitions often occur at zero or low fields, where the magnetic noise spectral density peaks due to unpolarized spin baths, and addressing them requires stringent field alignment, partially limiting the robustness of this method.

In this chapter, we report millisecond coherence times of electron spins of $^{167}Er^{3+}$ in the yttrium oxide host. Instead of addressing ZEFOZ transitions, we probe weakly mixed electron spin transitions with low g-factors. By freezing the impurity spins and employing customized dynamical decoupling we demonstrate consistent Er^{3+} spin coherence time over a millisecond threshold. We investigate 20 parts per million (ppm) doped $^{167}Er^{3+}$ ensembles in Y_2O_3 polycrystalline hosts using electron spin resonance (ESR) spectroscopy. Rather than host nuclear spins, we identify paramagnetic impurity spins as the primary source of decoherence. By freezing them at milliKelvin temperatures, we obtain Hahn echo [78] coherence time of 1.46 ms, and T_2^{XY8} of 7.1 ms after dynamical decoupling (DD) of spectral diffusion. By further designing customized DD sequences to simultaneously mitigate spectral diffusion and instantaneous diffusion we achieved an even longer coherence than what is obtainable with conventional XY8 sequence. The strategies demonstrated in this work are applicable to a variety of host materials for erbium and other Kramers rare-earth spins, including those containing nuclear spins and paramagnetic impurities. Thus, this work provides a general recipe for engineering long-coherence rare-earth spins as appealing resources for quantum technologies.

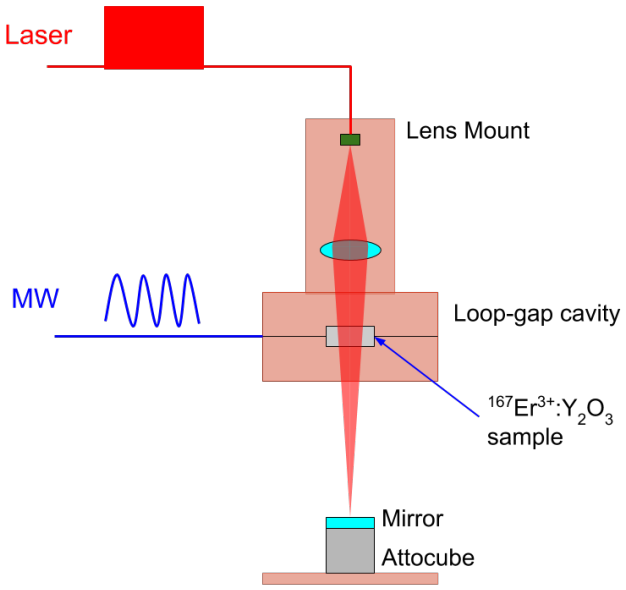
5.2 Spin dynamics of $^{167}Er^{3+}$:Y_2O_3 at sub-Kelvin temperatures

5.2.1 Experimental Methods

We use yttrium oxide (Y_2O_3) as a host matrix for $^{167}Er^{3+}$ dopants, which have been synthesized in diverse forms such as single crystals, polycrystalline ceramics, nanoparticles, and



(a)



(b)

Figure 5.1: (a) Cryogenic mounting of three dimension loop gap cavity with optical double pass setup on the mixing chamber (10 mK) stage. (b) Schematics of the microwave-optical spectroscopy setup. The Er^{3+} doped Y_2O_3 sample is placed at the center of the microwave cavity, along the optical double pass setup, where it can be addressed with both microwave and optics. The laser was focused on a mirror placed on a nanopositioner below the cavity with a beam spot size on sample $\approx$ 2 mm and reflected light was coupled back to the fiber in a double-pass configuration.

thin-films [208], with ultra-narrow, sub-kilohertz optical linewidths already demonstrated in Er^{3+} doped Y_2O_3 transparent ceramics [205][70]. The sample under study is a 20 ppm $^{167}Er^{3+}$ doped Y_2O_3 ceramics with 95 % isotopic purity prepared by sintering Er^{3+} doped Y_2O_3 nanoparticles. The average grain size is 0.90 μm^2. Y_2O_3 has a cubic crystal structure (T_h^7 space group) with 16 formula units per unit cell [82] [149]. These 32 Y^{3+} sites can be grouped into two classes with 24 sites of C_2 point group symmetry (Fig. 5.2(a)), and 8 sites for C_{3i} point group symmetry (Fig. 5.2(c)), where each of the 32 Y^{3+} ions in a unit cell have been shown to be substituted with an Er^{3+} ion with an equal probability [159] [160].

Er^{3+} ion has a $[Xe]4f^{11}$ configuration with $^{2S+1}L_J = {}^4I_{15/2}$ ground state. In a crystal field of low symmetry, the J = 15/2 ground state splits into 8 Kramers doublets with the lowest

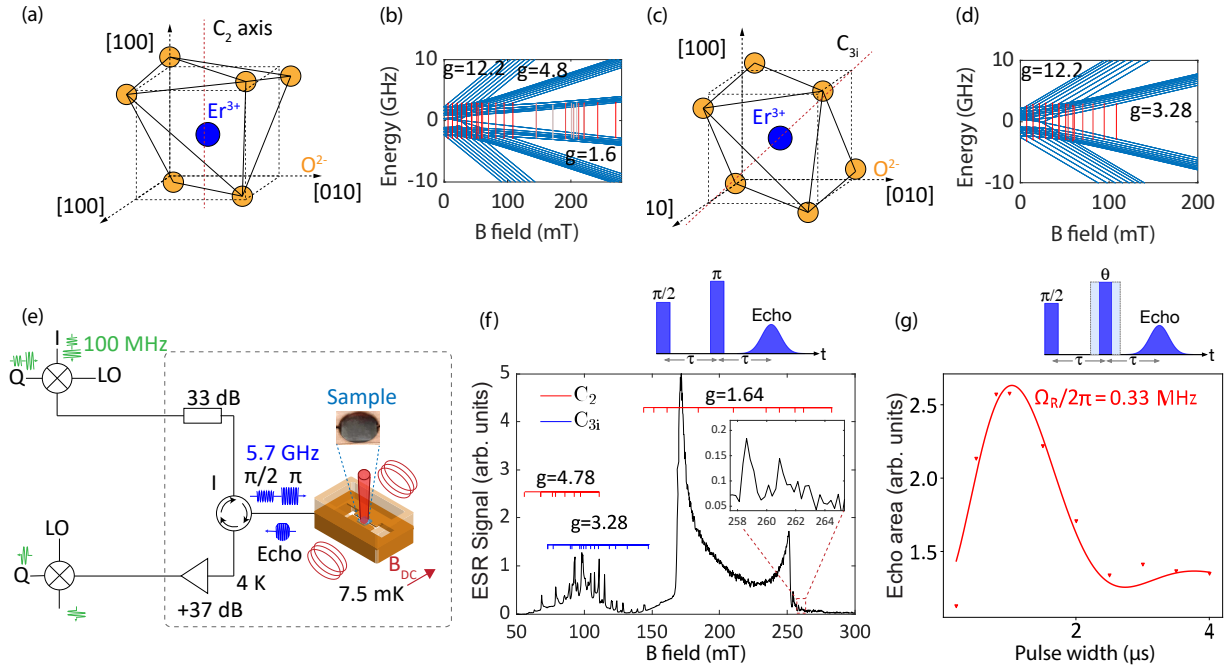


Figure 5.2: (a), (c) Er^{3+}:Y_2O_3 crystal structure showing the unit cell and Er^{3+} substituting in C_2 and C_{3i} sites, respectively. (b), (d) Zeeman and hyperfine energy levels for $^{167}Er^{3+}$ in C_2 and C_{3i} sites, respectively generated with Easyspin [175]. The red lines show the allowed ESR transitions at 5.67 GHz resonance frequency. (e) MilliKelvin pulsed ESR setup. (f) Echo detected field sweep of $^{167}Er^{3+}$: Y_2O_3 showing predicted transitions as dashes grouped by their g factors. (g) Rabi nutation of echo signal obtained by varying refocusing pulse length.

doublet being occupied at cryogenic temperatures, leading to an effective $S = 1/2$. Erbium has 5 stable isotopes ($^{162,164,166,168,170}Er$) with zero nuclear spin, and a ^{167}Er isotope with $I = 7/2$ nuclear spin. The spin Hamiltonian of the lowest Kramers doublet of $J = 15/2$ manifold of $^{167}Er^{3+}$ in Y_2O_3 can be modelled as,

$$\mathcal{H} = \mu_e \mathbf{B} \cdot \mathbf{g} \cdot \mathbf{S} + \mathbf{I} \cdot \mathbf{A} \cdot \mathbf{S} + \mathbf{I} \cdot \mathbf{Q} \cdot \mathbf{I} - \mu_n g_n \mathbf{B} \cdot \mathbf{I} \tag{5.1}$$

where μ_e is the Bohr magneton, $\mathbf{B}$ is the external magnetic field, $\mathbf{g}$ is the g-factor tensor, $\mathbf{A}$ is the hyperfine tensor, g_n is the nuclear g factor, and $\mathbf{Q}$ is the nuclear quadrupole tensor.

We use the principle values of g, A, and Q tensors for C_2 and C_{3i} sites obtained from a

separate study [141] to calculate the spin energy levels with the magnetic field as shown in Fig. 5.2(b, d). Due to the random orientation of crystal grains in a polycrystalline sample, while ESR transitions from $g = 12.2, g = 4.78$ and $g = 3.28$ overlap, we can individually address transitions with $g = 1.64$ in the region of 160-275 mT at $\approx$ 5 GHz ESR frequency (Fig. 5.2(b, d)). The transitions with $g = 1.64$ are of interest in this study due to their lowest sensitivity to noise, and strong coupling to microwaves given the high transverse g factor up to 12.2 [136].

We perform ESR spectroscopy on a sample with dimensions of $4.6\,\text{mm} \times 4.6\,\text{mm} \times 1\,\text{mm}$, which is mounted in between the two halves of a 3D copper loop-gap resonator [89]. The resonator was made with oxygen-free copper and was assembled with two halves with a gap exactly matching the sample size for good thermal conduction (Fig. 5.2(e)). The resonator was mounted on the mixing chamber stage of a dilution refrigerator (Bluefors LD 250) and had a 5.67 GHz resonance frequency with a loaded Q of 3500 at 7.5 mK base temperature. A 3-axis vector magnet (AMI Model 430) was used to apply a DC bias field. Laser illumination was applied to the sample using an objective lens with a weak focus on the sample with $\approx$ 2 mm beam spot size on the sample.

3D resonators offer certain advantages over 2D superconducting microresonators for ESR, including higher field homogeneity, the ability to apply out-of-plane magnetic fields, easier integration with optics, as well as compatibility with diverse sample geometry [215]. However, reduced sensitivity of 3D resonators typically requires the use of high power pulses ($\approx$ Watts) leading to heating and elevated temperatures [111] of the ESR spectrometer. We use a heterodyne detection technique along with a low noise preamplifier (HEMT) (Fig. 1e) to enhance the spectrometer sensitivity, allowing for low power ($\approx 100\,\mu\text{W}$) pulsed ESR measurements. This results in the lowest possible temperature of the sample stage of 7.5 mK during the experiment, allowing us to maximally polarize the spin population. Rabi frequency of 0.33 MHz is obtained in a two-pulse echo sequence with varying refocusing

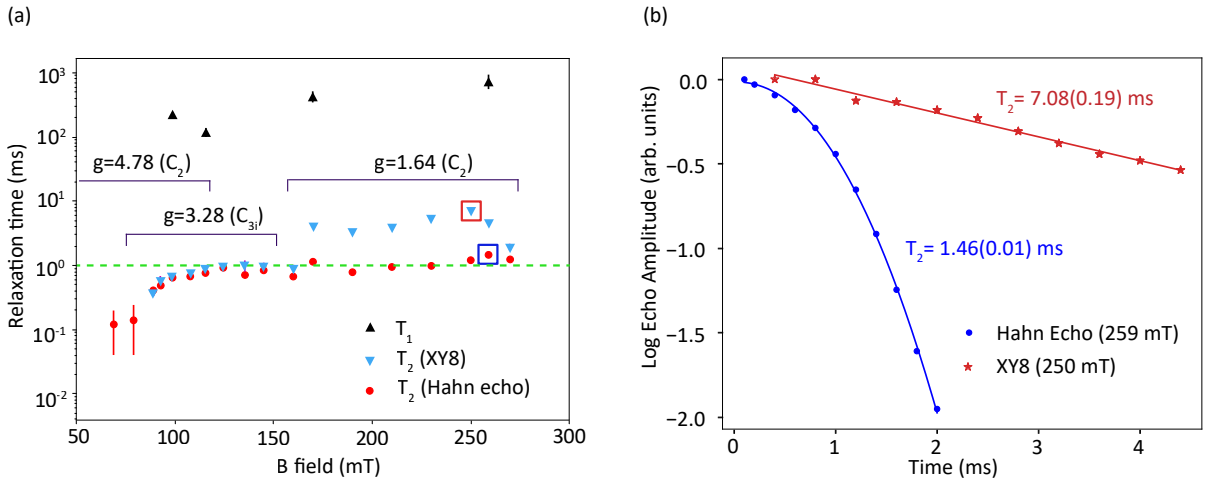


Figure 5.3: Electron spin coherence and relaxation times of $^{167}Er^{3+}$: Y_2O_3 at milliKelvin temperatures. (a) Spin lifetime (T_1) (black triangles) was measured using saturation recovery. Spin coherence time measured with two pulse echo (T_2, red dots) and with XY8 dynamical decoupling (T_2^{XY8}, blue triangles) showed coherence times exceeding 1 millisecond spin coherence time (green dashed line) for lower g transitions. Red and blue boxes highlight the longest XY8 and Hahn echo coherence times, respectively. (b) Echo decays for the two transitions with the longest Hahn echo and XY8 coherence times, as highlighted in (a).

(second) pulse length (Fig. 5.2(g)), which allows us to estimate a transverse g factor 7.5, in close agreement with expected transverse g factor of ≈ 8 for the g=1.64 transitions.

To identify all ESR transitions of $^{167}Er^{3+}$, we perform echo detected field sweep (EDFS) measurement by sending 1 μs-long $\pi/2$ and π pulses at a separation of 5 μs, and sweep magnetic field to detect the spin echo from different transitions (Fig. 5.2(f)). We observe spin echoes from g=4.78, g=3.28 in the <150 mT region and g=1.64 transitions extending from 160 mT to 275 mT, seen as a long tail in the spectra.

5.2.2 Spin coherence and relaxation times

For the ESR transitions observed in Fig. 5.2(f), we measure spin relaxation times, Hahn echo coherence times, and coherence times under XY8 dynamical decoupling at the base temperature. Fig. 5.3(a) shows T_1 (black), Hahn echo T_2 (red) and dynamically decoupled

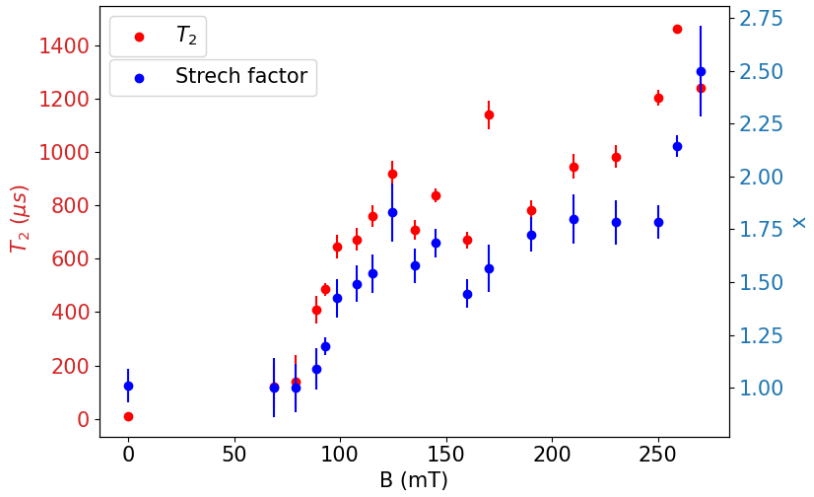


Figure 5.4: Spin coherence time (red, left) and stretch factor(blue, right) of $^{167}Er^{3+}$: Y_2O_3 at milliKelvin temperatures. An increase in stretch factor with the B field is indicative of the predominance of spectral diffusion as a source of decoherence for higher field transitions.

T_2^{XY8} (blue) as a function of B field. We fitted the decay of integrated echo amplitudes with a stretched exponential $\exp(-2\tau/T_2)^n$, where n is the stretch factor. Figure. 5.3(a) shows T_2 coherence times approaching or exceeding 1 ms (green dashed line) for the majority of the transitions above 100 mT, with the highest T_2 of 1.46 ms measured around 259 mT from g=1.64 transitions (blue box in Fig. 5.3(a)). The coherence time increases with fields due to lower sensitivity of high field (lower effective g) transitions to spectral diffusion (SD) and instantaneous diffusion (ID) [112] noise. At a 5.67 GHz splitting, the sensitivity of ESR transition to magnetic noise ($\partial E/\partial B$) is simulated to be $\approx g\mu_B$ (Section 5.2.5), therefore electron-nuclear spin mixing does not play a significant role in the measured long coherence time [142]. The measurable lowest field transition at 70 mT showed a T_2 of 100 μs along with strong modulation of echo amplitudes due to superhyperfine couplings [152] [36] [70]. Fig. 5.4 shows stretch factor n increased from 1 for the lowest field transition (70 mT) to 2.5 for the highest field transition (270 mT), indicating spectral diffusion as a decoherence mechanism for the latter transitions [122].

Decoherence due to spectral diffusion can be suppressed with dynamical decoupling [177].

XY8 sequence in particular offers robust performance for an arbitrary initial state, as well as compensates for pulse errors [171]. Fig. 5.3(a) shows a clear increase in coherence times from $\approx$ 1 ms with Hahn echo to beyond 3 ms with XY8 for the high field (> 150 mT) transitions, with the longest T_2^{XY8} of 7.08 ms for the 250 mT transition (red box). The echo decays with XY8 sequence were well fitted with a single exponential decay. In this measurement, we sent N= 248 π pulses. Further,N did not yield longer coherence, indicating effective filtering of the low-frequency noise [39]. Therefore, we expect that the measured T_2^{XY8} is limited by instantaneous diffusion (ID) and possible contribution from higher frequency noise. The coherence time improvement with XY8 was less pronounced for lower field transitions, which suggests an increase in instantaneous diffusion with higher effective g factors, scaling approximately as g_{eff}^2 [100]. This explains the sharp increase in T_2^{XY8} at around 170 mT. The measured T_2^{XY8} is in good agreement with the estimated ID limit for g=1.64 transitions of 7 ms (Section 5.2.3). Spin T_1 for a few transitions was also measured using saturation-recovery sequence and is found to be in the range of 100 ms to 0.7 s (Fig. 5.3(a) black).

ESR transitions between 150-250 mT could have mixed contributions from Er and other paramagnetic impurities. Therefore it is imperative to verify those transitions are indeed from Er spins. By illuminating the sample with a laser pulse on resonance with the C_2 site optical transition around 1535.6 nm, we observe a clear optically modulated spin echo signal for the ESR transition around 259 mT, which cannot be attributed to other heating effects (Section 5.2.4), thereby validating its assignment to $^{167}Er^{3+}$ spins in the C_2 site.

5.2.3 Decoherence and relaxation processes at sub-Kelvin temperatures

Temperature dependence of decoherence and relaxation processes

We perform temperature-dependent relaxation and coherence time measurements for the 259 mT (g=1.64) transition to understand decoherence mechanisms below 1 K. We use a continuous-wave off-resonant laser at 191 THz (1570 nm) to heat the sample directly. The

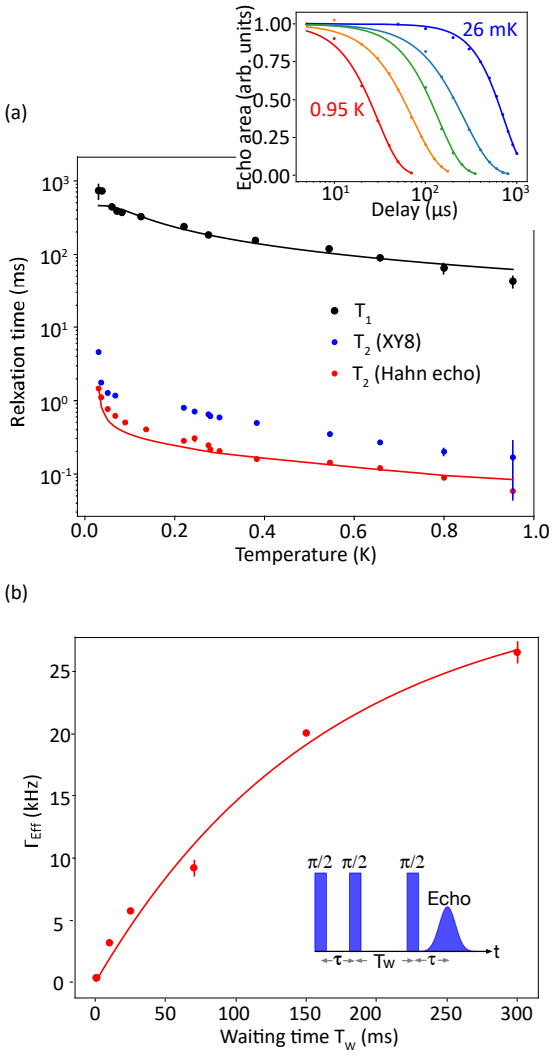


Figure 5.5: Decoherence mechanisms at sub-Kelvin temperatures for the $^{167}Er^{3+}$ g=1.64 (259 mT) transition. (a) Temperature dependence of relaxation and decoherence processes: spin lifetime (T_1, black dots) fitted with Eq. 5.2 (black line); coherence time (T_2, red dots) fitted with the T_2 model described in the text (red line); XY8 dynamical decoupling coherence time (T_2^{XY8}) measured by sending 30 XY8 pulses. Inset shows time domain Hahn echo decays for the range of temperatures measured. (b) Spectral diffusion was measured with three pulse echoes at a base temperature of 26 mK.

actual sample temperature was estimated from the electron spin echo amplitudes and by correlating it to the recorded stage temperature [111]. A sample temperature of 26 mK is determined based on the spin polarization model when the stage temperature is 7.5 mK as described below.

Estimation of the sample temperature

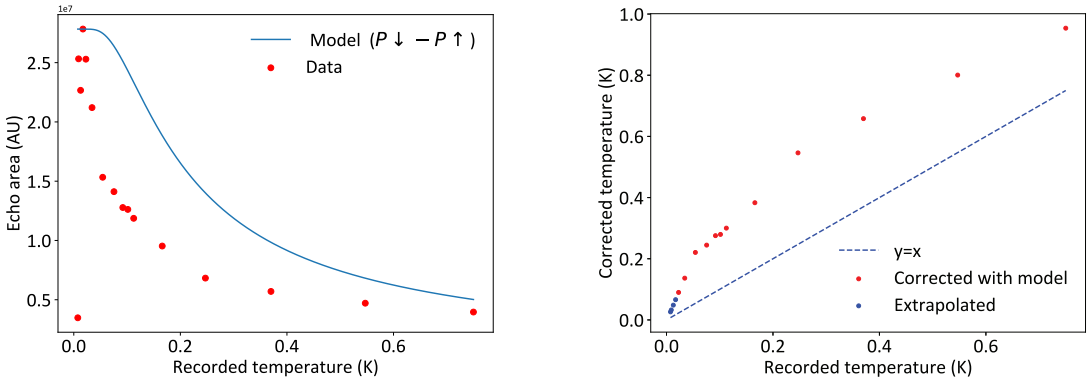
Actual sample temperature was deduced from the spin echo amplitude as a measure of electron spin polarization [111] [59]. The spin echo was first normalized for T_2 using $\text{echo}(0) = \text{echo}(\tau)e^{\frac{2\tau}{T2}}$. The echo area shows an increase with decreasing temperature until 17.1 mK, below, which it decreases due to an increase in T_1 as the repetition rate of 0.5 Hz is comparable to T_1^{-1} (Fig. 5.6(a). The actual temperature was deduced using the roots of the equation $\text{echo}(T_{\text{recorded}}) = P(T_{\text{corrected}}) = K\tanh(\Delta E/2k_B T_{\text{corrected}})$, where the free parameter K of spin polarization model was set equal to the maximum echo amplitude at 17.1 mK. This produced a corrected temperature table for the recorded base temperature values in 17.1 mK - 750 mK (Fig. 5.6(b) red points). For temperature values lower than 17.1mK the model was not applicable due to saturation effects, therefore corrected temperature was deduced by linearly extrapolating to lower temperatures (Fig. 5.6(b) blue points). The corrected temperature lies above the y=x line, which indicates that the actual sample temperature is higher than the recorded temperature. This could be due to reasons including a thermal gradient between the mixing chamber stage and the cavity, and imperfect thermalization between the sample and the cavity.

The electron spin lifetimes (T_1) measured using saturation recovery (black dots, Fig. 5.5(a)) show an increase from 42 ms at 0.95 K to 0.73 s at 26 mK. The spin T_1 temperature dependence for rare-earth dopants at a temperature below 4K can be modeled by a combination of direct phonon process R_D, the flip-flop R_{ff} process and a temperature independent component R_0 (black line) [116], with f being the transition frequency,

$$\frac{1}{T_1} = R_0 + R_{ff}\text{sech}^2\Big(\frac{hf}{2k_B T}\Big) + R_D\coth\Big(\frac{hf}{2k_B T}\Big) \tag{5.2}$$

The fitted coefficients are R_D= 2.19 Hz, R_{ff} = 0.87 Hz and R_0 =1.67×10^{-8} Hz.

The Hahn echo spin coherence times T_2 show a strong dependence on temperature (Fig. 5.5(a)) from 58 μs at 0.95 K to 1.46 ms at 26 mK. The echo decay was fitted with



(a) (b)

Figure 5.6: Calibration of sample temperature:(a) Spin echo area and the spin polarization model as a function of temperature (b) Recorded temperature is corrected using spin polarization model (red points). The lowest temperature data points are calculated by linear extrapolation of the corrected temperature model (blue points).

a stretched exponential and exhibited a stretch factor in the range of 1.3 to 2.1, pointing to spectral diffusion as the dominant decoherence mechanism throughout the temperature range. Improvement in coherence times with XY8 dynamical decoupling ($T_2, (XY8)$) in the same temperature range is also indicative of spectral diffusion-dominated decoherence (blue dots in Fig. 5.5(a)).

To model the temperature dependence of T_2 and to obtain spectral diffusion parameters for the environment spin bath, we consider three contributions: spectral diffusion limited coherence time, $T_{2,SD}$, instantaneous diffusion $T_{2,ID}$ and spin relaxation limit $2T_1$, so $T_2^{-1} = T_{2,SD}^{-1} + T_{2,ID}^{-1} + (2T_1)^{-1}$. Spectral diffusion limited coherence, $T_{2,SD}$ can be modeled using a Lorentz diffusion model with a stretch factor 2 [100] [112],

$$T_{2,SD}^{-1} = \frac{\sqrt{\pi \Gamma_{SD} R}}{2} \tag{5.3}$$

where Γ_{SD} represents the spectral diffusion linewidth due to dipolar interaction with environmental spins, and R, is the flip rate of the environment spins. The temperature-dependent Γ_{SD} can be modelled as [143],

$$\Gamma_{SD} = \Gamma_{Max}\text{sech}^2(g_{env}\mu_B B)/(2k_B T) \tag{5.4}$$

where g_{env} is the effective g factor and Γ_{Max} is the maximum dipolar broadening with environment spins causing spectral diffusion.

We first assume the total flip rate R(T) for the environment spin bath with the inverse of Er T_1 from the fit (black curve) in Fig. 5.5(a). The contribution of decoherence from instantaneous diffusion $T_{2,ID}$ can be estimated from the measured coherence time after XY8 dynamical decoupling, as it represents the remaining decoherence that cannot be canceled by the XY8 sequence. By fitting the coherence decay, we obtain spin bath parameters Γ_{Max} = 2.80(0.51) MHz and $g_{env} = 0.70$, which are not consistent with $^{167}Er^{3+}$ spin induced spectral diffusion. While Γ_{Max} of 2.80 MHz is significantly larger than the spectral diffusion linewidth of 124 kHz due to erbium spins, $g_{env} = 0.70$ is smaller than the lowest g (1.64) of $^{167}Er^{3+}$. This thus indicates spin bath is primarily comprised of impurity spins with a low g factor. Indeed we observe a broad ESR signal at 300-900 mT fields (g=1.3-0.4), with peaks at g=0.71 and g=0.81 (5.2.4). Impurity transitions at fields higher than 900 mT (g=0.4) could not be measured due to the field limit of our magnet. Spins with g=0.4(0.7) are relatively unpolarized even at our lowest measurement temperature, with 87.1(98.1)% polarization as compared to 99.996% polarization for the $^{167}Er^{3+}$ g=1.64 transition around 259 mT. Therefore, the spectral diffusion measured is attributed to the unpolarized paramagnetic impurities within the host matrix.

Estimated spectral diffusion linewidth due to $^{167}Er^{3+}$ spins

The upper bound on maximum spectral diffusion linewidth due to erbium ions for 259 mT transition was estimated as,

$$\Gamma_{Max,Er} = \frac{\pi\mu_0 g g_{env}\mu_B^2 n_{env}}{9\sqrt{3}h} \tag{5.5}$$

where g=1.6 for 259 mT transition, g_{env} corresponds to the effective g factor of erbium spins contributing to the spectral diffusion, and n_{env} is the environment spin density. Due to the presence of multiple grains with random orientations of the crystal axis, the effective g_{env} for the erbium spin bath is difficult to estimate. We therefore make an approximation $g_{env} \approx g_{avg} = (g_x + g_y + g_z)/3 = 6.2$, which is the same for both C_2 and C_{3i} site. Moreover, the estimation of n_{env} is also difficult in the presence of multiple crystal orientations as well as 8 hyperfine sublevels with different occupations at 26 mK base temperature. We, therefore, estimate the upper bound on $n_{env} \approx n_{spin,Er}$ where $n_{spin,Er}$ is the total concentration of spins including the two sites, hyperfine sublevels and different crystal orientation in a 20 ppm $Er^{3+} : Y_2O_3$ sample. Therefore $n_{env} \approx 5.2 \times 10^{23}$ spins/m^3 for 20 ppm doped Y_2O_3. Using these approximations, we get $\Gamma_{Max,Er} \leq 124.80$ kHz.

Spectral diffusion

Next, we study the residual spectral diffusion at the lowest temperature of 26 mK to further validate our model of spectral diffusion. We use three pulse echo (stimulated echo) technique with three $\pi/2$ pulses with a delay τ between the first and second pulses and a wait time T_W between the second and third pulses. For each value of T_W we sweep τ to measure the effective linewidth $\Gamma_{Eff} = 1/(\pi T_2)$ (Fig. 5.5(b)),

$$\Gamma_{Eff} = \Gamma_0 + \frac{1}{2}\Gamma_{SD}(1 - e^{-RT_w}) \tag{5.6}$$

where Γ_{SD} is spectral diffusion linewidth, R is total spin flip rate and Γ_0 is the linewidth in absence of spectral diffusion [112] [143] .

We obtain Γ_{SD} of 64.5(8) kHz, R of 5.6(1.5) Hz and Γ_0 of 0.6(0.8) kHz at 26 mK. The fitted R and Γ_{SD} predict spectral diffusion limited coherence time ($T_{2,SD}$) of 1.87 ms from Eq. 5.3, which is in good agreement with the predicted $T_{2,SD}$ of 2.2 ms at 26 mK from the temperature-dependent spectral diffusion model. The total spin-flip rate R from three pulses

echo 5.6(1.5) Hz is higher than the measured 1.4(0.6) Hz spin-flip rate of $^{167}Er^{3+}$ g=1.64 transition, further supporting the presence of paramagnetic impurity spins.

Close agreement between the spectral diffusion measurements from three pulse-echo and the temperature dependence model substantiates our understanding of decoherence processes. Decreasing temperature lowers the spectral diffusion linewidth Γ_{SD} by a factor of $\mathrm{sech}^2(g_{env}\mu_B B)/(2k_B T)$, and slows the total spin-flip rate R by freezing the direct phonon ($\coth(g_{env}\mu_B B)/(2k_B T)$) and flip-flop processes ($\mathrm{sech}^2(g_{env}\mu_B B)/(2k_B T)$). The residual decoherence at 26 mK is dominated by slow spectral diffusion of ≈ 5 Hz spin flips and a smaller contribution from instantaneous diffusion (Section 5.2.3).

To further investigate the spectral diffusion induced by paramagnetic impurities in Y_2O_3, we perform pulsed ESR on a Y_2O_3 sample with no intentional erbium doping and observe spin echo signals from impurity spins in the host matrix (Section 5.2.4). The T_2 measured on an impurity transition in undoped Y_2O_3 is comparable to T_2 measured in $^{167}Er^{3+}$ doped Y_2O_3 at the same field, as expected. This also puts an upper limit on magnetic noise from flip-flops of yttrium nuclear spins (δB_Y) as $\approx 1/(\pi g \mu_B T_2) = 9\,\mathrm{nT}$. The $^{167}Er^{3+}$ transition with 1.46 ms T_2 at 26 mK shows a non-exponential decay with a stretch factor of 2.1, indicating the presence of a frozen core of yttrium nuclei in direct proximity to Er^{3+} with suppressed flip-flop dynamics [72][103]. While the estimated nuclear spin-bath limited T_2 based on yttrium density in Y_2O_3 is $\approx$ 1 ms [93], we can expect a longer T_2 due to the frozen core effect [207] [103].

We note that spin homogeneous linewidth deviates from a linear dependence on temperature as expected in the case of a magnetic two-level system (TLS) dominated decoherence in ceramics [70]. We observe a broad feature around g $\approx$ 2, as well as a sharp g=1.97 signal (F^+ defect center [104]) at high temperature, pulsed ESR, witnessing the presence of vacancy defects and magnetic TLS in the host matrix (Section 5.2.4). However, spins with g $\approx$ 2 would be frozen with 99.9997 % polarization at 26 mK and 259 mT, and are not expected

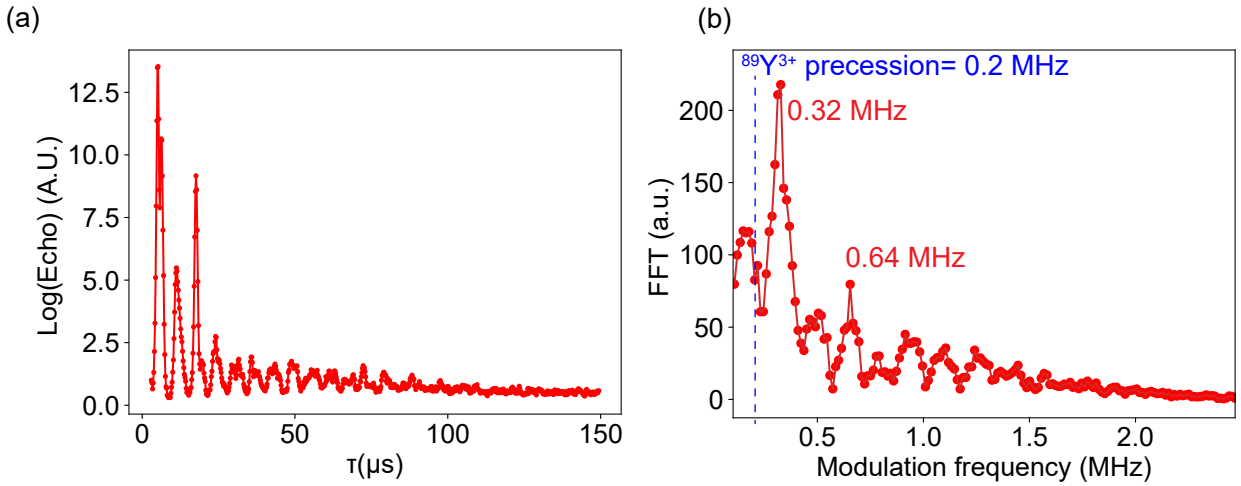


Figure 5.7: (a)Electron spin echo modulation (ESEEM) obtained two pulse-echo measurements for C_2 transition at a field 98.75 mT shows strong modulation of spin echo amplitude due to interaction with $^{89}Y^{3+}$ nuclei. (b) The Fourier transform of echo amplitude reveals a sharp peak around 0.34 MHz due to dipolar interaction between Er^{3+} electron spin and $^{89}Y^{3+}$ nuclei.

to contribute significantly to spectral diffusion [135].

Superhyperfine interaction

Strong modulation of the spin echo envelope (ESEEM) with periodic revivals is observed for C_2 transition at a field 98.75 mT in Fig. 5.7(a), which is indicative of coupling to $^{89}Y^{3+}$ nuclear spins. The fast Fourier transform of the echo amplitude Fig. 5.7(b) shows a sharp peak around 0.34 MHz and distribution of peaks in 0.15 - 1.5 MHz. The expected Larmor precession frequency of $^{89}Y^{3+}$ nuclei ($\mu \approx 0.275\mu_N$) at 98.75 mT is 0.2 MHz [135] (blue dashes), which is smaller than the observed superhyperfine modulation frequency. The spread of modulation frequencies of $^{89}Y^{3+}$ nuclei is expected due to varying hyperfine couplings and distances from Er^{3+} spin [36] [74] [137] [30].

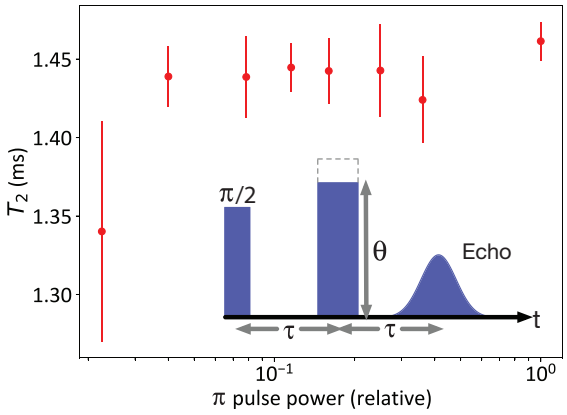


Figure 5.8: Instantaneous diffusion measured at 26 mK by repeating Hahn echo measurement as a function of π pulse power shows no dependence of the spin coherence time on pulse power within uncertainties.

Instantaneous diffusion

We perform Hahn echo measurement with varying π pulse power at 26 mK to study instantaneous diffusion (ID). The coherence time shows no dependence on π pulse power within experimental uncertainties (Fig. 5.8) indicating a low ID. The low effective density of $^{167}Er^{3+}$ ions being addressed could be attributed to the low Rabi frequency of the pulse compared to inhomogeneous linewidth as well as a thermal distribution of spin populations among the 8 hyperfine sublevels of $^{167}Er^{3+}$. The instantaneous diffusion limited T_2 can be estimated as [112],

$$T_{2,ID}^{-1} = \frac{2\pi^2 \mu_0 h n_{eff} \gamma^2}{9\sqrt{3}} \langle \sin^2 \frac{\theta}{2} \rangle \tag{5.7}$$

where n_{eff} is the effective density of spin ensemble excited by the pulse bandwidth and $\langle \sin^2 \frac{\theta}{2} \rangle$ is spin-flip probability. Average spin-flip probability is obtained by integrating spin-flip probability over the ensemble [112]. For estimated spin linewidth of 30 MHz and Rabi frequency of 0.33 MHz, $\langle \sin^2 \frac{\theta}{2} \rangle \approx 0.023$. Next We estimate n_{eff} as,

$$n_{eff} = n_{C_2} n_{hyperfine} \tag{5.8}$$

where $n_{C_2} = 4 \times 10^{17}$spins/cm^3 for 20 ppm, $n_{hyperfine} = 0.0292$ for the ground state (one of the 8 hyperfine levels) based on the thermal occupation of the level at 26 mK and 259 mT resonance field. Substituting these values, we get $T_{2,ID} = 7$ ms, which is close to the experimentally observed XY8 T_2 of 4 ms for the transition. This estimated homogeneous linewidth broadening due to ID is at least 3.5 times smaller than the broadening due to spectral diffusion, which is consistent with spectral diffusion-dominated decoherence.

5.2.4 Impurities and paramagnetic defects in Y_2O_3

Impurities and defects in $^{167}Er^{3+} : Y_2O_3$ and verification of Er spins

Echo detected field sweep (EDFS) measurements carried out using a 4.96 GHz cavity (Fig. 5.9(a)) show the presence of a background spin echo signal up to fields as high as 900 mT. The spectrum also shows two broad peaks around 450 mT (g=0.8) and 500 mT (g=0.7). These spin transitions would require higher fields to polarize and therefore would be unpolarized at lower fields (B <270 mT). This observation is consistent with the $g_{env} = 0.70$ obtained for environmental spin baths, supporting the claim spectral diffusion for the transition around 259 mT is caused by unpolarized spins. These broad peaks at high fields could be attributed to paramagnetic impurities incorporated from the synthesis process, and the broad background signal has a possible contribution from two-level systems (TLS) [125]. The fact that the broad signal is observed only at high fields indicates the magnetic nature of the TLS.

Pulsed ESR measurements with continuous-wave laser heating show a sharp peak at g = 1.97 in the EDFS spectra (Fig. 5.9(b)). The g=1.97 signal has been observed in CW-ESR on $Eu^{3+} : Y_2O_3$ transparent ceramics and is attributed to F^+ center, corresponding to an oxygen vacancy with a trapped electron [104]. Interestingly, while the strong echo signal

from F^+ center is observed at 60 mk with laser heating, the signal is absent in the same measurement performed at 7 mK with no laser heating. The observation of spin echo also suggests F^+ center possesses relatively good coherence properties at cryogenic temperatures.

In order to verify the Er^{3+} spins around 259 mT transition, optical saturation measurement of spin echo was carried out. An optical pulse of 100 ms duration was sent to the cavity and was followed by the spin echo sequence (Fig. 5.9(c)) after a waiting time of 1 ms. The electron spin echo amplitude was obtained after averaging 25 times for each measurement. Figure 5.9(c) shows a reduction of electron spin echo signal amplitude (red) as the laser frequency was scanned across the Er C_2 site optical absorption profile. This modulation of spin echo is consistent with the optical pumping of the ground state spin population. To rule out the heating effect due to optical absorption by the crystal, we change the order of the laser saturation pulse and the spin echo sequence, keeping the duty cycle for all the pulses the same. The laser pulse sent before the spin echo sequence shows saturation as compared to sending laser after the spin echo sequence (Fig. 5.9(d)), with the same sample stage temperature in both cases. This rules out steady-state heating in the experiment. Furthermore, changing the waiting time between the laser pulse and spin echo from 1 μs to ms does not show a noticeable change in spin echo amplitude either, and this rules out transient heating. Therefore we verify the g=1.6 transition around 259 mT belongs to Er^{3+} C_2 site.

Comparison with measurements on undoped Y_2O_3 sample

ESR measurements were performed on an undoped Y_2O_3 sample to further study the presence of impurities as the source of spectral diffusion. The transitions in undoped Y_2O_3 are expected to have a contribution from impurities as well as residual Er^{3+}. The spin echo measurements were performed using the same setup and a 5.7 GHz cavity was used for $^{167}Er^{3+} : Y_2O_3$ measurements. Fig 5.10(a)) shows the EDFS for $^{167}Er^{3+} : Y_2O_3$ (black) and undoped Y_2O_3 sample (red) scaled by the sample size for comparison. We observe the

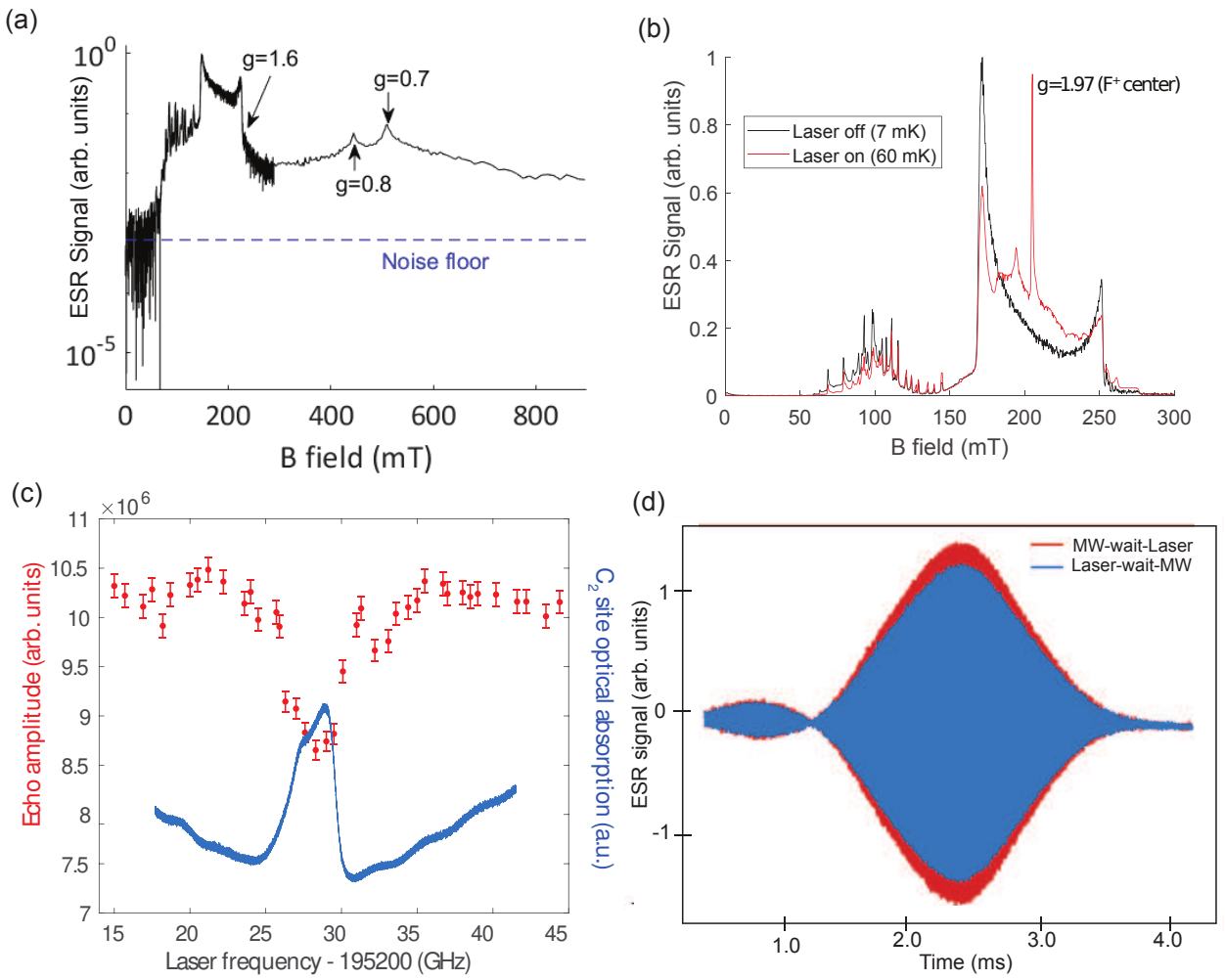


Figure 5.9: Presence of impurities, defects, and verification of Er for transition around 259 mT in $^{167}Er^{3+} : Y_2O_3$. (a) High-field echo-detected field-swept (EDFS) spectra for $^{167}Er^{3+} : Y_2O_3$ st 4.96 GHz shows the presence of ESR transitions up to 900 mT, with broad peaks around 450 mT (g=0.8) and 500 mT(g=0.7). (b) EDFS spectra taken with continuous wave laser heating show a sharp peak at g = 1.97 corresponding to F^+ center vacancy defect. (c) Er 259 mT transition shows saturation of spin echo in response to pulsed laser resonant with $^{167}Er^{3+} : Y_2O_3$ which is coincident with measured C_2 site optical absorption at the same field. (d) A comparison of the spin echo signal with the sequence of microwave and optical pulses reversed shows a stronger echo, thereby ruling out steady-state heating as a mechanism of spin echo saturation after the optical pulse.

presence of a broad feature from impurity transitions in 165-240 mT region in both samples. We notice the absence of Er features in undoped Y_2O_3, including peaks in 50-150 mT from g=4.8, 3.3 and a long tail from g=1.6 transitions starting from 150 mT and ending in a

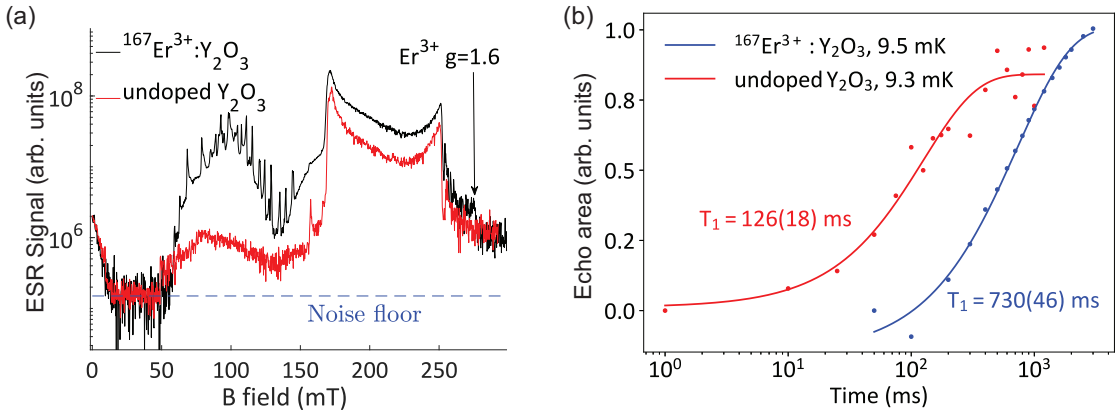


Figure 5.10: Measurements on undoped Y_2O_3 sample. (a) EDFS spectra of $^{167}Er^{3+}$: Y_2O_3 (black) and undoped Y_2O_3 sample (red). Features from $^{167}Er^{3+}$ including hyperfine lines from g=4.8, 3.3 and g=1.6 plateau (270 mT) are not present in undoped Y_2O_3 sample. Broad impurity transitions are seen in 165-250 mT for both samples. (b) Transition around 259 mT for undoped Y_2O_3, shows 126 ms spin T_1 compared to 730 ms for same field transition in $^{167}Er^{3+}$: Y_2O_3 at similar temperature.

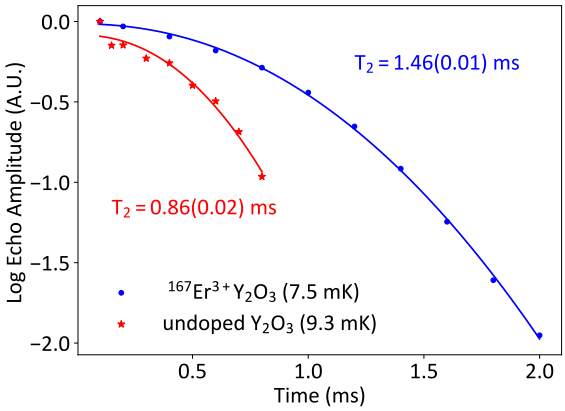
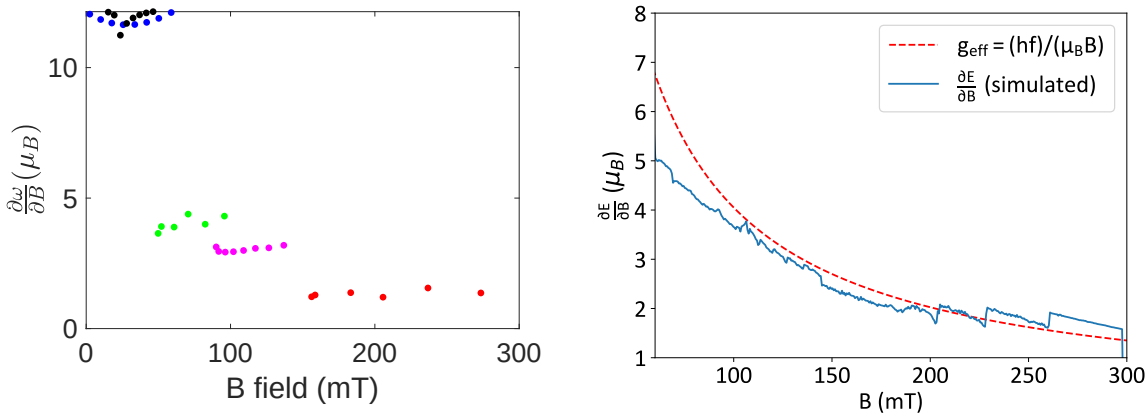


Figure 5.11: Transition at 259 mT for undoped Y_2O_3, shows 0.86 ms coherence time at 9.3 mK compared to 1.46 ms for same field transition in $^{167}Er^{3+}$: Y_2O_3 at 7.5 mK.

plateau around 270 mT (arrow in Fig 5.10(a)). The transition in undoped Y_2O_3 shows a T_1 of 126(18) ms as compared to T_1 of 730(46) ms in the case of $^{167}Er^{3+}$ in Y_2O_3 at similar temperature 5.10(b). The distinct T_1 indicates the transition in the undoped sample belongs to different spin species than $^{167}Er^{3+}$.

Further, spin coherence time measurements performed on the impurity transition at 259 mT on undoped Y_2O_3 yielded a T_2 of 0.86(0.02) ms at a recorded base temperature of



(a) (b)

Figure 5.12: (a) Noise sensitivity (∂E/ ∂B) in units of μ_B for ESR transitions in $^{167}Er^{3+} : Y_2O_3$ at 5.67 GHz for crystallites with magnetic field aligned with the principal axis of the g tensor was simulated using Easyspin. Points with the same color belong to the same site and orientation of crystallite and correspond to different hyperfine transitions. (b) Average noise sensitivity (∂E/ ∂B) in units of μ_B was calculated by averaging over all possible orientations of crystallites that are on-resonant at a given B field. Average (∂E/ ∂B) was found to be $\approx g_{eff}$ indicating electron-nuclear mixing does reduce the magnetic noise sensitivity of the transitions measured at 5.67 GHz.

9.3 mK. When taking the temperature dependence of T_2 into account, this would imply a coherence time of 1.16 ms at a recorded base temperature of 7.5 mK in undoped Y_2O_3, which would be comparable to the 1.46 ms T_2 measured at the same field in $^{167}Er^{3+} : Y_2O_3$ (Fig. 5.11). Since spectral diffusion is shown to be the dominant source of decoherence, magnetic field noise can be estimated as $B_{noise} = 1/(\pi T_2 \gamma_{eff})$, where $\gamma_{eff} = g_{eff}\mu_B$. Observing similar coherence time in $^{167}Er^{3+} : Y_2O_3$ and undoped Y_2O_3 at same field (similar g_{eff}) confirms non-erbium spins in the material as the source of spectral diffusion.

5.2.5 Magnetic noise sensitivity of ESR transitions at 5.67 GHz

Magnetic noise sensitivity for ESR transitions in polycrystalline $^{167}Er^{3+} : Y_2O_3$ at 5.67 GHz was calculated by numerical simulations using Easyspin as described in the appendix. The estimated noise sensitivity was found to be $\approx g_{eff}\mu_B$ as shown in Fig.5.12b.

5.2.6 Dynamical decoupling noise spectroscopy

Dynamical decoupling spectroscopy can be used to study the spectral diffusion spectrum as well as the effect of pulse errors on the coherence time. We used a modified setup with high-power pulses with ≈ 0.5 W peak power at the microwave cavity. This increased the Rabi frequency and allowed us to obtain a pi pulse of 50 ns as compared to 1 μs used in previous sections. Fig. 5.13 shows the coherence time under CPMG, XY8, XY16 sequences as a function of the separation between the pulses 2τ. We observe longer coherence time under CPMG dynamical decoupling sequences, however, CPMG sequences only preferentially preserve states orthogonal to the pi pulse axis. Therefore, more robust sequences like XY8 and XY16 are required to preserve an arbitrary quantum state for a long time. We observe the better performance of XY8 sequences over XY16, which might suggest the accumulation of pulse error as a mechanism of decoherence for short pulse separation. Nevertheless, all XY8, X16 and CPMG observe a similar dependence of $T_{2,DD}$ on 2τ in the range of 2 - 20 μs, suggesting a local maxima in noise spectrum around $2\tau = 12$ μs or 83 kHz. While XY8 and XY16 measurement could not be performed for 2τ larger than 25 μs, CPMG sequences shows a $1/\tau^{\alpha}$ behaviour for large 2τ suggesting $1/f^{\alpha}$ noise spectrum for low frequency limit.

5.3 Spin dynamics in $^{166}Er^{3+}$:Y_2O_3 at sub-Kelvin temperatures

Continuous wave (CW) and Pulsed ESR measurements on a 20 ppm purified $^{166}Er^{3+}$: Y_2O_3 using aluminum loop gap cavity $^{166}Er^{3+}$ (I=0) offers advantages for applications requiring a strong coupling to an ensemble of spins such as quantum transduction, microwave quantum memory, as well as offers simpler spin initialization and readout due to the lack of hyperfine structure. CW ESR was performed on this sample by measuring the dispersive frequency shifts of the cavity as a function of the magnetic field. We observed transitions from C_2 g=12.2, 4.8 and 1.64 as well as C_{3i} g=3.2 (Fig. 5.14,red line). To study the coherence

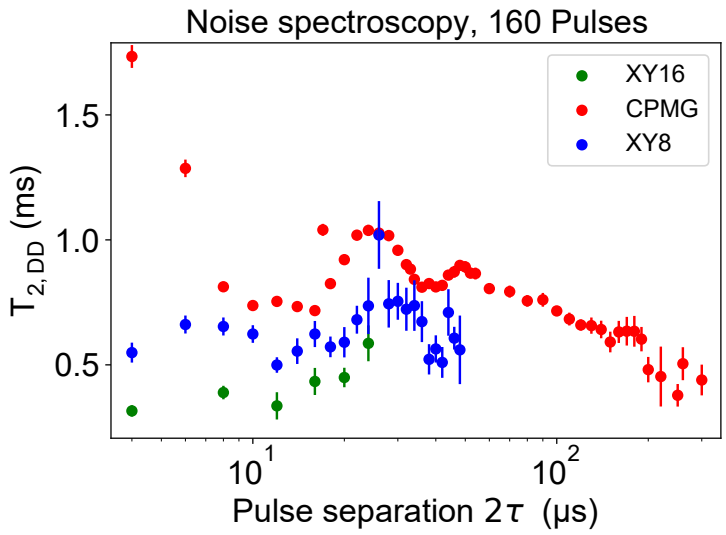


Figure 5.13: Dynamical decoupling noise spectroscopy performed on g=1.6 transition of $^{167}Er^{3+} : Y_2O_3$ using a modified setup with high power pulses. Measuring the coherence time under dynamical decoupling sequence $T_{2,DD}$ as a function of pi pulse separation 2τ allows obtaining the noise spectrum of the spectral diffusion noise.

properties of the transitions we performed spin echo detected field sweep (EDFS) by detecting two-pulse (Hahn) echo with a pulse separation of 5 μs. We observe a strong spin echo signal from the high field transitions (Fig. 5.14, blue line). The strong spin echo signal can be explained by an increase in spin coherence time T_2 for the high field(low g transitions) as shown by green dots. The high field transitions show long spin T_2 approaching 0.8 ms while the low field transition show a T_2 20-50 μs. The reduced coherence time for low field(high g) transitions can be explained by an increase in instantaneous diffusion scaling as g_{eff}^2. Nevertheless, coherence times approaching ms in $^{166}Er^{3+} : Y_2O_3$ makes it an interesting candidate for spin photon interfaces owing to its simpler level structures S= 1/2 and I=0 as compared to $^{167}Er^{3+} : Y_2O_3$ with S= 1/2 and I=7/2, which would simplify spin initialization for the former case.

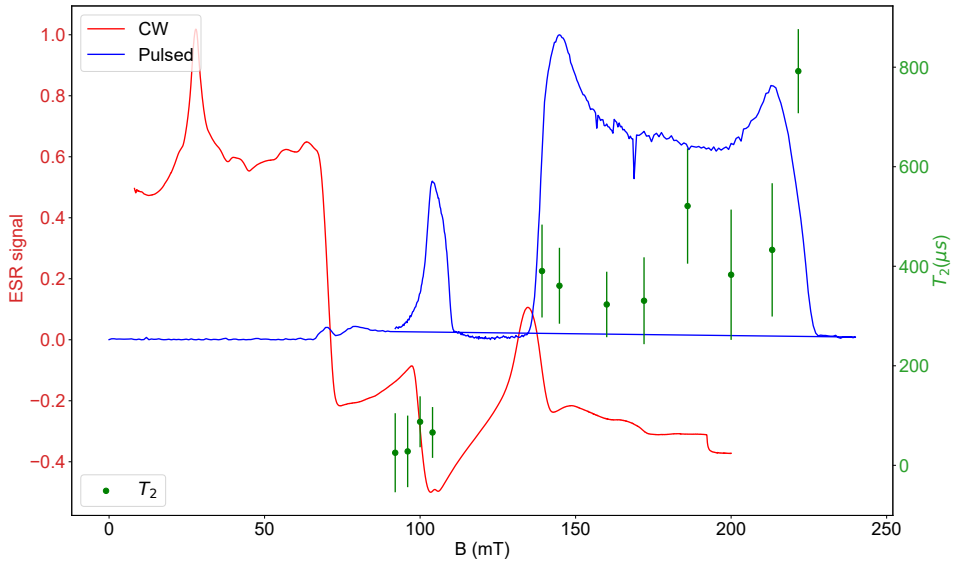


Figure 5.14: Continuous wave (CW) and Pulsed ESR measurements on purified $^{166}Er^{3+} : Y_2O_3$. Red lines denote the CW-ESR signal and blue lines denote the two pulse echo detected field sweep (EDFS) signal. While all transitions from g=12.2, 3.2, 4.8, and 1.6 are resolved in the CW-ESR spectrum, the EDFS scan showed a stronger signal from the high field(low g transitions). The two pulse echo spin coherence time measurements for different transitions (green dots) show an increase in spin T_2 for the high field transitions.

5.4 Discussion

Our results show milliseconds erbium spin coherence time is reliably achievable despite the presence of nuclear spins (e.g. yttrium) and paramagnetic impurities in the host matrix. To generalize, we obtain long spin coherence times by addressing low g-factor transitions and by freezing paramagnetic impurity spins at moderate fields and milliKelvin temperatures. The remaining decoherence is attributed to unpolarized spins and dipolar interactions in the weakly interacting Er spin ensembles, which can be further mitigated by a custom-designed dynamical decoupling sequence to simultaneously suppress spectral diffusion and dipolar interactions (see Appendix A.2). This set of methods is generally applicable to erbium or other Kramers ions in wide-ranging hosts with low site symmetries and anisotropic g tensors. According to [9], a plethora of crystalline hosts for Er in trigonal, tetragonal, monoclinic,

and orthorhombic crystal field symmetries exhibit a lowest g tensor component less than 2. A subset of them are also low noise hosts with nuclear spin magnetic moments comparable or less than yttrium, such as $CaWO_4$ (tetragonal), $SrWO_4$ (tetragonal), ZnS (tetragonal), MgO (tetragonal), Si (monoclinic), Y_2SiO_5 (monoclinic) [9] [93]. In these hosts, millisecond erbium spin coherence times are expected following our strategy.

Our work along with a similar report in $^{167}Er^{3+}$:$CaWO_4$ [146] shows low g paramagnetic impurities as the dominant source of spectral diffusion in moderately doped ($\mathcal{O}(10)$ ppm) hosts at milliKelvin temperatures. Reaching nuclear spin limited coherence times would require hosts with higher chemical purity and a very low concentration of paramagnetic dopants and defects on the $\approx$ ppb level [48]. In such highly dilute systems, the instantaneous diffusion limit is lifted, therefore spin coherence approaching the T_1 limit is expected after efficient dynamical decoupling of spectral diffusion noise. On the other hand, for applications based on rare-earth ensembles (($\mathcal{O}(10)$ ppm)), such as optical quantum memories and quantum transducers, either dipolar interactions or paramagnetic impurities are likely the coherence limiting factors, rather than nuclear spins. In those cases, hosts with weak nuclear spins (e.g. yttrium) can provide coherence times on par with nuclear spin-free hosts.

The polarized and reduced magnetic noise environment also indicates $^{167}Er^{3+}$ nuclear spin T_2 reaching a second is anticipated in Y_2O_3 at a similar field and temperature, which bodes well for high-fidelity long-term storage using nuclear spin registers [153]. With the known hyperfine interactions [141], the $^{167}Er^{3+}$ nuclear spins can be initialized into one hyperfine level by sequential hyperpolarization via the Er electron spin, or via optical pumping, [147]. This promising combination of long-lived electron-nuclear spins and strong hyperfine couplings will enable efficient quantum memories and multi-qubit quantum nodes that are capable of remote entanglement generation and storage at the telecom band.

CHAPTER 6

ERBIUM SPINS IN EPITAXIAL YTTRIUM OXIDE THIN FILMS INTERFACED WITH SUPERCONDUCTING RESONATORS

6.1 Introduction

This chapter discusses the spin dynamics of Er^{3+} in Y_2O_3 thin-films using high sensitivity ESR with superconducting resonators and near-quantum limited Joshepson parametric amplifiers. Thin films with thickness $\lessapprox 1.5\,\mu$m and 10-100 parts-per-million doping level present a significant challenge for ESR studies due to a small magnetic volume. Three-dimensional resonators with cryogenic HEMT amplifiers used in previous chapters have pulsed ESR sensitivity of $N_{spin} = 10^9$ spins, which is inadequate to address spins in thin films ($N_{spin} \approx 10^6$). Therefore, improvements in sensitivity by several orders of magnitude are required in order to study the spin dynamics in thin films. We accomplish this by employing low impedance superconducting resonators, which have an extremely small mode volume $V_m \approx 200\,\mu m^3$ and single spin coupling g= 100-1000 Hz as compared to three-dimensional resonators with g =0.05 Hz and mode volume $V_m \approx 1\,mm^3$. Therefore we gain at least by a factor of 2000 in g and overall a factor of $g^2 = 4 \times 10^6$ in cooperatively. This brings the expected minimum number of detectable spins N_{spin} down to 2500 for low impedance resonators with a single spin coupling strength g = 100 Hz with and an assumed quality factor of 3000.

We first demonstrate the coupling of Er^{3+} in Y_2O_3 thin-films to superconducting resonators by performing angle-dependent CW-ESR measurements. An anisotropic ESR signal is measured, which confirms a single crystal growth on a $40 \times 40\ \mu m^2$ area. We then perform high-sensitivity pulsed and demonstrate milliseconds spin coherence time and seconds spin lifetime on a wafer scale. We further, perform ESR on a high density Er^{3+} doped Y_2O_3 thin-film sample and discuss the path towards obtaining high cooperativity coupling

of the spin ensemble to superconducting resonators, a key requirement for high-efficiency microwave-to-optical transducers.

6.2 Epitaxial Er^{3+}:Y_2O_3 thin film grown on silicon

Er^{3+}-doped Y_2O_3 thin-films were grown epitaxially on silicon (111) direction using molecular beam epitaxy [167] technique owing to a small lattice mismatch between Y_2O_3 and Si (111) direction as described in ref. [167]. The Y_2O_3 samples used in ESR measurements in Section. 6.4 were taken from a slice from a 3 inch Y_2O_3 wafer with a thickness of 1.5 μm and $\approx$ 13 ppm Er^{3+} doping with 40 nm buffer layer at the top surface and silicon interface with no erbium doping. The samples in Section. 6.5 were taken from a Y_2O_3 wafer with a thickness of 700 nm with $\approx$ 200 ppm doping and 40 nm buffer layer at the top surface and silicon interface with no erbium doping. The ESR samples were annealed in air at 600 C for 1 hour to heal oxygen vacancies.

6.3 Low impedance superconducting microwave resonators

6.3.1 Resonator fabrication

The resonator was fabricated on a high-resistivity silicon substrate cleaned with toluene, acetone, methanol, and isopropanol. Superconducting niobium film was deposited using e-beam evaporation and patterning was done with either Reactive ion etching(RIE) or a liftoff process.

Reactive ion etching (RIE) process

The ion-etching method involved baking the Si substrate in a vacuum (<1e-7 mBar) at 300 C for 1 hour prior followed by an overnight vacuum pump. A 75 nm niobium layer was deposited with e-beam evaporation, followed by optical lithography on a positive photoresist

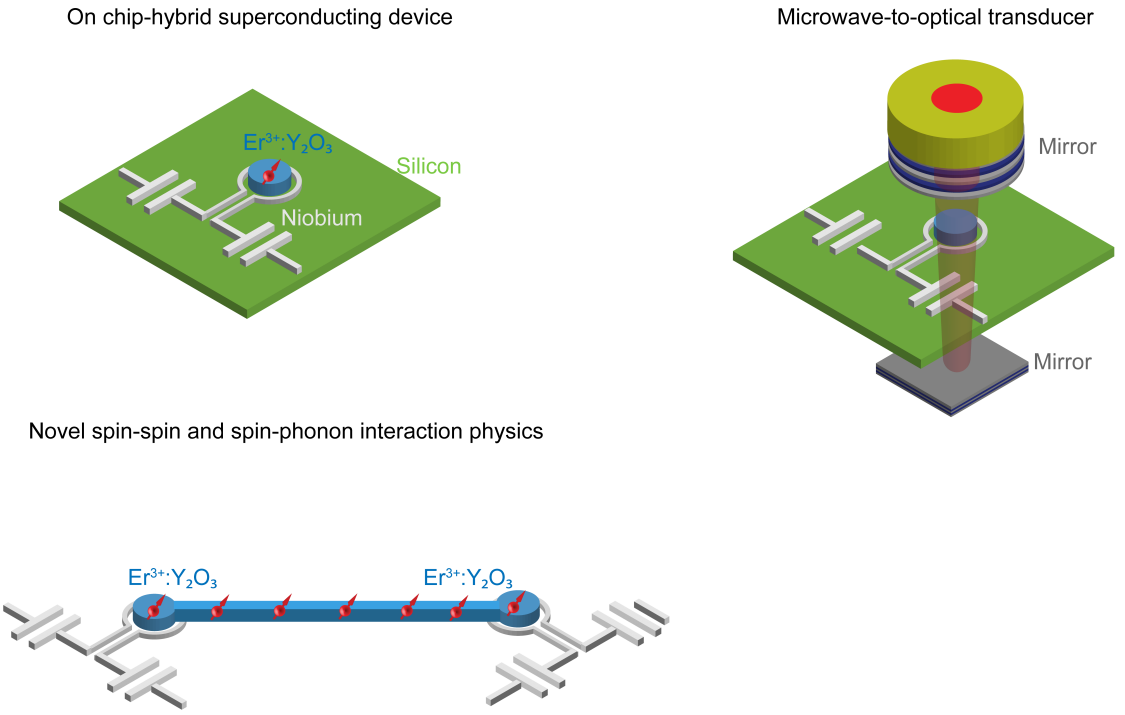


Figure 6.1: On-chip superconducting resonators can serve as a sensitive instrument to study small magnetic volume paramagnetic samples such as thin films as discussed in this chapter. Integrating lithographically defined paramagnetic thin cylinders will enable the development of microwave-to-optical transducers, as well as the study of novel physics of spatial spin-spin relaxation.

mask (Az 703 MIR) and reactive-ion etching (RIE) with CF_4, CHF_3 and Ar plasma. The etch time varied between 3 min 20 sec- 4 min 30 sec for etching a 75 nm niobium layer. The RIE method produced devices with intrinsic quality factors in the range of 10,000 - 300,000 and was followed for all the devices used in the measurement of the low Er^{3+} concentration thin-film sample.

Liftoff process

The liftoff process is an alternative method to pattern superconducting resonators and is advantageous for protecting the substrate layer from the ion plasma. The process involves priming the silicon substrate with an HMDS layer followed by patterning of a negative liftoff photoresist (Az nLof2020). The sample is then loaded in a chamber and 75 nm niobium

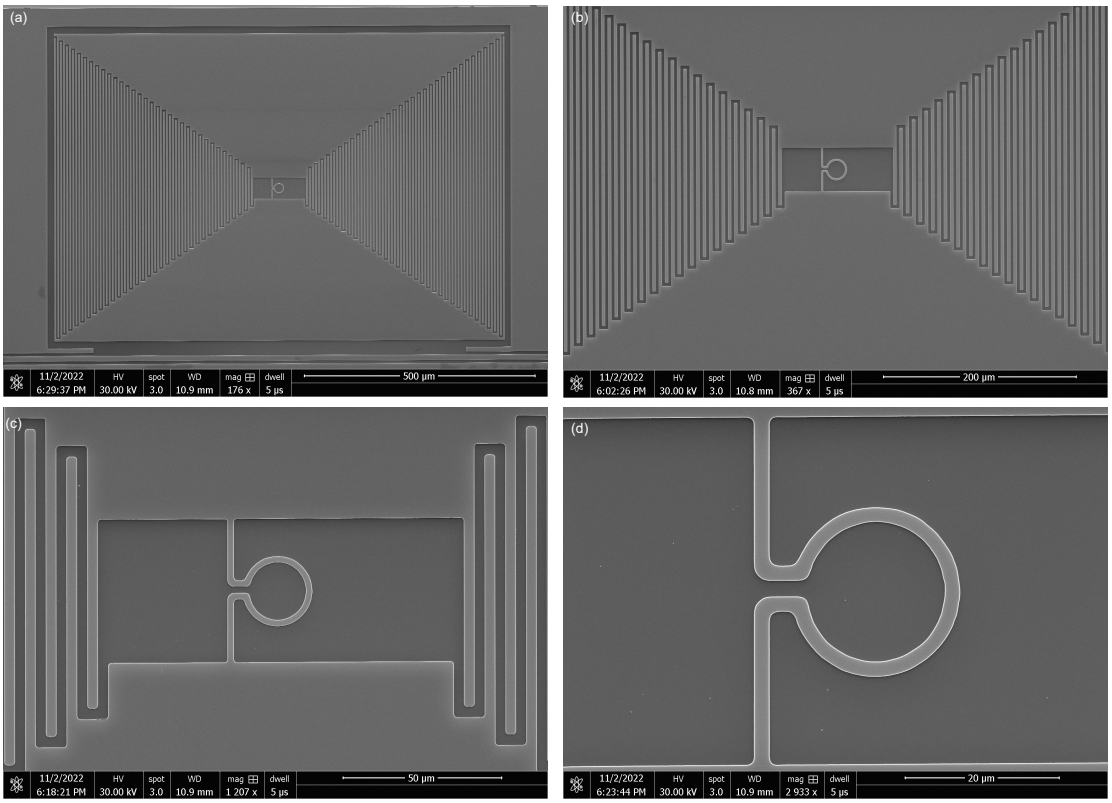
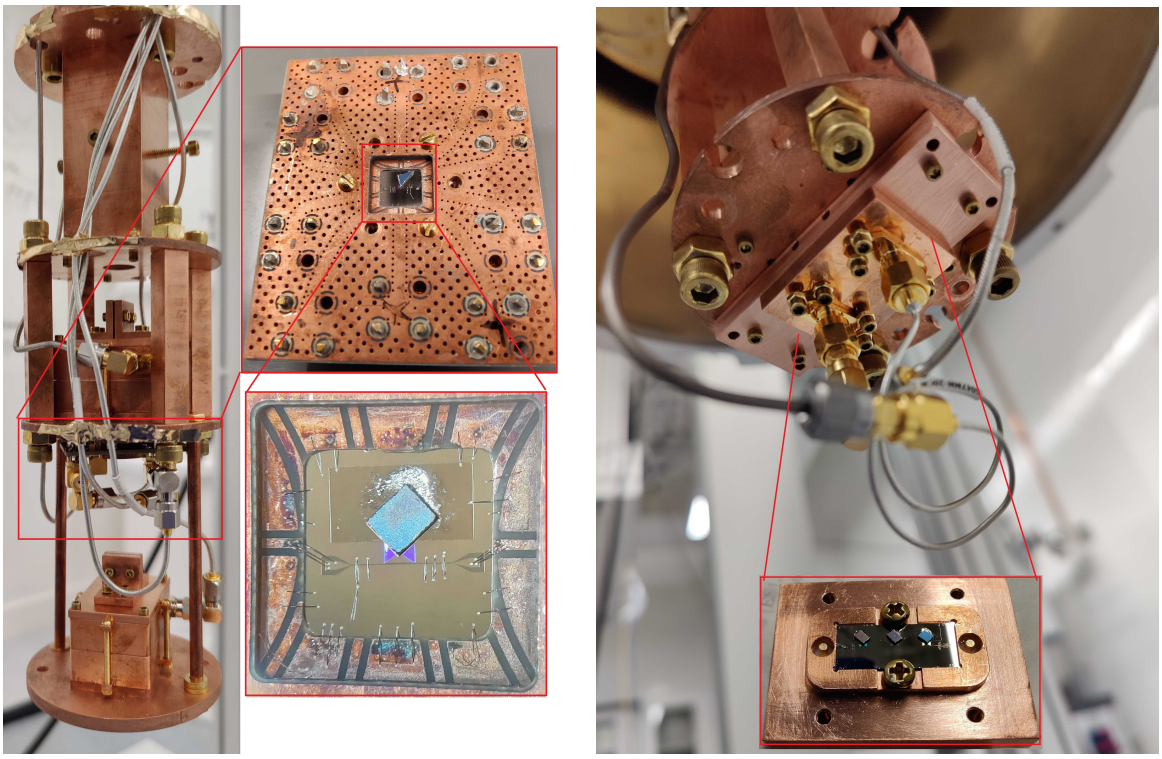


Figure 6.2: High-resolution images of the low impedance niobium superconducting resonator on silicon taken with scanning electron microscope (SEM) with increasing levels of magnification from (a)-(d) show the interdigitated finger capacitors in a triangular pattern surrounding the center omega loop inductor. The resonator is capacitively coupled to a superconducting transmission line.

was deposited. The final step involves overnight soaking in Az NMP rinse solution at 80 C for 10 hours and sonication with fresh NMP to remove the photoresist. The liftoff devices exhibited a quality factor in the range of 20,000 - 70,000 and were used in the measurement of the high-doping thin-film sample.

Table 6.1 lists the internal and external quality factor for all the test devices measured at 10 mK and an input power of $\approx$ -60 dbm. While the devices fabricated with the RIE process showed a higher internal quality factor, nearly all the devices showed a measured frequency of around 6 GHz, close to the design frequency. The external quality factor was measured to be tunable by changing the capacitive gap between the device and the transmission line



(a) (b)

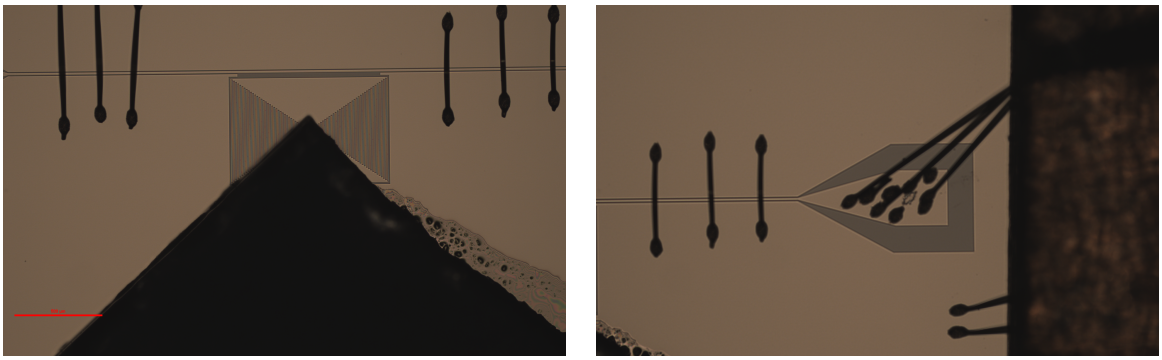
Figure 6.3: Cryogenic mounting of the superconducting resonator with Er^{3+} doped Y_2O_3 film sample flip-chip mounted (a) A copper PCB (top right) was used to mount the niobium superconducting resonator device (bottom right) consisting of a Er^{3+} doped Y_2O_3 film mounted on a niobium superconducting resonator. The PCB was mounted on a cold finger on the mixing chamber stage (left) (b) A copper holder was used to mount the superconducting device consisting of three niobium superconducting resonators (bottom), each mounted with Er^{3+} doped Y_2O_3 film samples taken from different positions along a slice of Y_2O_3 wafer. The copper holder was also mounted on the mixing chamber stage (top).

as shown in Table 6.1.

6.3.2 Resonator fabrication

Resonator and sample mounting

A 100 nm niobium spacer layer was further patterned on some of the resonator chips using the liftoff process (Az nLof2020 photoresist), in order to protect the resonator from damage during the mounting of the Er^{3+} doped thin-film samples. The thin-film samples were



(a) (b)

Figure 6.4: (a) Er^{3+} doped Y_2O_3 film sample flip-chip mounted on superconducting resonator using vacuum grease applied to the side of the resonator chip. Wire bond bridges are applied across the transmission line to obtain a common ground throughout the chip (b) Wire bonding of the resonator chip to the copper PCB. 3-4 wire bonds are made between the transmission line pads and the coaxial line on the copper PCB. Additional wire bonds are added between the ground plane of the resonator chip and the chassis ground of the copper PCB.

mounted with the Er^{3+} doped side facing the superconducting film on the spacer and held in place with vacuum grease (Apiezon N). The triangular end of the sample was localized over the inductor wire, in order to avoid dielectric losses from a strong electric field above the IDF capacitor.

The resonator was then mounted on a copper PCB (Fig. 6.3a) or on a cooper holder (Fig. 6.3b). Wire bonds were placed between the transmission line pads and the sma connectors on the copper holder/PCB. Additional wire bonds were placed between the ground plane of the chip and the copper holder/PCB chassis, in order to connect the chip to a common ground.

6.3.3 Simulated coupling of microwave resonator

Resonator simulations

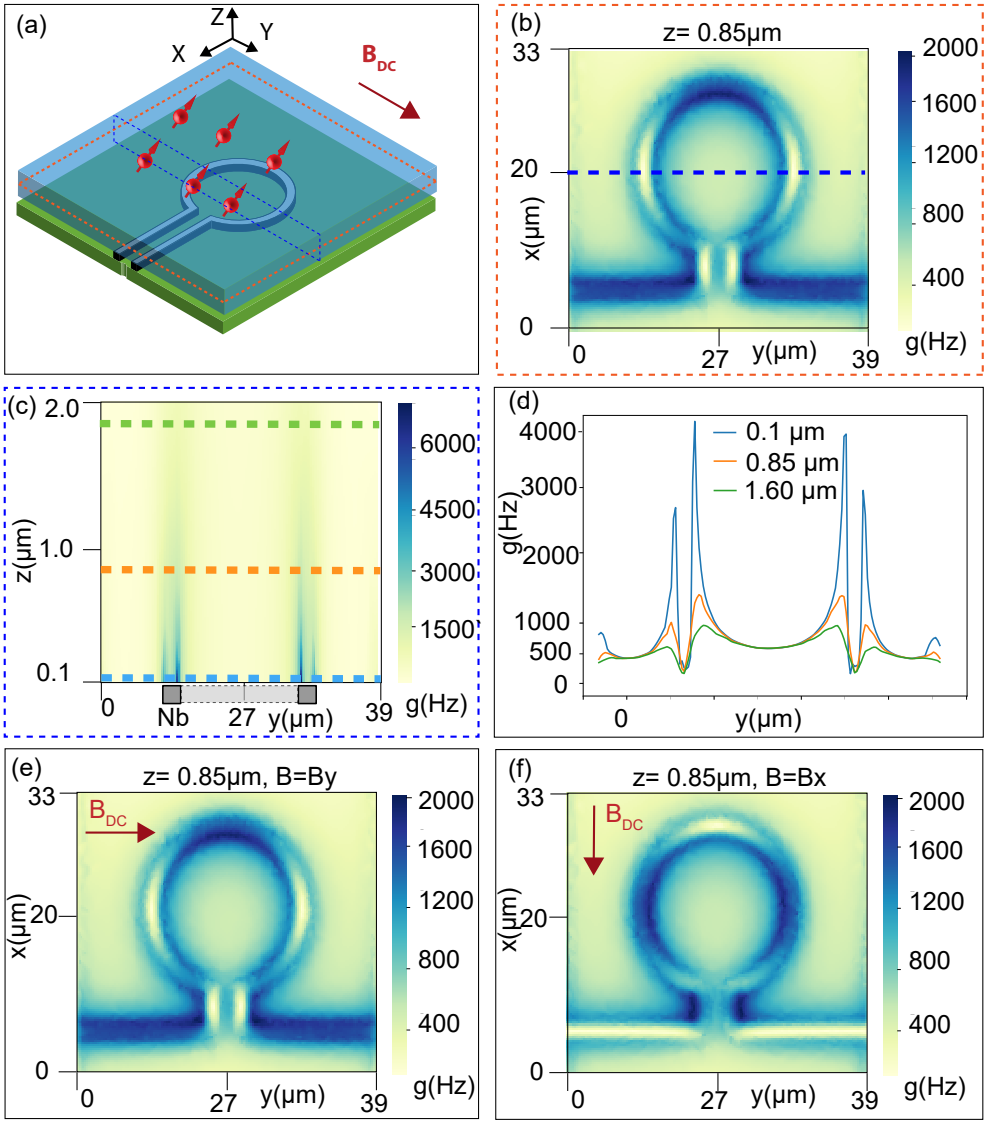
The spatial and spectral mode profile of the low-impedance resonators used in ESR measure-

Substrate	Method	Capacitive gap	ω	Q_i	Q_e
Si	RIE	30 μm	6.368 GHz	1403476	52802
Si	RIE	15 μm	6.459 GHz	420373	2242
Si	Liftoff	15 μm	6.0490 GHz	69800	4938
Y_2O_3/Si	RIE	30 μm	6.0260 GHz	2100	28000

Table 6.1: Summary of measured Niobium devices on Silicon at ≈ -60 dBm power at 10 milliKelvin. All fit uncertainties are <5 %.

ments were simulated numerically with ANSYS®HFSS [13]. Fig. 6.5 shows the simulated single spin coupling g (Hz) in the plane above the resonator for spins with transverse g factor $g_{AC} = 7$ and magnetic field applied along the Y direction. Fig. 6.5(b) shows the spatial profile of g at a distance z of 0.85 μm above the resonator with strong fringing fields along the omega inductor leading to increased single spin coupling. Fig. 6.5(c) and (d) show a cross-section and a line cut respectively taken in the plane x= 20 μm. While the single spin coupling shows a decrease from the peak value of 4 kHz at z=100 nm to ≈ 800 Hz at z=1.6 μm, there is greater a spatial uniformity of g at z=1.6 μm, which could be advantageous in uniform driving of the spin ensemble.

We observe a direction dependence of the spin coupling profile over the inductor as the DC magnetic field is swept in the XY plane. While the Z component of the resonator AC magnetic field is always perpendicular to the applied DC B field in the XY plane, as the DC field is swept along the XY plane, the segments of the inductor wire, which are parallel to the DC B field additionally couple to the spins through the XY component of the resonator AC magnetic field. This leads to a variation in the spatial profile of single spin coupling strength (g) as well as total ensemble coupling $g_{ens} = \sqrt{\sum_i g_i^2}$. Fig. 6.5(e) shows when the DC B field is applied along the Y direction, the horizontal sections of the inductor loop, as well as the straight segment of the wire on the base of the inductor loop, show stronger coupling strength g (dark blue regions). As the B field direction is changed to X (Fig. 6.5(f)), the vertical components of the inductor wire now have a stronger spin coupling g. We observe



.

Figure 6.5: Simulated single spin coupling above the resonator for spins with $g_{AC} = 7$ a) Device schematic with the sample mounted on the resonator in a flip-chip configuration b) Coupling in the plane z=0.83 μm above the resonator c) Coupling along a cross-section taken in the plane x=20 μm d) Three line cuts from (c) show a decrease in amplitude and an increase in spatial homogeneity of g over the inductor loop with distance z.

a slightly higher average spin coupling g_{avg} of 843 Hz when the B field is applied along y (Fig. 6.5(e)) as compared to 795 Hz when the B field is applied along X (Fig. 6.5(f)) due to an additional contribution from the long horizontal straight section of the inductor wire. The average spin coupling strength $g_{avg} = g_{ens}/\sqrt{N}$ was calculated by averaging g over z=

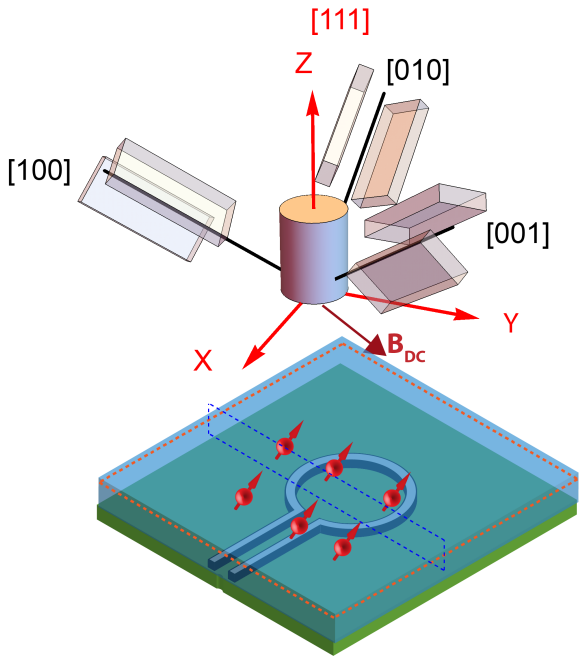


Figure 6.6: Resonator geometry and magnetic field scan angle compared to orientations of the C_2 (cuboid) and C_{3i} (cylinder) sub-sites of Er^{3+} in Y_2O_3.

0.1 to 2 μm and the cross-sectional area x= 0 to 30 μm, y= 0 to 39 μm.

6.3.4 ESR measurement setup and resonator characterization

Cryogenic measurement setup

Microwave resonators were mounted on a copper PCB/sample holder and mounted on a cold finger on the 10 milliKelvin stage of a Bluefors LD-250 dilution refrigerator. Table. 6.2 shows the simulated and measured frequency and quality factors for the resonators used in the ESR measurements. All measurements were performed at 8 mK and an on-chip power of $\approx$ -80 dBm and had a design capacitive gap of 15 μm, which was chosen to obtain an external quality factor $Q_e \approx 1500 - 3000$ based on the measurements on the silicon test device. Device 1 in the table corresponds to the device used in single device ESR measurement in

Fig. 6.12 and Fig. 6.14 in and devices 2,3,4 were used in the wafer-scale ESR measurements in Fig. 6.21. The simulated and measured frequencies show an offset of ≈ 300 MHz, which could be accounted for by the unknown dielectric constant of the Y_2O_3 thin films, however, the relative spacing of individual resonator frequencies is consistent between the two.

A 3-axis vector magnet (AMI Model 430) was used to apply a magnetic field in-plane of the resonator. The field was aligned by maximizing the cavity frequency ω with small steps of the B field, and the field was iteratively ramped along the in-plane direction. The alignment procedure produced a ratio of Bxy to Bz required to align the field in-plane of the resonator for each in-plane angle θ [214]. The alignment was performed at 4 Kelvin in order to allow for thermal cycling above 9 Kelvin to cancel the magnetic vortex.

Continuous-wave (CW) ESR

CW ESR was performed by measuring the resonator transmission spectrum S_{21} as a function of an in-plane magnetic(B) field with a vector network analyzer (Keysight E5071B). The estimated on-chip power was ≈ -80 dBm and the magnetic field was ramped in steps of 0.1 mT. The resonator spectrum was fitted to the model for LC superconducting resonators coupled to a transmission line from ref [52](eqn. 6.1) to obtain the center frequency ω_0 and Quality factors Q_i, Q_e and Q_α,

$$S_{21} = \frac{1 + 2jQ_i(\frac{\omega-\omega_0}{\omega_0})}{1 + \frac{Q_i}{Q_e} + j\frac{Q_i}{Q_\alpha} + 2jQ_i(\frac{\omega-\omega_0}{\omega_0})} \tag{6.1}$$

where ω_0 is the cavity frequency, Q_i is the intrinsic quality factor, Q_e is the external quality factor, and Q_α is introduced to account for the asymmetry of the transmission spectrum [52]. The fitted intrinsic linewidth k_i and frequency ω from the fit were plotted against the B field and the background trend was subtracted to obtain the spectrum in Fig. 6.12 and Fig. 6.14.

Device	ω (simulated)	ω (measured)	Q_i	Q_e
1	5.55 GHz	5.81 GHz	370043	3001
2	5.55 GHz	5.88 GHz	11776	1484
3	5.31 GHz	5.58 GHz	13650	2666
4	5.23 GHz	5.52 GHz	11054	1620

Table 6.2: Simulated and measured frequency and quality factor of microwave resonators using in Section. 6.4.

Pulsed ESR

The setup used in the pulsed spin echo measurements is shown in Fig. 6.7. An arbitrary waveform generator (Zurich Instrument HDAWG) was used to generate 200 ns long I and Q pulses at 200 MHz frequency and upconverted to 5.7 GHz using an IQ mixer (MX1: Marki MMIQ 0218LXPC) with the estimated on-chip π pulse power about -65 dBm (300 pW) at the sample after room temperature amplification (G1:Mini-Circuits ZX60-83-LNS+) and 45 dB cryogenic attenuation. A pulsed pump generated using IQ upconversion (S2: Signal Core SC5511A and Marki MMIQ 0307LXP) was sent to the TWPA during spin echo acquisition time to turn on the gain of the TWPA. The TWPA pump frequency and power were tuned to obtain a maximum signal-to-noise (SNR) gain of 10 dB while avoiding spurious pump tones interfering with the spin echo frequency. The spin echo signal was amplified by TWPA (+15 dB) at the 8 mK stage, followed by HEMT (Low noise factory $\mathrm{LNF-LNC4_8F}$ +44 dB) at the 4K stages. Dual Junction cryogenic isolators (I1: Low noise factory $\mathrm{LNF-CICIC4_8A}$) were placed in between the resonator and TWPA and the TPWA and HEMT to prevent signal reflection and thermal noise leakage to the 8 mK stage. A diode limiter (PIN1: Pasternack PE8023) and an isolator (I2: Fairview Microwave SFC0206S) isolator were added to protect the room temperature readout electronics during pulses. Bandpass filters with 4.9-6 GHz passband (BP1: Mini-Circuits VBFZ-5500-S+) were placed in the pulse generation and readout chain to avoid amplifier saturation. The spin echo was further amplified with room temperature amplifier (G1:ZX60-83-LNS+,+21 dB)

followed by demodulation (Marki MMIQ0218LXPC mixer) to obtain I′, Q′ signals at 200 MHz. The local oscillator (LO) signal to the demodulation mixer was supplied by the same source used for pulse generation (S1:Keysight N5181A) after amplification (Mini-Circuits ZVA-183-S+, +26 dB) and splitting (SP1: Mini-Circuits ZX10-2-71-S+). The demodulated spin echo was further amplified by a low noise amplifier (G2: Mini-Circuits ZX-60-P103LN+, +23 dB), and band-pass filtered (BP2: Mini-Circuits ZX75BP-204-S+) to obtain I′, Q′ traces on a fast oscilloscope (OSC1:Tektronix TDS5104). We note that the I′, Q′ signals obtained after demodulation have a phase offset with respect to the input I and Q signal used in pulses. Nevertheless, we measure only the amplitude of the spin echo signal and therefore we ignore the phase offset.

The time domain spin echo signal I′(t) (Fig. 6.8(a)) was Fourier-transformed over an integration window of 1500 ns. Fast Fourier transform (FFT) spectrum of the signal I′(ω) in Fig. 6.8(b) shows a spin echo peak at 200 MHz sitting on a noise background pedestal (blue dashes). An integrated over bins in a bandwidth of 20 MHz around 200 MHz was performed in the FFT spectrum and the area under the background noise pedestal (blue dashes) was subtracted to obtain the spin echo area (between the blue dash and red line). The background noise pedestal (Fig. 6.8(b) blue dashes) was estimated by summing the integral over two adjacent 10 MHz bandwidth bins (green dashes) around the signal integration window. Finally, the background subtracted spin echo signal for each channel I′ and Q′ was added in quadrature to obtain the total spin echo area.

6.3.5 Near quantum-limited ESR with TWPA

TWPA optimization

Continuous wave optimization

Continuous wave (CW) optimization was carried out by measuring the device spectrum with a vector network analyzer and the pump was supplied by an external source. Fig. 6.9(a)

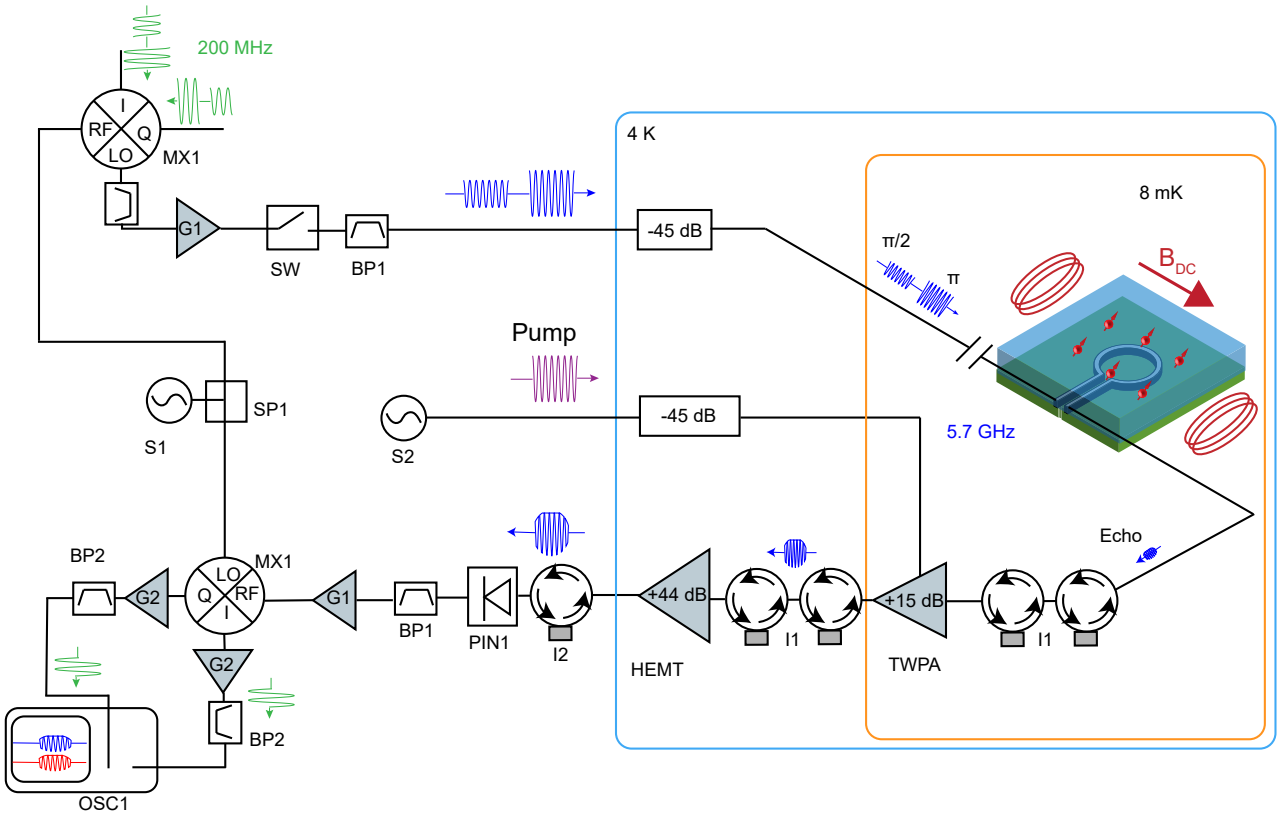


Figure 6.7: Pulsed ESR setup used for studying two-dimensional resonators coupled with Er^{3+} doped thin-films. Electronics depicted here include room-temperature electronics and instruments as well as cryogenic amplifiers and isolators.

shows the TWPA gain (dB) in 3.5 - 7.7 GHz as a function of pump power for on-chip signal power ≈ -105 dBm. The pump was supplied using a spectrum analyzer operating as a microwave source in zero-span mode at a pump frequency of 6.026 GHz. The pump power in Fig. 6.9(a) represents the power at the source with the total attenuation in the pump line of 52 dBm (5 (cable) + 32 (attenuator) + 20 (directional coupler)). The TWPA gain profile showed an increase in gain with pump power followed by a sharp decrease. The ripples in the gain profile are expected to be due to flux trapping and could be removed by improved mu-metal shielding around the TWPA. Red dashes in Fig. 6.9(a) show the optimum pump power of -7.5 dBm at the microwave source. The pump frequency was optimized by fixing the pump power to -7.5 dBm and scanning the pump frequency in 6.2 - 6.325 GHz. Fig. 6.9(b)

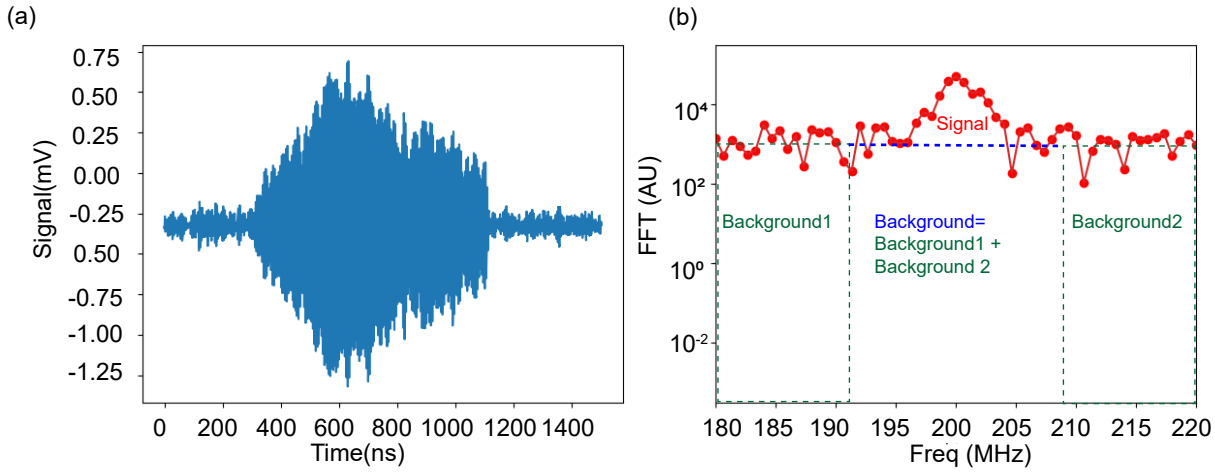


Figure 6.8: Processing of the spin echo signal (a) Time domain spin echo signal (I′ quadrature) (b) Fast Fourier transform (FFT) of the signal over 1500 ns window. The signal is integrated over a 20 MHz window and the noise background (blue) is estimated by integrating the FFT in two 10 MHz windows to the left and right of the signal integration area (green). The total noise background(blue dash) can be estimated as a sum of the area in green dashes (background 1 and background 2) and is subtracted from the signal to get the background-subtracted signal for each I′ and Q′ quadrature.

shows the gain profile as a function of pump frequency. The profile shows ripples in gain and the optimum pump frequency for maximum gain in 5-6 GHz range was found to be 6.258 GHz (blue dashes). To study the saturation response, the average gain was measured in 5-6.1 GHz for varying signal power. Fig. 6.9(c) shows the TWPA response with a maximum gain of 22 dB with saturation effects for signal powers beyond -100 dBm. To quantify the increase in signal-to-noise ratio (SNR), we supplied a continuous wave signal at 6.026 GHz frequency and measured the spectrum with pump off (Fig. 6.9(d), orange line) and pump on (Fig. 6.9(d), blue line). A gain of 22 dB (red arrow) is consistent with previous measurements and the increase in noise level by 12 dB (green arrows) suggests the device noise is limited by the TWPA noise floor. The optimum settings of pump power and frequency, therefore, correspond to a total 10 dB gain in SNR.

Pulsed optimization

To perform a finer optimization of the electronics used in generating TWPA pulses, we used

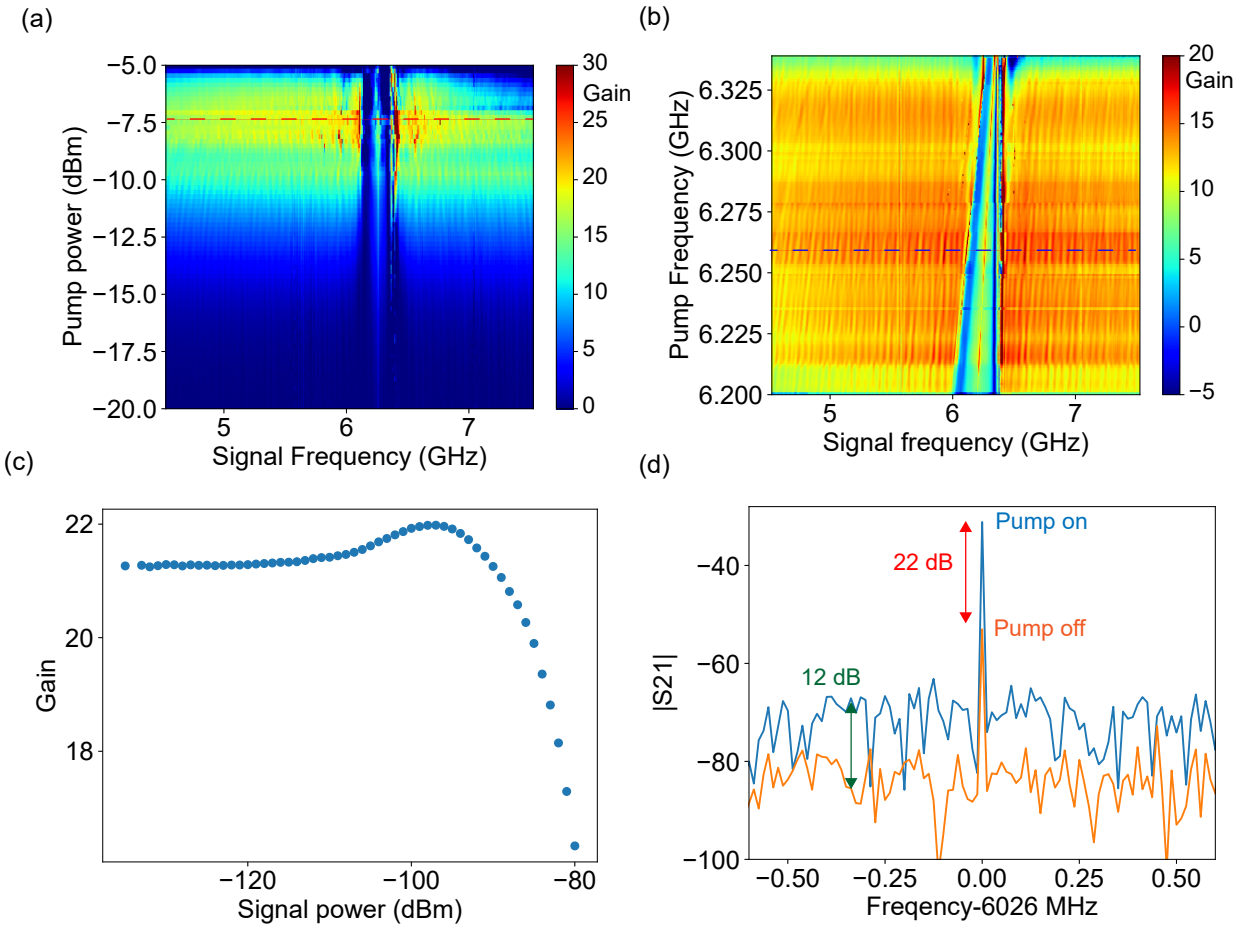


Figure 6.9: Continuous-wave optimization of the pump power and frequency of the traveling wave parametric amplified (TWPA) (a) Scan of pump power at a fixed frequency of 6.026 GHz (b) Scan of the pump frequency at a fixed power of -7.5 dBm (c) Gain of the TWPA as a function of input signal power (d) Gain of 22 dB in signal and 12 dB in noise floor is observed when TPWA is turned on, leading to a total SNR gain of 10 dB.

the CPMG spin echo signal from C_2 g=3.6 transition at 113 mT, 40 degrees in Fig. 6.12. Fig. 6.10(a) shows the train of spin echo under the CPMG pulse sequence with TWPA pump off (red) and pump on (blue). The spin echo signal shows an increase in amplitude with the TWPA pump turned on. To further quantify the increase in signal-to-noise ratio, we integrated each spin echo in Fig. 6.10(a) red, to get the noise background and spin echo signal with TWPA off. We followed the method described in the previous section to calculate the spin echo signal and the noise background. After obtaining the spin echo signal

and noise background with TWPA off, we swept the pump power by sweeping the voltage ($\sqrt{\text{Pumppower}}$) to the IQ mixer used to generate pump pulses and normalize the resulting spin echo signal and noise. Fig. 6.10(b) shows the increase in noise level (dB) as a function of pump power and time (time of each spin echo signal in Fig. 6.10(a)). Fig. 6.10(c) and Fig. 6.10(d) show gain in spin echo signal (dB) and the total SNR (Gain-Noise) respectively. The noise and gain in Fig. 6.10(b)-(d) are normalized with respect to the case when TWPA is off. We observe an increase in spin echo signal gain with increasing pump power in Fig. 6.10(c) and the maximum gain point corresponds to $\sqrt{\text{Pumppower}}$=0.36. Fig. 6.10(b) shows a sharp increase in noise level for higher pump power, which results in an overall decrease in SNR of the spin echo signal in Fig. 6.10(d). Therefore the optimum TWPA operating pump power for maximum SNR corresponds to TWPA gain of $\approx$ 12-15 dB and increasing the pump power beyond the optimum point results in a disproportionate increase in noise level.

6.4 Er^{3+} spins in Y_2O_3 thin films with milliseconds coherence time

The sample used in this section was grown with MBE on silicon (111) and had an expected doping of $\approx$ 13 ppm, in order to minimize spin-spin interaction.

6.4.1 Coupling Er^{3+} spins to superconducting resonators

Field alignment

The magnetic field was aligned to the plane of the superconducting resonator for each in-plane angle θ by finding an optimum ratio of B_{XY} and B_Z for each θ. The optimum ratio of the XY and Z fields is found by maximizing the resonator frequency by tuning the Z field and the field is then ramped iteratively in the optimum direction [214]. The alignment procedure was performed at 4 Kelvin in order to allow for quick thermal cycling above 9 Kelvin to cancel the magnetic vortex. Figure 6.11a and 6.11b show the dependence of the

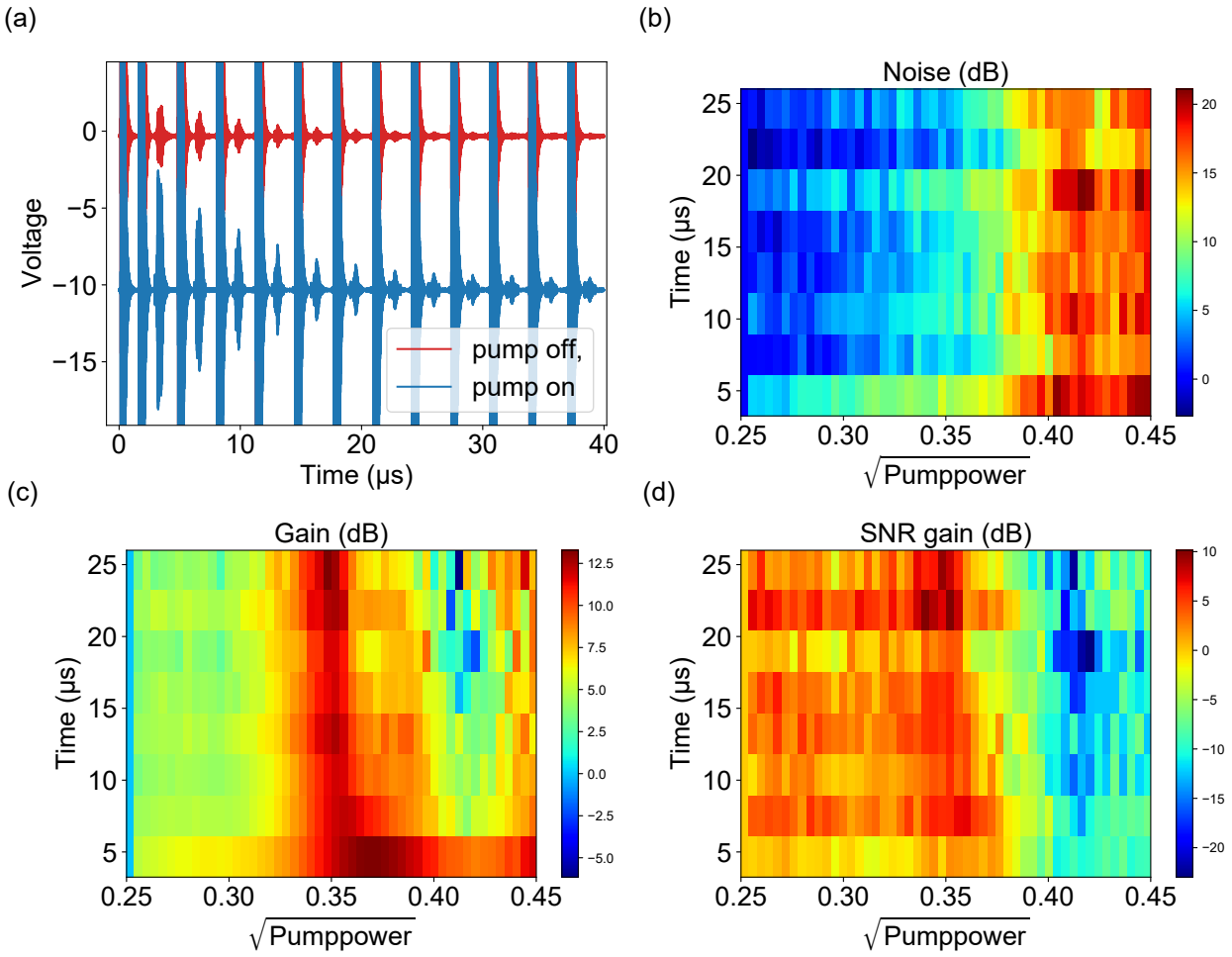


Figure 6.10: Pulsed optimization of the pump power of the traveling wave parametric amplified (TWPA) using CPMG spin echo sequence (a) CPMG signal from C_2 g=3.6 transition with pump off(red) and pump on (blue) (b) Increase in the noise background of the spin echoes with pump power (c) Gain of spin echo area as a function of pump power (d) Total in gain in signal to noise ratio of spin echo. Data in (b)-(d) is normalized with respect to the signal and noise with TWPA off.

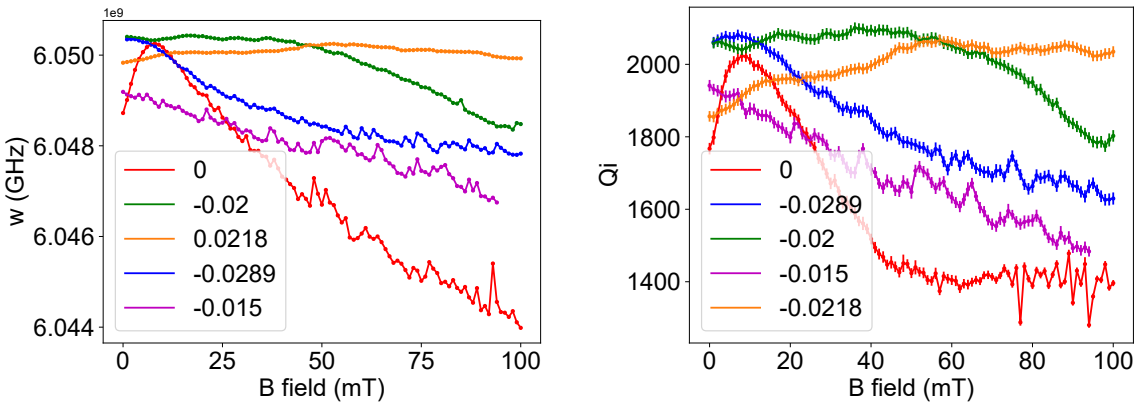
resonator frequency and intrinsic quality factor on the magnetic field for the different ratios of Bz over Bxy. The optimum ratio can be obtained by maximizing the resonator frequency and/or quality factor with the magnetic field. The resonator frequency and quality factor in Figure 6.11a and 6.11b exhibit significant reduction noise due to magnetic flux for the field sweeps with aligned field (orange curve). The alignment procedure can be summarized as follows

- Choose an in-plane angle of magnetic field (θ) in the magnet XY plane
- Ramp XY magnetic field starting with 5 mT and apply Z magnetic field to maximize the resonator frequency
- Ramp magnetic field in the new in-plane direction corresponding to the ratio of Bz and Bxy obtain in the last step
- Further fine-tune Bz and repeat the process iteratively increasing the step size until the maximum target field Bmax
- Thermal cycle and fine-tune the ratio by ramping field from 0 to Bmax around the optimum ratio, with thermal cycle after each sweep
- Compare the fitted resonator frequency and quality factor vs B field plot for different ratios (see Fig. 6.11a and 6.11b) to obtain the optimum ratio
- Repeat the process by changing θ in XY plane

At the end of the alignment process, we obtain a table of ratio vs θ, which corresponds to the optimum direction of field sweeps for each in-plane angle θ. Following the alignment procedure, CW-ESR angle scans are performed at 8 milliKelvin base temperatures. The optimum ratio minimizes the noise due to flux tuning in the superconducting resonator and therefore maximizes the sensitivity of the CW-ESR measurement to detect small changes in resonator frequency and quality factor due to coupling to Er^{3+} electron spins.

Absorptive and dispersive ESR coupling

Absorptive and dispersive coupling results in linewidth broadening and frequency shift of the resonator following the expressions [58], $\kappa = \kappa_0 + \Omega^2\gamma_s/(\gamma_s^2 + \Delta^2)$, and $\omega = \omega_0 - \Omega^2\Delta/(\gamma_s^2+\Delta^2)$, where κ_0 is the uncoupled resonator linewidth, ω_0 is the uncoupled resonator frequency, Ω is the spin ensemble coupling strength, γ_s is the spin inhomogeneous half-width and $\Delta = g\mu_B(B - B_0)/\hbar$.



(a) (b)

Figure 6.11: (a) Resonator frequency (ω) with magnetic field for different ratios of B_z and B_{xy}. The optimum ratio (orange) corresponds to the weakest dependence of resonator frequency on the magnetic field (b) Resonator intrinsic quality factor (Q_i) with magnetic field for different ratios of Bz and Bxy. The optimum ratio (orange) corresponds to the minimum degradation of the internal quality factor with the magnetic field.

We observe the dispersive, as well as absorptive coupling of Er^{3+}, spins to superconducting resonator as the magnetic field (B) is scanned at in plane the plane of the resonator at an angle θ (Fig. 6.12, Fig. 6.14). Yellow dots show the center of the measured transition for both Fig. 6.12 and Fig. 6.14.

The white dashes in Fig. 6.12 and Fig. 6.14 show predicted transitions based on the g tensor of Er^{3+} in Y_2O_3 [141] for an applied magnetic field at an in-plane angle θ. To take into account a relative tilt between the (111) plane of the thin film and the XY plane of the resonator, we used an analytical expression for the tilt angle $\delta\phi_{\text{offs}}$ varying between $\phi_{\text{offs1}} = 2.8^\circ$ and $\delta\phi_{\text{offs2}} = 0.2^\circ$ as a function of θ following the analytical expression,

$$\begin{aligned}\delta\phi_{\text{offs}}(\theta) = \tan^{-1}(&\tan(\delta\phi_{\text{offs1}})\cos(\theta+\theta_0) \\ &+\tan(\delta\phi_{\text{offs2}})\sin(\theta+\theta_0))\end{aligned} \tag{6.2}$$

where $\theta_0 = 30$ degrees was an in-plane angle offset between the X axis of the magnet and

direction [2,1,-1] in the plane of the Y_2O_3 thin film. The above expression for a variable tilt angle ϕ_{offs} was taken into account in simulations to generate the predicted transitions (white dashes) from C_2 and C_{3i} sites as a function of angle for Fig. 6.12 and Fig. 6.14

Fig. 6.12 shows the dispersive resonator frequency shifts as a function of field (B) for different angles (θ). The resonator frequency after field alignment shows a quadratic decrease in resonator frequency (ω) as a function of the B field due to an increase in kinetic inductance ($\omega = \omega_0 - cB^2$) [59]. The quadratic dependence field on the resonator frequency shifts is subtracted to obtain the frequency shifts $\Delta\omega$ plotted in Fig. 6.12 (see Fig. 6.13 for a line cut). We observe dispersive frequency shifts for both high and low-field transitions as shown by the regions with a change in color from red(light blue) to blue(dark blue).

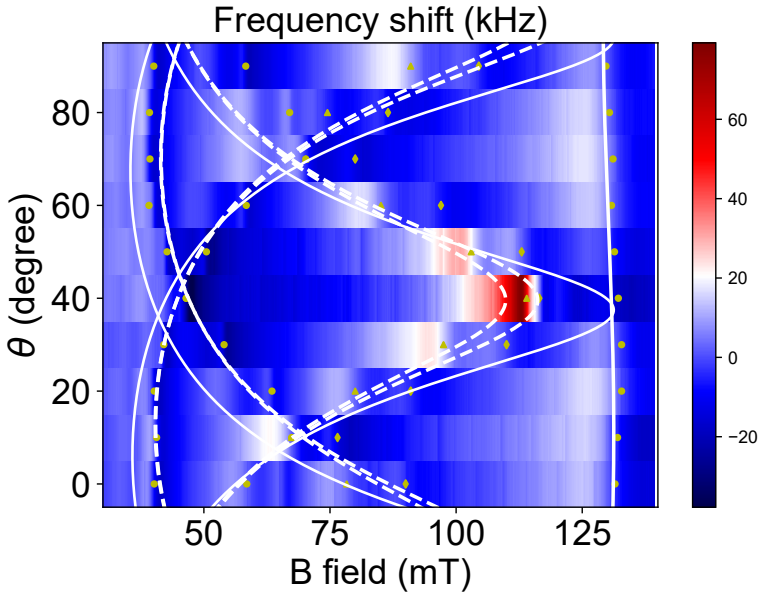


Figure 6.12: Dispersive coupling of Er^{3+} spin in Y_2O_3 to superconducting resonators. Cavity frequency shows dispersive shifts ($\Delta\omega$) when on-resonant with spins resulting in a characteristic increase of cavity frequency followed by a decrease as the magnetic field is swept. A strong dispersive signal can be clearly resolved for high field transitions with lighter shades of blue(red) representing lower(higher) cavity frequency around zero. White dotted line show predicted transitions based on simulations and yellow dots show the center of the measured transition.

Fig. 6.14 shows the increase in resonator linewidth due to absorptive coupling to spins.

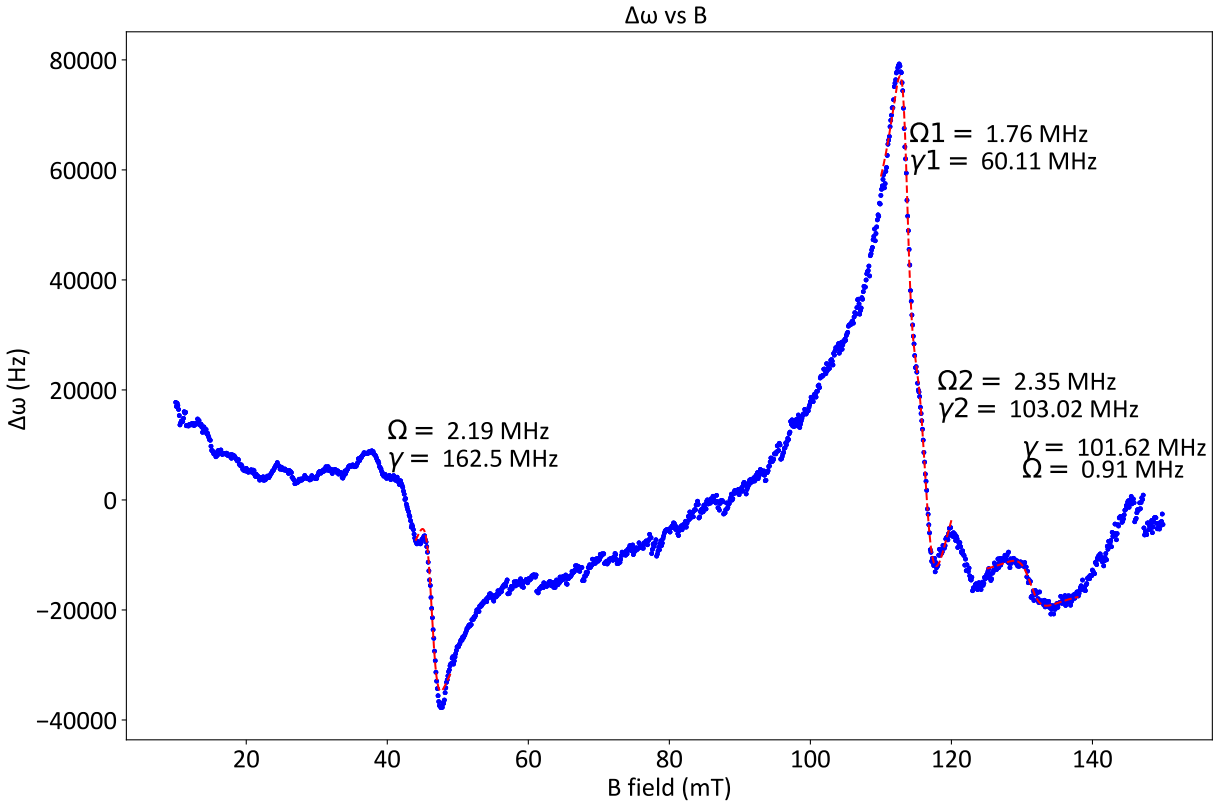


Figure 6.13: Dispersive coupling signal for $\theta = 40^\circ$ showing transitions from C_2 site at 46 mT, 113 mT, 116 mT and a transition from C_{3i} site at 135 mT. Dashed red lines show the fit to the expression $\Delta\omega = \omega_0 - \Omega^2\Delta/(\gamma_s^2 + \Delta^2)$ used to extract the ensemble coupling strength and inhomogeneous linewidth. The narrowest inhomogeneous linewidth for C_2 site was measured to be 60.1 MHz for the transition at 113 mT.

The intrinsic quality factor (Q_i) was obtained by fitting the model in eqn. 6.1 to the resonator spectrum for each B field. The intrinsic linewidth $k_i = \omega/Q_i$ was subtracted with the average intrinsic linewidth $k_{i,avg}$ for each scan θ to obtain the linewidth broadening $\Delta k_i = k_i - k_{i,avg}$ plotted in Fig. 6.14. The strongest high field transition for C_2 g=3.4 at 113-117 mT ($\theta = 40$ degree) as well as low field transitions are clearly resolved in both absorptive and dispersive signals. However, an increase in k_i for a high B field leads to a background to the broadening signal and some of the high field transitions could not be clearly resolved in the absorptive broadening signal. The narrowest inhomogeneous linewidth with absorptive ESR coupling was measured for this sample in another round of measurement. Fig. 6.15 shows the absorptive ESR signal (Linewidth vs magnetic field) for two low-field transitions from Er^{3+} in C_2

site. The linewidth broadening signal was fitted to a Lorentzian inhomogeneous linewidth model ($\kappa = \kappa_0 + \Omega^2\gamma/(\gamma^2 + \Delta^2)$) to obtain the narrowest inhomogeneous linewidth of 67.5 MHz.

Estimated erbium concentration

We use the dispersive coupling signal from Fig. 6.12 to estimate erbium concentration. The maximum ensemble coupling g_{ens} = 1.76(0.029) MHz for the transition from C_2 subsites at B= 113 mT, θ = 40 degrees (see Fig. 6.13 for the fit) corresponds to a number of spin N > 595.0(0.01) $\times 10^6$ spins assuming g < 74.5 Hz (g < 128 Hz for C_{3i} transition with $g_{AC} = 12$, therefore for C_2 transition with $g_{AC} = 7$ we get g < 128 (7/12) Hz). Dividing by the sample volume of 1256 μm^2 × 1.4 μm we get a density n_{Er,C_2} of 3.38×10^{17} spins/cm^3 or 12.7 ppm ($n_Y = 2.66 \times 10^{22}$spins/cm^3) for Er^{3+} in C_2 site. Multiplying by a factor of 6 (six C_2 site orientations) we get a total density of 76.1 ppm for all Er^{3+} in C_2 sites. Similarly the maximum g_{ens} of 3.07 (0.02) MHz for the transition from C_{3i} subsite at B= 130 mT, θ = 10 degree with with $g_{AC} = 12$ and single spin coupling g < 128 Hz, corresponds to N > 574.7 $\times 10^6$ spins. Dividing by the sample volume of 1256 μm^2 × 1.4 μm we get density $n_{Er,C_{3i}}$ of > 3.29 $\times 10^{17}$ spins/cm^3 or 12.4 ppm for Er^{3+} in C_{3i} site.

Angle dependence of spin inhomogeneous linewidth

The angle dependence of the spin inhomogeneous linewidth of spins with an anisotropic g factor can be described by a perturbation of the g factor by an amount δg due to distortion of the local crystalline environment due to static strain. The square of g factor g^2 and gδg follow a similar expression in this case [192][108],

$$g^2 = a\cos^2\theta + 2b\cos\theta\sin\theta + c\sin^2\theta \tag{6.3}$$

and

$$g\delta g = a'\cos^2\theta + 2b'\cos\theta\sin\theta + c'\sin^2\theta \tag{6.4}$$

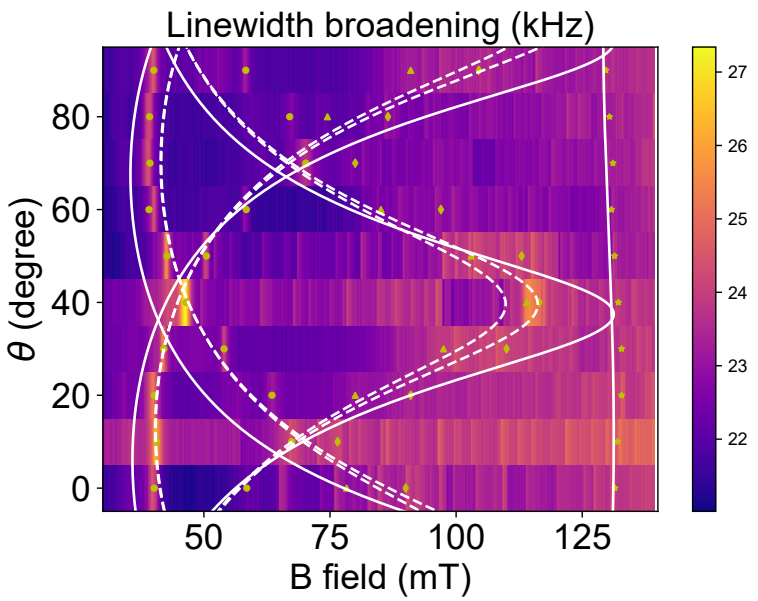


Figure 6.14: Absorptive coupling of Er^{3+} spin in Y_2O_3 to superconducting resonators. Absorptive coupling results in a broadening of resonator intrinsic linewidth (Δk_i) when on resonant with spins. Low-field transitions show up with greater contrast in the absorptive scan. White dotted line show predicted transitions based on simulations and yellow dots show the center of the measured transition.

where a,b,c and a′, b′, c′ are coefficients depending on the g tensor and the plane of the angle scan, θ is the in-plane angle of the magnetic field. The inhomogeneous linewidths δB measured in Fig. 6.12 were converted to δg following the expression $\delta g = g(\delta B/B_{res})$, where B_{res} is the resonance B field. Fig. 6.16 shows both the measured g^2 and δg for a C_2 sub-site are in close agreement with the model (red and blue lines) with both g^2 and $g\delta g$ fitted with the same functional dependence on θ with different coefficients a,b,c and a′, b′, c′ respectively. A similar functional dependence of δg and g^2 on the angle of the magnetic field θ suggests a strain-induced variation of the local environment as a mechanism of inhomogeneous linewidth broadening. It is to be noted, that $\theta = 40°$ where δg is minimum, 4 out of the 6 C_2 subsites have the same g value. This indicates anisotropic spin-spin interaction as a possible mechanism for the broadening of the spin inhomogeneous linewidth.

Angle dependence of spin ensemble coupling to resonator

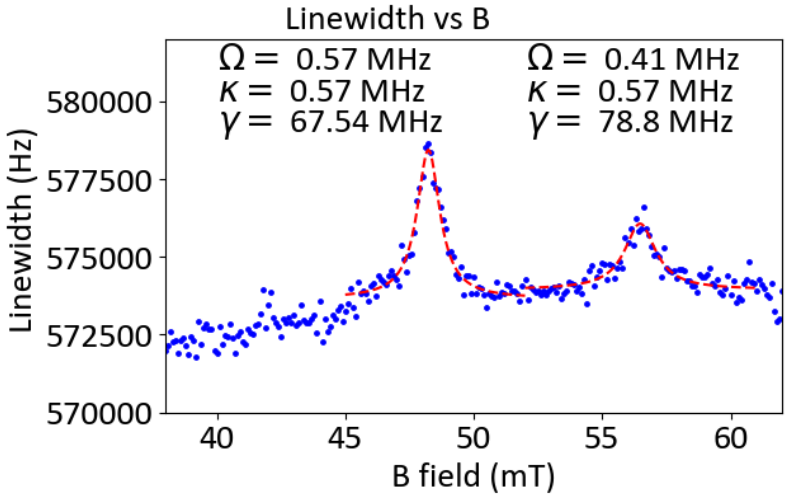
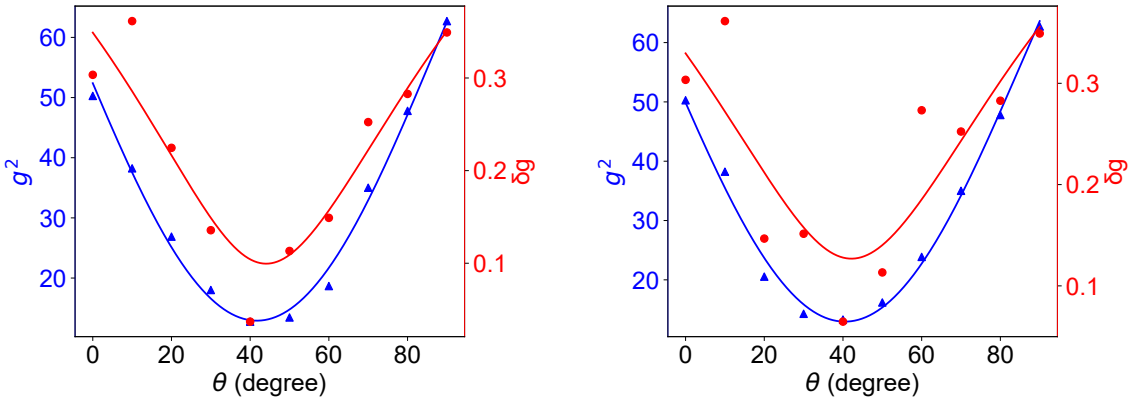


Figure 6.15: Absorptive coupling signal showing narrowest spin inhomogeneous linewidth measured for Er^{3+} in C_2 site. A Lorentzian fit was performed on the absorptive coupling signal to extract the spin inhomogeneous linewidth (γ), ensemble coupling strength to the resonator (Ω).



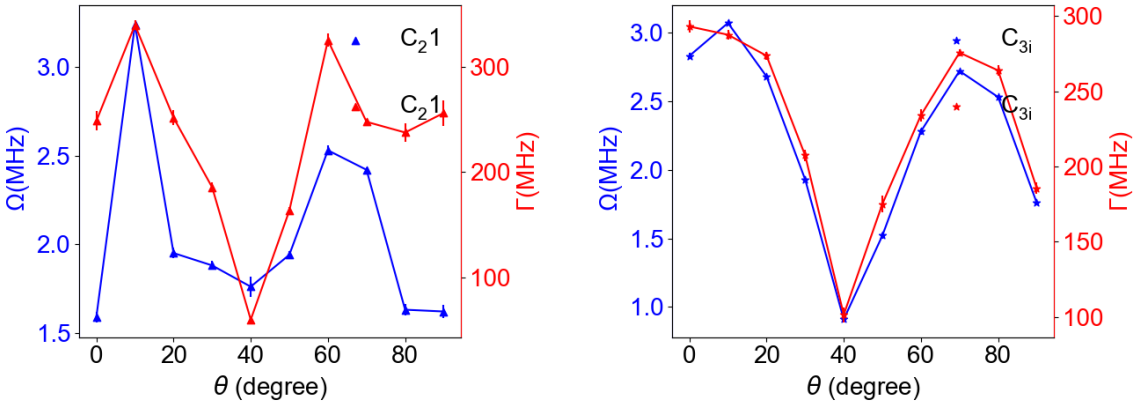
(a) (b)

Figure 6.16: Angle dependence of spin inhomogeneous linewidth δg (red dot) and effective g factor squared g^2 (blue triangle) for Er^{3+} ions in two C_2 sub-sites ((a) and (b)) show close agreement with the model (blue, red line) with a similar functional dependence on the angle of the magnetic field θ suggesting strain induced variation of the local environment as a mechanism of inhomogeneous broadening.

The ensemble coupling to the resonator Ω shows a dependence on the in-plane angle for both C_2 and C_{3i} sites. Fig. 6.17 shows the angle dependence of spin inhomogeneous linewidth Γ

(red triangle) and ensemble coupling strength to the resonator Ω (blue triangle) for both the sites. The C_2 site shows a weak angle dependence of Ω on the angle, which can be explained by a merging of transitions from different sub-sites in Fig. 6.12 leading to an increase in the effective number of spins N and hence the total coupling strength.

However, C_{3i} shows a strong dependence of both the collective coupling Ω and inhomogeneous linewidth Γ which follow an identical trend with θ. Interestingly the angle $\theta = 40°$, which corresponds to minimum linewidth also corresponds to the direction where the transitions from 6 different C_2 subsites merge into two groups(Fig. 6.12, Fig. 6.14). The observed variation in Γ cannot be explained by the site symmetry or strain and indicates a significant contribution of spin-spin interaction in the spin inhomogeneous linewidth. The observed variation in Ω however, cannot be explained and requires further studies.



(a) (b)

Figure 6.17: Angle dependence of spin inhomogeneous linewidth Γ (red triangle) and ensemble coupling strength to the resonator Ω (blue triangle) for Er^{3+} ions in (a) A C_2 sub-sites and (b) C_{3i} sub-site.

Spin echo detected field sweep

We perform two pulse-echo measurements at a pulse separation of tau = 4 μs and sweep the magnetic field at an angle of 40 degrees to obtain the echo detected field sweep (EDFS) spectrum in Fig. 6.18. The peaks around 113 and 117 mT correspond to the g=3.6 transition from C_2 site and the peak at 130 mT corresponds to g=3.2 transition from the C_{3i} site.

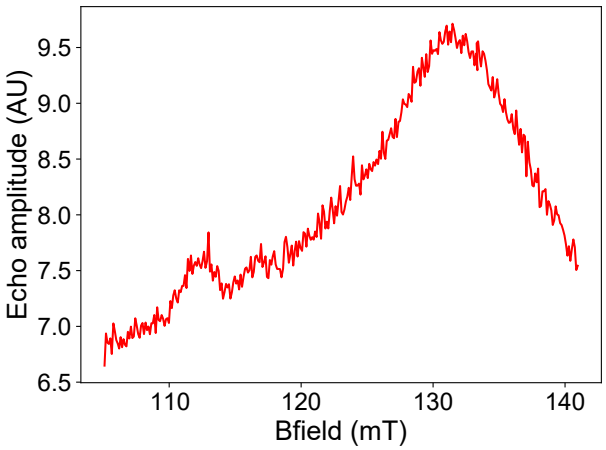


Figure 6.18: Echo vs field sweep spectrum obtained by performing two-pulse echo measurement at pulse separation τ =4 μs and sweeping field in 100-140 mT range. The large peak at 130 mT corresponds to C_{3i} site while the smaller peaks around 115 mT correspond to C_2 site.

Optimization of pi pulse

Pulse power optimization was carried out by varying the power of the refocusing pulse of a spin echo sequence and measuring spin echo (Fig. 6.19) for the C_2 transition at 113 mT, 40-degree field angle measured in Fig. 6.18. The spin echo amplitude (A) was fitted to the model [27],

$$A = B(1 - \cos\theta_p) \tag{6.5}$$

where θ_{p} is the flip angle of the pulse proportional to the square root of the pulse power $\theta_{\mathrm{p}} = \mathrm{C}\sqrt{\mathrm{P}}$.

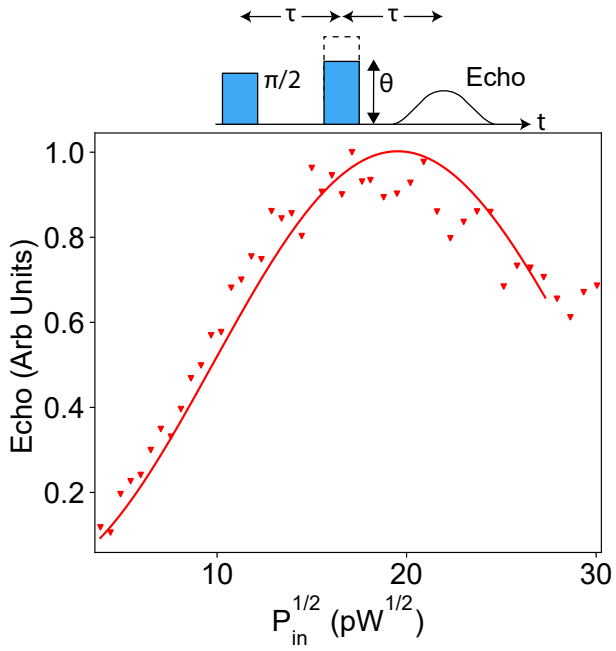
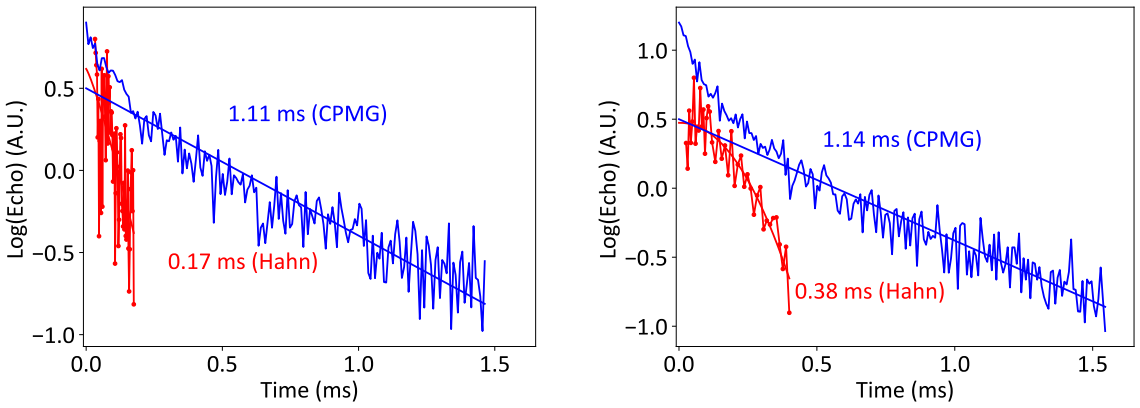


Figure 6.19: Rabi nutation experiments carried out varying the flip angle of the second pulse for the C_2 transition at 113 mT, 40-degree angle. Increasing the power leads to saturation of the spin echo amplitude due to the spatial inhomogeneity of the resonator driving field [165].

6.4.2 Decoherence and relaxation processes in thin-films at milliKelvin temperatures

Spin coherence time

We apply magnetic field along the direction θ= 40 degree (Fig 1(b)) and measure spin coherence time of C_2 transition with g=3.6 at 113 mT (Fig. 6.20a) and C_{3i} transition with g=3.2 at 130 mT (Fig. 6.20b). The C_2 transition with g=3.6 shows two-pulse (Hahn) echo spin coherence time T_2^{Hahn} of 0.18 ms following a stretched exponential decay $e^{-(2\tau/(T_2))^n}$ with a stretch factor n=1.18 suggesting spectral diffusion dominated decoherence. We use CPMG dynamical decoupling sequence with N=500 pulses and a pulse separation $2\tau = 8$ μs and to suppress the spectral diffusion noise and obtain a T_2^{CPMG} of 1.11 ms limited by instantaneous diffusion (ID) (for T_2^{CPMG} vs N). The C_{3i} transition with g=3.2 also shows



(a) (b)

Figure 6.20: (a) Spin T_2 for C_2 transition at a field of 113 mT was measured to be 0.17 ms with two-pulse echo and 1.11 ms with CPMG dynamical decoupling (b) Spin T_2 for C_{3i} transition at a field of 130 mT was measured to be 0.38 ms with two-pulse echo and 1.14 ms with CPMG dynamical decoupling.

long Hahn echo spin coherence time T_2^{Hahn} of 0.38 ms with a stretch factor n=2.11 and T_2^{CPMG} of 1.14 ms. Hahn echo measurement for both C_2 and C_{3i} transitions showed spin echo amplitude modulation due to superhyperfine interaction with yttrium nuclei [152].

Spin relaxation time

We did not observe a strong frequency dependence of T_1 (Purcell enhanced spin relaxation) due to a stronger contribution of spin-lattice and spin flip-flop processes to the spin relaxation of Er^{3+} in Y_2O_3 [141] [77]. We can constrain the maximum Purcell-enhanced T_1 to 5 seconds based on the frequency-dependent T_1 measurement, which puts the upper limit on average single spin coupling, g as g <128 Hz ($\Gamma_P \leq 0.034\,\text{Hz}$, $\kappa = 1.94\,\text{MHz}$). This indicates the spacing between the sample and resonator is significantly larger than 100 nm (niobium spacer layer thickness) as we expect g $\approx$ 800 Hz if the sample is at 100 nm distance from the resonator. This could be caused due to imperfect sample mounting leading to an angle offset as well a vertical gap between the plane of the resonator and the Y_2O_3 sample. We indeed observed an angle offset up to 2.8° between the plane of the resonator and the sample

in the CW-ESR angle scan (Fig. 6.14) and directly measured air gaps up to 2 μm between the sample and the resonator using SEM (Fig. 8.5). This projects a further increase in ensemble spin coupling by optimization of the mounting process to reduce the gap between the resonator and the sample, which would allow for Purcell-enhanced spin relaxation through the resonator.

Spin coherence and relaxation properties on a wafer scale

To study spin coherence and relaxation times on a wafer scale, we perform pulsed ESR on three samples taken from different radial positions (r) from the center of a slice of Er^{3+} doped Y_2O_3 wafer (Fig. 6.21(a)). The samples were mounted on three superconducting resonators coupled to the same transmission line and the resonators were offset in the frequency domain with a frequency of 5.50, 5.58, and 5.8 GHz as shown in the measured device transmission spectrum (Fig. 6.21(b)).

The C_{3i} transition with g=3.2 measured in Fig. 6.20b did not show a strong angle (θ) dependence of the resonance fields and the coherence time (Fig. 6.26). Therefore, we performed spin coherence measurements on the same C_{3i} transition for each sample. We used the same pulse width (200 ns) and performed measurements at a similar temperature ($\approx$ 8.5 mK) across the samples allowing us to compare the spin relaxation and coherence time on a wafer scale.

A long spin coherence time in the range of 0.38-0.47 ms (Fig. 6.21(d), T_2^{Hahn}, red dots) was measured using two-pulse echo sequence, suggesting a low fluctuating magnetic noise amplitude on a wafer scale. We further suppressed spectral diffusion using N=500 CPMG dynamical decoupling sequence pulses with a separation 2τ= 8 μs and obtained coherence time in the range of 1.14 - 1.72 ms (Fig. 6.21(d), T_2^{CPMG}, blue dots) with an increase for larger r. The spin lifetime T_1 in the range of 0.76 -1.30 s was measured using saturation recovery sequence (Fig. 6.21(d), black triangles) exhibiting a small increase for the samples

with larger r. The observed increase in T_2^{CPMG}, T_1 with r could be attributed to decreased dipolar interaction between resonant spins for samples farther from the center of the wafer (larger r). Fig. 6.22a, Fig. 6.22b and Fig. 6.22c show the time domain decay corresponding to the Hahn echo, CPMG and T_1 measurement in Fig. 6.21 respectively.

Direct-process limited relaxation rate scales as $B^{-5}\coth(g\mu_B B/2k_B T)$ [112] at low temperatures while cross relaxation limited spin relaxation scales as the square of density (n^2) [46], therefore long spin lifetime can be expected by operating at lower magnetic fields and/or lower Er^{3+} density [46]. Indeed T_1 of 15 s limited by direct process was observed for a low density(0.7 ppb) of Er^{3+} in $CaWO_4$ (10 mK, 500 mT) [48]. Low magnetic field measurements of Er^{3+} in Y_2SiO_5 have demonstrated direct process limited T_1 of 45 s (0.5 K, 11 mT) [140] and even longer phonon-bottlenecked direct process limited T_1 of 10 hours at lower fields and temperature (20 mK, 6.5 mT) [35]. This suggests a significant prospect of increasing the spin lifetime by operating at lower Er^{3+} densities and magnetic fields, typically used in experiments on optically addressed single RE qubits [98] [140].

The measured T_2^{Hahn}, T_2^{CPMG} allow us to estimate the fluctuation magnetic noise amplitude δB between 11-13 nT at different points on the wafer (Fig. 6.21(c), red dots), which is close to the yttrium nuclear spin-bath limit of magnetic noise $\leq$ 9 nT in Y_2O_3 [77]. We observed saturation of T_2^{CPMG} for the number of pulses (N) larger than 200 and therefore the CPMG results shown in Fig. 6.21(d) are expected to be primarily limited by dipolar interaction between resonant spins [80] (Section 6.4.2). Assuming dipolar interaction limited T_2^{CPMG}, we can estimate the effective concentration of spins between 4.1 $\times 10^{14}$ spins/cm^3 at r=14 mm to 2.8 $\times 10^{14}$ spins/cm^3 at r=30 mm (Fig. 6.21(c), blue dots). We note that the effective density estimated here corresponds to the spin sub-ensemble addressed within the resonator and pulse bandwidth. Nevertheless, an estimated reduction in the spectral density of spins by a factor of 1.46 towards the edges is consistent with $\gtrapprox$ 3.4 broader spin inhomogeneous linewidth measured on samples farther from the center of the wafer (Section

6.4.2).

We, therefore, report a long electron spin coherence time and slow spin relaxation on a wafer-scale in Er^{3+} doped Y_2O_3 thin-films. These long relaxation times are on par with or exceeding best demonstrations on Er^{3+} doped bulk single crystals suggesting the suppression of fast decoherence processes in MBE grown Y_2O_3 thin-films due its high purity, crystalline quality, and a low defect density.

Spectral diffusion

To study spectral diffusion dynamics, we performed three pulses (stimulated) echo measurements for C_{3i} site g=3.2 transition of 130 mT at the base temperature of 8 mK. The waiting time (T_W) between the second and third pulses was scanned in the range of 100 μs to 10 ms for the separation between the first and second pulse τ = 25, 30, 35, 40, 45, and 50 μs. The echo amplitude decays as a function of pulse delays τ, T_W can be expressed as [112],

$$\frac{A(\tau, T_W)}{A_0)} = \exp\Big[\frac{T_W}{T_1} + 2\pi\tau\Gamma_{eff}\Big] \tag{6.6}$$

where Γ_{eff} is the effective linewidth given as,

$$\Gamma_{eff} = \Gamma_0 + \frac{1}{2}\Gamma_{SD}(R\tau + 1 - e^{-RT_W}) \tag{6.7}$$

The terms Γ_{SD} represent the spectral diffusion linewidth due to dipolar coupling with environmental spin bath, R represents the effective spin-flip rate, and Γ_0 represents instantaneous diffusion and homogeneous linewidth. We fit stimulated the echo amplitude as a function of T_W for different values of τ (Fig. 6.23a) with eqn. 6.6 and eqn. 6.7 to obtain Γ_{SD} = 8.2(0.9) kHz, Γ_0 = 0.3(0.1) Hz and R= 151(38) Hz.

In the limit of $R\tau << 1$, we can further simplify eqn. 6.7 to $\Gamma_{eff} = \Gamma_0 + \frac{1}{2}\Gamma_{SD}(1 - e^{-RT_W})$ [143] and fit effective linewidth Γ_{Eff} for fixed T_W by sweeping τ (Fig. 6.23b). Following this

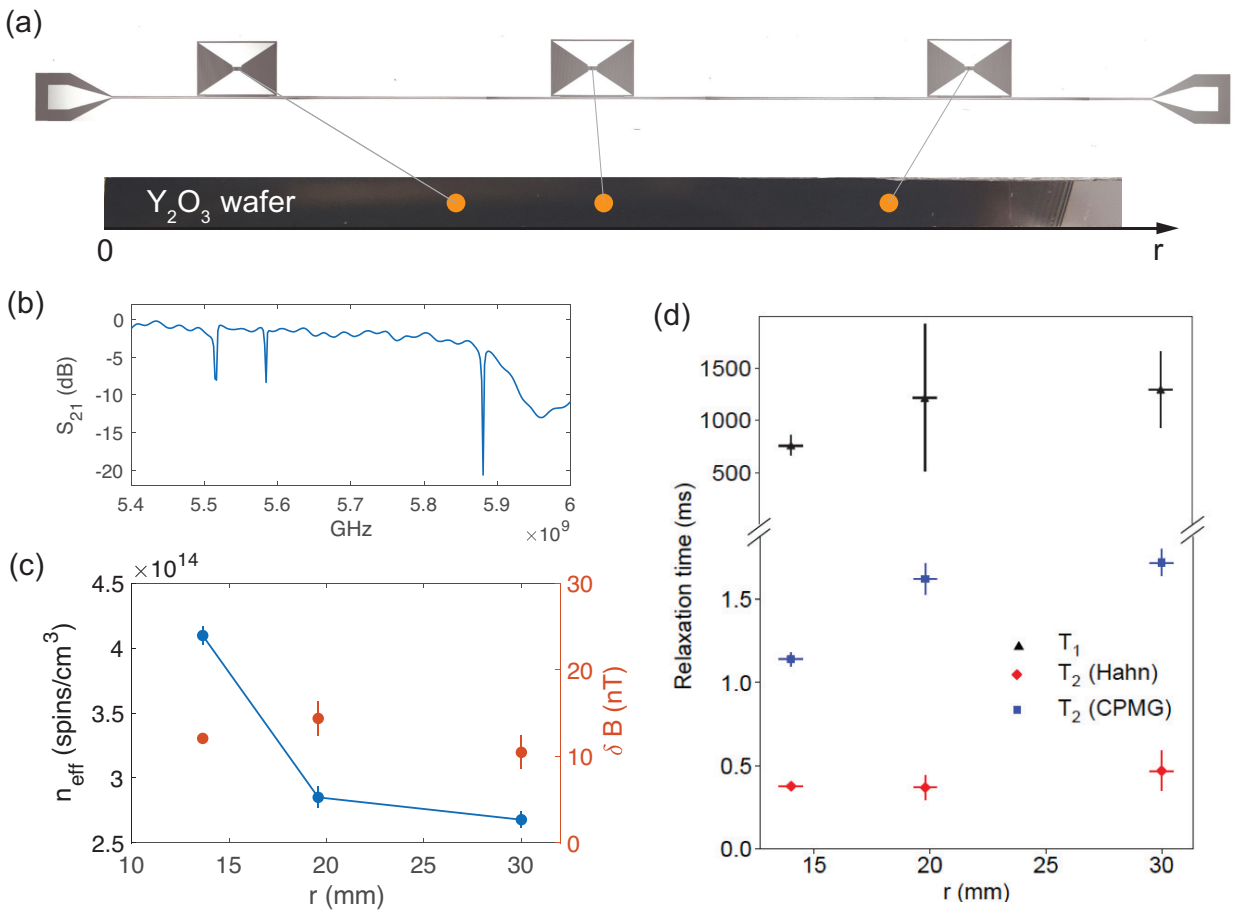


Figure 6.21: Spin coherence properties on a wafer scale (a) Samples were taken from three different radial positions (r) with respect to the center of a slice of Er^{3+} doped Y_2O_3 wafer and mounted separately on three spectrally separated microwave resonators coupled to the same transmission line (b) Transmission spectrum of the device at 12.5 mK shows three distinct features from the three resonators (c) Estimated effective Er^{3+} spin density (n_{eff}) and fluctuating magnetic noise amplitude (δB) plotted as a function of distance from the center were obtained from (d) Hahn echo (T_2^{Hahn}, red dots) and CPMG (T_2^{CPMG}, blue dots) spin coherence time and spin lifetime (T_1, black triangles) measurements. Low magnetic noise amplitude δB=11-13 nT is obtained on a wafer-scale with increasing T_2^{CPMG},T_1 indicating a reduction in spin-spin interaction for larger r (edges of the wafer) due to decreased spin spectral density.

fitting method, we obtain Γ_{SD} = 4.4(0.7) kHz, R= 287(140) Hz and Γ_0 = 0.7(0.3).

While the fitted R and Γ_{SD} values among the two methods differ by a factor of 2, the product RΓ_{SD} for the sweeping T_W method (1.24 kHz^2) and sweeping τ method (1.26 kHz^2) is in close agreement. Thus, both methods predict a similar spectral diffusion limited

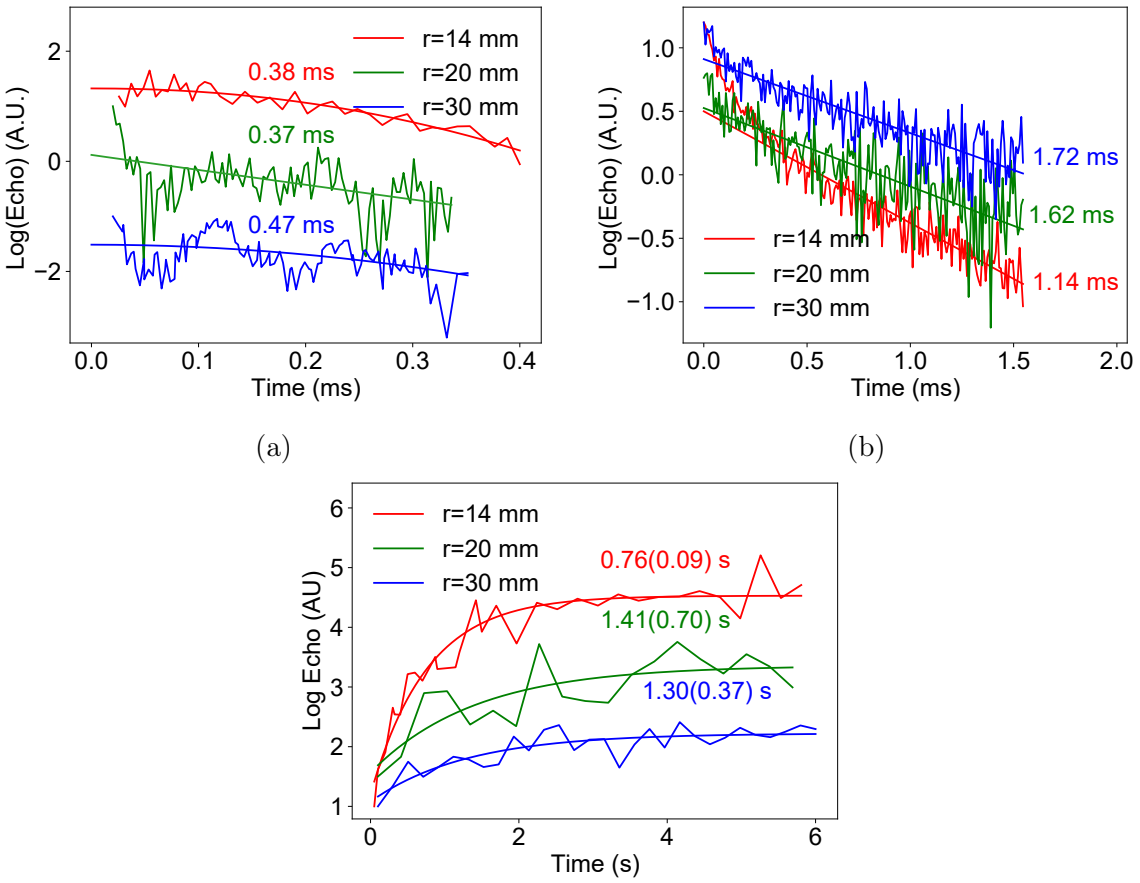
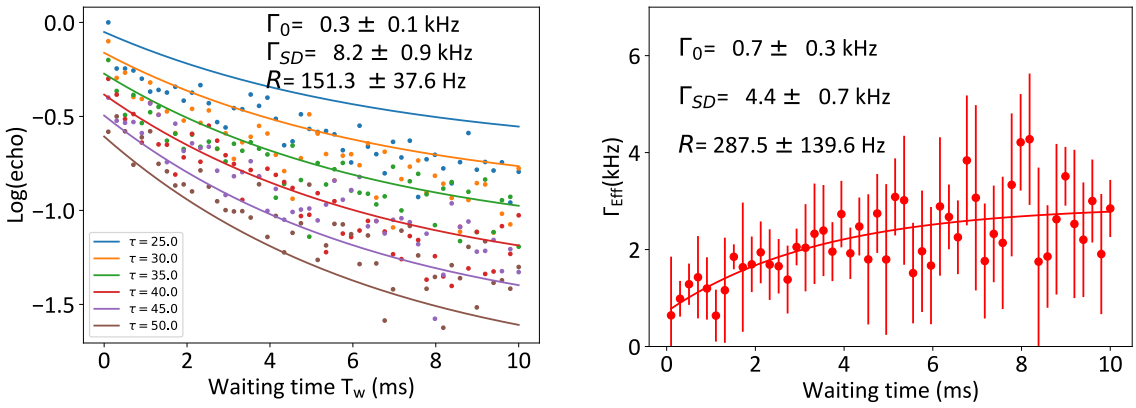


Figure 6.22: Time domain data for the spin coherence properties for C_{3i} transition with g=3.2 for samples taken from different points on the wafer (r) (a) Hahn echo spin T_2 was fitted with a stretched exponential decay $e^{-(2\tau/(T_2))^n}$ with n=2.1,10,2.0 for r=14, 20 and 30 mm respectively (b) CPMG spin coherence time T_2 and (c) Spin lifetime T_1, measurements.

coherence time ($T_{2,SD}^{-1} = \frac{\sqrt{\pi \Gamma_{SD} R}}{2}$) of 1.005 ms ($\tau$ sweep) and 1.013 ms (T_W sweep). The covariance among the spectral diffusion parameters R and Γ_{SD} observed here has also been reported in similar works [143].

The spin-flip rate R in the range of 50-300 Hz is comparable with slow spectral diffusion previously reported in bulk rare-earth doped crystals [59] [112]. The short timescale linewidth Γ_0 of 0.7(0.3) kHz is in agreement with the homogeneous linewidth of 0.8(0.03) kHz from two pulse-echo measurements.



(a) (b)

Figure 6.23: (a) Effective linewidth $\Gamma_{\mathrm{Eff}} = 1/\pi T_2$ as a function of waiting time (T_W) obtained by sweeping τ for C_{3i} g=3.2 transition at 130 mT and fitting the linewidth (b) Spin echo area (A) as a function of τ obtained by sweeping waiting time(T_W) for C_{3i} g=3.2 transition at 130 mT.

Temperature dependence of decoherence processes

Spin T_2 was measured for the C_{3i} transition at a field 130 mT, θ= 40 degree with increasing temperature. The spin echo area for pulse separation τ=0 was extrapolated as $A(T) = A(0,T) = A(\tau,T)e^{(\tau/T_2)}$ and fitted to temperature dependent spin polarization model (Fig. 6.24(a)),

$$A(T) = A_{max}\tanh(T_{Ze}/T_{Corr}) \tag{6.8}$$

where A_{max} is a normalization factor set equal to 1, T_{Ze} is the spin Zeeman temperature set to 0.2788 K (5.8 GHz spin transition splitting) and T_{Corr} is the corrected spin temperature obtained by multiplying the measured sample stage temperature by a fitting parameter C, with $T_{Corr} = CT$. The fit of data in (Fig. 6.24(a)) to eqn. 6.8 gives us a correction factor C = 1.45(0.06). A good agreement between the data and model validates the fitting and suggests a corrected base temperature of 12.5 mK.

After correcting the temperature, the temperature dependence of $1/T_2$ was modeled as

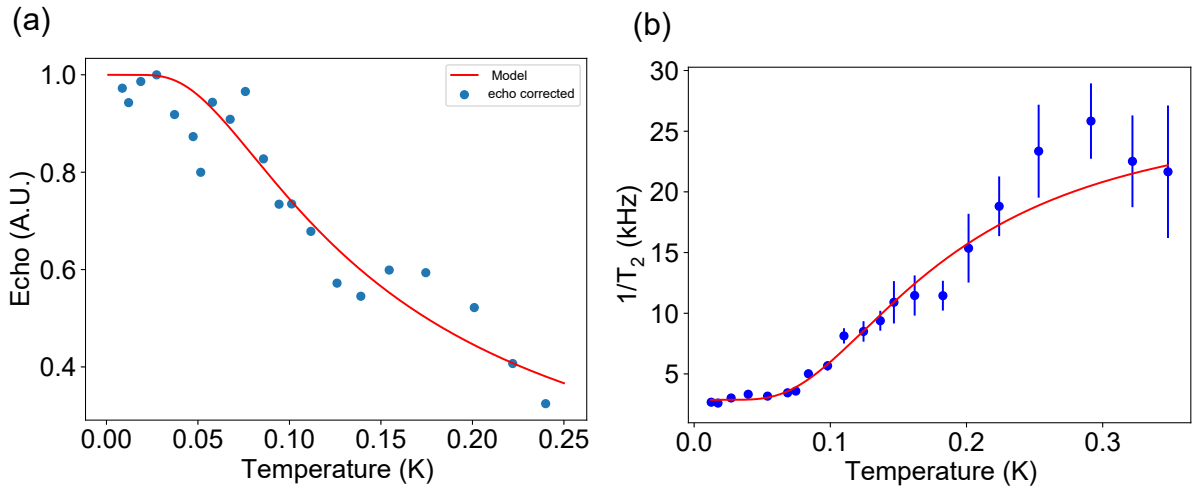


Figure 6.24: Spin T_2 temperature dependence measured for the C_{3i} transition at 130 mT with g=3.2 (a) Spin echo area corrected for T_2 fitted to the polarization model (b) $\gamma = 1/T_2$ (blue dots) as a function of corrected temperature (T_{Corr}) and the fitted paramagnetic spin bath induced decoherence model (red line).

[135] [178],

$$\frac{1}{T_2(T)} = \Gamma_0 + \frac{\xi}{(1+e^{T_{Ze}/x})(1+e^{-T_{Ze}/x})} \tag{6.9}$$

where Γ_0 is a temperature-independent part of decoherence such as instantaneous diffusion, ξ is a temperature-independent parameter with strength proportional to the dipolar coupling to paramagnetic spin bath inducting spectral diffusion, and T_{Ze} is the Zeeman temperature of the spin bath. We fit the model to the data in Fig. 6.24 to obtain ξ= 96.8(9.7) kHz, Γ_0= 2.9(0.1) kHz and T_{Ze} = 0.337 K. The spin Zeeman temperature corresponds to a spin bath splitting of 6.9 GHz (equivalently g=3.8 GHz) and suggests Er^{3+} in C_2 sites with g $\approx$ 3.8 as the primary source of decoherence at higher temperatures. Indeed, out of the six C_2 subsites, two orientations have a g= 3.6 (two orientations) and four have g= 8.6 for the in-plane magnetic field direction (θ=40 degrees) corresponding to this measurement. The saturation of γ for low temperature suggests suppression of spin-bath flip-flops due to spin polarization.

To verify the polarization of the paramagnetic spin bath, we repeat the T_2 measurement

on the same C_{3i} transition with g=3.2 at a different in-plane angle θ = 10 degrees where all the C_2 subsites have a different g =6.2 (all six orientations) or equivalently a splitting of f=11 GHz at 132 mT. We observe near identical spin coherence times (T_2^{Hahn}) of 0.373(0.038) ms and 0.378(0.012) ms for the transition corresponding to θ = 10 and θ = 40 degree respectively at 12.5 mK temperature (Fig. 6.26). This confirms the Er^{3+} C_2 subsite spin-bath is polarized at the base temperature of 12.5 mK and the low-temperature linewidth $\gamma = \Gamma_0 = 2.9$ kHz is dominated by temperature-independent processes. We estimate 1 kHz contribution of instantaneous diffusion to Γ_0 based on CPMG measurements ($\Gamma_{ID}=1/T_2^{CPMG}$), which allows us to put a limit on decoherence due to residual magnetic noise as $\Gamma_{Res,Mag} = \Gamma_0 - \Gamma_{ID} = 1/(526\mu s)^{-1}$, which could be due to combination of superhyperfine contribution and residual magnetic noise due to paramagnetic spin flip-flops. We note that the dipolar coupling of the C_{3i} spin to C_2 site spin-bath with concentration of n_{C_2} of 13.8 ppm and g=3.8 is $\nu_{dd} = (h\mu_0\gamma_{C_{3i}}\gamma_{C_2}n_{C_2})/(4\pi) = 50$ kHz, which is close to ξ = 96.8 kHz within a factor of two [59]. However, given that ξ does not have a closed-form expression and anisotropy of g factor leads to a complex dipolar interaction [112] [111], the similarity between the two numbers by itself does not allow drawing a further conclusion on the nature of spin-bath.

Strong modulation of the spin echo envelope (ESEEM) with periodic revivals is observed for C_{3i} transition at a field 135 mT in Fig. 6.25(a), which is indicative of coupling to $^{89}Y^{3+}$ nuclear spins. After the first few cycles of clear oscillation, the phase is randomized due to the accumulation of relative phase offsets among nuclei precessing with slightly different frequencies [122]. The fast Fourier transform of the echo amplitude Fig. 6.25(b) shows a broad peak around 0.55 MHz. The expected Larmor precession frequency of $^{89}Y^{3+}$ nuclei ($\mu \approx 0.275\mu_N$) at 0.135 mT is 0.28 MHz [135] (blue dashes) and estimated magnetic dipolar interaction between Er^{3+} electron spin in C_{3i} site and nearest $^{89}Y^{3+}$ nuclear spin at a distance of 3.5 [206] is 0.4 MHz (green dashes). While the data had limited resolution to observe finer peaks in the Fourier spectrum, a spread of modulation frequencies of $^{89}Y^{3+}$

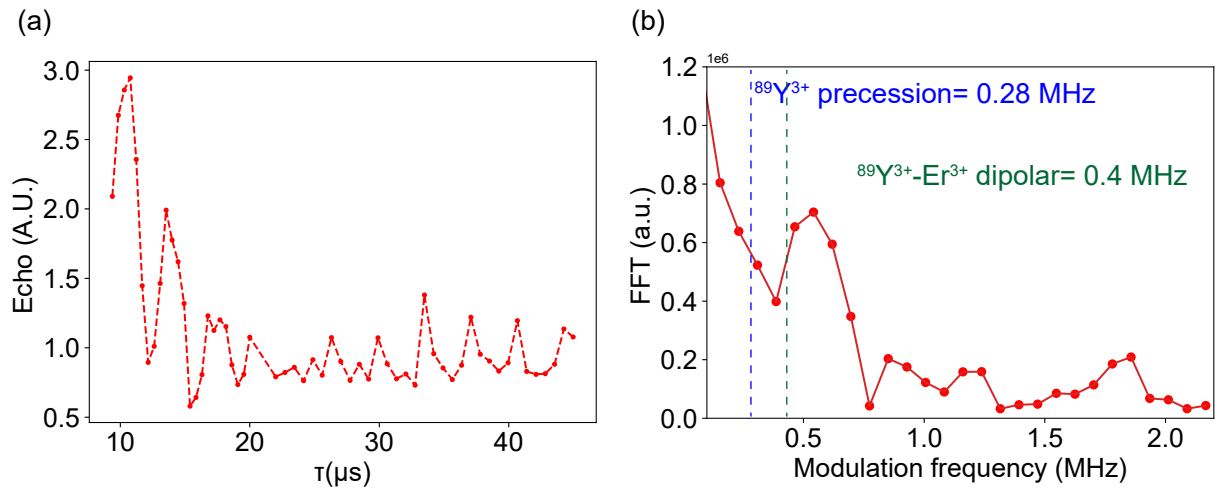


Figure 6.25: (a)Electron spin echo modulation (ESEEM) obtained two pulse-echo measurements for C_{3i} transition at a field 135 mT shows modulation of spin echo amplitude due to interaction with $^{89}Y^{3+}$ nuclei. (b) The Fourier transform of echo amplitude reveals a broad peak centered around 0.55 MHz due to contribution from different $^{89}Y^{3+}$ nuclei.

nuclei is expected due to varying hyperfine couplings and distances from Er^{3+} spin [36] [74] [137]. Nevertheless, this suggests a contribution from nuclear spin-bath magnetic noise to the low-temperature linewidth Γ_0.

Instantaneous diffusion

Measured instantaneous diffusion limit

To study the instantaneous diffusion limit we performed CPMG dynamical decoupling measurements as a function of the number of pulses N for samples taken from different radial positions (r) along the wafer (Fig. 6.27) at 12.5 mK. While all samples follow the trend of an initial linear increase in T_2^{CPMG} with a number of π pulses followed by a saturation for N=200, the samples towards the edges (large r) show a greater T_2^{CPMG}. We also note a slight decrease in T_2^{CPMG} for N= 400 and 500 pulses, which could be attributed to the accumulation of pulse errors [177]. Increasing the number of pulses can lead to efficient decoupling from the spin bath due to a narrower filter function. Nevertheless, the saturation of T_2^{CPMG} with N suggests instantaneous diffusion between resonant spins as the limiting

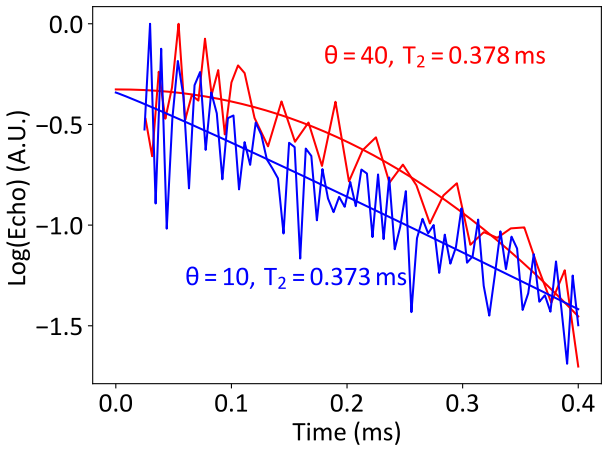


Figure 6.26: Identical spin coherence time (T_2^{Hahn}) was measured for C_{3i} g=3.2 transition for different in-plane angle θ corresponding to different g factor of C_2 subsites, thereby confirming the near unity polarization of Er^{3+} C_2 site spin-bath at the base temperature of 12.5 mK.

source of decoherence [213]. This also allows us to estimate the effective spin concentration n_{eff} from the ID-limited CPMG coherence time as,

$$n_{eff} = \frac{9\sqrt{3}}{2\pi^2 \mu_0 h \gamma^2 T_2^{CPMG}} \tag{6.10}$$

The higher saturation value of T_2^{CPMG} for large r suggests an increase in instantaneous diffusion limited T_2 for the samples towards the edges. This could be partly explained by an increase in spin inhomogeneous linewidth towards the edges. Indeed, Fig. 6.28 compares the spin inhomogeneous linewidth for both low and high field transitions between samples taken from different points of the wafer (r). The low field transition (Fig. 6.28(a)) measured using CW ESR shows 3.4 times broader linewidth for the sample farther from the center (r=20 mm, red) as compared to the sample closest to the center (r=14 mm, blue). The high field transition measured using spin echo detection (Fig. 6.28(b)) also shows a broader inhomogeneous linewidth by a factor of 5 for the sample farthest from the center (r=33 mm) as compared to the sample closest to the center (r=14 mm). Therefore a significant increase in spin inhomogeneous linewidth with distance (r) for both low and high field transitions

suggests a reduced spin spectral density and hence reduced instantaneous diffusion for larger r, which is in close agreement with measurements in Fig. 6.27. This increase in inhomogeneous linewidth towards the edges along with the modeled strain-induced angle dependence of linewidth in Fig. 6.16 suggests an increase in lattice strain towards the edges.

Theoretical instantaneous diffusion limit

To estimate the theoretical ID limit, we first estimate the number of photons corresponding to -65 dBm on-chip power as $\langle n \rangle = (P/hf) \times (k_e/k^2) = 41085$ corresponding to $f = 5.8 \times 10^9$ Hz, $k \approx k_e = 1.9$ MHz for the device used in Fig. 2 in the main text. We then estimate the Rabi frequency as $\Omega = g\sqrt{\langle n \rangle} \lessapprox 0.78$ MHz using $g \lessapprox 128$ Hz. The ID limit can therefore be estimated as,

$$T_{2,ID}^{-1} = \frac{2\pi^2 \mu_0 h n \gamma^2}{9\sqrt{3}} \langle \sin^2 \frac{\theta}{2} \rangle \tag{6.11}$$

where $\langle \sin^2 \frac{\theta}{2} \rangle$ is the average spin-flip probability evaluated by integrating the spin-flip probability over the inhomogeneous linewidth [112]. Using inhomogeneous linewidth of 100 MHz, Rabi frequency $\lessapprox 0.78$ MHz, we get $\langle \sin^2 \frac{\theta}{2} \rangle \lessapprox 0.016$. Using these values and the estimated C_{3i} density of 32.4×10^{16}spins/cm^3 we get $T_{2,ID} \gtrapprox 0.50$ ms. The measured $T_2^{CPMG} \approx 1.1$ ms is consistent with the theoretical lower bound on ID and the largest source of uncertainty in this calculation is the estimated single spin coupling g, which could only be bounded by 128 Hz.

6.4.3 Minimum number of spin sensitivity (N_{spin}^{min})

We use the CPMG measurement on the 130 mT transition from C_{3i} site for the device in Fig .6.20a to estimate the minimum number of spins detectable. For the CPMG spin echo at time = 82 μs, we measure a signal with SNR = 60 for 24 $\times 10^6$ spins being addressed, which leads to a minimum sensitivity of 36 $\times 10^4$ spins. This number can be further reduced by a factor of 50 by increasing the resonator quality factor by matching the designed external

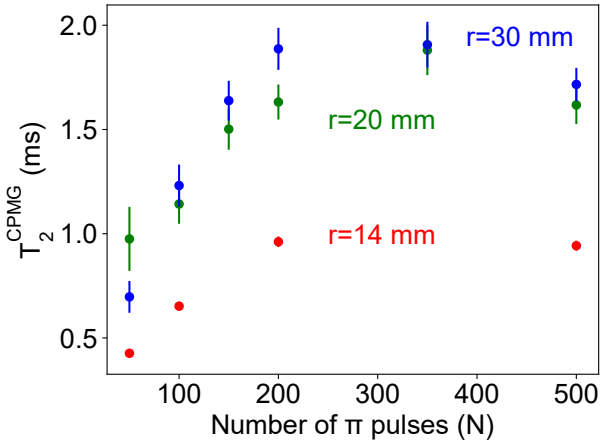


Figure 6.27: Spin coherence time with CPMG dynamical decoupling pulses (T_2^{CPMG}) as a function of the number of pulses (N) for samples taken from different positions (r) on the wafer.

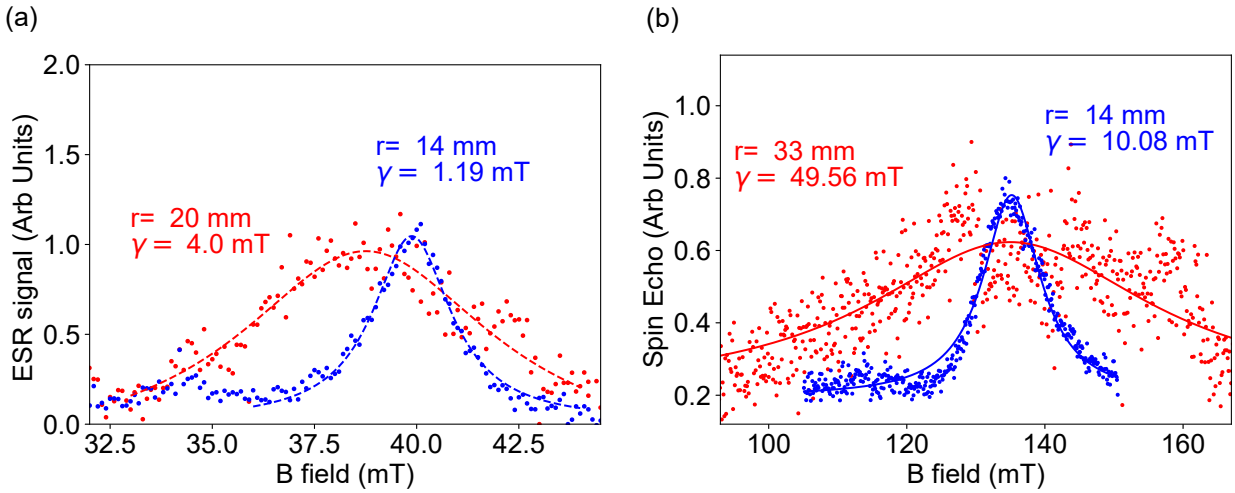


Figure 6.28: Comparison of the spin inhomogeneous linewidth as a function of distance from the center of the wafer (r) for low and high field transitions (a) The inhomogeneous linewidth of a low field transition for the sample closer to the center of the wafer (r=14 mm, blue) compared to the sample farther from the center (r= 20 mm, red). The Er^{3+} spin ensemble far from the center (red) shows at least 3.43 times larger inhomogeneous linewidth than the broadest linewidth measured for a similar transition for the sample closest to the center (blue) (b) The inhomogeneous linewidth for a high field transition for another sample even farther from the center (r= 33 mm, red) compared with the same sample closest to the center (r=14 mm, blue). The sample even farther from the center shows a 5 times broader inhomogeneous linewidth than the same transition for the sample closer to the center (blue).

Device	Q_{i0}	Ftanδ	nc	α
1(r=20 mm)	13422	3.92×10^{-5}	3.8×10^{6}	0.36
2(r=30 mm)	14088	3.10×10^{-5}	2.6×10^{5}	0.54
3(r=33 mm)	13082	3.78×10^{-5}	1.1×10^{6}	0.54

Table 6.3: Power dependence fit parameters for superconducting devices used in Fig. 6.21

coupling q factor (Q_e=3000) to the measured intrinsic quality factor Q_i of $300,000$. Further increase in the single spin coupling (g) from 100 Hz to 4 kHz, by a factor of 40 by minimizing the air gap between the sample and the resonator will also improve the sensitivity by a factor proportional to $g^2 = 1600$. This can be done by fabricating superconducting resonators around lithographically defined RE-doped cylinders or by optimization of the sample flip-chip mounting process to minimize the air gap. Therefore, we expect to reach spin sensitivity $N_{spin} = O(100)$ by modest improvement in the device design and sample integration.

6.4.4 Magnetic and electrical TLS in rare-earth/superconducting hybrid devices at wafer-scale

Figure 6.29 (a) shows a broad g $\approx$ 2.07 background signal observed in CW ESR measurement on the device used in Fig. 6.14 and Fig. 6.12. The signal has an asymmetric lineshape, which could be explained by the presence of a broad background of multiple sub-species with slightly different g. Fitting the model $\kappa_i = \kappa_{i,0} + \Omega^2\gamma_s/(\gamma_s^2 + \Delta^2)$ provides as with ensemble coupling Ω of 2.68 MHz and spin half-width of $\mathcal{O}$(800 MHz). This allows us to estimate a total paramagnetic number of defects 8 $\times 10^7$ spins distributed over the inductor area of $\approx$ 1256 μm^2. Therefore the magnetic TLS has an area density of 64000 spins/μm^2. Assuming the TLS are localized in the thin film with 1.5 μm thickness, we get a total magnetic TLS density of 4 $\times 10^{16}$ spins/cm^3. These defects could be paramagnetic impurities or defects like negatively charged oxygen vacancies (F^+ center) and interstitial defects, which have been

previously reported in Y_2O_3 thin-films as well as ceramics (Fig. 6.29(d). Another possible contribution to the magnetic TLS signal could be from silicon substrate or niobium surface oxides.

Power dependence quality factor measurements of superconducting resonators can be used to obtain the density of states and dynamics of electrical TLS. We perform power dependence measurements on the three resonators used in Fig 3. This allows us to obtain the variation of TLS density and interaction throughout the thin-film sample. Fig 6.29 (b) shows the inverse of intrinsic quality factor (Q_i) as a function of the number of photons in the microwave resonator $\langle n \rangle$. The data were fitted to the model [50],

$$\frac{1}{Q_i} = \frac{1}{Q_{i0}} + \frac{F\tan\delta}{(1 + (x/nc)^{\alpha})} \tag{6.12}$$

where Q_{i0} is the quality factor due to power-independent losses, in the low power limit $F\tan\delta$ is proportional to the TLS loss tangent δ times the filling factor F in the resonator, nc is the critical photon number for saturation and α is the exponent of the power dependence. The fitting parameters for all 3 devices are shown in Table 6.3 and fit Fig. 6.29(a) decrease in α from 0.5 is indicative of interacting TLS leading to weaker power dependence of the quality factor. We observe a weaker power dependence for Dev 1, which suggests an increased TLS interaction for Device 1. All devices exhibited a similar power-independent internal quality factor (Q_{i0}) between 13,000-14000 as well as similar $F\tan\delta$ suggesting a similar density of electrical TLS on RE/superconducting surfaces across the wafer scale.

The presence of magnetic and electrical TLS suggests further improvement in device performance and/or spin coherence times by optimizing the annealing conditions to heal bulk defects in Y_2O_3/Si and passivization techniques to remove surface spins on rare earth/niobium surface.

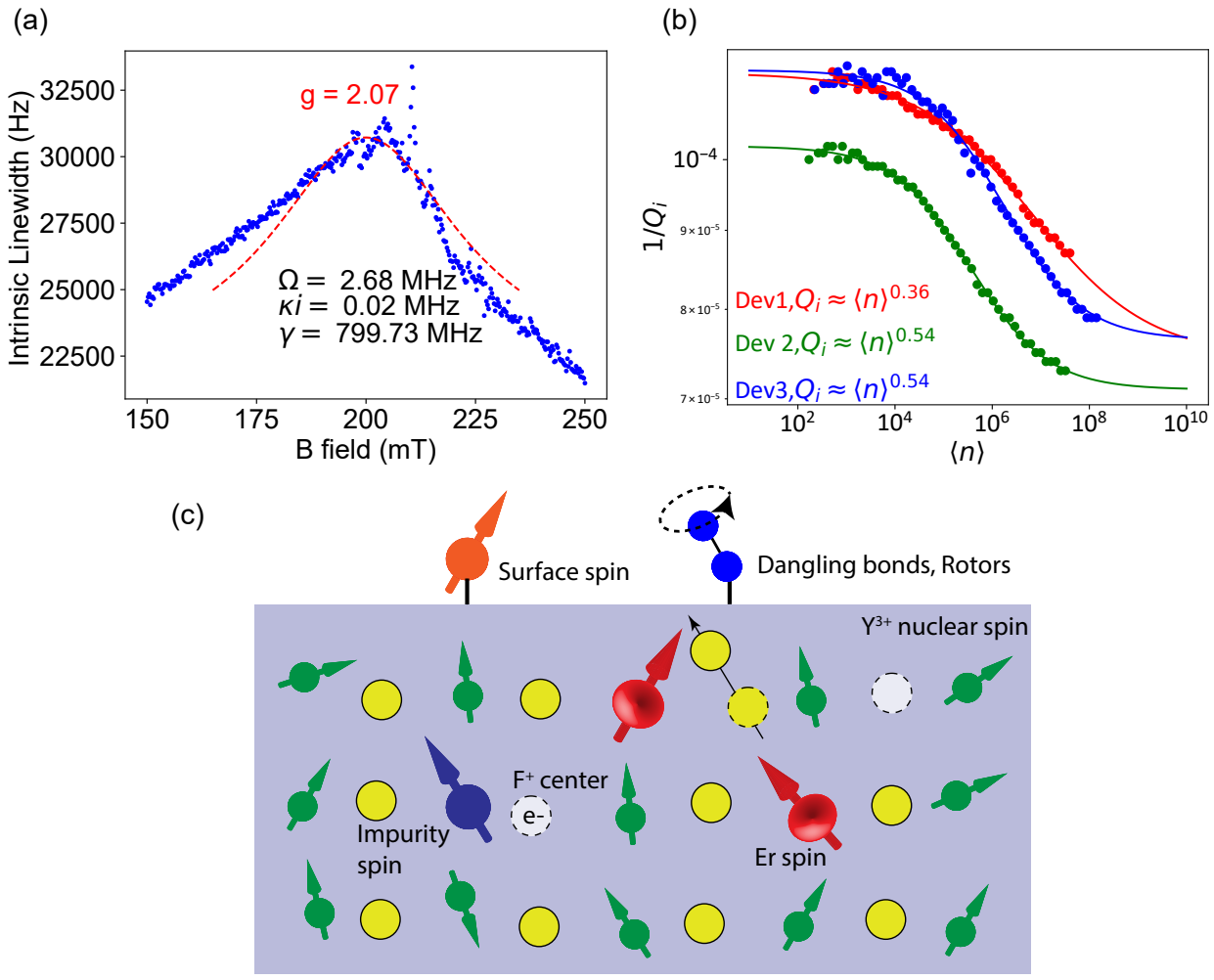


Figure 6.29: Magnetic and electrical TLS in rare-earth/superconducting hybrid device (a) A broad g=2 feature was observed along with a smaller satellite peak CW-ESR scans suggesting the presence of magnetic TLS for the device used in Fig 2. The magnetic TLS could be attributed to paramagnetic defects or impurities in the bulk of material or surface spins (b) Electrical TLS: Power-dependent quality factor measurements on three different devices from Fig. 6.21. indicate the presence of electrical TLS (c) Noise sources in rare-earth/superconducting hybrid devices: Magnetic TLS such as paramagnetic impurities, surface spins, defects, Er in different sub-sites, and electrical TLS such as dangling bonds and vacancy defects can be a significant source of loss and decoherence in hybrid devices.

6.5 Towards high cooperatively Er^{3+}spins-resonator coupling

The film used in this measurement had a high doping ≈ 200 ppm, which could be useful for applications requiring high cooperativity coupling of spins to a superconducting resonator

such as microwave to optical upconversion.

Device design and characterization

The resonator exhibited a frequency of 5.96 GHz, loaded Q of 5000 at 7 milliKelvin, with an external Q of 7000 and intrinsic Q of $\approx 12,000$ in low power limit (Section 6.5.3). $Er^{3+} : Y_2O_3$ thin film was mounted on the resonator using the flip-chip technique and spatially confined above the inductor in order to avoid dielectric losses from the strong electric field above the IDF capacitor

6.5.1 Continuous wave ESR

ESR spectroscopy was performed on Y_2O_3 film with 640 nm Er^{3+} doped layer and 40 nm top capping and 40 nm buffer layer between Y_2O_3 and Si. A 3-axis vector magnet was used to scan the B field in the plane of the resonator. The resonator spectrum was monitored with a vector network analyzer at an on-chip power of ≈ -80 dbm, and the magnetic field was ramped in steps of 0.25 mT.

The field was scanned in the range of 0 - 150 mT and the in-plane angle of the field was varied from -25 to 15 degrees with respect to the magnet x-axis. Er^{3+} in C_2 symmetry site occupies 6 orientationally inequivalent subsites with two sites with symmetry axis (g_z principal axis) along crystallographic [1,0,0], [0,1,0] and [0,0,1] direction each. Therefore, 3 sets of ESR lines are expected when the B field is scanned in the plane of the resonator, perpendicular to the crystallographic [111] direction as shown in dotted lines Fig. 6.30a. The observed broadening of resonator linewidth closely matches the predicted transition fields based on the anisotropic g tensor of C_2 site and confirms the coupling of Er^{3+} spins from C_2 site to the superconducting resonator. Magnetic field alignment procedure, which was described in Section. 6.4 was not applied to the measurements on this device, as a result, the resonator frequency suffered with drifts and jumps induced due to flux tuning, and this prevented the acquisition of spin resonance signal from the dispersive frequency shifts.

Coupling of spins with the resonator results in an increase of resonator linewidth κ following the expression [58],

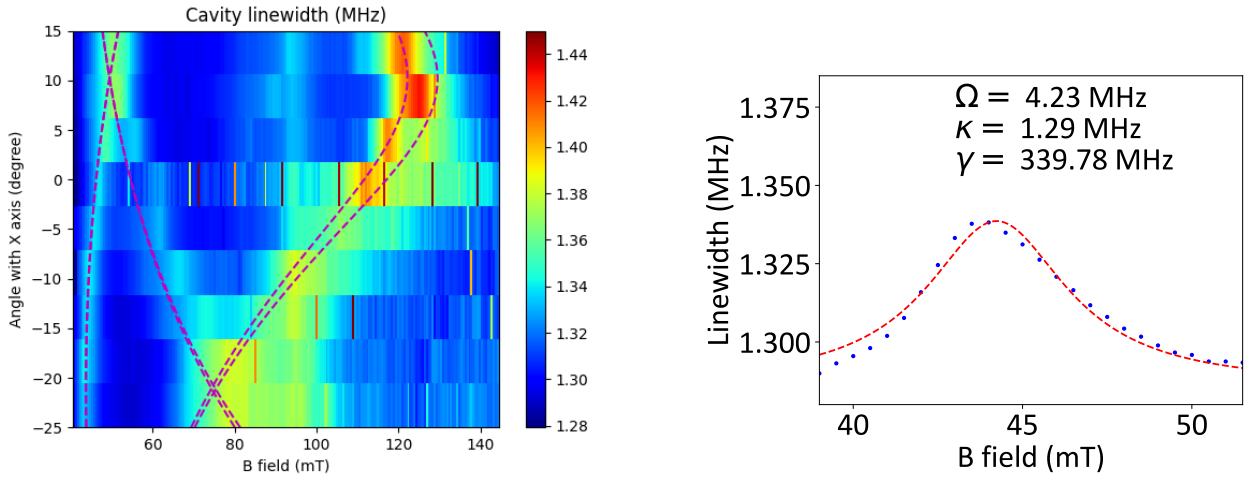
$$\kappa = \kappa_0 + \Omega^2 \gamma_s / (\gamma_s^2 + \Delta^2) \tag{6.13}$$

where κ_0 is the resonator linewidth off-resonant to spins, γ_s is the spin inhomogeneous half-width and $\Delta = g\mu_B(B - B_0)/\hbar$. We fit the above expression to the low field transition observed at -15 degrees scan (Fig. 6.30b) and obtain an ensemble coupling Ω of 4.23 MHz and inhomogeneous half-width γ of 339 MHz for 45 mT (g=9.4) transition. The narrowest inhomogeneous linewidth for this sample is 5 times larger than the linewidth measured for the lower density sample, indicating the accumulation of strain for higher density of Er^{3+} or an increase in spin-spin interaction.

A stronger linewidth broadening for higher field transitions in Fig. 6.30a is due to a higher ac g factor (g_1) of high field (low g) transitions [136]. The highest cooperatively of C=$g^2/\kappa\gamma = 6.8^2/(1.2 * 330)$=0.115 was obtained for the high field transition at 120 mT magnetic fields and angle of 5 degrees in Fig. 6.30a. With intrinsic quality factors Q_i up to 3×10^6 already demonstrated, we can expect cooperatively values approach 400 by utilizing similar high-Q devices on the current sample. This anticipated high cooperativity coupling is on par with the best demonstrations on Er^{3+} in bulk single crystals.

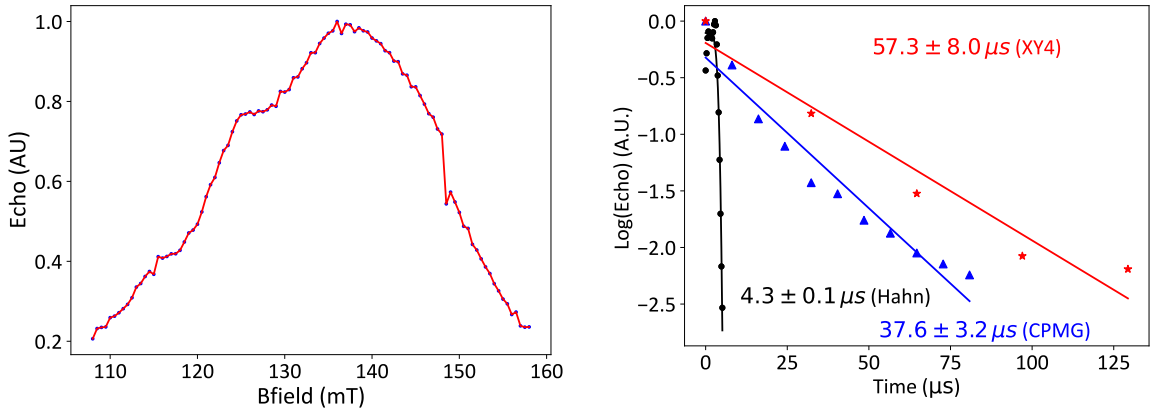
6.5.2 Spin coherence and relaxation time in high Er^{3+} density sample

We choose the lowest g (3.4) transition of the C_2 site at 125 mT to perform pulsed ESR measurements at 7.5 milliKelvin. 200 ns long pi and pi/2 pulses were generated using IQ upconversion and peak on-chip pi pulse power was estimated as 12 nW. Spin echo was preamplified by TWPA at 7 mK stage, operating at a gain of +15 dB for optimum SNR and further amplifier by HEMT at 4 Kelvin stage.



(a) (b)

Figure 6.30: (a) Continuous wave-ESR on high doping sample shows the cavity linewidth as a function of the in-plane angle of the field. The cavity linewidth shows a strong broadening signal, which is consistent with predicted transitions from C_2 site (b) Spin inhomogeneous linewidth of 339.8 MHz was measured for low field transition at -15 degree angle. A relatively large linewidth for the higher Er^{3+} density samples indicates the accumulation of strain and increased spin-spin interaction.



(a) (b)

Figure 6.31: (a) Echo vs field sweep spectrum obtained by performing two-pulse echo measurement as a function of the magnetic field. The peak at 125 mT corresponds to Er^{3+} in C_{3i} site while the peak around 135 mT could be likely from C_2 site (b) Spin coherence time for 125 mT transition was measured to be 4.3 μs with two pulse echo, 37.6 μs with CPMG and 57.3 μs with XY4 dynamical decoupling.

Spin coherence time

We perform two pulses (Hahn) echo measurements at a pulse separation τ= 4 μs and sweep the magnetic field in 110 to 160 mT range at an applied in-plane angle of 15 degrees(Fig. 6.31a). We observe a spin echo signal from the C_2 high field transition at 125 mT as well as a peak at 140 mT, which could be attributed to C_{3i} site.

We perform two-pulse echo spin coherence time measurement by sweeping separation τ between pi and pi/2 pulses and observe a fast decaying signal fitted with stretched exponential of the form $\exp(-2\tau/T_2)^n$ (Fig. 6.31b,black). The fitted $T_{2,\mathrm{Hahn}}$ of 4.3 μs and large stretch factor of 5.4 [168] suggesting fast spectral diffusion noise. Dynamical decoupling sequences can be utilized to mitigate spectral diffusion [177]. We observe an increase in coherence time with CPMG sequence ($T_{2,\mathrm{CPMG}}$) to 37.6 μs ((Fig. 6.31b, blue)) and further improvement to 57.3 μs with more robust XY4 sequence ((Fig. 6.31b, red)).

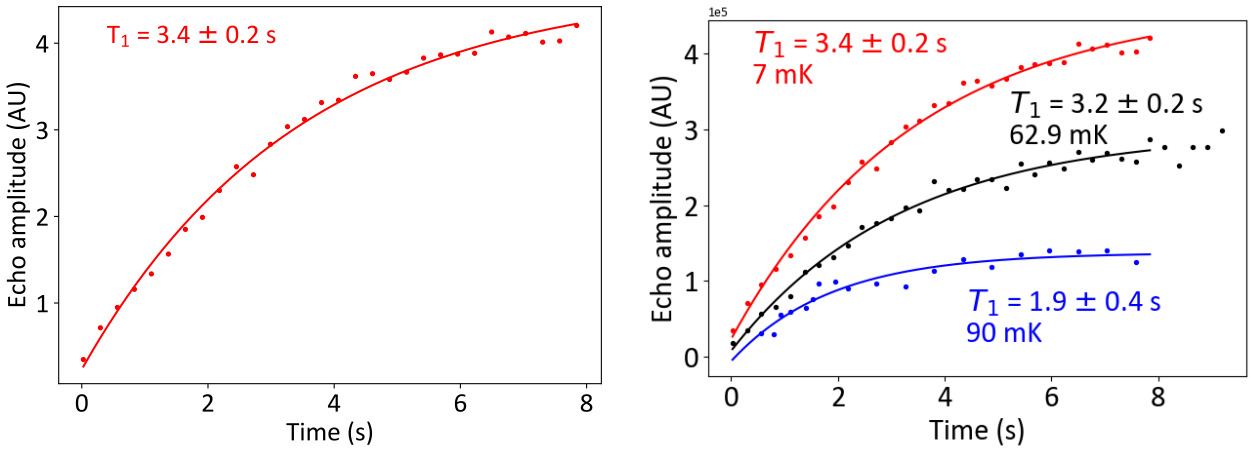
Spin relaxation time

Spin relaxation time T_1 was measured using a saturation recovery sequence with a 10 ms saturation pulse and pi/2, pi pulse with a separation of 4 μs. The spin echo shows a slow recovery with a $T_1 = 3.4$ seconds (Fig. 6.32a). Spin T_1 showed weak temperature dependence (Fig. 6.32b) and no dependence on MW frequency offset from the resonator suggesting direct process limited relaxation.

Spectral diffusion

To study spectral diffusion dynamics, we performed three pulse (stimulated) echo measurements. Waiting time T_W between the second and third pulses was scanned in the range of 10 μs to 1 ms for different values of τ. The echo amplitude decays as a function of pulse delays τ, T_W can be expressed as [112],

$$\frac{A(\tau, T_W)}{A_0)} = \exp\Big[\frac{T_W}{T_1} + 2\pi\tau\Gamma_{\mathrm{eff}}\Big] \tag{6.14}$$



(a) (b)

Figure 6.32: (a) Long spin relaxation time of 3.4 s was measured for the 125 mT transition C_{3i} at 7 milliKelvin (b) Spin relaxation time vs temperature for 125 mT transition. A weak dependence of spin lifetime on temperature up to 90 mK indicates a direct process-dominated spin relaxation.

where Γ_{eff} is the effective linewidth given as,

$$\Gamma_{\text{eff}} = \Gamma_0 + \frac{1}{2}\Gamma_{\text{SD}}(\text{R}\tau + 1 - \text{e}^{-\text{RT}_\text{W}}) \tag{6.15}$$

The term Γ_{SD} represents the spectral diffusion linewidth due to dipolar coupling with environmental spin bath, R represents the effective spin-flip rate, and Γ_0 represents spectral diffusion on a short timescale ($< 10\,\mu$s), instantaneous diffusion and homogeneous linewidth. We obtained $\Gamma_{\text{SD}} = 117$ kHz and R$= 2.3$ kHz, which is comparable with slow spectral diffusion previously reported in bulk rare-earth doped crystals [70]. The short timescale linewidth Γ_0 includes the contribution from instantaneous diffusion and homogeneous linewidth [59]. Nevertheless, we show spectral diffusion can be mitigated with XY4 dynamical decoupling close to the instantaneous diffusion limit, which can be further improved in samples with lower Er density.

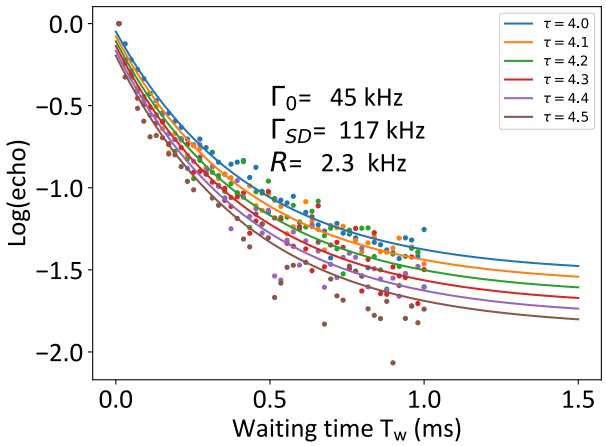


Figure 6.33: Threepulse echo measurement on the C_2 125 mT transition. A spin-bath flip rate R of 2.3 kHz measured here is 10 times larger than the measurement on the low-density sample in Section. 6.4.2, indicating a strongly interacting dense Er^{3+} spin-bath.

6.5.3 Magnetic and electrical TLS on rare-earth/superconducting surface

Magnetic TLS

The observation of a broad ESR signal with g ≈ 1.98 (Fig. 6.34a) is indicative of paramagnetic species, which would be 93% polarized at 125 mT, and contribute significantly to magnetic spectral diffusion due to flip-flops. The observed g ≈ 1.98 impurity signal suggests the presence of F^+ center in Y_2O_3, which contains oxygen vacancy with trapped electron [104]. This shows further improvement in coherence time is possible with optimized MBE growth conditions as well as post-growth annealing to reduce the density of paramagnetic oxygen defects. Further, due to a high Er^{3+} density (≈ 170 ppm), erbium spin flip-flops could also contribute to spin decoherence, therefore, a reduction of Er^{3+} density to $\mathcal{O}(10)$ ppm would also enhance the coherence time.

Electrical TLS

We also observe a signature of coherent electrical TLS as a background echo signal for all devices when measuring at a frequency off-resonant to the superconducting resonator (Fig. 6.34b), which is attributed to TLS coupling to the transmission line. The TLS echo exhibits no magnetic field dependence in (0-0.5 Tesla range) and a $T_2 \approx 1.5$ μs and short spin

Q_{i0}	Ftanδ	nc	α
64303	7.2×10^{-5}	1.2×10^{6}	0.26

Table 6.4: Power dependence fit parameters for superconducting devices used in Fig. 6.30a.

T_1 of 5.6 μs (Fig. 6.34c) The TLS signal was also observed in a range of devices, including the devices with Nb patterned directly on Y_2O_3 as well as the devices described in this manuscript with Nb patterned on silicon at Y_2O_3 bonded over the inductor with flip-chip. The latter devices had an insignificant overlap of the rare-earth doped thin film with the coplanar waveguide field and this suggests the electrical TLS could originate from niobium surface oxides. While the TLS shows coherent properties, its presence poses a challenge to detecting the spin echo signal over a constant background and it could play a role in reducing the resonator loss rate as well as decoherence of superconducting qubits due to a short T_1.

Power dependence quality factor measurements were also performed on the device to obtain the TLS parameters. Fig. 6.34d shows the inverse of intrinsic quality factor (Q_i) as a function of the number of photons in the microwave resonator $\langle n \rangle$. The data were also fitted to the model [50],

$$\frac{1}{Q_i} = \frac{1}{Q_{i0}} + \frac{F\tan\delta}{(1 + (x/nc)^{\alpha})} \tag{6.16}$$

where Q_{i0} is the quality factor due to power-independent losses, in the low power limit Ftanδ is proportional to the TLS loss tangent δ times the filling factor F in the resonator, nc is the critical photon number for saturation and α is the exponent of the power dependence. The fitting parameters are shown in Table 6.4 and fit in Fig. 6.34d. The observed $\alpha = 0.26$ is indicative of interacting TLS leading to weaker power dependence of the quality factor. We observe a weaker power dependence for the device with a high density of Er^{3+} as compared to devices with a low density of Er^{3+} measured in Fig. 6.29 and table. 6.3.

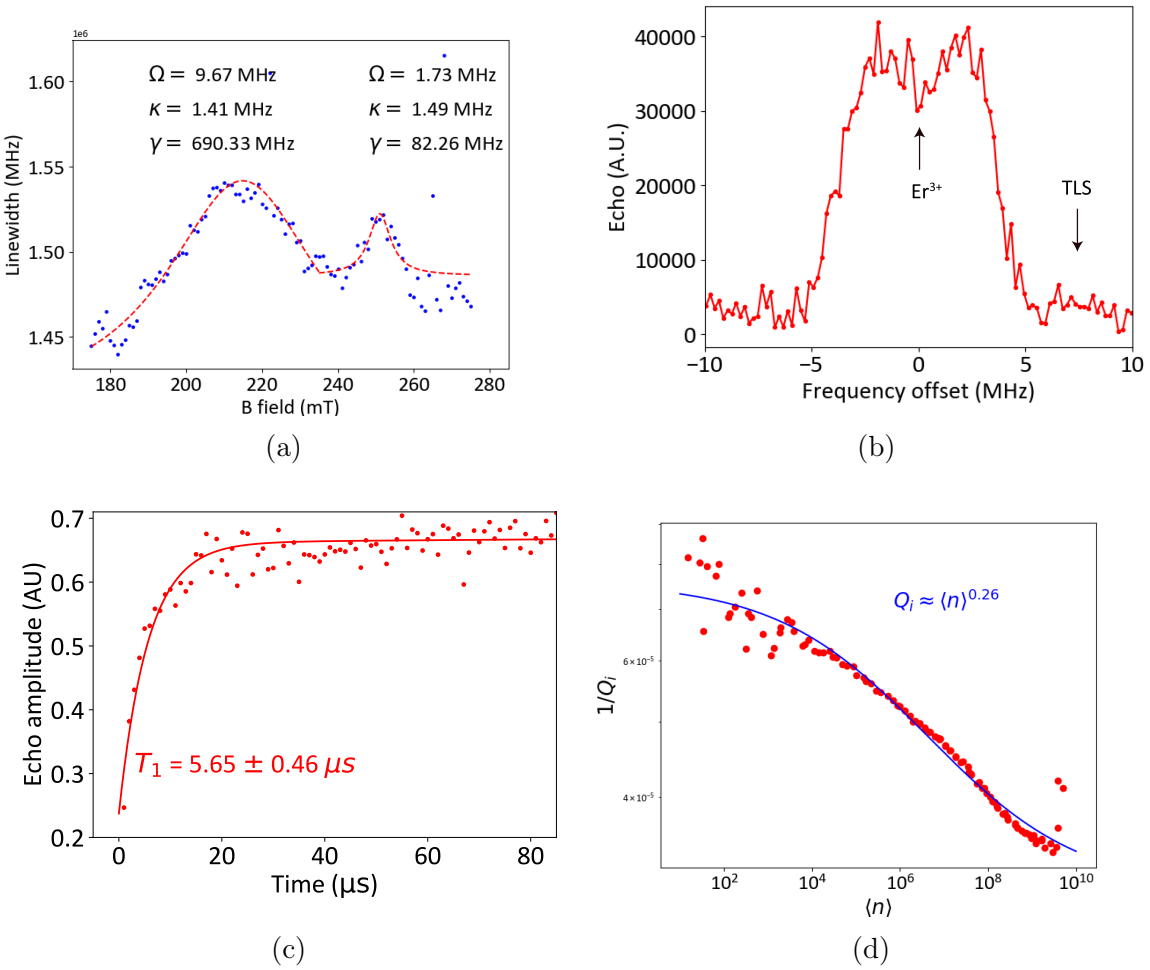


Figure 6.34: Noise from rare-earth superconducting interfaces in ESR device (a) Signature of magnetic TLS was observed in CW-ESR scans as g=2 signal along with a smaller satellite peak. The g=2 signal could be attributed to surface spins or paramagnetic specie in the bulk of material while the smaller satellite peak can be attributed to surface hydrogen (b) Measuring spin echo while scanning microwave frequency across the superconducting resonators shows a fast decaying broadband background signal off-resonant to the resonator. This suggests coupling of electrical TLS to superconducting coplanar waveguide (c) Observed electrical TLS signal shows fast relaxation with timescale 5.6 μs (d) Resonator intrinsic quality factor (Q_i) shows weak dependence on intracavity photons $\langle n \rangle$ suggesting interacting TLS.

6.6 Discussion

We have demonstrated the coupling of Er^{3+} spins in Y_2O_3 to high-quality superconducting low impedance resonators. Measurements on high-density sample show coupling to resonator with cooperativity of 0.1, which can be significantly improved beyond 1 by modest

improvement in the device design and optimization of material growth to demonstrate narrow inhomogeneous linewidth. This high cooperativity coupling will enable technologies such as microwave-to-optical transducers, and ensemble microwave quantum memories. High-density samples, however, suffer from a faster spin relaxation with $T_2 = 57\,\mu$s due to interaction with a dense spin bath of other Er^{3+} spins. The coherence time was improved significantly with samples with lower Er^{3+} density approaching 1.7 ms, which is on par with or exceeding demonstrations on Er^{3+} doped bulk crystals. Further, long spin relaxation times of seconds and spin coherence times exceeding ms were demonstrated on a wafer scale in the low-density sample. A comprehensive study of two-level systems in the hybrid devices was performed, which indicated the presence of magnetic and electrical TLS, which could offer insight into the dynamics and structure of TLS.

A combination of long coherence times along with the demonstrated Er^{3+} spin-coupling to superconducting resonators will enable the development of rare-earth ion-based scalable hybrid systems.

CHAPTER 7

OPTICALLY ADDRESSED SINGLE ERBIUM IN YTTRIUM OXIDE THIN-FILMS

7.1 Introduction

This chapter discusses optically addressed Er^{3+} qubits in epitaxial thin films. The measurements on C_2 site were all performed by Dr. Yizhong Huang and measurements on C_{3i} were performed by Shihan Liu.

Er^{3+} doped Y_2O_3 single crystal thin-films have been grown with molecular beam epitaxy (MBE) on silicon along the crystallographic direction [111]. Er^{3+} substitutes Y^{3+} in two sites, a lower symmetry C_2 site with electric and magnetic dipole allowed optical intra-4f ($^4I_{15/2}\,Z_1 \rightarrow^4 I_{13/2}\,Y_1$) transition as well as a higher symmetry C_{3i} with magnetic dipole only optical transition. A rich site symmetry of Er^{3+} in Y_2O_3 allows for complete a characterization of electric and magnetic noise in the thin films. The magnetic dipole-only nature of C_{3i} site makes it first-order insensitive to electric field noise, making it ideal for applications requiring narrow linewidths.

Fig. 7.1 shows the schematics of the Er^{3+} qubit device, consisting of a tunable fiber Fabry-Perot cavity coupled to the 1.5 μm telecom-C band transition between the lowest-lying doublets (Z_1) and (Y_1) of the crystal field levels $^4I_{15/2}$ and $^4I_{13/2}$ respectively and the superconducting microwave resonator coupled to the $\approx$ 6 GHz electron spin transition of the optical ground state $^4I_{15/2}$. Cavity-enhanced microwave-optical spectroscopy allows for correlated noise analysis on epitaxial thin films.

7.2 Erbium optical transition in yttrium oxide

C_2 site possesses both electric and magnetic dipole contribution to the linewidth leading to

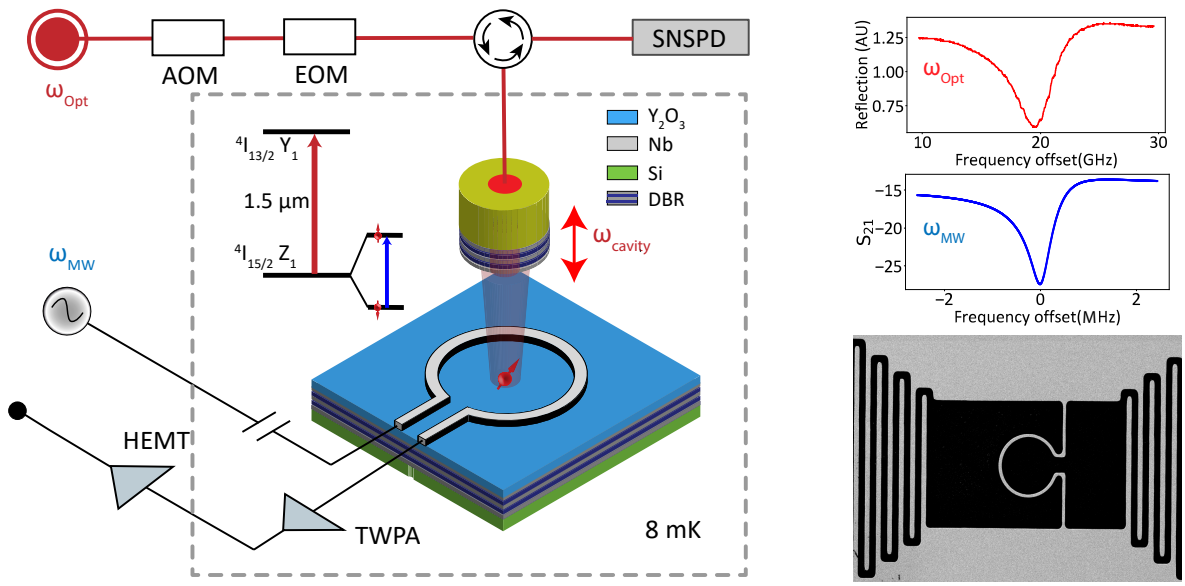


Figure 7.1: (a) Schematics of the experimental Er^{3+} qubit device concept. It consists of a tunable cryogenic fiber Fabry-Perot cavity coupled to ${}^4I_{15/2}\,Z_1 \rightarrow {}^4I_{13/2}\,Y_1$ optical transition of Er^{3+} in Y_2O_3 and a low impedance superconducting microwave resonator coupled to Er^{3+} spin transition at 5.8 GHz. The illustration shows a coplanar superconducting resonator based on niobium. (b) The reflection spectrum of the fiber Fabry-Perot cavity shows a Q of $50,000 - 300,000$ and mode volume of $5(\frac{\lambda}{n})^3$. The superconducting microwave resonator shows low power intrinsic Q of $\approx 12,000 - 370,000$ and an estimated maximum single spin coupling strength $\approx$ 4 kHz. SNSPD: superconducting nanowire single photon detector; TWPA: traveling wave parametric amplifier; HEMT: high electron mobility transistor.

sensitivity to magnetic and electric fields as well as an overall stronger dipole moment with an optical lifetime of 8.5 ms. These properties make Er^{3+} in C_2 site ideal for application as cryogenic quantum sensor.

C_{3i} site, due to its high symmetry, has a zero first-order sensitivity to electric fields making it suitable for applications in quantum memory requiring narrow optical linewidths for the emission of indistinguishable photons. Further, due to a high symmetry, the principal axis of the optically ground and excited state g tensors are aligned leading to a high cyclicity

optical readout of the spin transition [140].

7.3 Cryogenic fiber Fabry-Perot cavity

7.3.1 Setup and characterization

The fiber Fabry-Perot cavity is comprised of a distributed Bragg reflector (DBR) stack deposited on a fiber dimple, forming the top mirror of the cavity and allowing for high-efficiency coupling of light into an optical fiber and a bottom DBR mirror below the Er^{3+} doped Y_2O_3 thin-film. For preparing the bottom mirror with the sample, the thin-film and DBR mirrors are diced into chips and put in hot N-Methyl-2-pyrrolidone (NMP) for >5 hours for cleaning. Following the NMP dip, the mirror, and thin-film samples are cleaned with solvents (acetone/IPA) with ultrasonic sonication and finally cleaned in water and dried with N_2. The thin film sample with 100 nm thickness is bonded on the mirror using the HSQ e-Beam resist. A few drops of hydrogen silsesquioxane (HSQ) are placed on the thin-film surface and spin-coated at 3000 rpm, and 1000 rpm for 60 s. The thin film is then placed on the mirror, with the top surface facing the distributed Bragg reflector (DBR) mirror, and the two samples are brought in close contact using tweezers. The samples are pressed together using a homebuilt clamp and baked on a hot plate at 250 °C for an hour. The samples are then allowed to cool and removed from the clamp and annealed in rapid thermal processing (RTP) tool at 600/500 °C in air for 1 hour, which turns the HSQ to thermally stable oxide. Finally, once the bonding is successful, the back silicon handle is removed from the thin film by etching under a deep silicon etch (DSE) tool to remove $\approx$ 0.385 mm of the 0.5 mm silicon later. The remaining silicon layer is etched using the XeF_2 tool and any leftover island of silicon is further removed using potassium hydroxide (KOH) wet etch. A spacer layer of SiN was deposited on the film to coarsely adjust the cavity length. The fiber tip containing the top mirror is mounted on a fiber chuck from Thorlabs and held in place with

thin copper shims. The shim is glued in place with epoxy to secure the fiber. The fiber chuck is subsequently loaded on the setup and the fiber tip and the thin-film sample with mirror are bought in contact to form a $3\lambda/2$ thickness layer stable cavity. The bottom mirror with the sample was placed on a piezoelectric nanopositioner allowing for coarse tuning of cavity frequency in the range of 80 nm by the coarse piezo scan as well as fine-tuning with a rate of 1.29 GHz/V by adjusting the piezo voltage. The optical setup comprised three acousto-optic modulators (AOM) in series for the generation of pulses with a high extinction ratio of (180 dB) and an electro-optic modulator (EOM) for a fine sweep of the laser frequency. Photoluminescence from erbium was counted by a superconducting nanowire single photon detector (SNSPD).

7.3.2 Mode volume and quality factor

At the rigid contact, we find the cavity length to be $3/2\lambda$ with a measured quality factor (Q_{exp}) of 50,000. The mirrors have a reflectivity R of 0.99985, which allows for estimating the theoretical quality factor of a Fabry-Perot cavity as,

$$Q_{th} = \frac{2\pi(nL)}{(\lambda/n)(1-R^2)} \tag{7.1}$$

where n≈2 for the silicon oxide spacer layer, L= 2.25 μm. Plugging in these numbers we obtain a theoretical quality factor Q_{th} of 125,673, which is higher than the experimental quality factor Q_{exp} and indicates a decrease in the quality factor due to effects such as scattering from sample surface or air gaps in the bonded film. Indeed quality factors as high as $150,000$ were measured on the bare mirrors without Y_2O_3 thin-film indicating a further improvement in the quality factor by optimization of the sample surface/bonding technique as well as by addition of an XY translation stage in the sample stack to allow access to different points on the sample chip.

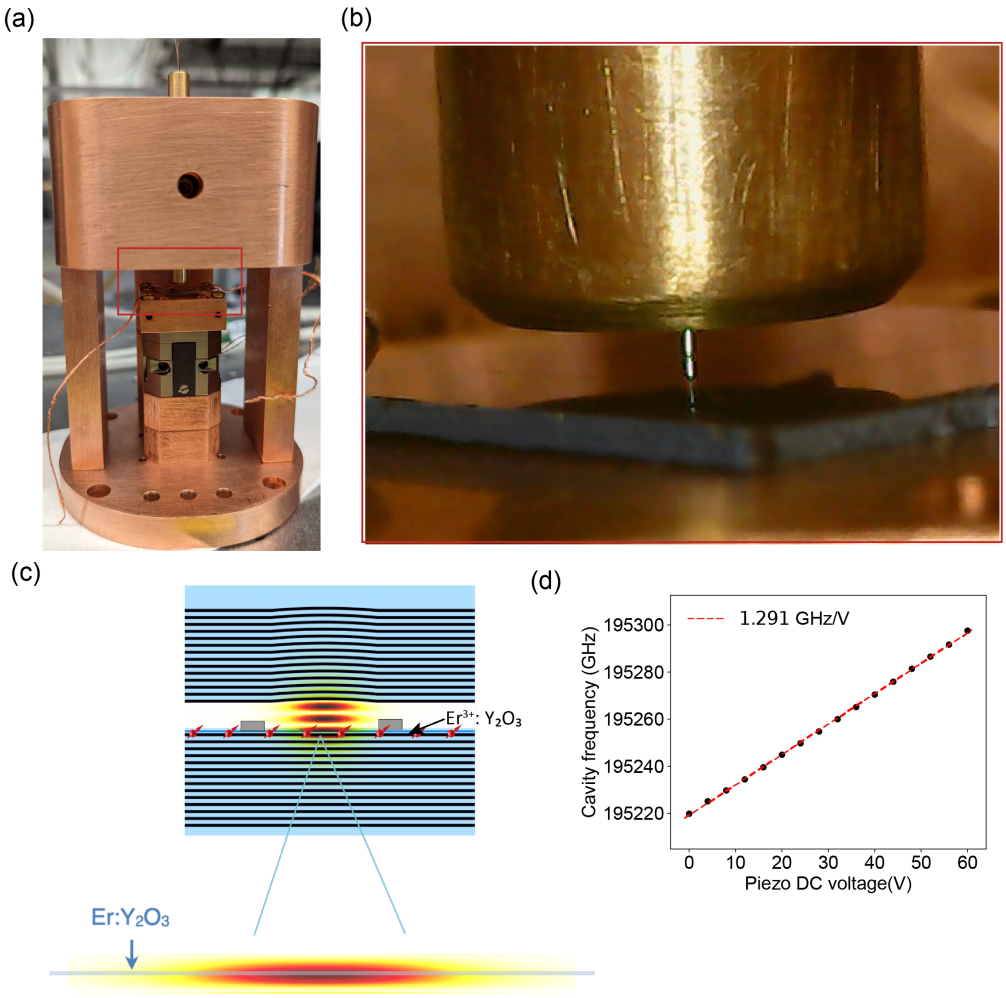


Figure 7.2: (a) The cryogenic mount for the fiber Fabry-Perot cavity consists of a bottom mirror and sample sitting on a nanopositioner (b) Fiber with top mirror is mounted on a fiber chuck and nanopositioner is moved to bring the sample in contact with top mirror (c) The cavity operated in $3\lambda/2$ length. The optical mode shows maximum overlap with the Y_2O_3 thin film (d) The cavity can be fine-tuned with piezo voltage with a rate of 1.3 GHz/V.

7.3.3 Cavity tuning and operation

The fiber cavity allows for fine-tuning over 80 GHz with piezo voltage with a slope of 1.3 GHz/V (Fig. 7.2(d)). Coarse tuning over the stepped piezo mode allows for a scan over a range larger than 20 nm.

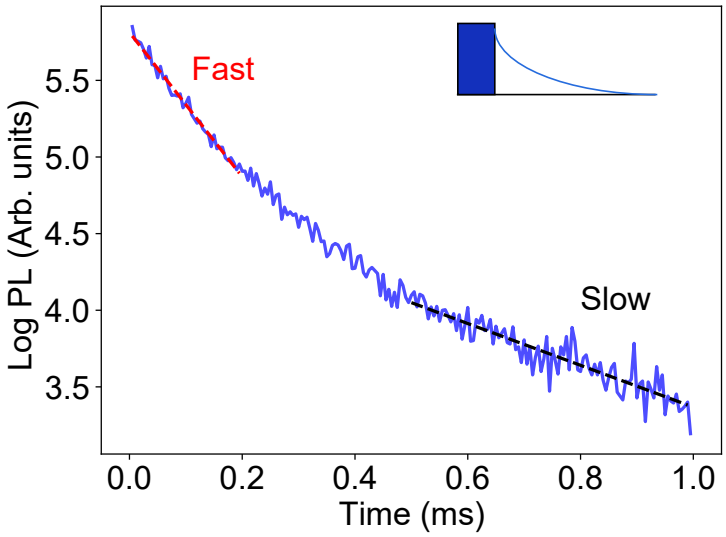


Figure 7.3: Photoluminescence after an excitation pulse shows a range of decay rates between a fast and a slow PL decay rate due to a distribution of Purcell enhancement rates among different ions.

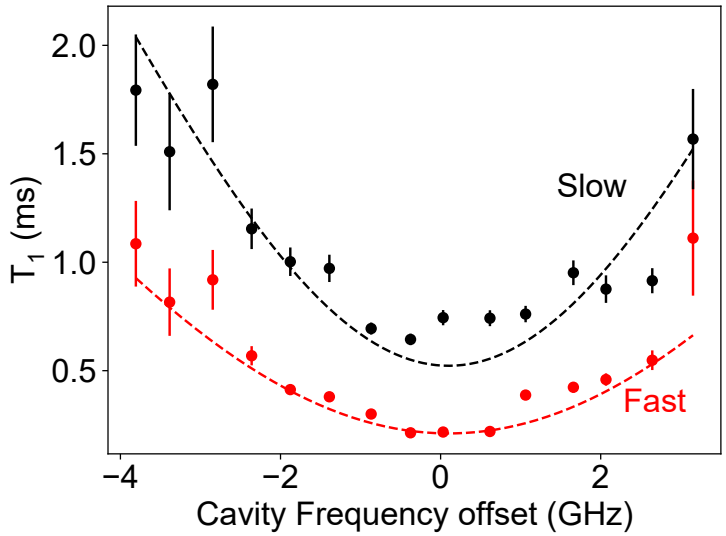


Figure 7.4: Fast and slow PL decay rate, as a function of detuning between the laser and the cavity center show close agreement with the Purcell enhanced T_1 model.

7.4 Er^{3+} ions in C_2 site addressed with fiber cavity

The samples used in this section had a thickness of 100 nm and a magnetic field of 350 mT was applied along (111) the direction using a permanent magnet. Fig. 7.3 shows the

logarithm of PL as a function of time after the excitation pulse. The log of PL shows a distribution of decay rates, with a fast decay with $T_1 = 0.21$ ms and a slow decay with $T_1 = 0.73$ ms. This indicates the presence of ions with varying coupling strength (g) to the fiber cavity leading to a distribution of the Purcell enhancement from the cavity. This can be explained from a Gaussian mode profile in the transverse direction (Fig. 7.2(c)) where ions closer to the center of the mode experience a stronger field as compared to ions towards the edges of the mode.

7.4.1 Purcell enhancement of the spontaneous emission

Purcell enhancement refers to the enhancement of the spontaneous relaxation rate of an atom on-resonant to a cavity. The cavity enhances the density of states (DOS) by a factor proportional to the ratio of the (Q/V_m) of the cavity,

$$F_P = \frac{3}{4\pi^2 \chi_L^2} \left(\frac{\lambda}{n}\right)^3 \frac{Q}{V_m} \tag{7.2}$$

The Purcell enhanced T_1 depends on the detuning between the laser and the center of the cavity, following the expression,

$$\frac{1}{T_{1,cav}} = \frac{1}{T_{1,0}} \left(1 + \beta F_P \frac{(\gamma/2)^2}{((\gamma/2)^2 + \delta^2)}\right) \tag{7.3}$$

where $T_{1,cav}$ is the enhanced emitter decay measured from the cavity, $T_{1,0}$ is the intrinsic lifetime in absence of cavity enhancement, γ is the cavity linewidth, β is the branching ratio, F_P is the measured Purcell enhancement and δ is the laser detuning from the cavity center. Fig. 7.3 shows the measured T_1 as a function of detuning of the laser from cavity frequency, which shows close agreement with the fit based on equation 7.3.

7.4.2 *Single ion linewidth and Purcell enhancement measurement*

Individual Er qubits are coupled to the cryogenic fiber FP cavity described earlier and single ions were detected by sweeping the laser frequency using electro-optic modulators and collecting fluorescence with the laser locked to a gas cell to correct for long-term drifts. In order to detect single Er^{3+} ions the fiber cavity was tuned from the center of the inhomogeneous line, toward the tail of the distribution, and PL counts were registered as a function of the detuning from the center Δ in Fig. 7.5. We observe a scaling of the number of counts (N) with detuning Δ as $N = \Delta^{-1.6}$ and statistical fine structure (SFS) [210] towards the tail of the distribution indicative of discrete single ion spectra. The cavity was parked at the tail of the distribution in order to fine-scan for single ions.

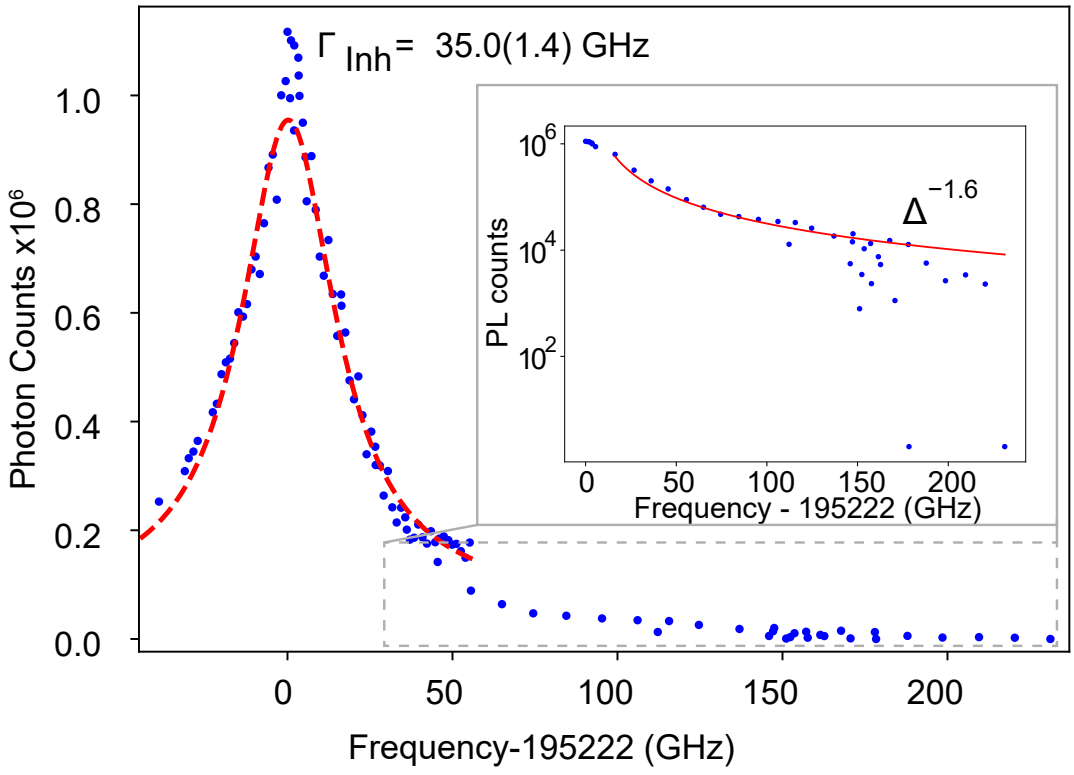


Figure 7.5: Inhomogeneous linewidth of Er^{3+} in C_2 site. Inset: Total PL counts (N) as a function of cavity detuning from the center of the inhomogeneous line for Er^{3+} in C_2 site.

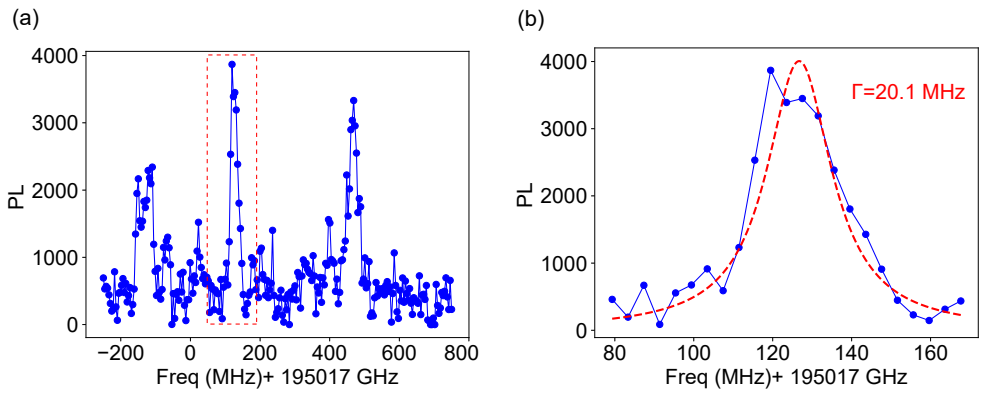


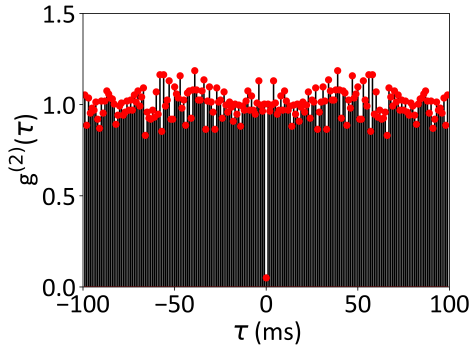
Figure 7.6: (a) Sharp lines from single ions from Er^{3+} in C_2 site (b) Fitted linewidth of single ion.

Fig. 7.6(a) shows several narrow lines potentially corresponding to single ions. Fig. 7.6(b) shows the zoomed-in scan on a highlighted feature. We observe a single ion linewidth of 20.1 MHz, which is comparable to the state of art [140], however, significantly broader than the transform limit of 2.2 kHz. This is primarily attributed to a high laser intensity with $\approx$ 11 MHz Rabi frequency. The remaining broadening of 9 MHz could be attributed to a combination of laser linewidth and electric noise. An applied magnetic field of 350 mT rules out broadening due to paramagnetic spin-bath as the residual source of broadening. An autocorrelation $g^{(2)}(\tau)$ analysis was performed on the time domain data for the feature and strong anti-bunching was observed in zero time bin with $g^{(2)}(0) = 0.06$ confirming a single ion (Fig. 7.7a).

Single Er^{3+} ion decay is Purcell enhanced from 8.5 ms to 0.14 ms (Fig. 7.8), which corresponds to an effective Purcell factor of 271.5 taking into account branching ratio ($\beta = 0.22$) for the decay from $^4I_{13/2}$ Y_1 to $^4I_{15/2}$ Z_1 [211],

$$F_P = \frac{(\tau_0/\tau_c - 1)}{\beta} = \frac{(8.5/0.14 - 1)}{0.22} = 271.4 \tag{7.4}$$

The Purcell factor F_P obtained here presents a lower limit on the maximum Purcell factor $F_{P,Max}$ due to misalignment between the dipole moment of Er^{3+} in the C_2 subsite and



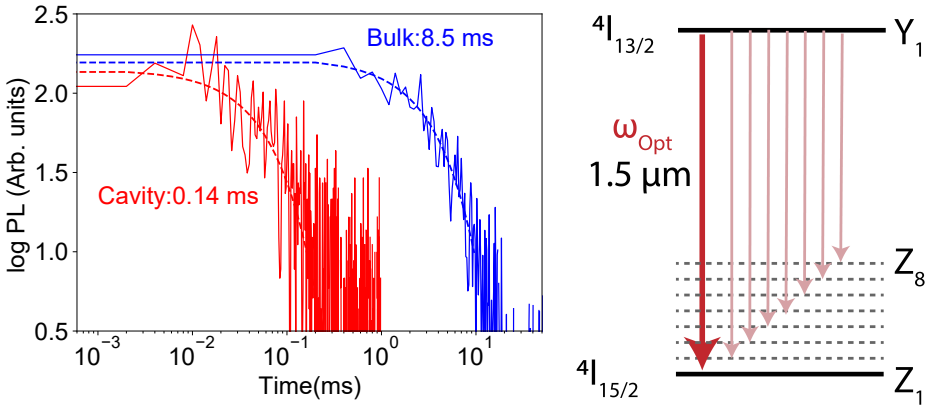
(a)

Figure 7.7: $g^{(2)}(\tau)$ autocorrelation measurement shows anti-bunching close to zero time bin with $g^2(0) = 0.06$ confirming emission from single Er^{3+}.

the cavity mode polarization. Nevertheless, this could be used to estimate the cavity mode volume (V_m) following equation7.2. Substituting for Q=50,000 (quality factor), $F_P = 271.5$ the measured Purcell factor, wavelength λ wavelength and the local correction factor to the electric field [210] $\chi_L = \frac{3n^2}{2n^2+1}$ in equation. 7.2 we get $V_m = 8.9\left(\frac{\lambda}{n}\right)^3$.

7.4.3 Homogeneous linewidth and spectral diffusion

The homogeneous linewidth and spectral diffusion broadened linewidth of a single ion can be studied by performing transient spectral hole burning technique (Fig. 7.9) [191]. The technique is based on the nonlinear dependence of the photoluminescence counts on the intensity of laser $\sqrt{I}$. The method involves creating two equal sidebands to the laser main band using electro-optic modulators (EOMs) and sweeping the separation between the sidebands by scanning the EOM frequency. The PL counts would show a $\sqrt{3I}$ dependence when the EOM sidebands are within the emitter homogeneous linewidth and as the sidebands are swept apart beyond single ion linewidth, the PL would saturate to $3\sqrt{I}$. This increase by a factor of $\sqrt{3}$ can be fitted to obtain the single ion half-width (Γ). The fitted linewidth is an upper limit on the homogeneous linewidth Γ_h as additional mechanisms such as power broadening, instantaneous spectral diffusion, and spectral diffusion can further increase the



(a) (b)

Figure 7.8: (a) Purcell enhanced decay time of single ion (T_1=0.14 ms) compared with bulk Er^{3+} (T_1=8.5 ms) in C_2 site corresponds to an enhancement factor of 50.1 (b) Taking into account the branching ratio (β=0.22) of the Er^{3+} optical transition in C_2 site, the effective Purcell factor is F_P = 271.4.

linewidth. In order to study the power and spectral diffusion contribution to the measured linewidth we further perform linewidth measurements as a function of laser power and the T_1.

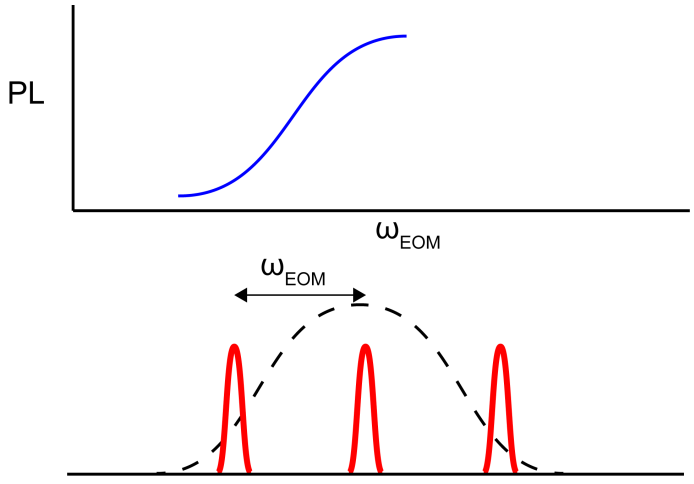


Figure 7.9: Transient spectral hole burning method measures the spectral diffusion broadened homogeneous linewidth.

Instantaneous spectral diffusion (ISD)

Excitation of Er^{3+} ions under driving pulses result in a sudden change in the resonance frequency of neighboring Er^{3+} ions leading to instantaneous spectral diffusion [143]. This leads to a dependence on the laser power(intensity) described as [180],

$$\Gamma = \Gamma_0 + \Gamma_{\mathrm{ISD}}(1 - \mathrm{e}^{-\mathrm{cP}}) \tag{7.5}$$

where Γ_0 is the linewidth of the ion in the absence of ISD, including homogeneous linewidth and spectral diffusion on a short timescale, Γ_{ISD} is the maximum linewidth broadening due to ISD and c is a constant [180]. The data in Fig. 7.10 shows close agreement with the fitted eq7.5 and allows us to extract $\Gamma_{\mathrm{ISD}} = 60$ MHz, $\Gamma_0 = 5.6$ MHz indicating a strong interaction between Er-Er, which could be used for performing fast two-qubit gates.

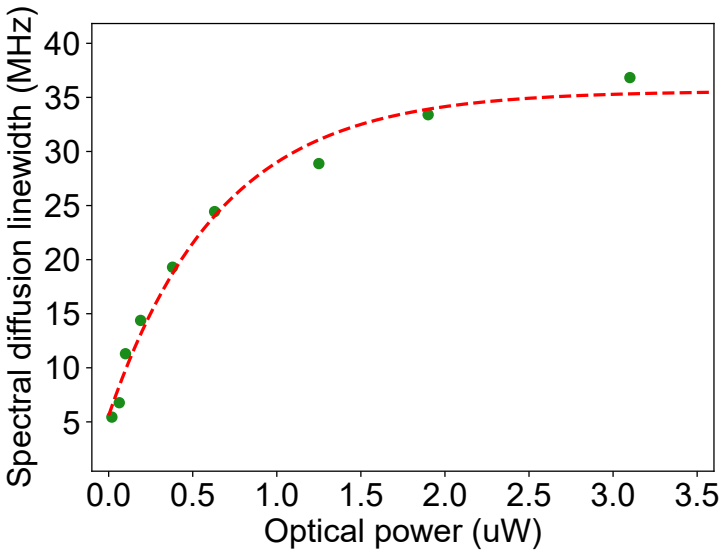


Figure 7.10: Spectral diffusion linewidth measured as a function of laser power shows close agreement with instantaneous spectral diffusion. Red dashed lines indicate fit to the model.

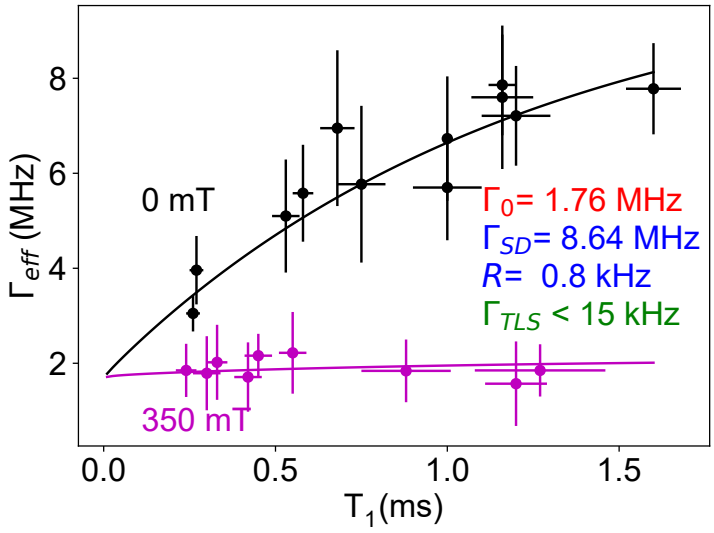


Figure 7.11: Changing laser detuning from cavity frequency allows tuning of Er^{3+} T_1 . Optical spectral diffusion measurement using transient spectral hole burning at zero fields (black) and 350 mT fields (violet) lines show freezing of magnetic spectral diffusion with an applied magnetic field.

Spectral diffusion as a function of T_1

Purcell enhancement from the cavity and therefore the T_1 can be tuned by changing the detuning between the laser and the center of the cavity, following the eqn. 7.3 as shown in Fig. 7.4. Fig. 7.4 shows the measured T_1 as a function of detuning of the laser from cavity frequency, which shows close agreement with the fit based on equation 7.3. Therefore by tuning the detuning between the cavity and laser, we can tune the Er^{3+} lifetime, which will allow for control of the duration of spectral diffusion-induced homogeneous linewidth broadening. Therefore, we perform transient spectral holeburning measurements in the low power limit ($\approx$) nW to reduce the broadening induced by ISD and power broadening.

Figure 7.11 shows the effective linewidth Γ_{eff} measured as a function of T_1 obtained by varying the detuning from the cavity frequency. Two sets of linewidth measurements are performed, at zero-field (black dots) and applied field of 350 mT (violet dots). The zero field linewidth measurement shows broadening with T_1 indicating the presence of a slow spectral diffusion on ms timescale. Application of magnetic field leads to a reduction of the linewidth

along with a weak dependence on T_1. The linewidth broadening trend can be modeled by a combination of broadening mechanisms,

$$\Gamma_{\text{eff}} = \Gamma_0 + \Gamma_{\text{SD,eff}}(1 - e^{-RT}) + \Gamma_{\text{TLS}}\log(T_1/t) \tag{7.6}$$

where Γ_0 is the linewidth in short timescale (t< 150μs) including homogeneous linewidth, fast spectral diffusion, superhyperfine broadening, and drift of laser during the measurement timescale, $P\Gamma_{\text{SD}}$ is the linewidth due to dipolar coupling to spin bath inducing spectral diffusion, R is the effective spin-bath flip rate and Γ_{TLS} is the dipolar coupling to electrical TLS. Further, $\Gamma_{\text{SD,eff}}$ has an explicit dependence on the nature and splitting of the spin bath and can be described as,

$$\Gamma_{\text{SD,eff}} = \Gamma_{\text{SD}}\,\text{sech}^2\Big(\frac{g_{\text{sb}}\mu_B B}{2k_B T}\Big) \tag{7.7}$$

where Γ_{SD} is the maximum dipolar coupling strength to the spin bath, g_{sB} is the effective g factor of the spin bath, B is the magnetic field and T is the temperature. We assumed g_{sB} =1.2, T= 100 mK, and fitted equation7.6 to obtain the parameters Γ_{SD}, Γ_0, Γ_{TLS} and R. The fitted parameter values as displayed in Fig. 7.11 indicate spectral diffusion induced by paramagnetic spin bath as the primary source of spectral diffusion at B=0, which is frozen by application of B = 135 mT. The contribution from electrical TLS is <0.01 MHz indicating the absence of slow spectral diffusion from electrical TLS. The short timescale linewidth Γ_0 of 1.76 MHz indicates broadening mechanisms such as short timescale spectral diffusion, superhyperfine broadening, and laser frequency drift as the sources of linewidth broadening. Indeed, homogeneous linewidths as narrow as 580 Hz have been reported for Er^{3+} in the same site [70], therefore the current linewidth is likely limited by laser drifts in the measurement timescale and could be improved further by stabilization of laser frequency by locking to a stable reference cavity.

7.5 Er^{3+} ions in C_{3i} site addressed with fiber cavity

7.5.1 Inhomogeneous linewidth

In order to measure PL from the C_{3i} site, the cavity frequency was scanned across the center of C_{3i} absorption at 1545 nm. A magnetic field of 350 mT was applied along the (111) direction for this measurement. An inhomogeneous of 48 GHz was measured, which could be broadened due to unresolved structure from different orientations of the g tensor of different C_{3i} subsites and therefore the measurement represents an upper limit on the inhomogeneous linewidth.

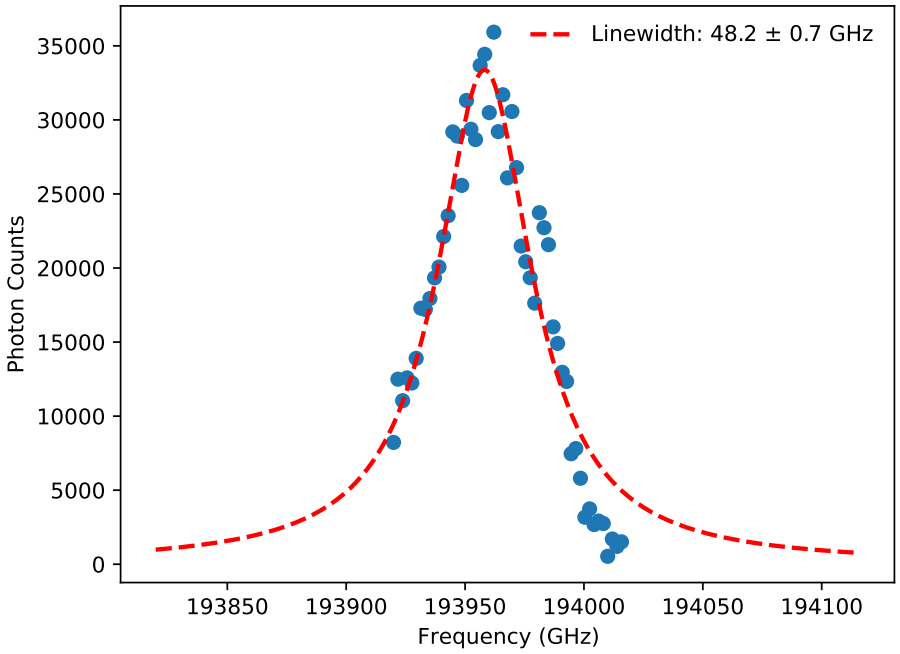
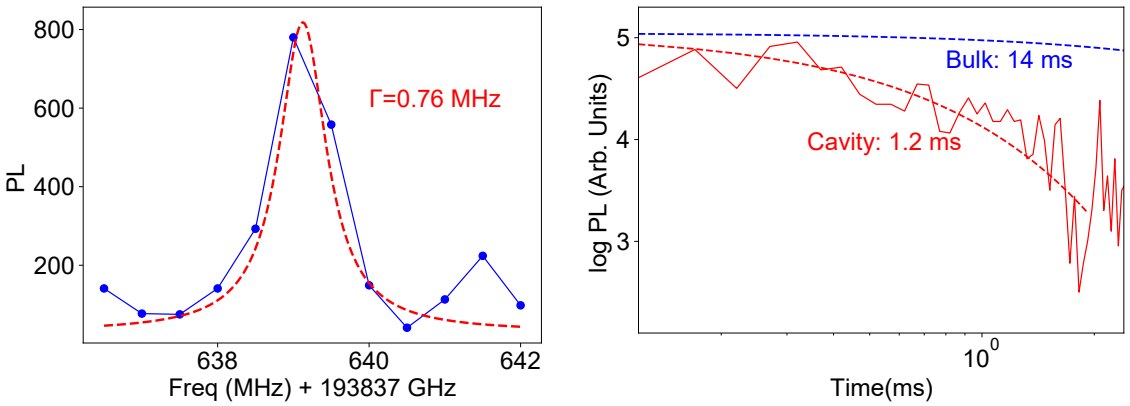


Figure 7.12: PL counts as a function of laser frequency measurement provides an inhomogeneous linewidth of 48.2 GHz for Er^{3+} in C_{3i} site.



(a) (b)

Figure 7.13: (a) Single ion linewidth of 0.76 MHz was measured for Er^{3+} in C_{3i} site at zero magnetic fields (b) Purcell enhanced decay of single ion compared with bulk Er^{3+} in C_2 site.

7.5.2 Single ion linewidth and Purcell enhancement measurement

Fig. 7.13(a) shows the photoluminescence from a single Er^{3+} in C_{3i} site measured at 0 mT magnetic fields at a temperature of 10 mK. The ion shows a narrow linewidth of 0.76 MHz, which can be further reduced by the application of a magnetic field or by reducing the excitation power. The ion exhibits Purcell-enhanced decay with a T_1 of 1.2 ms. While the decay is 6 times longer than the single ion decay reported for C_2 site in Fig. 7.8, the discrepancy could be accounted for by a 2 times lower quality factor of the cavity, 1.5 times weaker dipole moment of C_{3i} site and a factor of 2 from polarization selection rules for a magnetic dipole only allowed transition. A $g^{(2)}(\tau)$ autocorrelation measurement could not be performed on the transition due to a relatively weak overall emission rate from the C_{3i} site with fiber cavity.

7.5.3 Homogeneous linewidth and spectral diffusion

Linewidth vs magnetic field

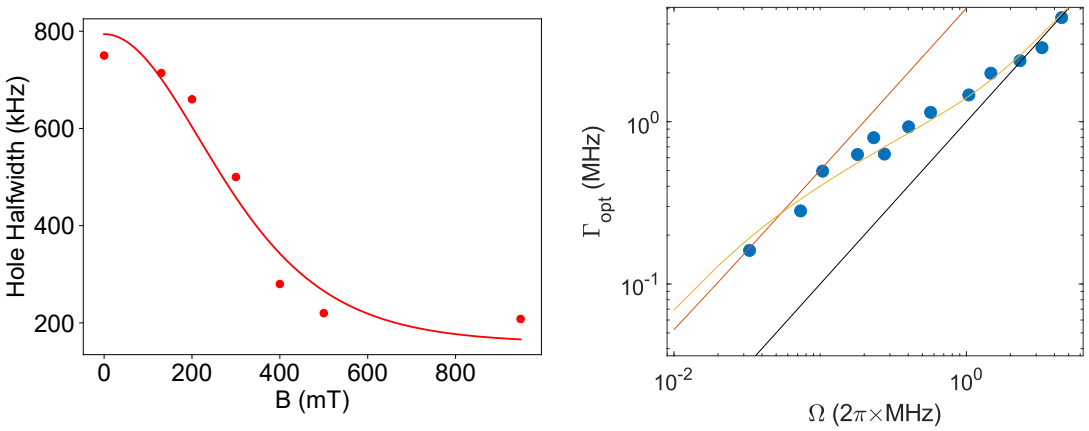
Homogeneous linewidth measured at 5 nW power using transient spectral holeburning (Fig. 7.14) shows a dependence on the magnetic field indicating the freezing of the spectral diffusion noise from a paramagnetic spin bath. The zero magnetic field linewidth of 800 kHz is in close agreement with the direction measured single ion linewidth thereby validating the spectral holeburning measurement. The magnetic field dependence is fitted with a spectral diffusion-induced linewidth broadening model,

$$\Gamma = \Gamma_0 + \Gamma_{\mathrm{SD}}\mathrm{sech}\Big(\frac{\mathrm{g}\mu_{\mathrm{B}}\mathrm{B}}{2\mathrm{k}_{\mathrm{B}}\mathrm{T}}\Big) \tag{7.8}$$

where Γ_{SD} is the dipolar linewidth due to coupling to a paramagnetic spin bath with an effective g-factor g and Γ_0 is the magnetic field independent part of the linewidth, which includes broadening due to laser power, laser linewidth, instantaneous spectral diffusion. We obtain Γ_0= 152(163) Hz, Γ_{SD}= 640(208) Hz, g= 2.6 and T=0.3 K. The limited dataset led to large relative uncertainties in the fitted parameters, which could be further reduced with higher-resolution scans.

Linewidth vs power

Optical Bloch equations are commonly used to describe the coherent transient response of a two-level following optical excitation. The two-level systems dynamics can be characterized by the longitudinal relaxation time T_1 and transverse relaxation time T_2 (T_2^*), which are expected to be independent of the laser intensity. Under Bloch formalism, the hole halfwidth depends on the optical Rabi frequency (χ), T_1 and T_2^* as [53],



(a) (b)

Figure 7.14: Spectral hole half-width shows a strong dependence on (a) magnetic field and (b) laser power (Rabi frequency) for Er^{3+} in C_{3i} site.

$$\Gamma = \left(\frac{1}{2\pi}\right)\left(\frac{1}{T_2^*} + \sqrt{\frac{1}{(T_2^*)^2} + \frac{\Omega^2 T_1}{T_2^*}}\right) \tag{7.9}$$

The limit of high laser intensity, eqn. 7.9 simplifies to $\Gamma = \frac{\Omega}{2\pi}\sqrt{\frac{T_1}{T_2^*}}$. However, free-induction-decay (FID) and transient nutation measurements of T_2^* in solids at liquid helium temperatures exhibit agreement with Redfield's description at higher laser powers where $\Gamma = \frac{\Omega}{2\pi}$ [53] [164]. The power dependence of linewidth in the intermediate regime has been described in ref. [101] (see Fig. 7.14, yellow line).

Fig. 7.14(b) shows the hole halfwidth measured as a function of laser power at a magnetic field B = 130 mT. The hole halfwidth shows a strong dependence on the laser Rabi frequency (Ω) down to the lowest power indicating that power broadening has dominant to the measured hole halfwidth. Under the assumption that the highest power hole halfwidth measurement corresponds to the Redfield limit, we can obtain the Rabi frequency of the measurements (black line, Fig. 7.14(b)). Next, assuming that the lowest power measurements correspond to the Bloch limit (red line, Fig. 7.14(b)), we can plug in the Rabi frequency ($\Omega/2\pi$) of 33 kHz, the measured T_1 of 3 ms, and the measured hole halfwidth (Γ) of 160

Hz in eqn. 7.9 to obtain $T_2^* = 136.6$ μs or homogeneous linewidth $\Gamma_h = 2.3$ kHz. This ultra-narrow linewidth is comparable to linewidth of 0.58 kHz measured in Y_2O_3 ceramics [70]. The analysis in this section assumes that the highest power linewidth and lowest power linewidth in Fig. 7.14(b) are described by Redfield and Bloch limit respectively. Further, the effect of ISD is ignored while studying the power dependence, which could be partially justified by a smaller dipole-dipole interaction for Er^{3+} in C_{3i} sites due to a lack of permanent electric dipole moment.

7.6 Comparison of C_2 and C_{3i} site optical homogeneous linewidth

Fig. 7.15 compares the single ion linewidth measured for the C_2 and C_{3i} site. The C_{3i} ion shows a significantly narrower linewidth than the C_2 site.

There are factors that could lead to a broader linewidth measurement for the C_2 site. The laser Rabi frequency for C_{3i} measurement was ≈ 1.5 MHz ($g = 500$ kHz and $n_{photon} = 9.6$) while the Rabi frequency for C_2 measurement was 11 MHz. Thus, for the 20.1 MHz linewidth from C_2 site, 11 MHz can be accounted for by the power-induced broadening. Further, during the measurements on C_2 site, the laser was locked to a gas cell, which could lead to long-term drifts up to 30 MHz, as compared to the C_{3i} site measurements where the laser was locked to a narrow, stable reference cavity with a laser linewidth of 50 kHz. Thus, if measurements are performed on C_2 site at lower power, with a locked laser, the resulting linewidths could be narrower than 10 MHz, close to the 1.8 MHz homogeneous linewidth measured using transient spectral holeburning.

There are factors that could result in a broader linewidth for the C_{3i} site. Firstly the measurement was performed at zero magnetic fields with a vector magnet. A zero magnetic field would result in strong spectral diffusion from an unpolarized spin-bath, leading to broader linewidths. This effect has been measured using spectral holeburning in Fig. 7.14(a). Further, magnetic field instability of the vector magnet could lead to drifts of the background

magnetic field, resulting in long-term drifts of the ion. Indeed, repeated measurements on the ion in Fig. 7.13(a) showed spectral diffusion of MHz over hours timescale. However, due to a low overall photon count rate and modest Purcell enhancement for the C_{3i} site the integration time was several minutes for each frequency and repeated single ions scans were prohibitively long. The low emission rate in conjugation with the field drifts made it challenging to obtain sufficient statistics for a $g^{(2)}(\tau)$ autocorrelation measurements to confirm a single ion from the C_{3i} site. These challenges could be addressed with photonic crystal cavities, which could provide a higher Purcell enhancement due to a smaller mode volume. Nevertheless, current results are promising for the application of $Er^{3+} : Y_2O_3$ as optically addressed spin-qubit in quantum repeaters.

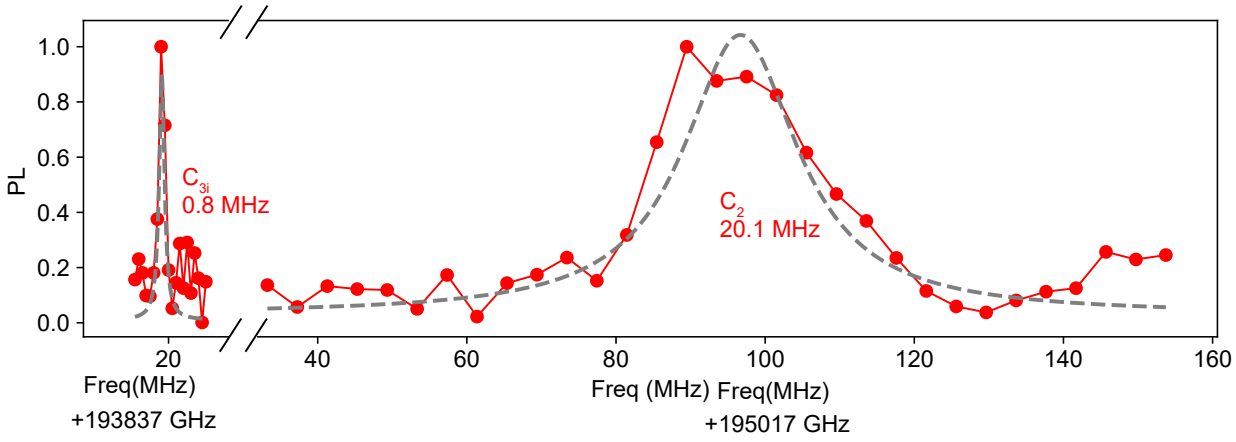


Figure 7.15: Single ion linewidth of Er^{3+} in C_2 compared with the potential single Er^{3+} in C_{3i} site.

CHAPTER 8

CONCLUSION AND OUTLOOK

8.1 Rare-earth ion-based scalable quantum interconnects

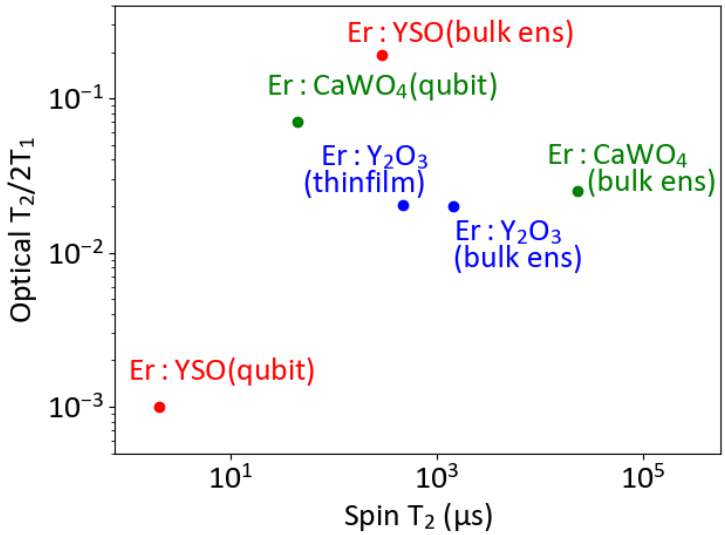


Figure 8.1: Er^{3+} doped Y_2O_3 thin-films provide coherence times rivaling those of their bulk polycrystalline counterparts. Thus Er^{3+} doped Y_2O_3 thin-films offer a material platform that can allow for integration with photonics without degradation of coherence properties as observed in bulk crystals([140] [87] [32] [128] [48]). This is due to a combination of a high-purity film with low impurity and defect concentration, and the controllable doping of erbium away from the interfaces.

We have evaluated Er^{3+} doped Y_2O_3 for application in quantum interconnects as a single emitter/ensemble-based quantum memory as well as for interfacing with microwave frequency qubits. Hyperfine and Zeeman tensor of Er^{3+} ions in Y_2O_3 polycrystalline ceramics were studied and the material was demonstrated to exhibit an anisotropic hyperfine interaction, which would result in clock transitions with long coherence times. Spin dynamics of Er^{3+} ions in Y_2O_3 were studied at 4 Kelvin and sub-Kelvin temperatures to understand the dominant source of spin decoherence and relaxation. Electron spin coherence times exceeding 1 ms were demonstrated for multiple transitions in $^{167}Er^{3+}$ doped Y_2O_3 at 26 millikelvin

temperatures. This was enabled by a combination of low temperatures (<100 mK) and moderate magnetic fields (<260 mT), which could simultaneously suppress magnetic noise generated due to spin flip-flops as well as spin-phonon relaxation. Paramagnetic impurities (non-erbium spins) in the ceramics were found to be the dominant source of decoherence down to the lowest temperature of 26 mK, which demonstrated the requirement for a high-purity material platform.

The insights gained from the studies in Er^{3+} doped Y_2O_3 ceramics motivated the study of molecular beam epitaxy (MBE) grown Er^{3+}, doped Y_2O_3 thin-films as a material platform which could allow for a large-scale device integration while simultaneously demonstrating long optical and spin coherence times. High sensitivity ESR measurements were performed on Er^{3+} doped Y_2O_3 thin films using low impedance superconducting microresonators using with near-quantum noise limited cryogenic Josephson traveling-wave parametric amplifiers (TWPA). Er^{3+} doped Y_2O_3 thin-films were demonstrated to exhibit spin coherence times exceeding milliseconds and spin relaxation times exceeding seconds on a wafer scale. The magnetic noise environment at 12 mK temperature was found to be near-limited by the yttrium nuclear spin bath, which testifies to a high purity of the film. Temperature-dependent coherence time measurements confirmed a spin-bath of Er^{3+} spins as the primary source of decoherence at sub-Kelvin temperatures, which indicated further improvements in coherence times for samples with reduced Er^{3+} density. The high symmetry C_{3i} site in particular exhibited longer Hahn echo coherence times than the low symmetry C_2 site.

The 1.5 μm optical transition of Er^{3+} in Y_2O_3 thin films was studied using a cryogenic tunable fiber Fabry-Perot cavity. Single Er^{3+} readout was demonstrated for both C_2 and C_{3i} site, enabled by the enhancement of the spontaneous emission of Er^{3+} by the fiber cavity (Purcell effect). The high symmetry C_{3i} site exhibited a zero field homogeneous linewidth of 0.8 MHz, significantly narrower than 20.1 MHz measured on the low symmetry C_2 site. This indicates a shielding of the optical transition in C_{3i} site from electric noise due to the absence

of a permanent electric dipole moment. Spectral holeburning measurements demonstrated a further narrowing of the homogeneous linewidth of Er^{3+} in C_{3i} site from 800 kHz at 0 mT to 200 kHz at 900 mT. Power dependence measurements at 135 mT confirmed power broadening as the dominant source of homogeneous linewidth broadening linewidth of 160 kHz was demonstrated at the lowest measurable power. The intrinsic homogeneous linewidth was found to be as narrow as 2.3 kHz after de-convoluting the power broadening from the measured 160 kHz hole halfwidth.

Milliseconds electron spin coherence time and narrow optical linewidths demonstrated in Er^{3+} doped Y_2O_3 thin-films are on-par with the measurements on bulk polycrystalline samples (Fig. 8.1). The spins addressed in Er^{3+} doped thin films can be integrated into nanophotonic cavities without further degradation of coherence times and thus these results pave the way for the development of scalable quantum interconnects.

8.2 Future directions

8.2.1 Addressing hyperfine clock transitions in $^{167}Er^{3+} : Y_2O_3$

An anisotropic spin Hamiltonian along with a large hyperfine interaction (A $\approx$ 600 MHz) leads to transitions with vanishing first-order sensitivity to magnetic noise, also known as zero-first-order-Zeeman sensitive (ZEFOZ) transitions. The first-order sensitivity to magnetic noise can be numerically calculated as $\partial\omega/\partial B = S_1$ and second-order sensitivity $\partial^2\omega/\partial B^2 = S_2$. At high magnetic fields, the electron Zeeman interaction is the dominant term and hyperfine interaction is a small perturbation in this regime, the sensitivity of ESR transitions with the magnetic field is $\approx g_{eff}\mu_B$, where g_{eff} is the effective g factor for the magnetic field direction. However, at low magnetic fields where the electron Zeeman interaction energy is comparable to the hyperfine splitting, we observe mixing between the electron-nuclear spin states. As a result, the electron-nuclear mixed state possesses low sensitivity to noise char-

acteristic of nuclear spins as well as strong magnetic moment, allowing for fast spin manipulation. The presence of an anisotropic spin Hamiltonian also leads to zero field transitions with zero first-order sensitivity to noise, when the magnetic field is applied along directions corresponding to the lower component of the g tensor. These low field and zero fields ZEFOZ transitions have been studied for $^{171}Yb^{3+}$ and $^{167}Er^{3+}$ in low symmetry (C_1) sites in Y_2SiO_5 [127] [142]. The C_2 and C_{3i} sites in Y_2O_3 also possess low symmetry resulting in anisotropic hyperfine interaction. Therefore, we expect two kinds of ZEFOZ transitions, namely zero field ZEFOZ when the magnetic field is applied along the low g direction (g=1.6,4.8 for C_2 and 3.3 for C_{3i}), and low field ZEFOZ when the field is applied along the highest g direction (g=12.2 for both C_2 and C_{3i}). The ZEFOZ transitions are evaluated by numerically solving the spin Hamiltonian for different magnetic field B to obtain the energy levels ω and calculating the first derivative for transition energy with magnetic field $\partial\omega/\partial B$. While there are up to 64 transitions between the 8 hyperfine levels of the electron spin and spin down state, only a subset of them have a strong intensity amplitude under ESR driving. The transition intensity matrix can be calculated as [175],

$$I = |V^T S_+ V|^2 + |V^T S_- V|^2 \tag{8.1}$$

where V is a matrix containing the 16 eigenvectors of the 16x16 spin Hamiltonian at a magnetic field B, and S_+ and S_- are matrices corresponding to the representations of the S_+ and S_- operators, I(ij) is a 16x16 matrix containing the signal intensity corresponding to a transition between states ($|i\rangle$) and ($|j\rangle$). The term I approaches 1 in the high field limit for transitions between electron spin states with the same nuclear spin quantum number while at low fields due to mixing has several non-zero elements corresponding to transitions between the electron-nuclear mixed states. We only select those transitions, which have an intensity ≥ 0.05, which corresponds to transition intensity being 5 % of the high field ESR transition. After evaluating the states $|i\rangle$ and $|j\rangle$, which have a non-zero transition intensity, we calculate

the first (S_1) and second order (S_2) Zeeman sensitivity for each state $|i\rangle$ and $|j\rangle$ and then we calculate the sensitivity for transitions between ($|i\rangle$) and ($|j\rangle$) as $S_{1,ij} = S_{1,i} - S_{1,j}$ and $S_{2,ij} = S_{2,i} - S_{2,j}$.

8.2.2 Zero field ZEFOZ

We calculated the energies of zero field ZEFOZ transition corresponding to B field applied along the g=1.64 direction for C_2 site (Fig. 8.2). We observe zero-field transition at 4.631, 4.610, 3.570, and 3.500 GHz, which possess S_1 approaching zero as well as significant transition intensity between 0.25- 0.4. These results are also applicable for the B field applied along g=4.8 directions, as when approaching the zero field the direction of the B field is not relevant. A similar level structure is also expected for C_{3i} transitions close to zero fields when the magnetic field is applied along the g=3.2 plane.

Low field ZEFOZ

When the magnetic field is applied along the largest g=12.2 direction for C_2 site (Fig. 8.3) we observe low field transition in 1.8 - 4 GHz range (5-35 mT field), which possess S_1 approaching zero as well as significant transition intensity between 0.25- 0.6. A similar level structure is also expected for C_{3i} transitions close to zero fields when the magnetic field is applied along the g=12.2 direction. We note that the presence of discontinuous lines in Fig. 8.2 and Fig. 8.2 are a result of either an avoided level crossing or due to a cutoff placed for transition intensity being 5 % of the high field (unmixed) ESR transition. As transitions drop in intensity below 5 %, the script automatically does not plot them. Therefore, these transitions with vanishing intensities are not experimentally relevant and the presence of such artifacts in the plot may be ignored.

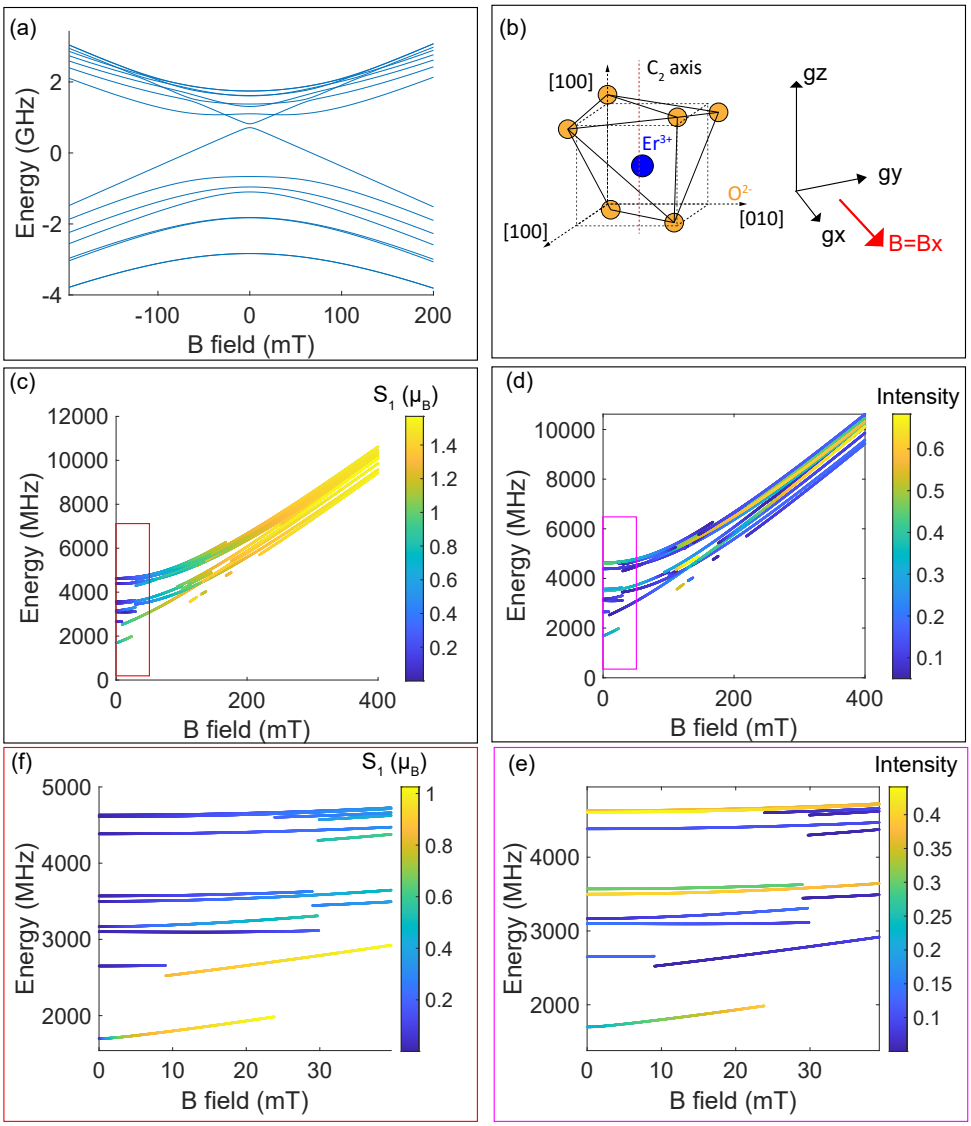


Figure 8.2: Zero field ZEFOZ transition for Er^{3+} in C_2 site for B field applied along the g_x (g=1.6) direction of the principal axis of the g tensor (a)(b) shows energy levels with zero gradients with the magnetic field (b) Shows the noise sensitivity S_1 (μ_B) as a function of B field for transitions among the energy levels (a) with intensity $\geq$ 5 % compared to the ESR transition intensity for high field transitions. (d) The transition intensity for high-field ESR transitions approaches 0.6. (e) (f) Zoomed in view of the transition in (c) (d) show the presence of zero fields ZEFOZ transitions with vanishing S1 and non-zero transition intensity, which offer reduced sensitivity to noise approaching zero at 0 fields.

Spectral diffusion limited coherence time at ZEFOZ points

The spectral diffusion limited coherence time can be estimated from the known magnetic noise sensitivity S_1, S_2 as [127],

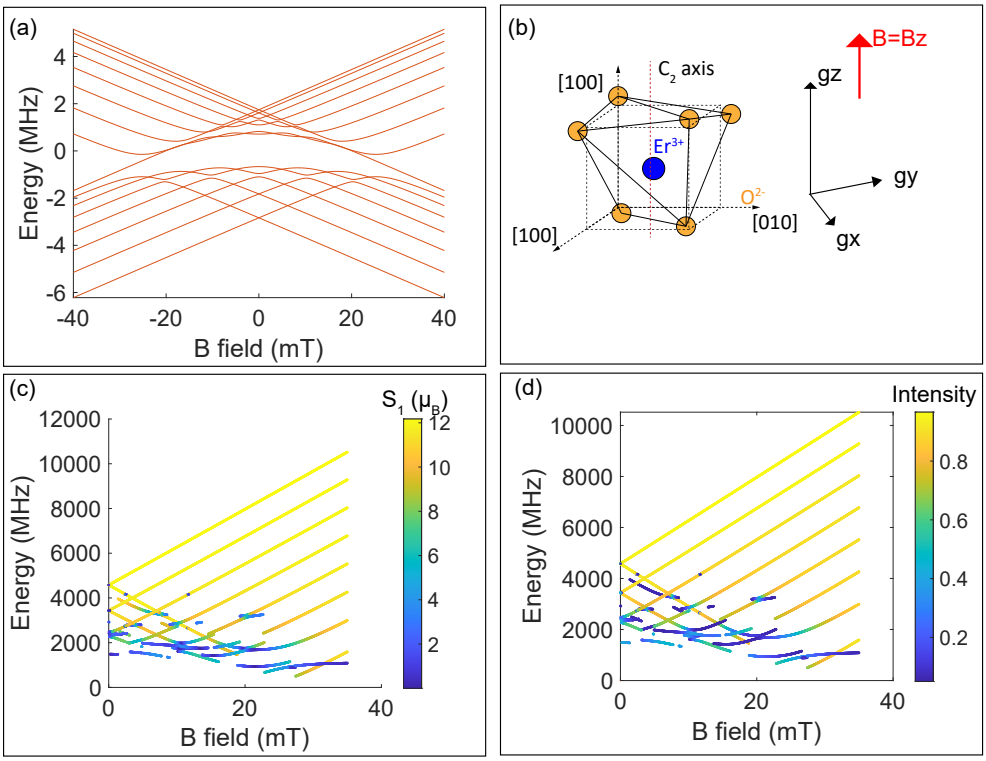


Figure 8.3: Low field ZEFOZ transition for Er^{3+} in C_2 site for B field applied along the g_z (g=12.2) direction of the principal axis of the g tensor (a)(b) shows energy levels with zero gradients with the magnetic field (b) Shows the noise sensitivity S_1 (μ_B) as a function of B field for transitions among the energy levels (a) with intensity $\geq$ 5 % compared to the ESR transition intensity for high field transitions. (d) The transition intensity for high field ESR transitions approaches 1. (c) (d) show the presence of zero fields ZEFOZ transitions with vanishing S1 and non-zero transition intensity, which offer reduced sensitivity to noise approaching zero at low fields.

$$1/T_2 = \pi(S_1\delta B + S_2\delta B^2) \tag{8.2}$$

where, δB is the magnetic noise fluctuation amplitude, which is found to be $\approx$ 10 nT for Y_2O_3 at 26 mK and 250 mT field. We calculated the spectral diffusion limited spin coherence time for transitions in Fig. 8.2 and Fig. 8.2. Fig. 8.4(c) shows a long coherence time reaching 80 ms can be expected for the zero-field ZEFOZ transitions due to their diminished sensitivity to noise. However, while the magnetic noise fluctuation here is assumed to be 10 nT, zero field transitions are expected to experience a significant increase in magnetic noise fluctuation

due to an unpolarized paramagnetic spin bath and a large frozen core of yttrium nuclei.

The low field ZEFOZ Fig. 8.4(d) also provides a long coherence time approaching 1 ms, and they could be advantageous as the application of moderate field would partially counteract the adverse effect of paramagnetic and nuclear spin bath. Nevertheless, these transitions allow for zero field or low field operation, which is compatible with interfacing with superconducting systems for microwave quantum memory and quantum transduction application.

8.2.3 Hybrid quantum systems with lithographically defined rare-earth films

The measurements in previous chapters involved positioning thin films on the superconducting resonator following the pick-and-place method (Fig. 8.5 (a),(c)), which allowed for high throughput sample characterization. However, the method suffers from low process yield and limited repeatability due to the requirement of positioning the thin film over the inductor within an accuracy of 100 μm with hand. Further, the glued sample can have an air gap up to 2 μm (Fig. 8.5 (b)), which leads to reducing coupling strength to the resonator at least by a factor of 10 (Fig. 8.5 (d)). Therefore, to improve the repeatability, and process yield and to enhance the single spin coupling strength beyond kHz a modified approach is required to integrate thin film into a superconducting resonator device.

One such possible implementation involves patterning Er^{3+} doped Y_2O_3 thin films into cylinders and patterning superconducting resonator with the inductor loop around the thin film. Fig. 8.6 shows the proof of concept device with a $\approx$ 120 nm Y_2O_3 thin-film layer patterned into a cylinder of 15 μm diameter by Argon reactive ion plasma etching (RIE) on an ICP Fluorine etch tool. A thick 20 μm layer of photoresist (AzP4620) was patterned as a mask prior to plasma etching. The superconducting resonator was patterned using the liftoff process described in the previous chapter. This proof of concept is advantageous for several reasons. Firstly, patterning the spin ensemble around the inductor will ensure maximum

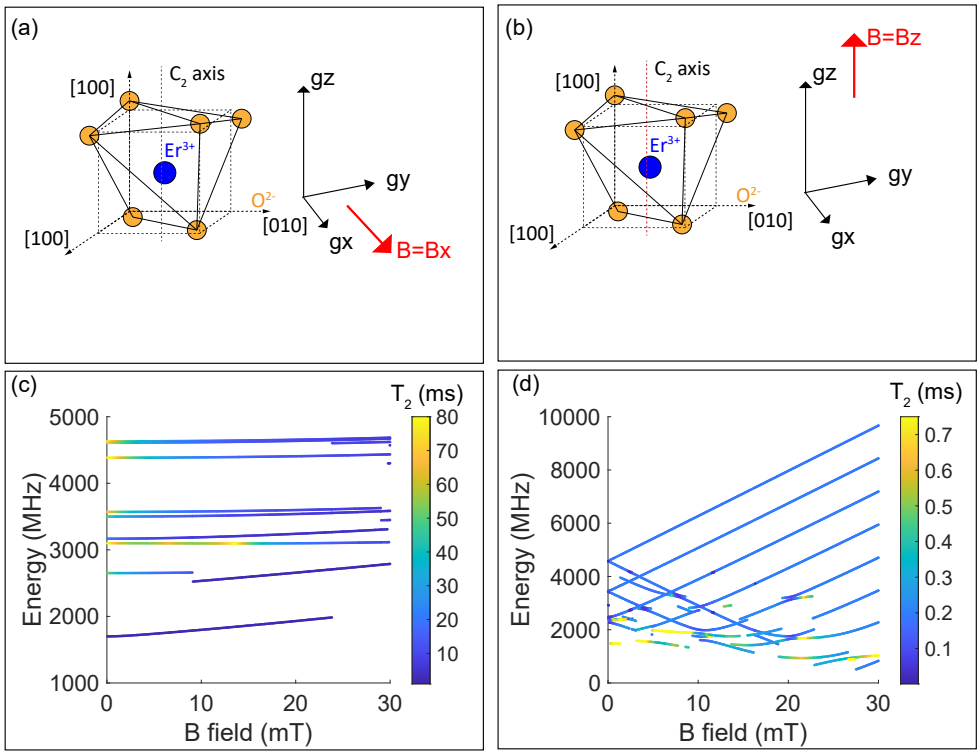


Figure 8.4: Spectral diffusion limited spin coherence time predicted for Er^{3+} in C_2 site for B field applied along the (a) g_x (1.64) and (b) g_z (g=12.2) direction of the principal axis of the g tensor. The magnetic noise fluctuation (δB) is assumed to be 10 nT, and both first-order (S_1) and second-order coefficients(S_2) are taken into account ($1/T_2 = \pi(S_1\delta B + S_2\delta B^2)$) (c) Shows the predicted coherence time(ms) in heatmap field for zero fields ZEFOZ transitions corresponding to B field applied along g_x (d) Shows the predicted coherence time (ms) for low field ZEFOZ transition for field applied along g_z. While zero field ZEFOZ transitions (c) show the lowest sensitivity to noise allowing for predicted coherence time up to 80 ms, the magnetic noise might be significantly larger than 10 nT due to the presence of an unpolarized spin bath at 0 field. The low field ZEFOZ transition (d) might be advantageous in this regard as the fluctuating magnetic field noise due to paramagnetic spin bath noise might be partially suppressed at low fields.

overlap of the spins with the microwave resonator mode as well as it will allow for optical access in the z-direction using a fiber cavity/free space laser setup. This will be helpful for high-efficiency microwave-to-optical transduction, as well as correlated microwave-optical spectroscopy of the Er qubit in a thin film. Secondly, the thin film can be patterned to control the spatial spin-spin interaction-induced relaxation, as well as engineering interactions with acoustic waves/phonons. Thirdly, the reduced distance between the thin film and

superconducting resonator will increase spin-resonator coupling strength (g) by more than one order of magnitude and will allow for higher sensitivity as well as significant Purcell enhanced relaxation of the Er^{3+} spins through the superconducting resonator. Therefore, patterned thin films will provide a novel platform for the study of the physics of spatial spin-spin interaction and spin-phonon interaction.

The device showed an intrinsic quality factor (Qi) of 30,000 in high power limit as shown in Fig. 8.6 with strong dependence of quality factor on power. The inverse of intrinsic quality factor dependence on power was fitted with the interacting TLS model described in previous sections. The fit parameters are described in Table. 8.1 show a higher Ftanδ by at least by a factor of 2 compared to previously measured devices suggesting an increased density of TLS. However, the quality factor showed a weaker than quadratic dependence on power $\alpha = 0.32$, which is consistent with previous measurements and suggests the presence of interacting TLS. Interestingly, the device with the sample with the highest density of Er^{3+} had $\alpha = 0.26$ while the devices with samples with further decreasing Er^{3+} densities had $\alpha \approx 0.3$ and $\alpha = 0.54$. A weaker power dependence of the quality factor for the devices with higher Er^{3+} density could hint at possible interaction between Er^{3+} and TLS.

Q_{i0}	Ftanδ	nc	α
34699	1.26×10^{-4}	1.6×10^{4}	0.32

Table 8.1: Power dependence fit parameters for superconducting devices patterned around Y_2O_3 cylinder.

Microwave to optical transduction

Coherent microwave-to-optical transduction using rare-earth spin ensembles coupled to microwave and optical cavities has been proposed in several works [195] [97] [21] [66], as well as

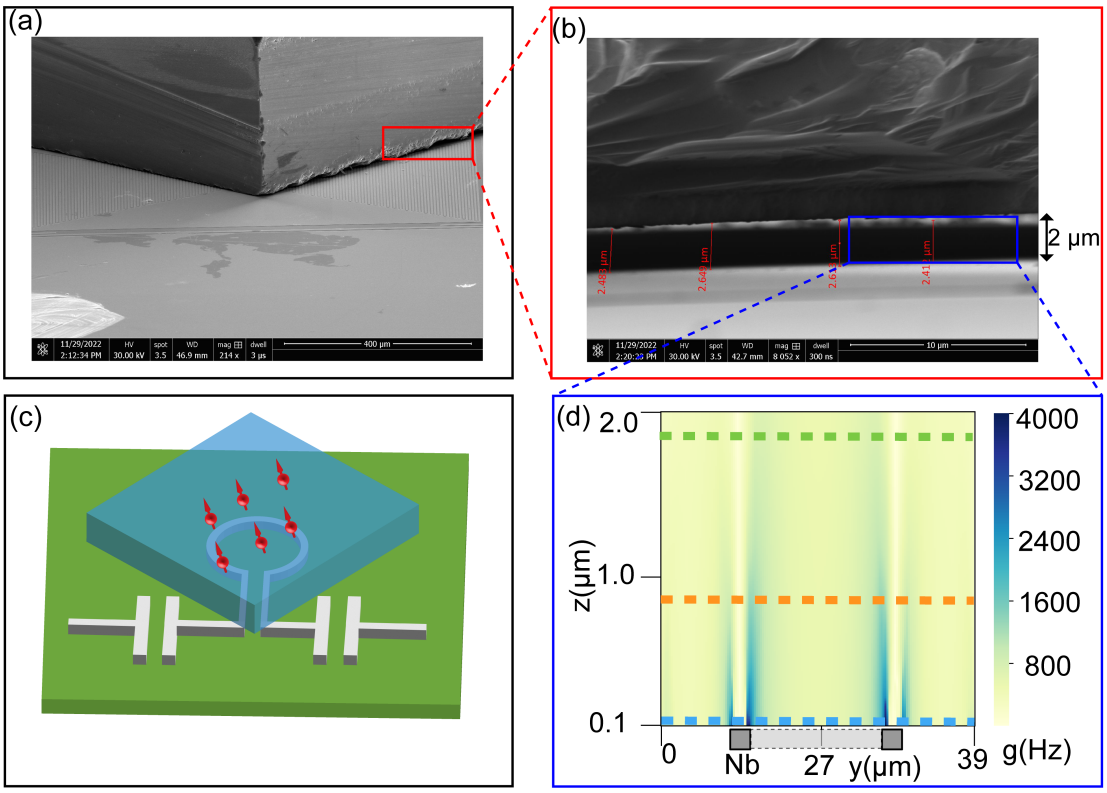


Figure 8.5: Pick-and-place method for coupling Y_2O_3 film to the superconducting resonator can lead to gaps between the film and resonator leading to reduced spin-resonator coupling strength g by a factor of 10.

proof-of-concept demonstrations have been carried out on spin ensembles of Er^{3+} [67] [68], [99] Yb^{3+} [23] [151]. Key metrics for quantum transduction include high efficiency, large bandwidth, and a low number of added noise photons. Rare-earth ions are unique among solid-state spin qubits due to their phenomenal optical properties, which provide a coherent emission of upconverted microwave photons utilizing the magneto-optical-susceptibility of rare-earth ions. Further, ensembles of rare-earth ions can provide a large bandwidth of transduction. Er^{3+} is particularly interesting due to its optical emission in the low-loss telecom-C band. Yb^{3+} ions on the other hand benefit from a stronger optical dipole moment, which increases the ensemble coupling to the optical cavity however an optical transition at 900 nm requires an additional optical frequency converter from visible to infrared (telecom-C band) photons. The primary challenges with rare-earth-based transducers involve the

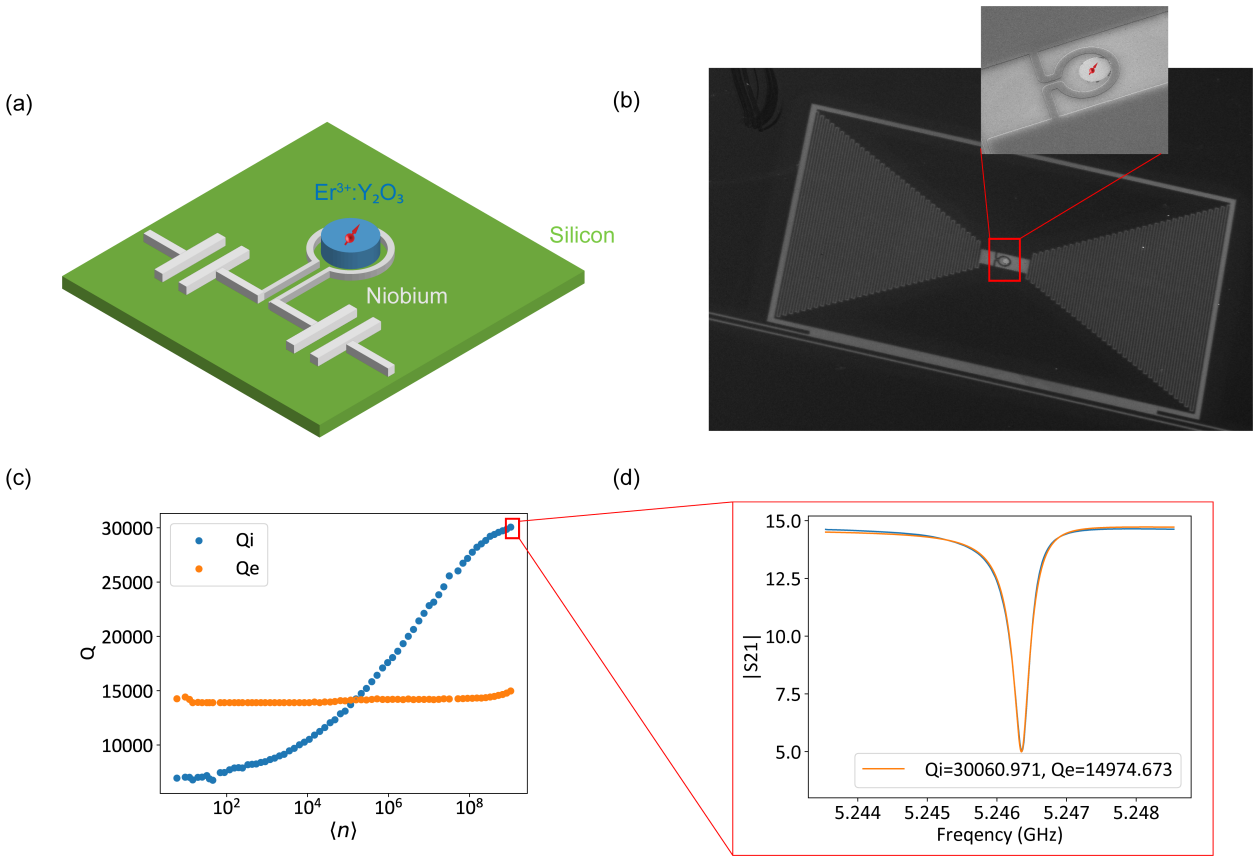


Figure 8.6: Power dependent quality factor measurements for niobium superconducting resonator with lithographically defined Y_2O_3 cylinder at 20 mK.

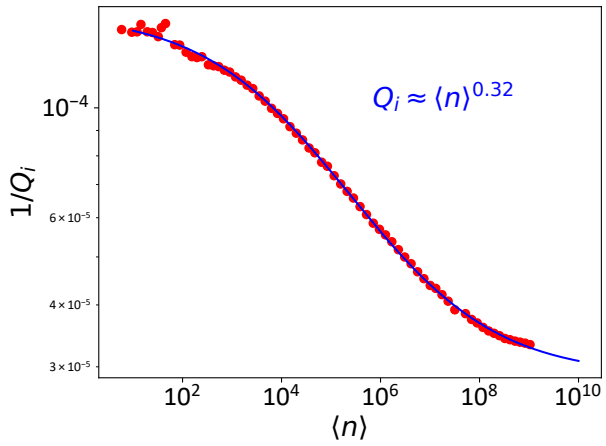


Figure 8.7: TLS model fitting for niobium superconducting resonator with lithographically defined Y_2O_3 cylinder.

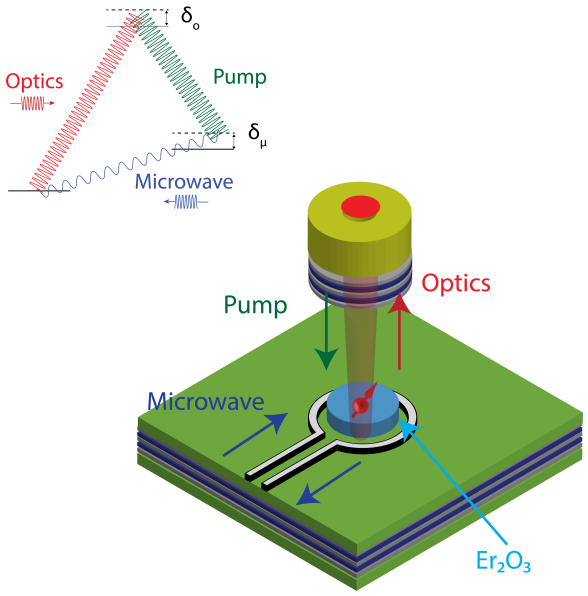


Figure 8.8: Microwave to optical transducer device employing niobium superconducting resonator with lithographically defined Er_2O_3 cylinder and optical fiber Fabry-Perot cavity.

requirement of high spin densities while maintaining narrow inhomogeneous linewidth and mode overall of the optical, microwave cavity, and spin ensemble. The former challenge is a material optimization problem while the latter is a device design problem.

While on-chip Er^{3+} based transducers have demonstrated efficiencies up to 10^{-8}, the highest efficiency of 10^{-5} has been demonstrated on a bulk transducer utilizing 3D microwave cavity and bulk resonator. Intuitively it can be expected that on-chip transducers could allow for significantly higher efficiencies due to orders of magnitude coupling strength g for the optical and microwave cavities. However, the relatively poor performance of the on-chip transducers hints at a poor mode overlap, and additional sources of parasitic losses for the demonstrated on-chip transducer. Therefore, ensuring a good mode overlap could help improve the transducer efficiency significantly. Further, the coupling to parasitic spins and two-level systems by the microwave resonator could contribute to the loss of efficiency.

The hybrid device with a lithographically defined cylinder could be integrated with the fiber Fabry-Perot cavity (Fig. 8.8). This design would ensure the highest overlap of the mode of the optical, microwave cavity with the spin ensemble and address some of the issues with

the current demonstrations of rare-earth-based transducers. Further, transduction based on Er_2O_3 could offer extremely high coupling strength to the magnonic modes due to a high density, which could improve transduction efficiency beyond the demonstrations based on dilute ensembles of rare-earth ions.

There remain several other challenges with rare-earth ion-based transducers. Additionally, the added noise photons have not been addressed in the demonstrations on rare-earth ion ensembles due to low efficiency. The heating due to laser pulses is an issue that induces noise in the superconducting resonator or adds thermal noise photons. While recent works have claimed a 1 MHz bandwidth of transduction, the transduction measurement was carried out with a pulse of 1 % duty cycle, therefore effectively the transduction bandwidth is 10 kHz, significantly below the state of the art [151]. Nevertheless, addressing these challenges can be a rewarding pursuit and could offer insight into the rich physics of these systems.

Coupling of rare-earth spins to acoustic wave resonators

The theory of electron spin coupling to acoustic waves has been developed and proof-of-concept demonstrations of acoustic paramagnetic resonance (APR) have been carried out starting from the 1960s [79] [11]. Experimental demonstrations commonly involve the integration of an X-band ESR spectrometer with an ultrasonic transducer. The acoustic waves produced by the transducer are propagated to a sample inside an ESR cavity. Application of magnetic field results in a spin resonance, which induces the absorption of acoustic waves. There has been renewed interest in the coupling of quantum systems to acoustic waves in recent years for several reasons. Firstly, microwave phonons due to their small wavelength O(100nm) can be spatially confined as compared to a microwave photon at the same frequency. This makes them attractive for application in quantum information processing using phonon-spin or phonon-superconducting qubit hybrid systems. The small spatial confinement of phonons can enable several orders of magnitude higher spin-phonon coupling,

as compared to spin-photon coupling. This can also enable high-efficiency microwave-to-optical transducer using small ensembles of spins confined in a nanophotonic and acoustic wave resonator. While acoustic waves can propagate as bulk acoustic waves(BAW) as well as surface acoustic waves(SAW), the latter are preferable due to their higher spatial confinement. Surface acoustic wave resonators on bulk crystals suffer from scattering due to bulk acoustic wave modes, due to the large dimensions of bulk crystals. Rare-earth doped thin films are especially attractive in this regard, as due to a small thickness $\lessapprox \mu$m, scattering from bulk-acoustic wave modes would be suppressed.

Proof of concept experiments for coupling of Er^{3+} spins in thin films could involve two possible approaches. Firstly, an all-acoustic approach where high-quality factor surface acoustic wave resonators could be patterned on the top of the Er^{3+} doped thin-film. Application of a magnetic field would result in resonant absorption of acoustic waves by the spin-ensemble, analogous to the demonstrations using microwave resonators in this thesis. The pulsed technique could be used to drive and detect acoustic spin echoes, which has not been reported, to the best of our knowledge. This could be accomplished by depositing a piezoelectric film such as aluminum nitride on top of the Er^{3+} doped thin-film, following which, interdigitated transducers could be patterned out of superconductor such as niobium on top of the piezoelectric film. The primary challenge with this approach would be obtaining a high enough quality factor for the acoustic wave resonators, in order to achieve high cooperativity coupling to spin ensembles. While surface acoustic waves are expected to obtain high single-spin coupling strength due to their small spatial confinement, the singe spin spin-phonon coupling strengths have not been well studied for rare-earth ions. Therefore, while the requirements on quality factors for SAW resonators might not be very stringent, further studies on spin-phonon coupling strength are needed. Nevertheless, provided the microwave losses and acoustic-wave losses of the SAW device in the piezoelectric and Er^{3+} doped thin-films are minimized, a modest-quality factor of a few thousand might be sufficient

to demonstrate the coupling of surface acoustic wave resonator to Er^{3+} spin-ensembles in thin-films.

Secondly, a hybrid approach can be adopted where a surface acoustic wave resonator is combined with a superconducting microwave resonator. This scheme would involve acoustic driving of the spin ensemble through an interdigitated transducer and detection of the spin population through a microwave resonator. This could be accomplished by either continuous-wave or pulsed ESR. For instance, the effect of the application of an acoustic wave pulse, prior to a microwave spin echo sequence can be visualized as an application of an additional microwave pulse prior to the spin echo sequence. Therefore, analogous to the inversion recovery and saturation recovery spin echo sequences already demonstrated in this work, a population change due to acoustic driving could be detected with the microwave spin echo technique. The key challenges for this approach are firstly, the requirement of spatial overlap of the mode of microwave and acoustic wave resonator and secondly, the spectral overlap of the microwave and acoustic wave resonator. The former challenge has already been addressed to some extent by the device with lithographically defined Y_2O_3 cylinder (Fig. 8.6). An acoustic wave resonator can be patterned to launch acoustic waves to the thin-film cylinder, where the resultant population difference could be detected with the microwave resonator. The latter challenge can be addressed to some extent by utilizing broadband interdigitated transducers, or low Q acoustic-wave resonators so that the effect of frequency offset between the acoustic wave and microwave resonator could be mitigated. While certainly challenging, with a sufficiently controlled and repeatable fabrication process for the acoustic wave and microwave resonators, the challenges could be addressed.

8.2.4 Single shot optical readout of Er^{3+} spin in Y_2O_3 thin-films

Er^{3+} doped Y_2O_3 thin-film platform possesses long spin coherence times and narrow optical linewidths, which makes it suitable for integration into photonic crystal cavities with

extremely small mode volumes « $((\lambda/n)^3)$. While Purcell enhanced ($F_P = 272$) readout of single Er^{3+} was already demonstrated in this work using fiber Fabry-Perot cavities, the extremely small mode volume of photonic crystal cavities along with a similar quality factor (2×10^5) would provide a Purcell enhancement higher by at least an order of magnitude and allow for fast readout of Er^{3+} in both C_2 and C_{3i} sites. This will enable the demonstration of the emission of indistinguishable photons, as well as single-shot optical spin readout. The C_{3i} site is suitable for demonstrations such as entanglement between Er^{3+} - Er^{3+} for quantum repeater owing to its narrow optical linewidths and long spin coherence time. Measurements on the C_{3i} have reported vanishing transition amplitude for the spin flipping transition [149], which would lead to a very high cyclicity spin readout. The C_2 site on the other hand due to the presence of a permanent dipole moment for the optical transition and an overall stronger dipole moment is especially suited for quantum sensing.

APPENDIX A

APPENDIX

A.1 Estimation of magnetic noise sensitivity of transitions using Easyspin

The following steps were followed to estimate the magnetic noise sensitivity of transitions at 5.6 GHz

- Orientation of crystal axis with respect to the magnetic field was chosen from a uniform distribution of θ, ϕ, with B field oriented along the Z axis.
- 5.6 GHz resonance magnetic fields were calculated for all hyperfine ESR transitions for given crystal orientation θ, ϕ.
- Noise sensitivity was calculated for each hyperfine transition for a given θ, ϕ by taking numerical derivative (∂E/ ∂B) at the resonance B field.
- Calculated (∂E/ ∂B) was weighted with transition intensity and thermal occupation probability of the hyperfine level at 100 mK.
- Average noise sensitivity (∂E/ ∂B)(B) at 5.67 GHz was estimated from the weighted average of (∂E/ ∂B)(B) for all possible transitions on-resonant at the given B field.

A.2 Customized dynamical decoupling

This section had contribution from Xuntao Wu for the design of customized pulse sequence, filter function extraction, and analysis of data.

The spin coherence time measurements for g=1.64 transitions in Fig. 5.3(a) show instantaneous diffusion by dipolar interactions in the Er spin ensembles. This decoherence cannot

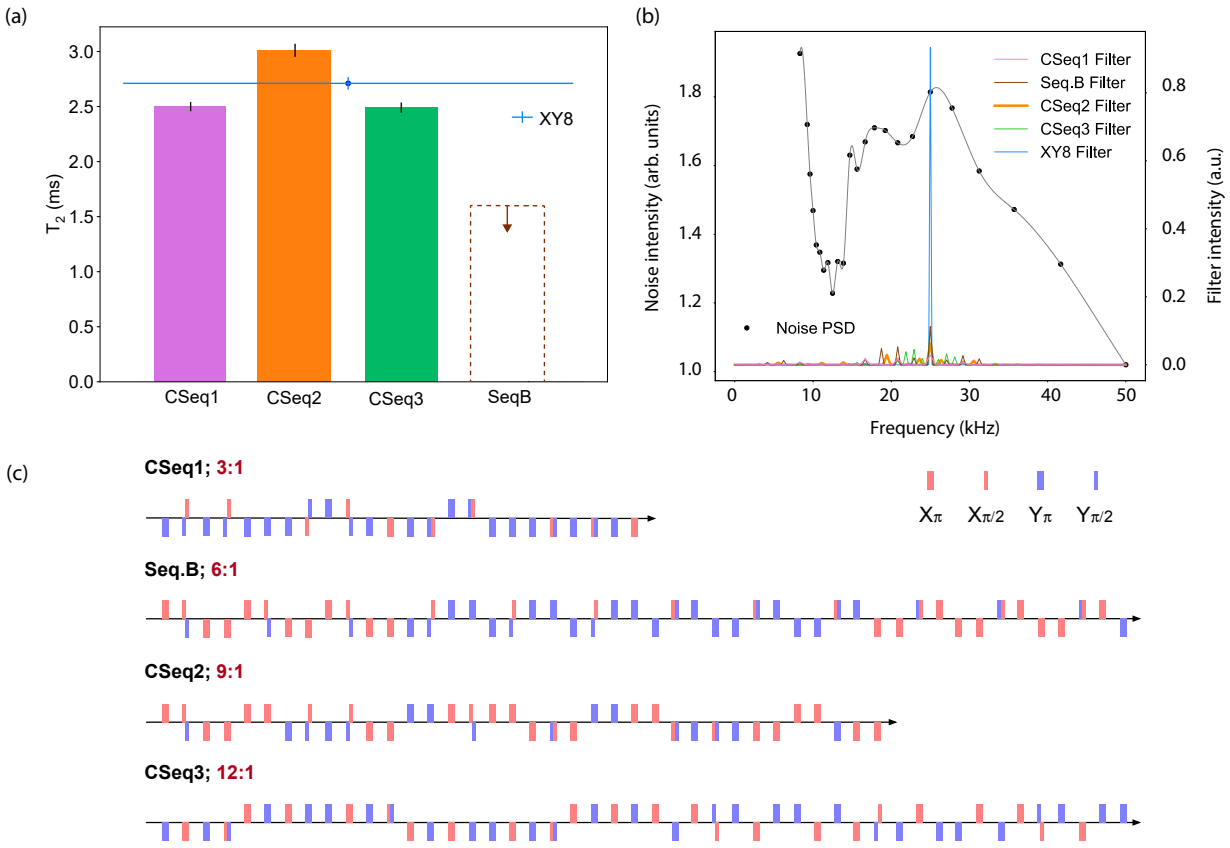


Figure A.1: Coherence enhancement with customized dynamical decoupling. (a) Comparison of coherence times under different dynamical decoupling sequences with a common 25 kHz filter center frequency. T_2 for Seq.B shown is an estimated upper bound. (b) Noise spectrum computed from CPMG T_2 measurement and comparison of the filter functions of all sequences. Filters are normalized in the whole spectrum, but, only the 0-50kHz range is shown given the measured noise spectrum range. (c) Customized dynamical decoupling pulse sequences in increasing order of the target ratio of disorder to interaction, along with Seq.B.

be canceled by standard dynamical decoupling sequences like XY8. A new sequence is desired so that it can mitigate both spectral diffusion and dipolar interactions with robustness to pulse errors at the same time [42]. A previously proposed sequence for disorder-dominated sequence (Seq.B) has shown improvement over XY8 dynamical decoupling for electron spins in NV centers [213] and Er: YSO [121]. These systems, however, had strong dipolar interactions with XY8 dynamically decoupled T_2 of $\approx 1\ \mu s$ as compared to T_2 of $\approx$ ms in our system. For systems with weaker dipolar interactions, customized sequences are thus

required. In this section, we describe the results of three customized sequences — CSeq1 for 3:1 (ratio between spectral diffusion and interaction decoupling), CSeq2 for 9:1, and CSeq3 for 12:1, together with existing XY8 (inf.:1) and Seq.B (6:1) on the 259 mT (g=1.64) transition. We note that the ratio assigned to a sequence is how fast it decouples from slow-varying spectral diffusion noise versus dipolar interaction-induced broadening, and it is an intrinsic property of the sequence. The actual ratio of spectral diffusion to dipolar interaction noise experienced by the spin system is difficult to predict when there is noise fluctuating faster than the sequence time scale. Therefore, it is important to design sequences with varying ratios to better match the actual noise characteristics of the system.

The starting point for the design of customized sequences is that a given sequence features different cycle lengths to mitigate either spectral diffusion or dipolar interactions by moving the system into a 'Toggling Frame' [42], where we can obtain a pictorial visualization of how the original spin Pauli operators evolve under the Floquet engineered version [183]. Figure A.1(a) presents coherence time measurements for different sequences with the same 25kHz filter center frequency. We observe that one customized sequence — CSeq2 outperforms all other sequences and even the XY8 sequence. All customized sequences yielded longer coherence than Seq.B, with CSeq2 reaching a near factor of 2 improvements over Seq.B. We also note that when measuring Seq.B, spin echo amplitudes quickly diminished below the noise floor after a few data points. Therefore, only an upper limit of 1.6 ms was placed on Seq.B T_2.

To understand the performance variations among different sequences, we calculate their effective filter functions and compare them with that of XY8 in Fig. A.1(b). We also plot the noise power spectrum density (PSD) experienced by the system obtained by CPMG (Carr-Purcell-Meiboom-Gill) sequences with varying pulse separations (Fig. A.2). While the dominant source of spectral diffusion is low-frequency noise with $\approx$ Hz flip rate as discussed in section IV, the noise PSD also exhibits a local maximum of around 25 kHz. Compared

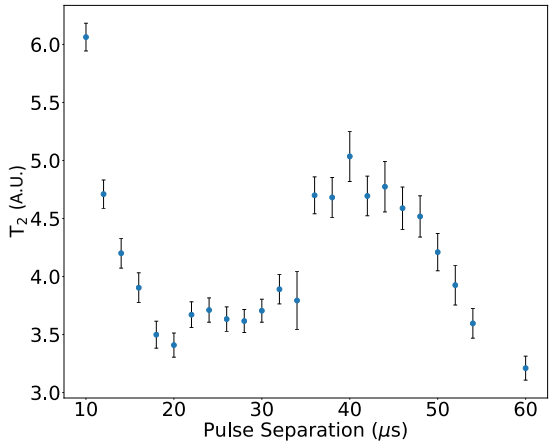


Figure A.2: Noise spectrum measurement using CPMG sequences.

with the XY8 sequence, the filter functions of the customized sequences generate sidebands that will sample fewer noises in total. We see from Fig. A.1(b) that some customized sequences have wider sidebands than CSeq2 (i.e. CSeq1 and Seq.B), but, do not outperform CSeq2 in terms of the coherence time, indicating that the amount of dipolar interaction suppressed vary among different sequences and the coherence enhancement is not solely due to the spread of the filter function. Nonetheless, due to the fact that the electronic spin g-tensor is highly anisotropic in Er^{3+} ions, customized sequences cannot fully cancel the dipolar interaction term in the spin Hamiltonian [121]. In this case, we can only tune the ratio between transverse (J_S) and longitudinal (J_I) coupling in the spin system by rearranging the pulse separations in the sequence, which give rise to relaxation and dissipation, respectively [213]. A longer coherence beyond the current best result remains possible if such a ratio can be fine-tuned. However, a full optimization was not performed in this work due to limitations of our experimental setup, such as the smallest accessible pulse width (1 μs) and the minimum pulse separation (10 μs).

REFERENCES

[1] A. Abragam and B. Bleaney. *Electron paramagnetic resonance of transition ions*. Oxford University Press, 2012.

[2] M. Afzelius, C. Simon, H. de Riedmatten, and N. Gisin. Multimode quantum memory based on atomic frequency combs. *Phys. Rev. A*, 79:052329, May 2009.

[3] S. Agnello, R. Boscaino, M. Cannas, and F. M. Gelardi. Instantaneous diffusion effect on spin-echo decay: Experimental investigation by spectral selective excitation. *Phys. Rev. B*, 64:174423, Oct 2001.

[4] B. Albanese, S. Probst, V. Ranjan, C. W. Zollitsch, M. Pechal, A. Wallraff, J. J. L. Morton, D. Vion, D. Esteve, E. Flurin, and P. Bertet. Radiative cooling of a spin ensemble. *Nature Physics*, 16(7):751–755, Jul 2020.

[5] A. L. Alexander, J. J. Longdell, M. J. Sellars, and N. B. Manson. Photon echoes produced by switching electric fields. *Phys. Rev. Lett.*, 96:043602, Feb 2006.

[6] J. Alexander, G. Dold, O. W. Kennedy, M. Šimėnas, J. O'Sullivan, C. W. Zollitsch, S. Welinski, A. Ferrier, E. Lafitte-Houssat, T. Lindström, P. Goldner, and J. J. L. Morton. Coherent spin dynamics of rare-earth doped crystals in the high-cooperativity regime. *Phys. Rev. B*, 106:245416, Dec 2022.

[7] A. Alkauskas, B. B. Buckley, D. D. Awschalom, and C. G. V. de Walle. First-principles theory of the luminescence lineshape for the triplet transition in diamond nv centres. *New Journal of Physics*, 16(7):073026, jul 2014.

[8] G. A. Álvarez, A. Ajoy, X. Peng, and D. Suter. Performance comparison of dynamical decoupling sequences for a qubit in a rapidly fluctuating spin bath. *Phys. Rev. A*, 82:042306, Oct 2010.

[9] C. A. J. Ammerlaan and I. de Maat-Gersdorf. Zeeman splitting factor of the Er^{3+} ion in a crystal field. *Applied Magnetic Resonance*, 21(1):13–33, Aug 2001.

[10] C. P. Anderson, E. O. Glen, C. Zeledon, A. Bourassa, Y. Jin, Y. Zhu, C. Vorwerk, A. L. Crook, H. Abe, J. Ul-Hassan, T. Ohshima, N. T. Son, G. Galli, and D. D. Awschalom. Five-second coherence of a single spin with single-shot readout in silicon carbide. *Science Advances*, 8(5):eabm5912, 2022.

[11] R. S. Anderson, R. G. Brabin-Smith, and V. W. Rampton. The acoustic paramagnetic resonance of x-irradiated ruby. *Journal of Physics C: Solid State Physics*, 3(12):2379–2386, Dec. 1970.

[12] Anonymous. Proceedings of the american physical society. *Phys. Rev.*, 69:674–674, Jun 1946.

[13] ANSYS. Ansys electronics suite 2022 r1, 2022.

[14] A. Antuzevics. Epr characterization of erbium in glasses and glass ceramics. *Low Temperature Physics*, 46(12):1149–1153, 2020.

[15] F. K. Asadi, S. C. Wein, and C. Simon. Protocols for long-distance quantum communication with single ^{167}Er ions. *Quantum Science and Technology*, 5(4):045015, sep 2020.

[16] T. Astner, P. Koller, C. M. Gilardoni, J. Hendriks, N. T. Son, I. G. Ivanov, J. U. Hassan, C. H. van der Wal, and M. Trupke. Vanadium in silicon carbide: Telecom-ready spin centres with long relaxation lifetimes and hyperfine-resolved optical transitions, 2022.

[17] D. Awschalom, K. K. Berggren, H. Bernien, S. Bhave, L. D. Carr, P. Davids, S. E. Economou, D. Englund, A. Faraon, M. Fejer, S. Guha, M. V. Gustafsson, E. Hu, L. Jiang, J. Kim, B. Korzh, P. Kumar, P. G. Kwiat, M. Lončar, M. D. Lukin, D. A. Miller, C. Monroe, S. W. Nam, P. Narang, J. S. Orcutt, M. G. Raymer, A. H. Safavi-Naeini, M. Spiropulu, K. Srinivasan, S. Sun, J. Vučković, E. Waks, R. Walsworth, A. M. Weiner, and Z. Zhang. Development of quantum interconnects (quics) for next-generation information technologies. *PRX Quantum*, 2:017002, Feb 2021.

[18] G. Balasubramanian, P. Neumann, D. Twitchen, M. Markham, R. Kolesov, N. Mizuochi, J. Isoya, J. Achard, J. Beck, J. Tissler, V. Jacques, P. R. Hemmer, F. Jelezko, and J. Wrachtrup. Ultralong spin coherence time in isotopically engineered diamond. *Nature Materials*, 8(5):383–387, May 2009.

[19] J. R. Ball, Y. Yamashiro, H. Sumiya, S. Onoda, T. Ohshima, J. Isoya, D. Konstantinov, and Y. Kubo. Loop-gap microwave resonator for hybrid quantum systems. *Applied Physics Letters*, 112(20):204102, 2018.

[20] N. Bar-Gill, L. M. Pham, A. Jarmola, D. Budker, and R. L. Walsworth. Solid-state electronic spin coherence time approaching one second. *Nature Communications*, 4(1):1743, Apr 2013.

[21] P. S. Barnett and J. J. Longdell. Theory of microwave-optical conversion using rare-earth-ion dopants. *Phys. Rev. A*, 102:063718, Dec 2020.

[22] J. G. Bartholomew, K. de Oliveira Lima, A. Ferrier, and P. Goldner. Optical line width broadening mechanisms at the 10 khz level in eu3+:y2o3 nanoparticles. *Nano Letters*, 17(2):778–787, 2017. PMID: 28099025.

[23] J. G. Bartholomew, J. Rochman, T. Xie, J. M. Kindem, A. Ruskuc, I. Craiciu, M. Lei, and A. Faraon. On-chip coherent microwave-to-optical transduction mediated by ytterbium in yvo4. *Nature Communications*, 11(1):3266, Jun 2020.

[24] C. H. Bennett, G. Brassard, S. Popescu, B. Schumacher, J. A. Smolin, and W. K. Wootters. Purification of noisy entanglement and faithful teleportation via noisy channels. *Phys. Rev. Lett.*, 76:722–725, Jan 1996.

[25] H. Bernien, B. Hensen, W. Pfaff, G. Koolstra, M. S. Blok, L. Robledo, T. H. Taminiau, M. Markham, D. J. Twitchen, L. Childress, and R. Hanson. Heralded entanglement between solid-state qubits separated by three metres. *Nature*, 497(7447):86–90, May 2013.

[26] M. K. Bhaskar, R. Riedinger, B. Machielse, D. S. Levonian, C. T. Nguyen, E. N. Knall, H. Park, D. Englund, M. Lončar, D. D. Sukachev, and M. D. Lukin. Experimental demonstration of memory-enhanced quantum communication. *Nature*, 580(7801):60–64, Apr 2020.

[27] A. Bienfait. *Magnetic resonance with quantum microwaves*. Theses, Université Paris Saclay (COmUE), Oct. 2016.

[28] A. Bienfait, J. J. Pla, Y. Kubo, X. Zhou, M. Stern, C. C. Lo, C. D. Weis, T. Schenkel, D. Vion, D. Esteve, J. J. L. Morton, and P. Bertet. Controlling spin relaxation with a cavity. *Nature*, 531(7592):74–77, Mar 2016.

[29] E. D. Black. An introduction to pound–drever–hall laser frequency stabilization. *American Journal of Physics*, 69(1):79–87, 2001.

[30] H. Bluhm, S. Foletti, I. Neder, M. Rudner, D. Mahalu, V. Umansky, and A. Yacoby. Dephasing time of gaas electron-spin qubits coupled to a nuclear bath exceeding 200 μs. *Nature Physics*, 7(2):109–113, Feb 2011.

[31] C. Bond, D. Brown, A. Freise, and K. A. Strain. Interferometer techniques for gravitational-wave detection. *Living Reviews in Relativity*, 19(1):3, Feb 2017.

[32] T. Böttger, C. W. Thiel, Y. Sun, and R. L. Cone. Optical decoherence and spectral diffusion at 1.5 μm in er^{3+} : y_2sio_5 versus magnetic field, temperature, and er^{3+} concentration. *Phys. Rev. B*, 73:075101, Feb 2006.

[33] A. Bourassa, C. P. Anderson, K. C. Miao, M. Onizhuk, H. Ma, A. L. Crook, H. Abe, J. Ul-Hassan, T. Ohshima, N. T. Son, G. Galli, and D. D. Awschalom. Entanglement and control of single nuclear spins in isotopically engineered silicon carbide. *Nature Materials*, 19(12):1319–1325, Dec 2020.

[34] E. Britannica. electron probabilities for gadolinium.

[35] R. P. Budoyo, K. Kakuyanagi, H. Toida, Y. Matsuzaki, W. J. Munro, H. Yamaguchi, and S. Saito. Phonon-bottlenecked spin relaxation of er3+:y2sio5 at sub-kelvin temperatures. *Applied Physics Express*, 11(4):043002, mar 2018.

[36] B. Car, J.-L. Le Gouët, and T. Chanelière. Superhyperfine induced photon-echo collapse of erbium in Y_2SiO_5. *Phys. Rev. B*, 102:115119, Sep 2020.

[37] H. Y. Carr and E. M. Purcell. Effects of diffusion on free precession in nuclear magnetic resonance experiments. *Phys. Rev.*, 94:630–638, May 1954.

[38] S. Chakravarthi, C. Pederson, Z. Kazi, A. Ivanov, and K.-M. C. Fu. Impact of surface and laser-induced noise on the spectral stability of implanted nitrogen-vacancy centers in diamond. *Phys. Rev. B*, 104:085425, Aug 2021.

[39] K. W. Chan, W. Huang, C. H. Yang, J. C. C. Hwang, B. Hensen, T. Tanttu, F. E. Hudson, K. M. Itoh, A. Laucht, A. Morello, and A. S. Dzurak. Assessment of a silicon quantum dot spin qubit environment via noise spectroscopy. *Phys. Rev. Applied*, 10:044017, Oct 2018.

[40] S. Chen, M. Raha, C. M. Phenicie, S. Ourari, and J. D. Thompson. Parallel single-shot measurement and coherent control of solid-state spins below the diffraction limit. *Science*, 370(6516):592–595, 2020.

[41] Y.-H. Chen, X. Fernandez-Gonzalvo, S. P. Horvath, J. V. Rakonjac, and J. J. Longdell. Hyperfine interactions of er^{3+} ions in y_2sio_5: Electron paramagnetic resonance in a tunable microwave cavity. *Phys. Rev. B*, 97:024419, Jan 2018.

[42] J. Choi, H. Zhou, H. S. Knowles, R. Landig, S. Choi, and M. D. Lukin. Robust dynamic hamiltonian engineering of many-body spin systems. *Phys. Rev. X*, 10:031002, Jul 2020.

[43] D. J. Christle, P. V. Klimov, C. F. de las Casas, K. Szász, V. Ivády, V. Jokubavicius, J. Ul Hassan, M. Syväjärvi, W. F. Koehl, T. Ohshima, N. T. Son, E. Janzén, A. Gali, and D. D. Awschalom. Isolated spin qubits in sic with a high-fidelity infrared spin-to-photon interface. *Phys. Rev. X*, 7:021046, Jun 2017.

[44] J. I. Cirac, P. Zoller, H. J. Kimble, and H. Mabuchi. Quantum state transfer and entanglement distribution among distant nodes in a quantum network. *Phys. Rev. Lett.*, 78:3221–3224, Apr 1997.

[45] A. A. Clerk, M. H. Devoret, S. M. Girvin, F. Marquardt, and R. J. Schoelkopf. Introduction to quantum noise, measurement, and amplification. *Rev. Mod. Phys.*, 82:1155–1208, Apr 2010.

[46] E. Z. Cruzeiro, A. Tiranov, I. Usmani, C. Laplane, J. Lavoie, A. Ferrier, P. Goldner, N. Gisin, and M. Afzelius. Spectral hole lifetimes and spin population relaxation dynamics in neodymium-doped yttrium orthosilicate. *Phys. Rev. B*, 95:205119, May 2017.

[47] V. Damon, M. Bonarota, A. Louchet-Chauvet, T. Chanelière, and J.-L. L. Gouët. Revival of silenced echo and quantum memory for light. *New Journal of Physics*, 13(9):093031, sep 2011.

[48] M. L. Dantec, M. Rančić, S. Lin, E. Billaud, V. Ranjan, D. Flanigan, S. Bertaina, T. Chanelière, P. Goldner, A. Erb, R. B. Liu, D. Estève, D. Vion, E. Flurin, and P. Bertet. Twenty-three-millisecond electron spin coherence of erbium ions in a natural-abundance crystal. *Science Advances*, 7(51):eabj9786, 2021.

[49] S. E. de Graaf, A. V. Danilov, and S. E. Kubatkin. Accurate real-time monitoring of quality factor and center frequency of superconducting resonators. *IEEE Transactions on Applied Superconductivity*, 24(6):1–5, 2014.

[50] S. E. de Graaf, L. Faoro, J. Burnett, A. A. Adamyan, A. Y. Tzalenchuk, S. E. Kubatkin, T. Lindström, and A. V. Danilov. Suppression of low-frequency charge noise in superconducting resonators by surface spin desorption. *Nature Communications*, 9(1):1143, Mar 2018.

[51] C. L. Degen, F. Reinhard, and P. Cappellaro. Quantum sensing. *Rev. Mod. Phys.*, 89:035002, Jul 2017.

[52] C. Deng, M. Otto, and A. Lupascu. An analysis method for transmission measurements of superconducting resonators with applications to quantum-regime dielectric-loss measurements. *Journal of Applied Physics*, 114(5):054504, 2013.

[53] R. G. DeVoe and R. G. Brewer. Experimental test of the optical bloch equations for solids. *Phys. Rev. Lett.*, 50:1269–1272, Apr 1983.

[54] A. M. Dibos, M. Raha, C. M. Phenicie, and J. D. Thompson. Atomic source of single photons in the telecom band. *Phys. Rev. Lett.*, 120:243601, Jun 2018.

[55] B. Diler, S. J. Whiteley, C. P. Anderson, G. Wolfowicz, M. E. Wesson, E. S. Bielejec, F. Joseph Heremans, and D. D. Awschalom. Coherent control and high-fidelity readout of chromium ions in commercial silicon carbide. *npj Quantum Information*, 6(1):11, Jan 2020.

[56] I. Diniz, S. Portolan, R. Ferreira, J. M. Gérard, P. Bertet, and A. Auffèves. Strongly coupling a cavity to inhomogeneous ensembles of emitters: Potential for long-lived solid-state quantum memories. *Phys. Rev. A*, 84:063810, Dec 2011.

[57] G. Dold, C. W. Zollitsch, J. O'Sullivan, S. Welinski, A. Ferrier, P. Goldner, S. de Graaf, T. Lindström, and J. J. Morton. High-cooperativity coupling of a rare-earth spin ensemble to a superconducting resonator using yttrium orthosilicate as a substrate. *Phys. Rev. Appl.*, 11:054082, May 2019.

[58] G. Dold, C. W. Zollitsch, J. O'Sullivan, S. Welinski, A. Ferrier, P. Goldner, S. de Graaf, T. Lindström, and J. J. Morton. High-cooperativity coupling of a rare-earth spin ensemble to a superconducting resonator using yttrium orthosilicate as a substrate. *Phys. Rev. Applied*, 11:054082, May 2019.

[59] G. P. Dold. *milliKelvin ESR of rare-earth doped crystals using superconducting resonators*. PhD thesis, UNIVERSITY COLLEGE LONDON, 2020.

[60] L.-M. Duan, M. D. Lukin, J. I. Cirac, and P. Zoller. Long-distance quantum communication with atomic ensembles and linear optics. *Nature*, 414(6862):413–418, Nov 2001.

[61] A. Dulčić and B. Rakvin. Frequency versus field modulation in magnetic resonance. *Journal of Magnetic Resonance (1969)*, 52(2):323–325, 1983.

[62] Z. E. Paramagnetic relaxation of liquid solutions for perpendicular fields. *Journal of Physics, USSR*, 9:211–216, 1945.

[63] Z. E. Spin magnetic resonance in the decimetre-wave region. *Journal of Physics, USSR*, 10:197, 1946.

[64] C. Eichler, A. J. Sigillito, S. A. Lyon, and J. R. Petta. Electron spin resonance at the level of 10^4 spins using low impedance superconducting resonators. *Phys. Rev. Lett.*, 118:037701, Jan 2017.

[65] R. E. Evans, A. Sipahigil, D. D. Sukachev, A. S. Zibrov, and M. D. Lukin. Narrow-linewidth homogeneous optical emitters in diamond nanostructures via silicon ion implantation. *Phys. Rev. Appl.*, 5:044010, Apr 2016.

[66] J. R. Everts, M. C. Berrington, R. L. Ahlefeldt, and J. J. Longdell. Microwave to optical photon conversion via fully concentrated rare-earth-ion crystals. *Phys. Rev. A*, 99:063830, Jun 2019.

[67] X. Fernandez-Gonzalvo, Y.-H. Chen, C. Yin, S. Rogge, and J. J. Longdell. Coherent frequency up-conversion of microwaves to the optical telecommunications band in an er:yso crystal. *Phys. Rev. A*, 92:062313, Dec 2015.

[68] X. Fernandez-Gonzalvo, S. P. Horvath, Y.-H. Chen, and J. J. Longdell. Cavity-enhanced raman heterodyne spectroscopy in er^{3+} : y_2sio_5 for microwave to optical signal conversion. *Phys. Rev. A*, 100:033807, Sep 2019.

[69] M. Fleischhauer, A. Imamoglu, and J. P. Marangos. Electromagnetically induced transparency: Optics in coherent media. *Rev. Mod. Phys.*, 77:633–673, Jul 2005.

[70] R. Fukumori, Y. Huang, J. Yang, H. Zhang, and T. Zhong. Subkilohertz optical homogeneous linewidth and dephasing mechanisms in Er^{3+}:Y_2O_3 ceramics. *Phys. Rev. B*, 101:214202, Jun 2020.

[71] J. M. Gambetta, J. M. Chow, and M. Steffen. Building logical qubits in a superconducting quantum computing system. *npj Quantum Information*, 3(1):2, Jan 2017.

[72] J. Ganem, Y. P. Wang, D. Boye, R. S. Meltzer, W. M. Yen, and R. M. Macfarlane. Nonexponential photon-echo decays of paramagnetic ions in the superhyperfine limit. *Phys. Rev. Lett.*, 66:695–698, Feb 1991.

[73] O. Guillot-Noël, P. Goldner, Y. L. Du, E. Baldit, P. Monnier, and K. Bencheikh. Hyperfine interaction of er^{3+} ions in y_2Sio_5: An electron paramagnetic resonance spectroscopy study. *Phys. Rev. B*, 74:214409, Dec 2006.

[74] O. Guillot-Noël, H. Vezin, P. Goldner, F. Beaudoux, J. Vincent, J. Lejay, and I. Lorgeré. Direct observation of rare-earth-host interactions in Er : y_2Sio_5. *Phys. Rev. B*, 76:180408, Nov 2007.

[75] M. Gulka, D. Wirtitsch, V. Ivády, J. Vodnik, J. Hruby, G. Magchiels, E. Bourgeois, A. Gali, M. Trupke, and M. Nesladek. Room-temperature control and electrical readout of individual nitrogen-vacancy nuclear spins. *Nature Communications*, 12(1):4421, Jul 2021.

[76] T. Gullion, D. B. Baker, and M. S. Conradi. New, compensated carr-purcell sequences. *Journal of Magnetic Resonance (1969)*, 89(3):479–484, 1990.

[77] S. Gupta, X. Wu, J. Yang, H. Zhang, and T. Zhong. Robust millisecond coherence time of erbium electron spins. *Physical Review Applied (Under review)*, 2022.

[78] E. L. Hahn. Spin echoes. *Phys. Rev.*, 80:580–594, Nov 1950.

[79] F. S. Ham. Acoustic paramagnetic resonance spectrum of cr^{2+} in mgo. *Phys. Rev. B*, 4:3854–3869, Dec 1971.

[80] J. R. Harbridge, S. S. Eaton, and G. R. Eaton. Comparison of electron spin relaxation times measured by carr–purcell–meiboom–gill and two-pulse spin-echo sequences. *Journal of Magnetic Resonance*, 164(1):44–53, 2003.

[81] W. N. Hardy and L. A. Whitehead. Split-ring resonator for use in magnetic resonance from 200–2000 mhz. *Review of Scientific Instruments*, 52(2):213–216, 1981.

[82] T. L. Harris. *Erbium-based optical coherent transient correlator for the 1.5-micron communication bands*. PhD thesis, MONTANA STATE UNIVERSITY, Aug. 2001. Provided by the SAO/NASA Astrophysics Data System.

[83] B. Hensen, H. Bernien, A. E. Dréau, A. Reiserer, N. Kalb, M. S. Blok, J. Ruitenberg, R. F. L. Vermeulen, R. N. Schouten, C. Abellán, W. Amaya, V. Pruneri, M. W. Mitchell, M. Markham, D. J. Twitchen, D. Elkouss, S. Wehner, T. H. Taminiau, and R. Hanson. Loophole-free bell inequality violation using electron spins separated by 1.3 kilometres. *Nature*, 526(7575):682–686, Oct 2015.

[84] S. L. N. Hermans, M. Pompili, H. K. C. Beukers, S. Baier, J. Borregaard, and R. Hanson. Qubit teleportation between non-neighbouring nodes in a quantum network. *Nature*, 605(7911):663–668, May 2022.

[85] H. Hirata, T. Kuyama, M. Ono, and Y. Shimoyama. Detection of electron paramagnetic resonance absorption using frequency modulation. *Journal of Magnetic Resonance*, 164(2):233–241, 2003.

[86] S. P. Horvath, C. M. Phenicie, S. Ourari, M. T. Uysal, S. Chen, Łukasz Dusanowski, M. Raha, P. Stevenson, A. T. Turflinger, R. J. Cava, N. P. de Leon, and J. D. Thompson. Strong purcell enhancement of an optical magnetic dipole transition, 2023.

[87] J.-Y. Huang, P.-Y. Li, Z.-Q. Zhou, C.-F. Li, and G.-C. Guo. Extending the spin coherence lifetimes of $^{167}Er^{3+}$:y_2sio_5 at subkelvin temperatures. *Phys. Rev. B*, 105:245134, Jun 2022.

[88] M. A. Hughes, N. A. Panjwani, M. Urdampilleta, N. Theodoropoulou, I. Wisby, K. P. Homewood, B. Murdin, T. Lindström, and J. D. Carey. Coupling of erbium-implanted silicon to a superconducting resonator. *Phys. Rev. Appl.*, 16:034006, Sep 2021.

[89] J. S. Hyde, W. Froncisz, and T. Oles. Multipurpose loop-gap resonator. *Journal of Magnetic Resonance (1969)*, 82(2):223–230, Apr 1989.

[90] J. S. Hyde, W. Froncisz, J. W. Sidabras, T. G. Camenisch, J. R. Anderson, and R. A. Strangeway. Microwave frequency modulation in cw epr at w-band using a loop-gap resonator. *Journal of Magnetic Resonance*, 185(2):259–263, 2007.

[91] Z. Instruments. Frequency up-conversion for arbitrary waveform generators, zurich instruments.

[92] T. Iwasaki, Y. Miyamoto, T. Taniguchi, P. Siyushev, M. H. Metsch, F. Jelezko, and M. Hatano. Tin-vacancy quantum emitters in diamond. *Phys. Rev. Lett.*, 119:253601, Dec 2017.

[93] S. Kanai, F. J. Heremans, H. Seo, G. Wolfowicz, C. P. Anderson, S. E. Sullivan, M. Onizhuk, G. Galli, D. D. Awschalom, and H. Ohno. Generalized scaling of spin qubit coherence in over 12,000 host materials. *Proceedings of the National Academy of Sciences*, 119(15):e2121808119, 2022.

[94] C. Karunakaran and M. Balamurugan. Chapter five - advances in electron paramagnetic resonance. In C. Karunakaran, editor, *Spin Resonance Spectroscopy*, pages 229–280. Elsevier, 2018.

[95] M. Kim, H. J. Mamin, M. H. Sherwood, K. Ohno, D. D. Awschalom, and D. Rugar. Decoherence of near-surface nitrogen-vacancy centers due to electric field noise. *Phys. Rev. Lett.*, 115:087602, Aug 2015.

[96] H. J. Kimble. The quantum internet. *Nature*, 453(7198):1023–1030, Jun 2008.

[97] F. Kimiaee Asadi, J.-W. Ji, and C. Simon. Proposal for transduction between microwave and optical photons using ^{167}Er-doped yttrium orthosilicate. *Phys. Rev. A*, 105:062608, Jun 2022.

[98] J. M. Kindem, A. Ruskuc, J. G. Bartholomew, J. Rochman, Y. Q. Huan, and A. Faraon. Control and single-shot readout of an ion embedded in a nanophotonic cavity. *Nature*, 580(7802):201–204, Apr 2020.

[99] G. G. G. King, P. S. Barnett, J. G. Bartholomew, A. Faraon, and J. J. Longdell. Probing strong coupling between a microwave cavity and a spin ensemble with raman heterodyne spectroscopy. *Phys. Rev. B*, 103:214305, Jun 2021.

[100] J. R. Klauder and P. W. Anderson. Spectral diffusion decay in spin resonance experiments. *Phys. Rev.*, 125:912–932, Feb 1962.

[101] T. Kohmoto, Y. Fukuda, M. Kunitomo, K. Ishikawa, Y. Takahashi, K. Ebina, and M. Kaburagi. Hole burning in a well-characterized noise field: Nonadherence to the bloch equations. *Phys. Rev. B*, 52:13475–13479, Nov 1995.

[102] T. Kornher, D.-W. Xiao, K. Xia, F. Sardi, N. Zhao, R. Kolesov, and J. Wrachtrup. Sensing individual nuclear spins with a single rare-earth electron spin. *Phys. Rev. Lett.*, 124:170402, Apr 2020.

[103] N. Kukharchyk, D. Sholokhov, O. Morozov, S. L. Korableva, A. A. Kalachev, and P. A. Bushev. Optical coherence of ^{166}Er :^{7} $LiYF_4$ crystal below 1 k. *New Journal of Physics*, 20(2):023044, feb 2018.

[104] N. Kunkel, J. Bartholomew, L. Binet, A. Ikesue, and P. Goldner. High-resolution optical line width measurements as a material characterization tool. *The Journal of Physical Chemistry C*, 120(25):13725–13731, Jun 2016.

[105] G. Kurizki, P. Bertet, Y. Kubo, K. Mølmer, D. Petrosyan, P. Rabl, and J. Schmiedmayer. Quantum technologies with hybrid systems. *Proceedings of the National Academy of Sciences*, 112(13):3866–3873, 2015.

[106] G. Kurizki, P. Bertet, Y. Kubo, K. Mølmer, D. Petrosyan, P. Rabl, and J. Schmiedmayer. Quantum technologies with hybrid systems. *Proceedings of the National Academy of Sciences*, 112(13):3866–3873, 2015.

[107] T. D. Ladd, F. Jelezko, R. Laflamme, Y. Nakamura, C. Monroe, and J. L. O'Brien. Quantum computers. *Nature*, 464(7285):45–53, Mar 2010.

[108] E. Lafitte-Houssat, A. Ferrier, S. Welinski, L. Morvan, M. Afzelius, P. Berger, and P. Goldner. Optical and spin inhomogeneous linewidths in $^{171}Yb3^{+}$:Y_2SiO_5. *Optical Materials: X*, 14:100153, May 2022.

[109] B. Lauritzen, J. c. v. Minář, H. de Riedmatten, M. Afzelius, and N. Gisin. Approaches for a quantum memory at telecommunication wavelengths. *Phys. Rev. A*, 83:012318, Jan 2011.

[110] Y. Lei, F. K. Asadi, T. Zhong, A. Kuzmich, C. Simon, and M. Hosseini. Quantum optical memory for entanglement distribution, 2023.

[111] P.-Y. Li, C. Liu, Z.-Q. Zhou, X. Liu, T. Tu, T.-S. Yang, Z.-F. Li, Y. Ma, J. Hu, P.-J. Liang, X. Li, J.-Y. Huang, T.-X. Zhu, C.-F. Li, and G.-C. Guo. Hyperfine structure and coherent dynamics of rare-earth spins explored with electron-nuclear double resonance at subkelvin temperatures. *Phys. Rev. Applied*, 13:024080, Feb 2020.

[112] H.-J. Lim, S. Welinski, A. Ferrier, P. Goldner, and J. J. L. Morton. Coherent spin dynamics of ytterbium ions in yttrium orthosilicate. *Phys. Rev. B*, 97:064409, Feb 2018.

[113] T. Lindström, J. Burnett, M. Oxborrow, and A. Y. Tzalenchuk. Pound-locking for characterization of superconducting microresonators. *Review of Scientific Instruments*, 82(10):104706, 2011.

[114] G. Liu and B. Jacquier. *Spectroscopic Properties of Rare Earths in Optical Materials*. Springer, 2005.

[115] T. Lutz, L. Veissier, C. W. Thiel, R. L. Cone, P. E. Barclay, and W. Tittel. Modification of phonon processes in nanostructured rare-earth-ion-doped crystals. *Phys. Rev. A*, 94:013801, Jul 2016.

[116] T. Lutz, L. Veissier, C. W. Thiel, R. L. Cone, P. E. Barclay, and W. Tittel. Modification of phonon processes in nanostructured rare-earth-ion-doped crystals. *Phys. Rev. A*, 94:013801, Jul 2016.

[117] C. Macklin, K. O'Brien, D. Hover, M. E. Schwartz, V. Bolkhovsky, X. Zhang, W. D. Oliver, and I. Siddiqi. A near–quantum-limited josephson traveling-wave parametric amplifier. *Science*, 350(6258):307–310, 2015.

[118] P. Mansfield. Symmetrized pulse sequences in high resolution NMR in solids. *Journal of Physics C: Solid State Physics*, 4(11):1444–1452, Aug. 1971.

[119] B. McCullian, H. Cheung, H. Chen, and G. Fuchs. Quantifying the spectral diffusion of n-v centers by symmetry. *Phys. Rev. Appl.*, 18:064011, Dec 2022.

[120] L. McKenzie-Sell, J. Xie, C.-M. Lee, J. W. A. Robinson, C. Ciccarelli, and J. A. Haigh. Low-impedance superconducting microwave resonators for strong coupling to small magnetic mode volumes. *Phys. Rev. B*, 99:140414, Apr 2019.

[121] B. Merkel, P. Cova Fariña, and A. Reiserer. Dynamical decoupling of spin ensembles with strong anisotropic interactions. *Phys. Rev. Lett.*, 127:030501, Jul 2021.

[122] W. B. Mims, K. Nassau, and J. D. McGee. Spectral diffusion in electron resonance lines. *Phys. Rev.*, 123:2059–2069, Sep 1961.

[123] J. J. Morton and P. Bertet. Storing quantum information in spins and high-sensitivity esr. *Journal of Magnetic Resonance*, 287:128–139, 2018.

[124] S. Muralidharan, L. Li, J. Kim, N. Lütkenhaus, M. D. Lukin, and L. Jiang. Optimal architectures for long distance quantum communication. *Scientific Reports*, 6(1):20463, Feb 2016.

[125] C. Müller, J. H. Cole, and J. Lisenfeld. Towards understanding two-level-systems in amorphous solids: insights from quantum circuits. *Reports on Progress in Physics*, 82(12):124501, oct 2019.

[126] M. Onizhuk, K. C. Miao, J. P. Blanton, H. Ma, C. P. Anderson, A. Bourassa, D. D. Awschalom, and G. Galli. Probing the coherence of solid-state qubits at avoided crossings. *PRX Quantum*, 2:010311, Jan 2021.

[127] A. Ortu, A. Tiranov, S. Welinski, F. Fröwis, N. Gisin, A. Ferrier, P. Goldner, and M. Afzelius. Simultaneous coherence enhancement of optical and microwave transitions in solid-state electronic spins. *Nature Materials*, 17(8):671–675, Aug 2018.

[128] S. Ourari, Łukasz Dusanowski, S. P. Horvath, M. T. Uysal, C. M. Phenicie, P. Stevenson, M. Raha, S. Chen, R. J. Cava, N. P. de Leon, and J. D. Thompson. Indistinguishable telecom band photons from a single erbium ion in the solid state, 2023.

[129] E. S. Petersen, A. M. Tyryshkin, K. M. Itoh, J. W. Ager, H. Riemann, N. V. Abrosimov, P. Becker, H. J. Pohl, M. L. W. Thewalt, and S. A. Lyon. Dynamical decoupling of interacting dipolar spin ensembles, 2018.

[130] B. Pingault, J. N. Becker, C. H. H. Schulte, C. Arend, C. Hepp, T. Godde, A. I. Tartakovskii, M. Markham, C. Becher, and M. Atatüre. All-optical formation of coherent dark states of silicon-vacancy spins in diamond. *Phys. Rev. Lett.*, 113:263601, Dec 2014.

[131] B. Pingault, D.-D. Jarausch, C. Hepp, L. Klintberg, J. N. Becker, M. Markham, C. Becher, and M. Atatüre. Coherent control of the silicon-vacancy spin in diamond. *Nature Communications*, 8(1):15579, May 2017.

[132] E. Poem, S. Gupta, I. Morris, K. Klink, L. Singh, T. Zhong, J. N. Becker, and O. Firstenberg. Transition metal ion ensembles in crystals as solid-state coherent spin-photon interfaces: The case of nickel in magnesium oxide, 2022.

[133] R. V. Pound. Electronic frequency stabilization of microwave oscillators. *Review of Scientific Instruments*, 17(11):490–505, 1946.

[134] S. Probst. *Hybrid quantum system based on rare earth doped crystals = Hybrides Quantensystem basierend auf Kristallen mit Seltenerddotierung*. PhD thesis, Karlsruher Institut für Technologie (KIT), 2015.

[135] S. Probst, H. Rotzinger, A. V. Ustinov, and P. A. Bushev. Microwave multimode memory with an erbium spin ensemble. *Phys. Rev. B*, 92:014421, Jul 2015.

[136] S. Probst, H. Rotzinger, S. Wünsch, P. Jung, M. Jerger, M. Siegel, A. V. Ustinov, and P. A. Bushev. Anisotropic rare-earth spin ensemble strongly coupled to a superconducting resonator. *Phys. Rev. Lett.*, 110:157001, Apr 2013.

[137] S. Probst, G. Zhang, M. Rančić, V. Ranjan, M. Le Dantec, Z. Zhang, B. Albanese, A. Doll, R. B. Liu, J. Morton, T. Chanelière, P. Goldner, D. Vion, D. Esteve, and P. Bertet. Hyperfine spectroscopy in a quantum-limited spectrometer. *Magnetic Resonance*, 1(2):315–330, 2020.

[138] I. Publishing and physicsworld. A roadmap for the quantum internet – Physics World — physicsworld.com. `https://physicsworld.com/a/a-roadmap-for-the-quantum-internet/`, 2021. [Accessed 26-May-2023].

[139] S. Putz. *Spin Echo Spectroscopy—Spin Refocusing*, pages 113–118. Springer International Publishing, Cham, 2017.

[140] M. Raha, S. Chen, C. M. Phenicie, S. Ourari, A. M. Dibos, and J. D. Thompson. Optical quantum nondemolition measurement of a single rare earth ion qubit. *Nature Communications*, 11(1):1605, 2020.

[141] T. Rajh, L. Sun, S. Gupta, J. Yang, H. Zhang, and T. Zhong. Hyperfine interactions and coherent spin dynamics of $^{167}Er^{3+}$ in Y_2O_3. *Materials for Quantum Technology (Under review)*, 2022.

[142] J. V. Rakonjac, Y.-H. Chen, S. P. Horvath, and J. J. Longdell. Long spin coherence times in the ground state and in an optically excited state of $^{167}Er^{3+} : y_2sio_5$ at zero magnetic field. *Phys. Rev. B*, 101:184430, May 2020.

[143] M. Rančić, M. Le Dantec, S. Lin, S. Bertaina, T. Chanelière, D. Serrano, P. Goldner, R. B. Liu, E. Flurin, D. Estève, D. Vion, and P. Bertet. Electron-spin spectral diffusion in an erbium doped crystal at millikelvin temperatures. *Phys. Rev. B*, 106:144412, Oct 2022.

[144] V. Ranjan, J. O'Sullivan, E. Albertinale, B. Albanese, T. Chanelière, T. Schenkel, D. Vion, D. Esteve, E. Flurin, J. J. L. Morton, and P. Bertet. Multimode storage of quantum microwave fields in electron spins over 100 ms. *Phys. Rev. Lett.*, 125:210505, Nov 2020.

[145] V. Ranjan, S. Probst, B. Albanese, A. Doll, O. Jacquot, E. Flurin, R. Heeres, D. Vion, D. Esteve, J. Morton, and P. Bertet. Pulsed electron spin resonance spectroscopy in the purcell regime. *Journal of Magnetic Resonance*, 310:106662, 2020.

[146] M. Rančić, M. L. Dantec, S. Lin, S. Bertaina, T. Chanelière, D. Serrano, P. Goldner, R. B. Liu, E. Flurin, D. Estève, D. Vion, and P. Bertet. Electron-spin spectral diffusion in an erbium doped crystal at millikelvin temperatures, 2022.

[147] M. Rančić, M. P. Hedges, R. L. Ahlefeldt, and M. J. Sellars. Coherence time of over a second in a telecom-compatible quantum memory storage material. *Nature Physics*, 14(1):50–54, Jan 2018.

[148] M. Razavi, M. Piani, and N. Lütkenhaus. Quantum repeaters with imperfect memories: Cost and scalability. *Phys. Rev. A*, 80:032301, Sep 2009.

[149] G. D. Reinemer. *Optical characterization of perturbed sites and C3i sites in rare earth doped oxide crystals*. PhD thesis, Montana State University, Jan. 2003. Provided by the SAO/NASA Astrophysics Data System.

[150] G. A. Rinard and G. R. Eaton. *Loop-Gap Resonators*, pages 19–52. Springer US, Boston, MA, 2005.

[151] J. Rochman, T. Xie, J. G. Bartholomew, K. C. Schwab, and A. Faraon. Microwave-to-optical transduction with erbium ions coupled to planar photonic and superconducting resonators. *Nature Communications*, 14(1):1153, Mar 2023.

[152] L. G. Rowan, E. L. Hahn, and W. B. Mims. Electron-spin-echo envelope modulation. *Phys. Rev.*, 137:A61–A71, Jan 1965.

[153] A. Ruskuc, C.-J. Wu, J. Rochman, J. Choi, and A. Faraon. Nuclear spin-wave quantum register for a solid-state qubit. *Nature*, 602(7897):408–413, Feb 2022.

[154] C. A. Ryan, J. S. Hodges, and D. G. Cory. Robust decoupling techniques to extend quantum coherence in diamond. *Phys. Rev. Lett.*, 105:200402, Nov 2010.

[155] R. G. Ryan, A. Stacey, K. M. O'Donnell, T. Ohshima, B. C. Johnson, L. C. L. Hollenberg, P. Mulvaney, and D. A. Simpson. Impact of surface functionalization on the quantum coherence of nitrogen-vacancy centers in nanodiamonds. *ACS Applied Materials & Interfaces*, 10(15):13143–13149, Apr 2018.

[156] D. R. H. F. R. S. The calculation of atomic structures. *Reports on Progress in Physics*, 11(1):113, jan 1947.

[157] N. Sangouard, C. Simon, H. de Riedmatten, and N. Gisin. Quantum repeaters based on atomic ensembles and linear optics. *Rev. Mod. Phys.*, 83:33–80, Mar 2011.

[158] M. Scarafagio, A. Tallaire, K.-J. Tielrooij, D. Cano, A. Grishin, M.-H. Chavanne, F. H. L. Koppens, A. Ringuedé, M. Cassir, D. Serrano, P. Goldner, and A. Ferrier. Ultrathin eu- and er-doped y2o3 films with optimized optical properties for quantum technologies. *The Journal of Physical Chemistry C*, 123(21):13354–13364, May 2019.

[159] G. Schäfer and S. Scheller. Paramagnetische resonanz von er3+ in y2o3. *Physik der kondensierten Materie*, 5(1):48–57, May 1966.

[160] G. E. Schäfer. Paramagnetische resonanz von er3+ und ce3+ in y2o3. *Physik der kondensierten Materie*, 9:359–366, 1969.

[161] A. Schweiger and G. Jeschke. *Principles of pulse electron paramagnetic resonance*. Oxford University Press, 1 edition, Dec. 2001.

[162] D. Serrano, C. Deshmukh, S. Liu, A. Tallaire, A. Ferrier, H. de Riedmatten, and P. Goldner. Coherent optical and spin spectroscopy of nanoscale $pr^{3+} : y_2o_3$. *Phys. Rev. B*, 100:144304, Oct 2019.

[163] D. Serrano, J. Karlsson, A. Fossati, A. Ferrier, and P. Goldner. All-optical control of long-lived nuclear spins in rare-earth doped nanoparticles. *Nature Communications*, 9(1):2127, May 2018.

[164] R. N. Shakhmuratov, F. M. Gelardi, and M. Cannas. Non-bloch transients in solids: Free induction decay and transient nutations. *Phys. Rev. Lett.*, 79:2963–2966, Oct 1997.

[165] A. J. Sigillito, H. Malissa, A. M. Tyryshkin, H. Riemann, N. V. Abrosimov, P. Becker, H.-J. Pohl, M. L. W. Thewalt, K. M. Itoh, J. J. L. Morton, A. A. Houck, D. I. Schuster, and S. A. Lyon. Fast, low-power manipulation of spin ensembles in superconducting microresonators. *Applied Physics Letters*, 104(22):222407, 2014.

[166] C. Simon and J.-W. Pan. Polarization entanglement purification using spatial entanglement. *Phys. Rev. Lett.*, 89:257901, Dec 2002.

[167] M. K. Singh, A. Prakash, G. Wolfowicz, J. Wen, Y. Huang, T. Rajh, D. D. Awschalom, T. Zhong, and S. Guha. Epitaxial er-doped y2o3 on silicon for quantum coherent devices. *APL Materials*, 8(3):031111, 2020.

[168] P. Siyushev, K. Xia, R. Reuter, M. Jamali, N. Zhao, N. Yang, C. Duan, N. Kukharchyk, A. D. Wieck, R. Kolesov, and J. Wrachtrup. Coherent properties of single rare-earth spin qubits. *Nature Communications*, 5(1):3895, May 2014.

[169] A. Skvortsov, D. Savchenko, Z. Potucek, L. Jastrabik, V. Trepakov, and A. Dejneka. Optical and epr characterization of er3+ centers in srtio3 single crystals. *physica status solidi (b)*, 251(11):2270–2273, 2014.

[170] Y.-I. Sohn, S. Meesala, B. Pingault, H. A. Atikian, J. Holzgrafe, M. Gündoğan, C. Stavrakas, M. J. Stanley, A. Sipahigil, J. Choi, M. Zhang, J. L. Pacheco, J. Abraham, E. Bielejec, M. D. Lukin, M. Atatüre, and M. Lončar. Controlling the coherence of a diamond spin qubit through its strain environment. *Nature Communications*, 9(1):2012, May 2018.

[171] A. M. Souza, G. A. Álvarez, and D. Suter. Effects of time-reversal symmetry in dynamical decoupling. *Phys. Rev. A*, 85:032306, Mar 2012.

[172] H. P. Specht, C. Nölleke, A. Reiserer, M. Uphoff, E. Figueroa, S. Ritter, and G. Rempe. A single-atom quantum memory. *Nature*, 473(7346):190–193, May 2011.

[173] P.-J. Stas, Y. Q. Huan, B. Machielse, E. N. Knall, A. Suleymanzade, B. Pingault, M. Sutula, S. W. Ding, C. M. Knaut, D. R. Assumpcao, Y.-C. Wei, M. K. Bhaskar, R. Riedinger, D. D. Sukachev, H. Park, M. Lončar, D. S. Levonian, and M. D. Lukin. Robust multi-qubit quantum network node with integrated error detection. *Science*, 378(6619):557–560, 2022.

[174] J. M. Stiles. System equivalent noise temperature.

[175] S. Stoll and A. Schweiger. Easyspin, a comprehensive software package for spectral simulation and analysis in epr. *Journal of Magnetic Resonance*, 178(1):42–55, 2006.

[176] D. D. Sukachev, A. Sipahigil, C. T. Nguyen, M. K. Bhaskar, R. E. Evans, F. Jelezko, and M. D. Lukin. Silicon-vacancy spin qubit in diamond: A quantum memory exceeding 10 ms with single-shot state readout. *Phys. Rev. Lett.*, 119:223602, Nov 2017.

[177] D. Suter and G. A. Álvarez. Colloquium: Protecting quantum information against environmental noise. *Rev. Mod. Phys.*, 88:041001, Oct 2016.

[178] S. Takahashi, R. Hanson, J. van Tol, M. S. Sherwin, and D. D. Awschalom. Quenching spin decoherence in diamond through spin bath polarization. *Phys. Rev. Lett.*, 101:047601, Jul 2008.

[179] C. Thiel, T. Böttger, and R. Cone. Rare-earth-doped materials for applications in quantum information storage and signal processing. *Journal of Luminescence*, 131(3):353–361, 2011. Selected papers from DPC'10.

[180] C. W. Thiel, R. M. Macfarlane, Y. Sun, T. Böttger, N. Sinclair, W. Tittel, and R. L. Cone. Measuring and analyzing excitation-induced decoherence in rare-earth-doped optical materials. *Laser Physics*, 24(10):106002, aug 2014.

[181] A. M. Tyryshkin, S. Tojo, J. J. L. Morton, H. Riemann, N. V. Abrosimov, P. Becker, H.-J. Pohl, T. Schenkel, M. L. W. Thewalt, K. M. Itoh, and S. A. Lyon. Electron spin coherence exceeding seconds in high-purity silicon. *Nature Materials*, 11(2):143–147, Feb 2012.

[182] G. Tóth and I. Apellaniz. Quantum metrology from a quantum information science perspective. *Journal of Physics A: Mathematical and Theoretical*, 47(42):424006, oct 2014.

[183] U.Haeberlan; J.S.Waugh. Coherent Averaging Effects in Magnetic Resonance. *Dk*, 53(9):1689–1699, 1968.

[184] S. J. van Enk, J. I. Cirac, and P. Zoller. Photonic channels for quantum communication. *Science*, 279(5348):205–208, 1998.

[185] J. Vincent, O. Guillot-Noël, L. Binet, P. Aschehoug, Y. Le Du, F. Beaudoux, and P. Goldner. Electron paramagnetic resonance and optical spectroscopy of er-doped $\beta - \mathrm{ga_2o_3}$. *Journal of Applied Physics*, 104(3):033519, 2008.

[186] K. Volkova, J. Heupel, S. Trofimov, F. Betz, R. Colom, R. W. MacQueen, S. Akhundzada, M. Reginka, A. Ehresmann, J. P. Reithmaier, S. Burger, C. Popov, and B. Naydenov. Optical and spin properties of nv center ensembles in diamond nano-pillars. *Nanomaterials*, 12(9), 2022.

[187] N. H. Wan, B. J. Shields, D. Kim, S. Mouradian, B. Lienhard, M. Walsh, H. Bakhru, T. Schröder, and D. Englund. Efficient extraction of light from a nitrogen-vacancy center in a diamond parabolic reflector. *Nano Letters*, 18(5):2787–2793, May 2018.

[188] S. Wang, L. Yang, M. Shen, W. Fu, Y. Xu, R. L. Cone, C. W. Thiel, and H. X. Tang. Er : linbo$_3$ with high optical coherence enabling optical thickness control. *Phys. Rev. Appl.*, 18:014069, Jul 2022.

[189] J. S. Waugh, L. M. Huber, and U. Haeberlen. Approach to high-resolution nmr in solids. *Phys. Rev. Lett.*, 20:180–182, Jan 1968.

[190] J. A. Weil and J. R. Bolton. *Electron paramagnetic resonance*. Wiley-Blackwell, Chichester, England, 2 edition, Dec. 2006.

[191] L. Weiss, A. Gritsch, B. Merkel, and A. Reiserer. Erbium dopants in nanophotonic silicon waveguides. *Optica*, 8(1):40–41, Jan 2021.

[192] S. Welinski, C. Thiel, J. Dajczgewand, A. Ferrier, R. Cone, R. Macfarlane, T. Chanelière, A. Louchet-Chauvet, and P. Goldner. Effects of disorder on optical and electron spin linewidths in er3+,sc3+:y2sio5. *Optical Materials*, 63:69–75, 2017. In honor of Professor Georges Boulon for his outstanding contributions to Optical Materials.

[193] S. Welinski, P. J. T. Woodburn, N. Lauk, R. L. Cone, C. Simon, P. Goldner, and C. W. Thiel. Electron spin coherence in optically excited states of rare-earth ions for microwave to optical quantum transducers. *Phys. Rev. Lett.*, 122:247401, Jun 2019.

[194] L. A. Williamson, Y.-H. Chen, and J. J. Longdell. Magneto-optic modulator with unit quantum efficiency. *Phys. Rev. Lett.*, 113:203601, Nov 2014.

[195] L. A. Williamson, Y.-H. Chen, and J. J. Longdell. Magneto-optic modulator with unit quantum efficiency. *Phys. Rev. Lett.*, 113:203601, Nov 2014.

[196] G. Wolfowicz, C. P. Anderson, B. Diler, O. G. Poluektov, F. J. Heremans, and D. D. Awschalom. Vanadium spin qubits as telecom quantum emitters in silicon carbide. *Science Advances*, 6(18):eaaz1192, 2020.

[197] G. Wolfowicz, F. J. Heremans, C. P. Anderson, S. Kanai, H. Seo, A. Gali, G. Galli, and D. D. Awschalom. Quantum guidelines for solid-state spin defects. *Nature Reviews Materials*, 6(10):906–925, Oct 2021.

[198] G. Wolfowicz, H. Maier-Flaig, R. Marino, A. Ferrier, H. Vezin, J. J. L. Morton, and P. Goldner. Coherent storage of microwave excitations in rare-earth nuclear spins. *Phys. Rev. Lett.*, 114:170503, Apr 2015.

[199] G. Wolfowicz, A. M. Tyryshkin, R. E. George, H. Riemann, N. V. Abrosimov, P. Becker, H.-J. Pohl, M. L. W. Thewalt, S. A. Lyon, and J. J. L. Morton. Atomic

clock transitions in silicon-based spin qubits. *Nature Nanotechnology*, 8(8):561–564, Aug 2013.

[200] R. L. Wood, W. Froncisz, and J. S. Hyde. The loop-gap resonator. ii. controlled return flux three-loop, two-gap microwave resonators for endor and esr spectroscopy. *Journal of Magnetic Resonance (1969)*, 58(2):243–253, 1984.

[201] H. Wu, R. E. George, J. H. Wesenberg, K. Mølmer, D. I. Schuster, R. J. Schoelkopf, K. M. Itoh, A. Ardavan, J. J. L. Morton, and G. A. D. Briggs. Storage of multiple coherent microwave excitations in an electron spin ensemble. *Phys. Rev. Lett.*, 105:140503, Sep 2010.

[202] K. Xia, F. Sardi, C. Sauerzapf, T. Kornher, H.-W. Becker, Z. Kis, L. Kovacs, D. Dertli, J. Foglszinger, R. Kolesov, and J. Wrachtrup. Tunable microcavities coupled to rare-earth quantum emitters. *Optica*, 9(4):445–450, Apr 2022.

[203] L. Yang, S. Wang, M. Shen, J. Xie, and H. X. Tang. Controlling single rare earth ion emission in an electro-optical nanocavity, 2022.

[204] H. D. Zeh. On the interpretation of measurement in quantum theory. *Foundations of Physics*, 1(1):69–76, Mar 1970.

[205] H. Zhang, J. Yang, S. Gray, J. A. Brown, T. D. Ketcham, D. E. Baker, A. Carapella, R. W. Davis, J. G. Arroyo, and D. A. Nolan. Transparent er3+-doped y2o3 ceramics with long optical coherence lifetime. *ACS Omega*, 2(7):3739–3744, Jul 2017.

[206] J. X. Zheng, G. Ceder, T. Maxisch, W. K. Chim, and W. K. Choi. Native point defects in yttria and relevance to its use as a high-dielectric-constant gate oxide material: First-principles study. *Phys. Rev. B*, 73:104101, Mar 2006.

[207] M. Zhong, M. P. Hedges, R. L. Ahlefeldt, J. G. Bartholomew, S. E. Beavan, S. M. Wittig, J. J. Longdell, and M. J. Sellars. Optically addressable nuclear spins in a solid with a six-hour coherence time. *Nature*, 517(7533):177–180, Jan 2015.

[208] T. Zhong and P. Goldner. Emerging rare-earth doped material platforms for quantum nanophotonics. *Nanophotonics*, 8:5821–5827, Sept 2019.

[209] T. Zhong, J. M. Kindem, J. G. Bartholomew, J. Rochman, I. Craiciu, E. Miyazono, M. Bettinelli, E. Cavalli, V. Verma, S. W. Nam, F. Marsili, M. D. Shaw, A. D. Beyer, and A. Faraon. Nanophotonic rare-earth quantum memory with optically controlled retrieval. *Science*, 357(6358):1392–1395, 2017.

[210] T. Zhong, J. M. Kindem, J. G. Bartholomew, J. Rochman, I. Craiciu, V. Verma, S. W. Nam, F. Marsili, M. D. Shaw, A. D. Beyer, and A. Faraon. Optically addressing single rare-earth ions in a nanophotonic cavity. *Phys. Rev. Lett.*, 121:183603, Oct 2018.

[211] T. Zhong, J. M. Kindem, E. Miyazono, and A. Faraon. Nanophotonic coherent light–matter interfaces based on rare-earth-doped crystals. *Nature Communications*, 6(1):8206, Sep 2015.

[212] Y. Zhong and J. Pilbrow. A consistent description of epr spectra. *Journal of Magnetic Resonance (1969)*, 93(3):447–457, 1991.

[213] H. Zhou, J. Choi, S. Choi, R. Landig, A. M. Douglas, J. Isoya, F. Jelezko, S. Onoda, H. Sumiya, P. Cappellaro, H. S. Knowles, H. Park, and M. D. Lukin. Quantum metrology with strongly interacting spin systems. *Phys. Rev. X*, 10:031003, Jul 2020.

[214] C. W. Zollitsch, J. O'Sullivan, O. Kennedy, G. Dold, and J. J. L. Morton. Tuning high-q superconducting resonators by magnetic field reorientation. *AIP Advances*, 9(12):125225, 2019.

[215] M. Šimėnas, J. O'Sullivan, C. W. Zollitsch, O. Kennedy, M. Seif-Eddine, I. Ritsch, M. Hülsmann, M. Qi, A. Godt, M. M. Roessler, G. Jeschke, and J. J. Morton. A sensitivity leap for x-band epr using a probehead with a cryogenic preamplifier. *Journal of Magnetic Resonance*, 322:106876, 2021.